The relationship between scrape-off layer filaments and density profiles in ASDEX Upgrade

Steven Thomas

Doctor of Philosophy

University of York

Physics

March 2022

Abstract

This thesis reports on the experimental analysis of the turbulence statistics of the ASDEX Upgrade scrape-off layer (SOL), and the filaments that populate it, for different L and H-mode discharges using the gas puff imaging (GPI) diagnostic. A synthetic GPI diagnostic is constructed and applied to a toy model to account for the smearing of filaments caused by imperfect alignment of the lines-of-sight and the local magnetic field.

Radial increases in relative fluctuation amplitude, skewness, and kurtosis are seen due to the presence of filaments whose characteristics vary as they propagate radially. The probability distribution functions (PDFs) of filament amplitude for a given pixel measurement at the GPI detector follow Gamma distributions which become increasingly skewed and flattened with increasing radius. These are similar between most of the discharge types, lending further evidence towards the so-called 'universality of the scrape-off layer', but the L-mode discharge with nitrogen seeding has an increase in each metric, and the most skewed and flattened PDFs, in the far SOL compared to the other discharge types. This is though to be caused by changes to the filaments and is corroborated with independent measurement of an increase in the filament amplitudes in the 2D GPI data.

Using GPI, independent measurements of individual filament poloidal sizes and radial velocities are made, and reported with respect to the Myra filament model. Most filaments are measured with sizes above the fundamental blob size with velocities under the sheath-limited regime velocity scaling, except for SOL locations closest to the separatrix. Distribution functions of filament sizes and velocities are measured, as well as the interdependence between different filament attributes, which are used as inputs to the Garcia-Militello SOL model.

This model is based on a statistical framework that links filaments and their motion to SOL density profiles. In the single-filament model it is shown that profile decay lengths are directly proportional to the the radial filament velocity, v_x, and parallel loss timescale, $\tau_{\|}$, the characteristic time at which filaments reduce in amplitude due to parallel losses. This model is expanded to show how radial changes of v_x or $\tau_{\|}$ can generate profiles with either increasing or decreasing decay lengths. From simulations of this model, measurements of the higher-order statistical profiles, as well as single-point PDFs, are compared to the experimental statistical characterisation of the SOL, allowing us fully use the model to determine which change of variable may result in the change of the density profile.

For the first time, this model is extended to include the distributions of filament attributes. It is shown, both analytically and in simulations, how the amplitude distribution is required for the quadratic scaling of kurtosis with skewness, seen for Gamma distributed fluctuation signals, and how the radial velocity distributions, in addition to spatial changes in v_x or $\tau_{\|}$, can lead to non-exponential decay profiles, as well as radial increases in higher-order statistical profiles. The model is first used in 1D and then extended to 2D, showing no change of the general results, and there is therefore no dependence of profile decay length on perpendicular filament size or velocity, even for large poloidal-to-radial velocity ratios.

Contents

List of Tables

List of Figures

Acknowledgments

Anyone who completes a PhD knows that it is a task of grand proportion, and very few would claim to have accomplished it without any assistance from other people, whether they help in a professional or personal capacity. I am no different and I would like to take this opportunity to express my gratitude.

First, I'd like to express my thanks to my supervisor, István Cziegler, for taking me on as his student in the first place and then proceeding to guide me through my research and help me learn what I've learned along the way. Particular thanks should be made for the arduous task of reading multiple iterations of this thesis.

Special thanks and gratitude are made to Michael Griener for assisting with our work on our visit to Garching, enabling us to take the data used throughout this thesis, as well as being a first port of call for help about multiple IPP services, systems, and information. I'd also like to thank Balazs Tal, Nicola Vianello, Nick Walkden, and Elisabeth Wolfrum, who were involved in helping, either practically or in organisation, during the visit.

Thank you to my TAP panel, David Dickinson and Sarah Thompson, for taking an interest in my research and facilitating a way for me to practice writing and presenting my work in a professional setting, as well as providing me with feedback that would only help to improve my thesis. My apologies for every time my writing and presenting went over the word count or allotted time.

A general thanks to anyone and everyone at the York Plasma Institute. This goes out to staff and friends alike whether it was for assisting with much of the administrative work that a four year project entails, someone in my office to discuss some work through with, or a group of friends to go for a drink with at the end of a difficult week, each are as important as the last. There are too many people to thank individually so, in fear of missing someone by writing a long list of names, know that I appreciate every one of you for making my time at the YPI so memorable.

A large appreciation to my parents, not just for the past four years, but in general. I'm very fortunate to have come from a loving and caring home, and their support and encouragement goes a long way to helping me reach this point in life.

Thanks to Floki, my fury four-legged friend, for keeping me company during some oth-

erwise lonely days working from home. He was always game for a walk round the local park, an excellent way to recharge for the afternoon.

Last, but certainly not least, my wonderful girlfriend, Alice. Thank you for being your lovely self for as long as I've known you, and thank you for being very supportive, caring, and loving throughout our time together, but especially during the final parts of writing this thesis. We're one step closer to a life of luxury and leisure.

Declaration

I declare that this thesis is a presentation of original work and I am the sole author. This work has not previously been presented for an award at this, or any other, University. All sources are acknowledged as References.

Chapter 1

Introduction

1.1 Nuclear fusion

The end goal of nuclear fusion is to contribute to the commercial production of electricity through the release of heat released from fusing small, light nuclei, recreating the energy production mechanism that powers the Sun. A few of fusion's greatest merits, in comparison with other means of electricity production, are: the fusion reactions do not directly produce or release carbon dioxide or other greenhouse gases; the fuel used has a high energy density, and therefore a relatively little amount of fuel is required; depending on the fusion reaction used, and thus the fuel type, the amount of reactants may be close to limitless, unlike fossil fuels such as coal and gas; it does not rely on unpredictable aspects of nature, such as the amount of wind or sunshine; fusion reactors are being designed from the ground-up with stringent limits of $\approx$100 years for the maximum timescale on which the radioactivity of materials can be an issue; and the disruption of a fusion reaction cannot lead to the same level of catastrophe seen in a nuclear reactor meltdown (e.g., Windscale, Chernobyl, or Fukushima).

Currently the fusion reaction thought most viable is between two isotopes of hydrogen, deuterium (^{2}D) and tritium (^{3}T), which fuse to produce one helium nucleus (^{4}He) and one neutron (n) per reaction

$$^2\mathrm{D} + {}^3\mathrm{T} \rightarrow {}^4\mathrm{He}(3.5\,\mathrm{MeV}) + \mathrm{n}(14.1\,\mathrm{MeV}). \tag{1.1}$$

This reaction has been chosen mainly due to the high reactivity/cross-section at lower ion

temperatures than other fusion reactions, and just so happens to release more energy than most other reactions. The reactivity, $\langle \sigma v \rangle$, which is the first moment of the cross-section of the reaction, σ, over the (assumed) Maxwellian velocity distribution of the ions, v, as a function of temperature for a few sample fusion reactions is shown in figure 1.1, where $\langle \sigma v \rangle_{\mathrm{DT}}$ is more than an order of magnitude greater than all other fusion reactions for $T \lesssim 60\,\mathrm{keV}$. Deuterium is naturally occurring in seawater (approximately 33 mg per litre [1]), whilst tritium is, unfortunately, radioactive with a half-life of 12.32 ± 0.02 years [2], and would need to be produced on-site through the interaction of the fusion neutrons with breeding blankets of lithium. It is because of this, coupled with extra restrictions or rules that limit the amount of tritium that can be both in a fusion reactor, and on-site in total (in the UK), most experimental fusion devices work with ^{2}D–^{2}D plasmas.* D–D is the next most-likely fusion reaction, from a reactivity viewpoint, and D–D experiments are the focus of this thesis. The D–D reaction is given by

$$^2\mathrm{D} + {}^2\mathrm{D} \rightarrow \begin{cases} {}^3\mathrm{He}(0.8\,\mathrm{MeV}) + \mathrm{n}(2.5\,\mathrm{MeV}) \\ {}^3\mathrm{T}(1.0\,\mathrm{MeV}) + {}^1\mathrm{H}(3.0\,\mathrm{MeV}). \end{cases} \tag{1.2}$$

For fusion to occur, the two nuclei must overcome the Coulomb repulsion between them and get sufficiently close to be within range of the strong nuclear force. This is obtained by heating the fuel to very high temperatures, whereby electrons are separated from their nuclei, and it becomes a plasma. It can be shown that in order to obtain ignition within a fusion plasma (i.e., the point at which the rate of fusion is high enough to sustain the fusion reaction with sufficiently high temperatures and densities for a long enough time through self heating by the emitted alpha particles, without the need for external energy application) the *Fusion Triple Product* must exceed

$$nT\tau_E \geq 5 \times 10^{21}\,\mathrm{keVs/m^3} \tag{1.3}$$

where n is the plasma density, T is the temperature, and τ_E is the energy confinement time, the timescale over which energy is lost from the plasma. This leads to two main approaches to achieving fusion: one is to compress the plasma to high densities, requiring

*The last time a tokamak ran with D–T fuel was JET, currently the only operational tokamak in the world to be able to run with D–T fuel, the last time being in 1997. Further D–T experiments have been planned there for this year. [3]

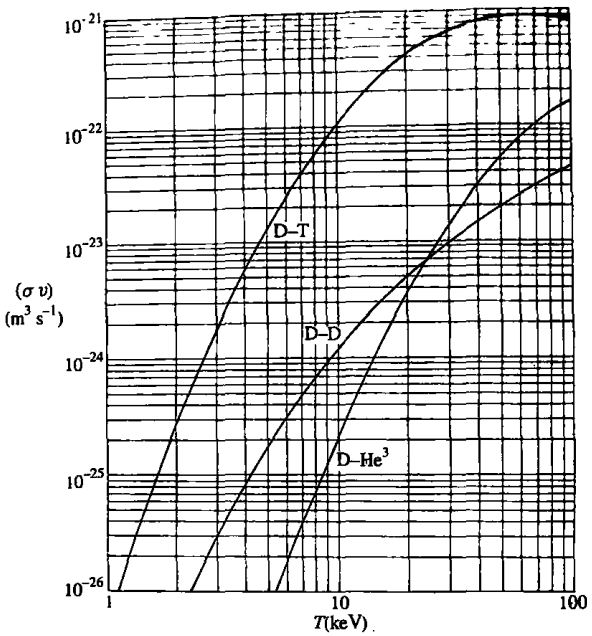

Figure 1.1: The reactivity for ^{2}D–^{3}T, ^{2}D–^{2}D, and ^{2}D–^{3}He fusion reactions, as functions of temperature, recreated from [4].

a shorter confinement time, such as inertial confinement fusion (ICF) experiments at the National Ignition Facility (NIF) [5]; the other is to use relatively low densities $\mathcal{O}(10^{19}\mathrm{m}^{-3})$ over longer confinement times $\mathcal{O}(10\,\mathrm{s})$, as in magnetically confined fusion (MCF). The latter will be the focus of this thesis.

1.2 Tokamaks

All MCF devices make use of the fact that charged particles gyrate around magnetic field lines due to the Lorentz force. The point around which particles gyrate is called the guiding centre. Initial research into fusion focused on *magnetic mirrors*. These are linear devices with a region of low magnetic field between two regions of high magnetic field, generated with solenoidal coils around the device. Whilst some particles are 'trapped' in the magnetic mirror if

$$\frac{v_\perp^2}{|\mathbf{v}|^2} > \frac{B_1}{B_2}, \tag{1.4}$$

where v is the particle's velocity, $\perp$ denotes the component of velocity perpendicular to the magnetic field, and B_1 and B_2 are the minimum and maximum magnetic field strengths in the mirror, respectively, any particles that do not meet this criteria have too high of a velocity

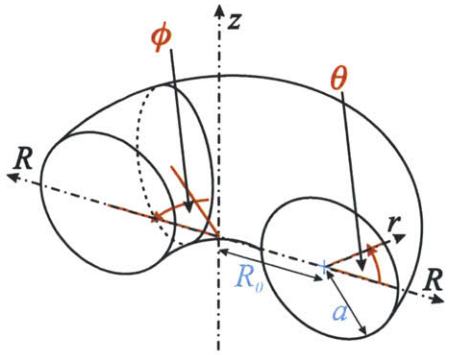

Figure 1.2: A torus cut in half to illustrate the coordinate system used in tokamaks. Reproduced from Ref. [6].

component parallel to the magnetic field and are not reflected before they reach the region of highest magnetic field, so are lost through the ends of the magnetic mirror. Collisions may redistribute a particle's velocity components such that particles initially trapped before a collision are no longer trapped after the collision, and we quickly foresee a situation, through multiple collisions, in which all particles are lost in these devices. By taking the linear magnetic mirror and bending the axis of the device into a circle, forming a torus shape, the problem of sealing the ends of the magnetic mirror was thought to be resolved.

Here we introduce the co-ordinate system used in toroidal magnetic devices. A torus, figure 1.2, is defined as a surface of revolution formed by revolving a circle around an axis coplanar with the circle, reminiscent of a ring doughnut.* The axis of rotation is the z axis, often referred to as the height, as it runs through the centre of the torus upwards, when the torus is laid flat, and the direction of rotation about this axis to form the torus is the toroidal, ϕ, direction. The distance between the axis of rotation and the centre of the circle is the major radius, R_0, and the axis aligned along this distance has the same name, R, sometimes referred to the major radial direction. So far, we have essentially defined the three axes of the cylindrical coordinate system, (R, ϕ, z), which is sufficient to uniquely describe each point inside, outside, and on the surface of the torus.

The distance between the centre of the circle, R_0, and the edge of the circle, a, is called the minor radius†, r, the ratio between these known as the aspect ratio, $A = R_0/a$, and rotating this axis about its intersection with R_0, starting aligned with R, is the poloidal direction, θ.

*The style of doughnut synonymous with Homer Simpson.

†In modern fusion devices the plasma shape is rarely a circle, although it is often simplified to one for numerical simulations, and usually only one minor axis measurement is used to describe the size of the rotational shape (along with extra parameters such as triangularity, elongation, etc.), yet the word torus is used throughout this thesis, and the literature as a whole.

We also have another commonly used toroidal coordinate system which may again uniquely define each point in space, (r, θ, ϕ). Both are used in this thesis. For example, the former is useful when describing a position in the torus, or some vector with no change in height (e.g., the path of a neutral beam injector) whilst the latter is often useful when discussing flows that happen about the magnetic axis (i.e., poloidal flow velocities). For completeness, we also introduce the binormal direction, which is orthogonal to both the local magnetic field (often referred to as the parallel direction) and the radial direction. This is particularly useful when motions between the poloidal and toroidal directions are indistinguishable, such as the barber-pole effect [7], or in numerical simulations [8, 9], for example.

Although the end losses issue was thought to be solved, it became quickly apparent confinement of particles was still poor in a toroidal device. Magnetic field lines are now curved from following the toroidal direction, and closer together at smaller major radii than larger major radii, leading to a gradient in the magnetic field pointing inwards along the major radius. These two effects combine to give rise to a drift of the guiding centres of charged particles through the curvature drift and the grad-B ($\nabla \mathbf{B}$) drift. Plasma particles are almost always subjected to both of these drifts in an inhomogeneous magnetic field, rarely just one of them, and the resulting drift velocity of the guiding centres is given by

$$\mathbf{v}_d = \frac{v_\parallel^2 + v_\perp^2/2}{\Omega_i} \frac{\mathbf{B} \times \nabla \mathbf{B}}{|\mathbf{B}|^2} \tag{1.5}$$

where Ω_i is the gyro-frequency (or Larmor frequency) given by

$$\Omega_i = \frac{ZeB}{m} \tag{1.6}$$

where $\parallel$ denotes the component of velocity parallel to the magnetic field, and Ze and m are the charge and mass of the particle in question. The charge dependence in equation (1.5) causes ions and electrons to drift in opposite directions in the z-direction. This charge separation leads to an electric field, $\mathbf{E}$, which in turn leads to an outward radial drift for positively and negatively charged particles, called the $\mathbf{E} \times \mathbf{B}$ drift, given by

$$\mathbf{v}_{E \times B} = \frac{\mathbf{E} \times \mathbf{B}}{|\mathbf{B}|^2}. \tag{1.7}$$

This drift was responsible for the majority of transport in early magnetic toroidal fusion

devices.

To counter these drifts, a poloidal magnetic field is introduced. The toroidal and poloidal field components add to result in magnetic field lines which twisting helically around the torus. This means particles now experience the top and bottom parts of the torus, and their drifts now cancel so that a particle will return back to its original position after traversing around poloidally, essentially shorting the electric field that would otherwise be generated. This so called *rotational transform*, ι, is crucial for good particle confinement and is defined as the poloidal angle subtended by a field line that traverses once around the torus toroidally. A more commonly used metric for the helicity of the magnetic field is the *safety factor*, q, given by $2\pi/\iota$, which is the number of times a field line twists toroidally to go around once poloidally. This is more commonly approximated in terms of the torus' physical dimensions and the toroidal and poloidal components of the magnetic field in the cylindrical approximation as

$$q = \frac{rB_\phi}{RB_\theta}. \tag{1.8}$$

As a helical magnetic field line wraps around the device, it traces out a surface known as a *flux surface*.

Today there are two main methods for generating the rotational transform of the magnetic field. One is through the complex use of current driven through specially shaped coils outside the torus. These devices are known as *stellarators*, the largest and newest named Wendelstein 7-X [10]. Stellarators are difficult to design due to the complicated geometry of the field coils required to generate the desired twisting magnetic field, however can theoretically run for as long as the external coils are running and fuel can be injected into the plasma. The other, more widely used, device types are called *tokamaks*, which drive a current toroidally through the plasma itself, called the plasma current, I_p, which produces the poloidal field. Tokamaks are more widely used and 'simpler' to design than stellarators, and as such more of them are operational around the world today, allowing more research to be conducted on tokamak plasmas than stellarators. It would be difficult to contest that tokamaks are currently the more mature of the two technologies, however driving the plasma current in them generally requires a large current ramp through a central solenoid aligned with the z-axis, which makes their operation inherently pulsed compared with the potentially long steady-state operation that stellarators provide. Currently under construction is ITER, which, when completed, will be the largest tokamak, and arguably the largest feat of human engineering, ever built,

with many smaller to medium to large tokamaks throughout the world contributing physics towards its design and operation. It is one tokamak in particular that will be the focus of this thesis.

1.3 ASDEX Upgrade

ASDEX Upgrade [11] (AUG, or sometimes known simply as ASDEX, although strictly speaking that name refers to its previous incarnation before an upgrade in 1991) is a medium sized, large aspect ratio tokamak based at the Max Planck Institute for Plasma Physics in Garching, Germany, and is the tokamak that the experiments discussed in this thesis were performed on. A diagram showing the cross-section of AUG is shown in figure 1.3. Its name is an acronym that stands for the 'Axially Symmetric Divertor EXperiment'. As the name suggests, ASDEX runs in a divertor configuration (section 1.4), the use of which preceded the discovery of the H-mode for plasma operation in 1982 [12]. It has a major radius of $R_0 = 1.65\,\mathrm{m}$, and a minor radius of $a \approx 0.5\,\mathrm{m}$, for an aspect ratio of $A \approx 3.3$. It has a maximum plasma height of $\approx 0.8\,\mathrm{m}$, and can achieve plasma volumes of up to $14\,\mathrm{m}^3$ with plasma densities as high as $n_e \approx 2 \times 10^{20}\,\mathrm{m}^{-3}$. It can achieve maximum plasma currents of $I_p = 1.4\,\mathrm{MA}$, maximum toroidal magnetic fields of $B_\phi = 3.9T$, and maximum discharge lengths of $\lesssim 10\,\mathrm{s}$, although not all simultaneously. It has a variety of heating mechanism: up to 20 MW of neutral beam injection (NBI) heating between two beams; up to 7 MW of ion cyclotron resonance heating (ICRH); up to 7 MW of electron cyclotron resonance heating (ECRH) between two antennas; and up to 1 MW of ohmic heating.

1.4 The scrape-off layer and the divertor

At some point, the magnetic field must come into contact with material surfaces. Early tokamak designs used limiters, which were used to limit the extent of the plasma and the position of the last closed flux surface (LCFS). Inside the LCFS the plasma is confined, and magnetic field lines and flux surfaces are closed, where they will trace toroidally and poloidally around the tokamak, eventually joining back onto themselves. Outside the LCFS, field lines and flux surfaces are open in a region called the *scrape-off layer* (SOL), and magnetic field lines pierce material surfaces. As limiters defined the edge of the confined plasma, plasma-wall interactions unavoidably occur close to the confined plasma, allowing

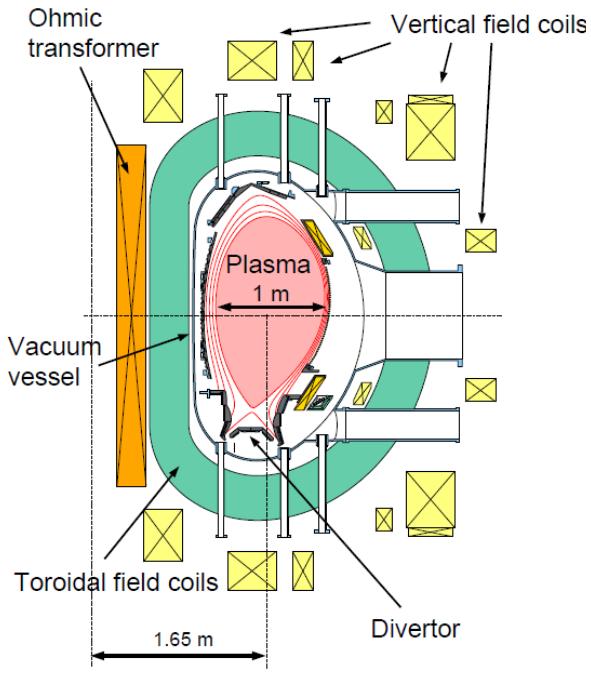

Figure 1.3: A cross-section of the ASDEX Upgrade tokamak. Reproduced from Ref. [13].

recombined neutrals or sputtered wall particles to enter into the plasma and degrade it.

A divertor is a device within a tokamak (or stellarator) designed to act like an exhaust for the plasma, acting to move as many of the plasma-wall interactions away from the bulk plasma as possible, and to allow control over the removal of fusion products, or other heavier contaminating species, to allow for cleaner plasmas to run for longer periods of time. A current in a coil located in the divertor is used to shape the magnetic field here to create a magnetic x-point on the LCFS in the radial-poloidal plane where $B_\theta = 0$. This creates a *separatrix* which divides the confined plasma and the SOL.

If the x-point is at the bottom of the tokamak the magnetic geometry is in a lower single null (LSN) configuration, and if it is at the top it is called an upper single null (USN) configuration. Operations with two x-points on the separatrix are called double null (DN) configurations. The points where the separatrix meet the divertor are called the strike points of the divertor legs, where the inner strike point is at a lower major radius than the outer strike point. The SOL extends poloidally around the tokamak from each of these strike points, with the part of the SOL at lower major radius referred to as the high field side (HFS), and the part at a larger major radius referred to as the low field side (LFS), due to their position with respect to the magnetic field strength. These regions are also often

referred to as the inboard and outboard sides, respectively.

It is here we introduce an addendum to the coordinate system, one commonly used when describing position in the edge of a fusion device. As certain quantities are first-order equal on a flux surface for all θ and ϕ (e.g., pressure and current), and the cross-section of a tokamak is rarely circular, it is useful to have a way to describe the many $r(\theta)$ positions a flux surface will occupy with one descriptor. In this thesis the *normalised poloidal flux radius* is used, given by [14]

$$\rho = \sqrt{\frac{\Psi - \Psi_a}{\Psi_s - \Psi_a}} \tag{1.9}$$

where Ψ is the poloidal flux, and subscripts a and s denote the poloidal flux at the magnetic axis and separatrix, respectively. In these coordinates, the magnetic axis has a coordinate of $\rho = 0$, $\rho < 1$ is in the confined plasma where flux surfaces are closed, $\rho = 1$ is the separatrix, and $\rho > 1$ is in the SOL. Note that ρ is dimensionless and equal values of ρ for differing values of θ are not necessarily the same distance away, in metres, from the magnetic axis. Confusingly, ρ is sometimes used in the literature in two other similar definitions of the normalised radius. The first is also dimensionless, defined as $\rho = r/a$ (e.g., in ref. [15]), where r and a are measured at the outboard midplane. The second is defined as $\rho = r - a$ (e.g., in ref. [16]), and now $\rho < 0$ is the confined plasma, $\rho = 0$ is the separatrix, and $\rho > 0$ is the SOL, measured in units of distance. We also introduce the term the *edge* of the tokamak, which has no specific positional definition in the same way the separatrix does, but is taken to be $\rho \gtrsim 0.9$, which is the edge of the confined region, through to the separatrix (e.g., in refs. [17,18]). The edge often also includes the SOL region (e.g., in refs. [19,20]), but doesn't necessarily, and is chosen at the author's discretion, usually depending on the focus of the work they are writing about.

1.5 Thesis outline

In chapter 2 a brief outline of some of the relevant scrape-off layer literature for this thesis will be given. This will include SOL transport and its link to filaments, some of the models behind the velocity scaling of filaments, an explanation of statistical measurements taken in the SOL, and a look at the link between filaments and the SOL profiles.

Chapter 3 will introduce gas puff imaging, the diagnostic used throughout this thesis to analyse the scrape-off layer. This will give a brief outline of the diagnostic in general, then

specifically the implementation of the diagnostic on ASDEX Upgrade, before detailing some modelling work undertaken to correct for the imperfectly aligned geometry of the diagnostic.

Chapter 4 showcases the experimental analysis of this thesis, including details of the different discharges, details of the analysis techniques used, and results for single-point measurements in the SOL, such as fluctuation distributions and other SOL statistics, and results utilising the 2-dimensional strength of the gas puff imaging diagnostic, such as simultaneous filament size and velocity measurements.

Chapter 5 focuses on the 1D and 2D modelling undertaken for this thesis. It uses a theoretical framework that connects filaments that are randomly generated from the experimentally measured distributions in chapter 4 with the scrape-off layer density profiles, allowing conclusions about the parallel timescales required in order to allow for non-exponential profile shapes.

Finally, chapter 6 summarises the conclusions of the preceding chapters, and suggests where areas of further work may be conducted to clarify or expand on some of the results of this thesis.

Chapter 2

Tokamak edge physics

2.1 Transport

Diffusive models of the scrape-off layer were insufficient to account for the large amounts of particle and heat transport incident on the main chamber walls. This was instead of the ideal solution a divertor was designed for, specifically energy and particles entering the SOL to travel along field lines to the divertor region. This aptly named *anomalous transport* [21] was seen to be an order of magnitude higher than predicted by *neoclassical* models and required an effective diffusion coefficient, D_{eff}, that increased with distance into the SOL [22] to account for the amount of measured cross-field transport, given by

$$D_{\text{eff}}(r) = \Gamma_{\perp}(r)/\nabla n(r) \tag{2.1}$$

where $\Gamma_{\perp}(r)$ is the radial particle flux. It was clear that these levels of particle transport could not be entirely due to diffusion, particularly in regions of the SOL with shallow electron density gradients where $D_{\text{eff}} \to \infty$ as $\nabla n \to 0$, and some convective mechanism must be involved, thought to be caused by filaments that dominate the SOL near the wall.

2.2 Filaments

Filaments are plasma structures that arise through turbulent fluctuations at the edge of tokamak plasmas. They are thought to arise through the interchange instability [23] and, as ballooning-type instabilities, are more prevalent on the low-field side of the plasma. Many names have been given to the phenomena of filaments throughout the literature. The other

most commonly used term is *blobs*, owing to the 'blob-like' appearance of their 2D cross-section in some diagnostics. These are the two terms that shall be used interchangeably in this thesis. Even if a blob was born at a single toroidal location the fast parallel transport, much faster compared with transport perpendicular to field lines, mean they are seen aligning along field lines and wrap around the plasma edge, and as such have large parallel length scales, compared with radial and poloidal size scales of a few centimetres. They are born with amplitudes on the order of the separatrix density, although they have amplitudes (and thus plasma densities) of up to several times the ambient SOL density further into the SOL.

Filaments propagate radially (and binormally) through the SOL, and whilst they may lose some energy and plasma during their journey, either through parallel losses to material surfaces, or through breaking up into smaller blobs or leaking some of their plasma to the background SOL behind them as they propagate, they can still deposit large amounts of hot plasma onto the main chamber walls. This is undesirable for multiple reasons: deterioration of the first wall, diagnostics, or other plasma facing components can be accelerated due to these large heat and particle loads; increased neutral pressures through plasma recycling lead to reduced divertor flows and further radial heat transport, ultimately leading to a cooling of the plasma; and sputtering of high-Z first wall atoms/ions into the main plasma can cause large energy losses due to line radiation and subsequent plasma cooling.

Filaments have been observed on all tokamaks: spherical tokamaks [24]; small [25], medium [26], and large [27] machines; high density and high magnetic field devices [28]; and other magnetised plasma devices, such as linear devices [29], stellarators [30], and reverse field pinches [31]. They have been detected with a plethora of diagnostics: reciprocating probes [32]; lithium beam emission spectroscopy [33]; and gas puff imaging [34].

Sergei Krasheninnikov was the first to propose a model considering a single filament in isolation, proposing the filament acted as an electrical circuit [35]. The total current in a blob must be divergence free to maintain quasi-neutrality and prevent the build-up of charge in one location, and any parallel current flowing along the filament must be closed by perpendicular currents across it. As such, the divergence of the current density, $\mathbf{J}$, is given by

$$\nabla \cdot \mathbf{J} = \nabla \cdot \mathbf{J}_\perp + \nabla_\parallel J_\parallel = 0. \tag{2.2}$$

This closure can happen at different locations along the parallel length of a filament, as shown in figure 2.1, and filaments are often divided into two regions: the region around

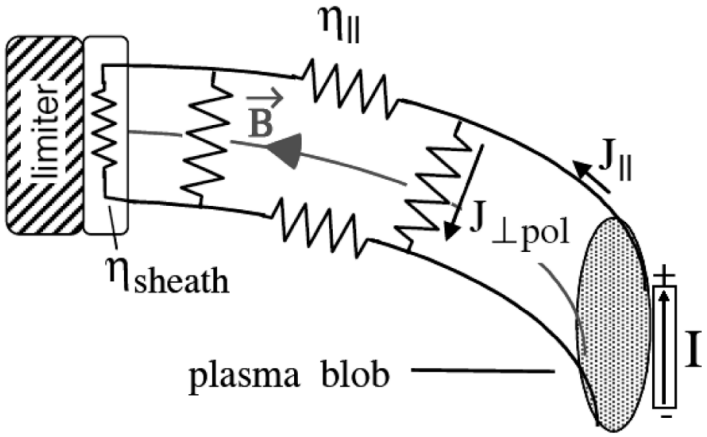

Figure 2.1: A diagram of the filament equivalent circuit, reproduced from [37]. The perpendicular current source driven by curved and inhomogeneous B fields, I, can be balanced by either parallel current, $J_{\parallel}$, or cross-field polarisation current, $J_{\perp,\mathrm{pol}}$.

and below the x-point; and the region above the x-point [36]. The potential of the blob, determined by the current balance, is, in Krasheninnikov's model, due to curvature and ∇B drifts and is closed by parallel current flowing to material surfaces through the sheath. The charge separation that these drifts create causes an electric dipole across the filament's density monopole and a resulting $\mathbf{E} \times \mathbf{B}$ drift velocity of a blob, v_b, is of the order given by

$$v_b = c_s \left(\frac{\rho_i}{\delta_\theta}\right)^2 \frac{L_\parallel}{R} \frac{n_b}{n_t}. \tag{2.3}$$

This equation was the first expression linking a blob's radial propagation velocity to its perpendicular size, $v_b \propto 1/\delta_\theta^2$. As this was derived assuming the filament is electrically connected to the wall, with the parallel current determined by the sheath velocity, this is often referred to as the *sheath limited* regime.

The terms in equation (2.3) are as follows: $c_s = \sqrt{T_e/m_i}$ is the sound speed for electron temperature T_e (in eV) for ion mass m_i; $\rho_i = c_s/\Omega_i$ is the ion gyro-radius (or Larmor radius); δ_θ is the perpendicular blob size in the poloidal direction; R is the tokamak major radius; $L_\parallel$ is the parallel connection length; and n_b and n_t are the blob densities at the midplane and target, respectively. We here make a note that in the literature the exact definitions of $L_\parallel$ and δ_θ are not often defined. For example, it is not usually clear if $L_\parallel$ is the parallel field line lengths from inner to outer divertor target plates, from the midplane to the x-point, or from the midplane to the outer divertor plate. Similarly, it is not clear if δ_θ refers to the filament's poloidal radius or diameter. Whenever $L_\parallel$ is used in this thesis the connection length is

measured from the outboard midplane to the outboard material surface (unless otherwise specified), and δ_θ will be the blob's diameter. For context, the connection length is on the order of 10s of metres and the filament diameters are on the order of 10s of millimetres in ASDEX Upgrade.

Later work by D'Ippolito, Myra, and Krasheninnikov [38] furthered the single blob analysis by also considering temperature and vorticity fields for the filaments, and first introduced the notion of averages of ensembles of filaments responsible for the scrape-off layer profiles, particularly in the far SOL where intermittency increases. In cases where filaments are electrically disconnected from the sheath [39] (for example, through high collisionality and therefore large parallel resistivity) or through high magnetic shear near the x-point, the parallel current in blobs becomes negligible and cross-field polarisation currents become responsible for maintaining quasi-neutrality. In this case, filament velocity is given by [40]

$$v_b = c_s \sqrt{\frac{2\delta_\theta \tilde{p}}{R}} \tag{2.4}$$

where $\tilde{p}$ is the pressure fluctuation of the filament. We now have the velocity scaling of $v_b \propto \delta_\theta^{1/2}$ in this *inertial* regime. The point at which the two current dissipation methods are approximately equal occurs at the *fundamental blob size* [41], given by

$$\delta_\theta^* = 2\rho_i \left(\frac{L_\parallel^2}{\rho_i R} \right)^{\frac{1}{5}} . \tag{2.5}$$

One way in which this model has been expanded is by accounting for the poloidal flux expansion and distortion of filaments around the height of the x-point in the *two-region model* [17] which splits filaments into two coupled regions: the midplane region above the x-point; and the divertor region below the x-point. In the first region, curvature drive is responsible for the charge separation in the poloidal direction, and the arising parallel current is closed either in the same region by cross-field polarisation currents, or, depending on parallel resistivity, in the second region either again through polarisation or currents, or through dissipation into the sheath. In this model, four filament regimes that change the velocity scaling dependent on the filament's size and parallel resistivity (determined by the plasma collisionality, Λ) is found. The phase space showing the velocity scalings is given in

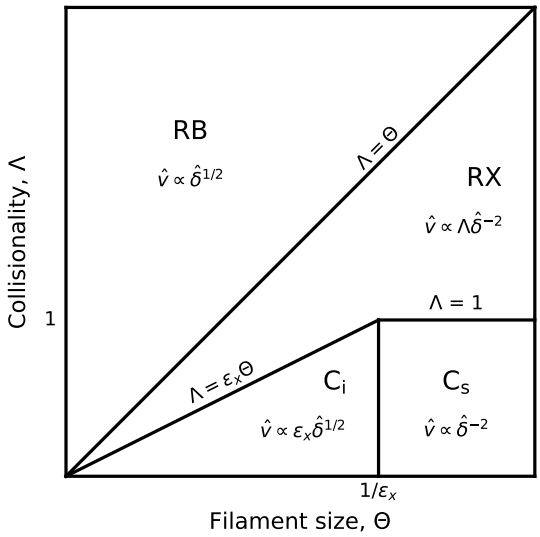

Figure 2.2: The collisionality-size phase space for filaments in the two-region model, recreated from [17]. The different regimes are: sheath connected interchange regime (C_s); connected ideal interchange regime (C_i); resistive x-point regime (RX); and resistive ballooning regime (RB). The filament velocity scaling dependencies are shown for each regime.

figure 2.2. The parameters which describe this model are: the collisionality

$$\Lambda = \frac{L_\parallel \nu_{\mathrm{ei}}}{c_s} \frac{\Omega_i}{\Omega_e} \tag{2.6}$$

where ν_{ei} is the electron-ion collision frequency, and parameters are often measured at the divertor surface, such as with divertor Langmuir probes [51]; the perpendicular size parameter

$$\Theta = \hat{\delta}^{\frac{5}{2}} = \left(\frac{\delta_\theta}{\delta_\theta^*}\right)^{\frac{5}{2}}, \tag{2.7}$$

the filament velocity parameter

$$\hat{v} = \frac{v_x}{c_s}\left(\frac{R}{\delta_\theta^*}\right)^{\frac{1}{2}}, \tag{2.8}$$

and the flattening parameter, ε_x, which is between 1 and 0. 1 corresponds to a blob which is perfectly circular in cross-section, and therefore experiences no shear, whilst 0 refers to a blob which is sheared completely flat.

The two region model predicts the following filament regimes:

- *Sheath connected interchange regime* (C_s) - for large filaments at low collisionality, they are connected to the target and the parallel currents dominate over small polarisation currents, and $\hat{v} \propto \hat{\delta}^{-2}$, returning the velocity scaling of equation (2.3).

- *Connected ideal interchange regime* (C_i) - small filaments at low collisionality are still connected with the lower region, although now flattening at the x-point of already smaller filaments allows polarisation currents to become more dominant. Here, $\hat{v} \propto \varepsilon_x \hat{\delta}^{1/2}$, in the only regime where there is a velocity dependence on the filament flattening.

- *Resistive x-point regime* (RX) - large filaments with increased parallel resistivity so that the filament is disconnected from the target but some coupling can occur between the two regions. Polarisation currents close the current loop somewhere above the target, giving a velocity scaling of $\hat{v} \propto \Lambda \hat{\delta}^{-2}$.

- *Resistive ballooning regime* (RB) - for sufficiently high collisionalities, or small enough filaments, the upper region is disconnected from the lower region and polarisation currents close the loop entirely in the upper region, local to the curvature current drive, causing a ballooning of the filaments. The inertial velocity scaling of equation (2.4), $\hat{v} \propto \hat{\delta}^{1/2}$, is recovered.

Later work by Peter Manz *et al.* [42] further expanded on this model with the inclusion of warm ions. Many assume that a temperature ratio of $\tau_i = T_i/T_e \approx 1$ although values of $\tau_i \gtrsim 3$ are more likely in tokamak SOLs owing to faster electron heat transport times compared with ions. The ion pressure contribution can have the effect of increasing the interchange drive in a filament, thus affecting vorticity in the filament, as well as inducing additional non-linearity which can break apart filaments. Ref [42] recovers the scalings that Myra *et al.* [17], with additional factors of $\leq (1 + \tau_i)$, as well as an additional *ion dominated resistive ballooning* (iRB) regime. This affects the smallest blobs, which append to the left hand side of figure 2.2 for all collisionalities, where the blob acceleration is down to the ion diamagnetic contribution to polarisation current, instead of the $\mathbf{E} \times \mathbf{B}$ drive for larger filaments, has a velocity scaling of $\hat{v} \propto \hat{\delta}^2$.

A series of papers released by Daniel Carralero *et al.* [39, 43, 44] have reported on the size and velocity of filaments in ASDEX-Upgrade, as well as comparison with measurements in COMPASS and JET [45]. These results are obtained use a multi-pin probe head [46]

attached to a manipulator which plunges it into the plasma. Firstly, the results presented do not analyse individual filaments but instead use the conditionally averaged waveforms, and the delay between filaments used with the known separation of the pins used to estimate velocities in the poloidal and radial directions. This poloidal velocity is then used with the autocorrelation time, which is noted to depend on the intensity threshold chosen for filament detection, to calculate the radial size. The convolution of the filament's size and velocity on its autocorrelation time draws questions about the validity of the sizes measured, all before one consider either the decorrelation of the filament over time, or the shadowing effect of the invasive probe head. They also claim to be able to measure filaments smaller than the separation between the pins on the probe, despite the filament size being larger than pin separation being one of the fundamental assumptions they make in their probe data analysis method. Gas puff imaging, the diagnostic used for analysis filaments in this thesis, produces temporally resolved 2D frames with a spatial resolution of $\approx 3\,\mathrm{mm}$ covering a region of $\approx 6 \times 6\,\mathrm{cm}$ allowing for simultaneous size, amplitude, and velocity measurements of filaments individually, at any location in the diagnostic field-of-view, with a relatively less perturbative technique.

2.3 SOL statistics

Intermittent fluctuations, which are responsible for the transport of plasma density, have been recorded in the edge of magnetic plasma devices and tokamaks for a long time [29]. The similar behaviour of these fluctuations has been reported as across devices for almost as long, leading to the theory of the universality of the scrape-off layer [47]. As such, there isn't a tokamak SOL, or SOL numerical simulation, that the results described in this section cannot be found reported for [23, 48].

For the time-series of fluctuation data from a single-point in the SOL, such as from Langmuir probes [49], gas puff imaging [50], or beam emission spectroscopy [18], are dominated by a series of intermittent 'events' caused by the traversing of a filament past the diagnostics' sampling location. In the near SOL, taken to be up to about 10–15 mm into the SOL from the separatrix in ASDEX Upgrade [45, 51] (up to $\rho \approx 1.02$), the mean of the signals is relatively high with the amplitudes of the blob events not much higher than the mean, whereas in the far SOL, the mean is much more reduced, and the events have amplitudes

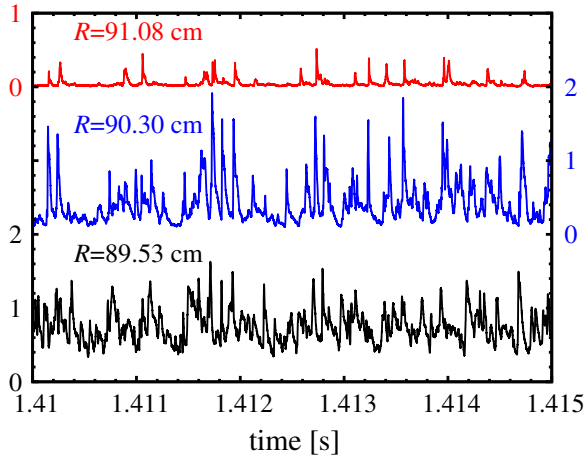

Figure 2.3: The fluctuation time series from three different locations in the SOL of Alcator C-Mod, taken with gas puff imaging. Reproduced from ref [52].

many times larger. An example of this is shown in figure 2.3. This shows how the far SOL has a relatively low signal mean, but with relatively large amplitude filaments this far into the SOL without decaying, so transport in the far SOL is caused by the convection of these filaments. In the near SOL, the filaments are harder to detect in the signal due to the larger amounts of background plasma density.

The time series can be quantified by the probability distributions functions (PDFs) of the fluctuation data. SOL density fluctuations are observed to follow a *Gamma distribution* [6, 53, 54], given by the probability density function

$$f(x;k,\theta) = \frac{1}{\Gamma(k)} x^{k-1} e^{-x/\theta} \tag{2.9}$$

where x is the amplitude of the fluctuating signal, k is the *shape parameter* and θ is the *scale parameter*, given by the expectation/mean value, $E[X]$, and variance, $\sigma[X]$, by

$$k = \frac{E[X]^2}{\sigma[X]}, \tag{2.10}$$

$$\theta = \frac{\sigma[X]}{E[X]}. \tag{2.11}$$

Γ is the *Gamma function* [55], given by

$$\Gamma(z) = \int_0^\infty e^{-t} t^{z-1} \, \mathrm{d}t \tag{2.12}$$

for all complex z except the non-positive integers. It can also be shown analytically that the Gamma distribution occurs when the fluctuation events have exponentially distributed amplitudes and waiting times [56]. As such, the fluctuation time-series can be statistically described solely by its mean and variance. The mean decreases and variance increases with distance into the SOL, and as a result the PDF of the fluctuation amplitudes vary from being near-Gaussian next to the separatrix to being positively skewed having exponential tails for large positive fluctuations in the far SOL, whilst always following the Gamma PDF [57]. As such, radial profiles of the relative fluctuation level, given by the signal's standard deviation (often referred to as the RMS) divided by the mean, increase with distance into the low field side scrape-off layer.

Whilst some comparisons between PDFs at different SOL locations (e.g., refs. [57,58]), or between statistical measurements in the SOL of different discharges types (e.g., ref. [50]) have been made, comparisons at multiple locations and for multiple discharges is less common. Work by Graves *et al.* [54] compares fluctuation PDFs across the SOL for one discharge type and later between discharges types at one location, but not both together. We will demonstrate this full comparison, as well as for other SOL statistical measurements, in this thesis.

Commonly used higher order moments that quantify how much the PDFs deviate from the normal distributions are *skewness* and *kurtosis* [59]. The former is a quantity describing the asymmetry of the distribution, where a zero value indicates a distribution equally centred around its mean, and a positive skewness means the distribution's tail is on right, so the mean is shifted to higher than the mode or median. The latter is a measure of how much the higher and lower extremities/wings of the distribution contribute to the signal. Sometimes the kurtosis is referred to as the *flatness*, or is spelled with a *c*, and the kurtosis of the normal distribution is 3*. The skewness and kurtosis are given by

$$S(x) = \frac{1}{N\sigma_x^3} \sum_i^N (x_i - \bar{x})^3 \tag{2.13}$$

and

$$K(x) = \frac{1}{N\sigma_x^4} \sum_i^N (x_i - \bar{x})^4 , \tag{2.14}$$

*We here note that some publications refer to the *excess kurtosis* simply as the kurtosis, which is shifted down by 3 such that the normal distribution has a kurtosis of zero. Throughout this work, unless otherwise specified, we do not perform this adjustment.

respectively, where σ_x is the signal's standard deviation, and $\bar{x}$ is the signal's mean. Radial profiles of S and K throughout the LFS SOL also increase, as the intermittency of the signal increases with distance into the scrape-off layer [6, 23, 60]. This is why the PDFs will often be described as having increased in skewness and flatness as a function of distance into the SOL. For signals following a Gamma distribution, the quadratic relationship between the skewness and kurtosis is given by

$$K = \frac{3}{2}S^2 + 3 \tag{2.15}$$

which SOL signals have also been demonstrated to follow [6, 61].

Some of the properties of the filaments themselves, and not just the time-series, can also be measured with single-point diagnostic tools. It has been repeatedly shown that the amplitudes of filaments are exponentially distributed [56,62,63], where the exponential PDF is given by

$$f(x;\lambda) = \frac{1}{\lambda}\exp\left(-\frac{x}{\lambda}\right) \tag{2.16}$$

where λ is the *scale parameter*, which is also the mean of the distribution. In addition, the filament waiting times, t_w, i.e., the difference between consecutive filaments' arrival times, $t_{i+1} - t_i$, where the arrival time is the time at which the signal's local maxima for a given location occurs, are also exponentially distributed [6, 50, 64] (alternatively, the arrival times themselves are uniformly distributed). This is in accordance with a Poisson process, which is often termed a 'memoryless' process, in which events occur randomly and at a constant average rate, implying the filaments detected in the SOL are uncorrelated with one another.

A stochastic model of the SOL has been built up using these measurements. An attempt to recreate the single-point fluctuation signals has been made using measurements of average waiting times, duration times, and amplitudes to describe the Gamma distribution input parameters [56,57] from a series of uncorrelated pulses. Synthetic signals have been generated which mimic experimental time series [65,66] these require values for the waiting time at least an order of magnitude higher than those measured in experiments. It is known that not all filaments are detected and as such recorded average waiting times are a minimum threshold on the value. Other filament detection methods have been tried to account for this, e.g., wavelet decomposition [67], a deconvolution algorithm [50, 68], or separation of signal and noise through respective distributions' characteristic functions [69], have been attempted, but none have satisfactorily managed to solve this issue. A resolution to this is outside the

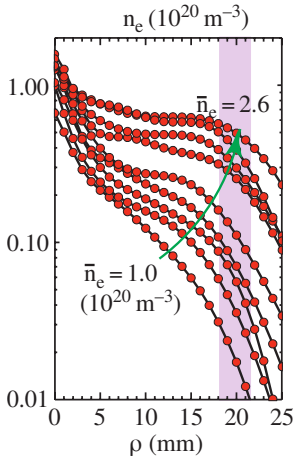

Figure 2.4: The electron density profile as line averaged density increases in Alcator C-mod. The shoulder/two decay lengths are clearly seen, even for the lowest density, and the far SOL decay length can be seen to increase as $\bar{n}_e$ increases. The near-far SOL boundary is seen to move closer to the separatrix for the highest line-averaged densities as the shoulder broadens. Reproduced from ref [73].

scope of this thesis, but it is highlighted here as it is important for a full stochastic model of the SOL to exist.

2.4 Profiles / Shoulder

Brian LaBombard was one of the first to report on the connection between the increased density profile gradients and the presence of filaments in the far scrape-off layer [70], and was also the first to use the term *far SOL*, drawing a distinction between the two differing regions with open field lines. Many tokamaks had recorded an increase in the far SOL decay length as plasma densities increased [71–73], so rather than a single exponential decay length describing the entire SOL profile, a steep gradient with short decay length was seen in the near SOL, with a shallow gradient and long decay length in the far SOL. This was referred to as the *shoulder*. Example profiles are shown in figure 2.4. In the near SOL, parallel conduction dominated transport processes, whilst the far SOL was dominated by perpendicular convection of filaments.

As densities increased further, the near-far SOL boundary was seen to move towards the separatrix [74] as the shoulder *broadened*, decreasing the near-to-far SOL size ratio. Eventually a flattened profile is seen over all the SOL. It has even been reported that filaments have been found now inside the last closed flux surface as the high cross-field transport

normally seen in the far SOL is seen all throughout it [75]. This phenomena could play a role in determining the edge density limit, also known as the Greenwald limit, or Greenwald density [76], approximated by

$$n_{\mathrm{G}} \approx \frac{I_p}{\pi a^2} \tag{2.17}$$

where the density is in $10^{20}\mathrm{m}^{-3}$, I_p is the plasma current in MA, and a is the minor radius in m. Plasma densities are often reported as the *Greenwald fraction*, $f_{\mathrm{G}} = n_e/n_{\mathrm{G}}$.

Results on JT-60U suggested that the shoulder formed when the divertor underwent detachment [39,72], and the increased decay length in the far SOL was linked with the increased convection of filaments, in this case disconnected through decreases in target temperatures and increases in parallel resistivity, see section 2.2. It was thought filaments would undergo this regime change, and therefore a density shoulder formed, when the divertor collisionality, equation (2.6), was raised above some threshold, $\Lambda > 1$ [36]. Further results seemed to confirm that $\Lambda > 1$ would cause the flattening of the far SOL [45], with evidence suggesting increases in filament sizes too. Recent experiments by Wynn *et al.* [77] showed how the divertor collisionality could be changed, such as through nitrogen seeding, and the shoulder would not be formed, instead showing that the outer divertor recycling rate had a stronger correlation to the upstream profiles.

Chapter 3

Gas puff imaging

3.1 Fundamentals

Gas puff imaging (GPI) is a plasma diagnostic technique that allows one to observe the fluctuations in a plasma by injecting a low temperature neutral gas into it which, with careful design, can be close to non-perturbative. This *gas puff* increases the local density of neutral species which are excited into higher energy states through collisions with plasma electrons, and spontaneously decay into lower energy states, emitting photons of discrete, known wavelengths corresponding to the difference in energy between these two electronic states. With a well positioned optics system this light emission can be collected and a chosen wavelength filtered out and imaged onto a detector, allowing for spatially and temporally resolved measurements of plasma fluctuations. Some imaging systems use light emission from the plasma passively, but as the signal is line integrated, analysis of signals of this type is typically limited to linear devices [78] or usually require tomographic inversion [24] and/or *a priori* knowledge of some other plasma parameter, such as another diagnostic [79]. With GPI, the amount of light emission from within the gas cloud produces signal measurements orders of magnitude above ambient light fluctuation levels, if the puff gas and filtered wavelength are chosen so as to be far away from other spectral lines inside the tokamak - i.e., using helium instead of deuterium. As such, the signal is mainly localised to from within the gas puff. An example of the signal increase when the gas puff is introduced is shown in figure 3.1. For a sufficiently localised gas puff in the toroidal direction, and viewing optics closely aligned with the magnetic field lines in the gas puff, a thin 2D lamina of a 3D filament can be illuminated, imaged, and analysed.

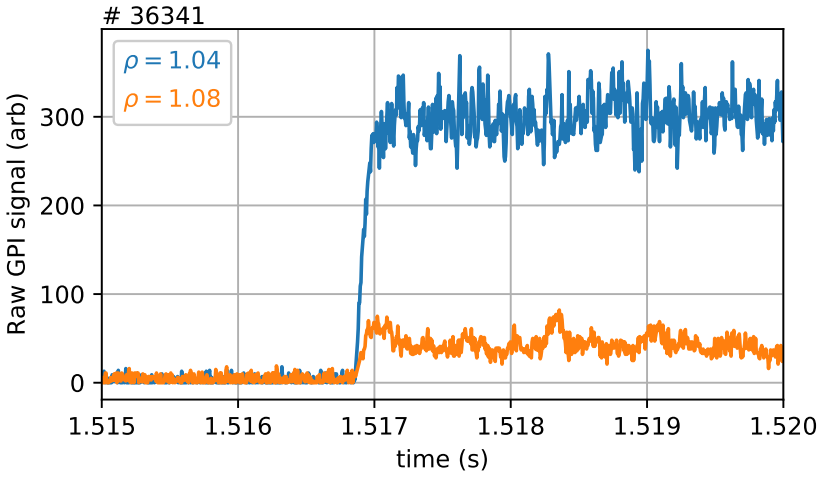

Figure 3.1: GPI signal from two SOL positions showing the increase in raw signal from a gas puff for a typical ASDEX Upgrade H-mode discharge (pre LH-transition). The difference in average signal before and after the gas puff is $\approx \times 120$ and $\times 9.4$, for the two positions.

The diagnostic measures fluctuations in the local light emission of the introduced neutral gas due to a combination of fluctuations in the electron density, n_e, and electron temperature, T_e. The emission rate is given by

$$I = n_0 f(n_e, T_e) \tag{3.1}$$

where f is the ratio between the densities of the upper excited state of the transmission responsible for the emission and the ground state multiplied by the rate of decay of the upper excited state, and n_0 is the local neutral density. On ASDEX, the 587.6 nm HeI emission line is used, which corresponds to the $3^3D \rightarrow 2^3P(1s3d \rightarrow 1s2p)$ electronic transition. The excited state density is determined by a balance between processes which populate the excited state (electron collision excitation from lower energy states, electron collision de-excitation from higher excited states, spontaneous emission from the higher energy states) and the processes which depopulate the state (electron collision excitation into higher energy states, spontaneous emission to lower states). As such, the total signal is a function of neutral density, electron density, and electron temperature. The local neutral density is assumed to vary more slowly than timescales of filaments or turbulence, so the emission's dependence on the neutral density can be eliminated through normalisation of the signal, see chapter 4.3.1. This normalisation also accounts for spatial distribution of the neutral gas. For the typical SOL densities and temperatures seen in the discharges used in this thesis ($1 \times 10^{18} < n_e < 5 \times 10^{19}\,\mathrm{m}^3$, and $15 < T_e < 70\,\mathrm{eV}$), it can be calculated [6, 19] that the

contribution to the light emission is dominated by the electron density, and the fluctuation signal is taken to be a proxy measurement of the electron density fluctuations.

3.2 GPI on ASDEX

On ASDEX Upgrade, the gas puff imaging diagnostic is located on the low-field side, just below the outboard midplane [80], see figure 3.2. The gas injection point is located at coordinates $(R, z) = (2.190, -0.158)$m, connected by a 400 µm wide, 66 mm long capillary to a piezoelectric gas valve [81], behind which sits the gas chamber. In this thesis, helium was used for each discharge. The gas flow rate is controlled by changing the gas chamber pressure, and the total gas injection controlled by the amount of time the valve is open for. The gas injection system is the same used by the thermal helium beam (HEB) diagnostic system [82].

The plasma is observed through an in-vessel mirror that allows a lens to be placed 'inside' the tokamak. A 25 mm focal length objective lens is placed against this mirror, focusing the light onto one end of a 6.7×5 mm coherent fibre bundle image guide, to be recorded outside of the tokamak. The other end of the image guide is attached to an $x - y$ translation pad that can be finely adjusted to change which part of the transmitted image is placed onto the focal plane of a 16 mm collimating lens. A narrow bandpass interference filter is used to filter out the HeI 587.6 nm emission line, and the filtered image is focused onto a camera with an 8 mm lens. The interference filter's central wavelength has a dependence on the angle of incidence of the light, hence a collimating lens is used to ensure all light is parallel with the principal axis of the lens system. This also allows for fine tuning of the central wavelength. However, effects due to Doppler broadening of the helium puff [83] or Doppler shifts due to plasma rotation [84] are negligible for our application.

For the experiments in this thesis, a Phantom v711 fast camera was used. The CMOS sensor is composed of 20 µm pixels and was operated at a 12bit 64×64 resolution at a 200 kHz temporal frequency. This combination allowed us to cover an approximate 6×6 cm viewing area in the low-field side scrape-off layer, just below the outboard midplane, covering from just inside the separatrix through the entire SOL to the limiter shadow. A higher temporal frequency could be used, but would result in an overall lower acquisition time, unable to cover the entirety of a discharge, and would require larger gas puffing rates for an equivalent

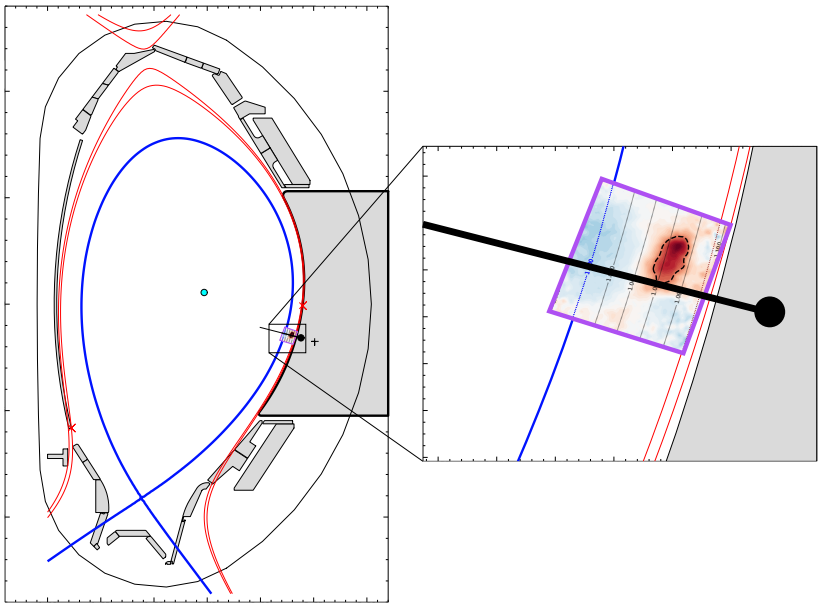

Figure 3.2: A radial-poloidal cross-section of ASDEX Upgrade for a typical lower single-null equilibrium. The separatrix (dark blue), magnetic axis (light blue), and limiter poloidal-flux surfaces (red) are shown in. The GPI view is included (purple) with the gas puff valve (black plus), gas puff injection point (black circle) and gas puff vector (black line) included. A zoom in on the GPI viewing position is shown on the right.

signal, at which point the gas puff starts to become perturbative. The $x - y$ translation pad allows one to move which part of the image is on the active part of the Phantom's CMOS sensor, and can be used to tune the GPI's view on a shot-to-shot basis, although this wasn't required for these experiments, as the separatrix and limiter flux-surface positions did not vary much between discharges. The final set-up was viewing between $2.09 \lesssim R \lesssim 2.18\,\mathrm{m}$ and $-0.19 \lesssim z \lesssim -0.10\,\mathrm{m}$. This covers a region at least several of the flattest profile decay lengths.

3.3 GPI geometry correction

To maximise the spatial resolution of a gas puff imaging diagnostic one wants to align the viewing angle of the detector with the magnetic field line as closely as possible. This is, obviously, impossible in the case of curved field lines, where the curve will result in a smearing of any features we see in the direction of the radius of curvature. This is less obvious with field lines with a larger radius of curvature, although this is largely set by the physical size of the tokamak. However we can minimise this effect by the introduction of

the gas puff. If we assume the light emission that contributes to the signal is negligible from outside of the gas puff, then as we reduce the toroidal extent of the gas puff, we confine the length of the field line that contributes to the signal, both reducing the effect of smearing due to the field line curvature and due to the misalignment of the view. In the limit of a perfectly thin gas puff, the emission is from a 2D slice in the blob with zero smearing.

In reality, the gas puff has a finite toroidal size, and the viewing angle between the field lines and detector is constrained by the available port positions on the tokamak. We must also consider that the magnetic field geometry can change on a shot to shot basis. Zweben [19] estimates spread due to an angle of θ_B between the line-of-sight and magnetic field, and the finite gas cloud size L_{cloud} as

$$\Delta x \approx L_{\text{cloud}} \tan \theta_B. \tag{3.2}$$

In ASDEX Upgrade, the angle between the magnetic field and the lines-of-sight varies between 17–24° ($0.34 \leq \tan \theta_B \leq 0.44$), and so must be taken into account when measuring blob sizes. To do this, a simple model of the plane around the detector viewing region is made to quantify the error due to these effects.

3.3.1 Gas puff size

The first step is to measure the finite size of the gas puff, employing the technique used in reference [81]. The mean emission from a gas puff during an L-mode section of the discharge is used. The gas puff from shot # 36340 is shown in figure 3.3. From this, the emission profile shape is measured in the direction perpendicular to the *gas puff vector* at multiple distances from the injection point. Here, the gas puff vector is down the centre of the gas puff cloud and is given by the cartesian/cylindrical equation $z = -0.259R + 0.409$ [m]. This also means our measurements of the emission are approximately parallel to $\rho = \text{const}$ lines. For this analysis, we make the following assumptions:

1. The gas cloud distribution is cylindrical about the gas puff vector.

2. The measured emission distribution along a line perpendicular to the gas puff vector yields the gas cloud profile along that line.

3. That emission distribution (and thus gas cloud distribution) can be approximated by

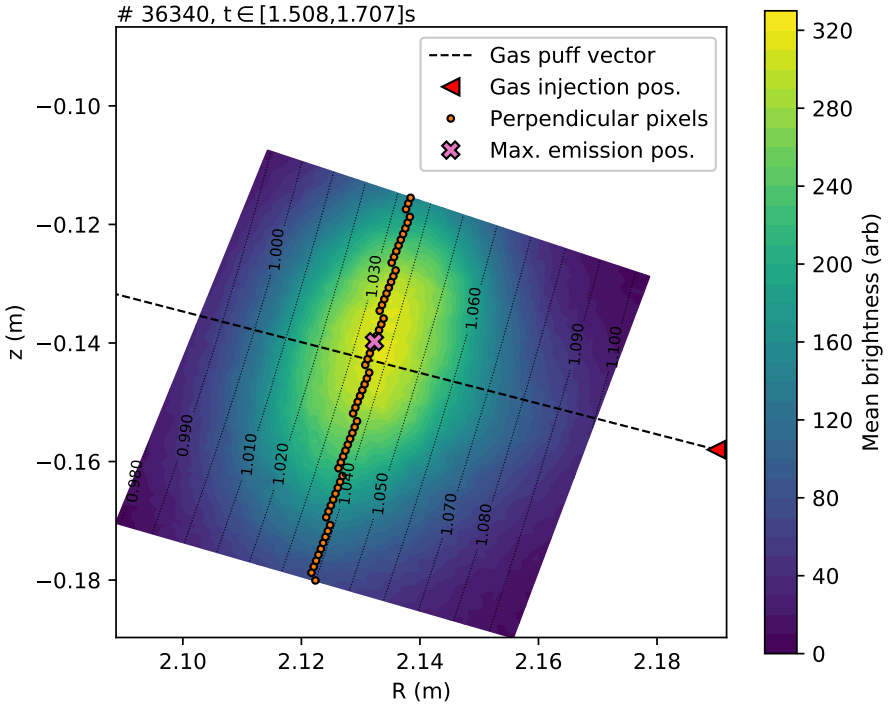

Figure 3.3: Mean emission profile of a gas puff. The gas puff vector (black deshed) starting from the nozzle injection position (red triangle) as shown. An example of the pixels used perpendicular to the gas puff vector are shown (orange dots) at the point of maximum mean emission.

a Gaussian function, given by

$$y = A \exp\left(-\frac{(x-\mu)^2}{2\sigma^2}\right), \tag{3.3}$$

where A is the maximum amplitude, μ is the x position of the node, and σ is the variance.

An example of this analysis for the perpendicular line that passes through the maximum emission location is shown in figure 3.4a. From the fit of equation (3.3) to the emission data, the full width at half maximum (FWHM), the distance in x between the points $y = A/2$, is calculated with

$$\text{FWHM} = 2\sqrt{2\ln 2}\sigma. \tag{3.4}$$

The error on the FWHM is then calculated with error propagation, as $\Delta_{\text{FWHM}} = 2\sqrt{2\ln 2}\Delta_\sigma$, where Δ_σ is the error on σ from the fitting routine. The process is repeated moving backwards

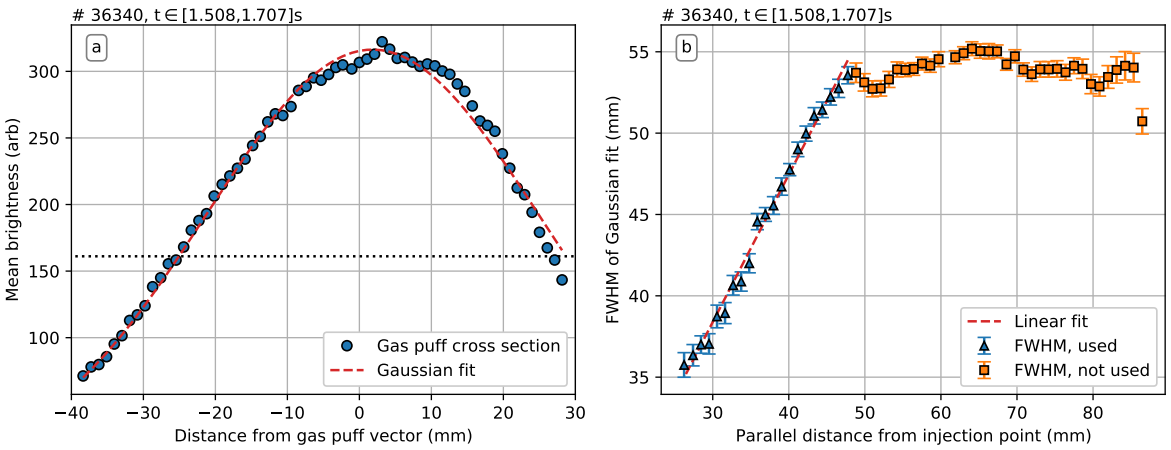

Figure 3.4: (a) The perpendicular emission profile of the highlighted perpendicular cross-section in figure 3.3 with a fitted Gaussian function with $R^2 = 0.9908$. The fit parameter values are $A = 316.3 \pm 1.6$, $\mu = 1.82 \pm 0.15\,\text{mm}$, and $\sigma = 23.15 \pm 0.19\,\text{mm}$. The black dashed line is half the maximum mean emission. (b) The FWHM of the fitted Gaussians against parallel distance from the gas injection point. The errorbars are calculated from the associated error on σ in the Gaussian fits. The minumum R^2 in the fits is 0.9478. Orange points are not used in the linear fit, where the gas puff can no longer be approximated by a cone past this point.

and forwards along the gas puff vector one pixel at a time, until the perpendicular no longer stretches the entire poloidal width of the detector view. The results are shown in figure 3.4b. After a certain distance along the gas puff vector from the injection point the gas puff can no longer be approximated by a cone due to neutral diffusion and ionisation. A linear fit of FWHM against parallel distance, d, up to this distance is performed, so

$$\begin{aligned} \text{FWHM}(d) &= md + C \\ \sigma(d) &= \frac{md + C}{2\sqrt{2\ln 2}}. \end{aligned} \tag{3.5}$$

In this instance, the fit is made up to $d_{\text{max}} = 47.8\,\text{mm}$. Assumption 3 is validated in each of the measurements up to d_{max} with a minimum R^2 in the fits of 0.9478. The linear fit gives $m = 0.91 \pm 0.02$, and $C = 11.2 \pm 0.7\,\text{mm}$. The region over which the FHWM increases linearly with distance from the capillary implies a $24.5 \pm 0.5°$ half-angle of the gas cloud cone. This is fed back into the model of the gas puff region.

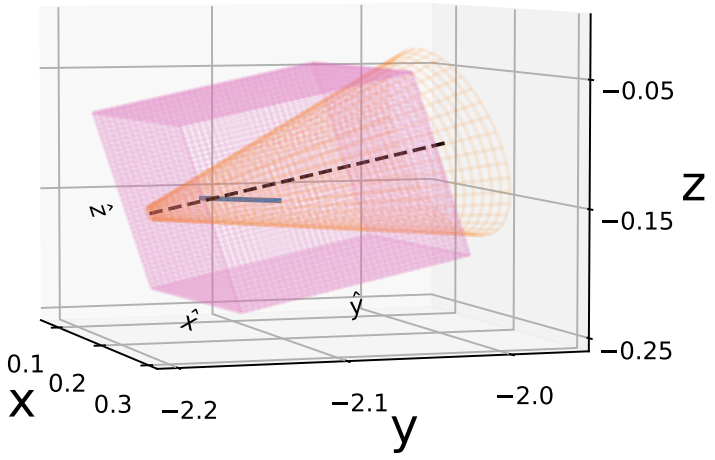

Figure 3.5: A diagram showing the simulated diagnostic domain in Cartesian coordinates (pink). The FWHM of the gas puff cone (orange) and the gas puff vector (black dashed) are included. An example field-line trace, the position a filament will follow, is shown (blue). The viewing location for the diagram is the approximate viewing location of the lens in the experimental GPI diagnostic, although zoomed out to include all the simulated domain.

3.3.2 Simulated diagnostic domain

Now that the gas puff has a measured size, we create a domain for it to exist in. The domain is a cube with 151 elements in each direction, positioned so that the gas puff vector is aligned with one of the axes of the domain and runs right through the centre. The coordinates of the box are then $\hat{x}$, which is approximately in the toroidal direction at the gas puff injection location, $\hat{z}$, which is mostly vertical, but also leaning slightly away from the centre of the tokamak, and $\hat{y}$, which is aligned with the gas puff vector, mostly in the radial direction and slightly upwards in height. The domain covers 15 cm in each direction, with each element being $1\,\mathrm{mm}^3$. A diagram showing the domain in Cartesian coordinates is shown in figure 3.5.

For each location in the domain, the normalised radius, ρ, is known, and therefore the electron density, n_e, and electron temperature, T_e, are known, from the lithium beam profiles [33]. The neutral density, n_0, from the gas puff is not known absolutely, and instead is only known in relative terms. In each concentric plane along $\hat{y}$ the neutral density profile is a 2D Gaussian in shape, inferred from the emission profile measured in section 3.3.1. The total neutral density in the first plane is set to some value, M, and calculated in subsequent planes using a simplified collisional radiative model.

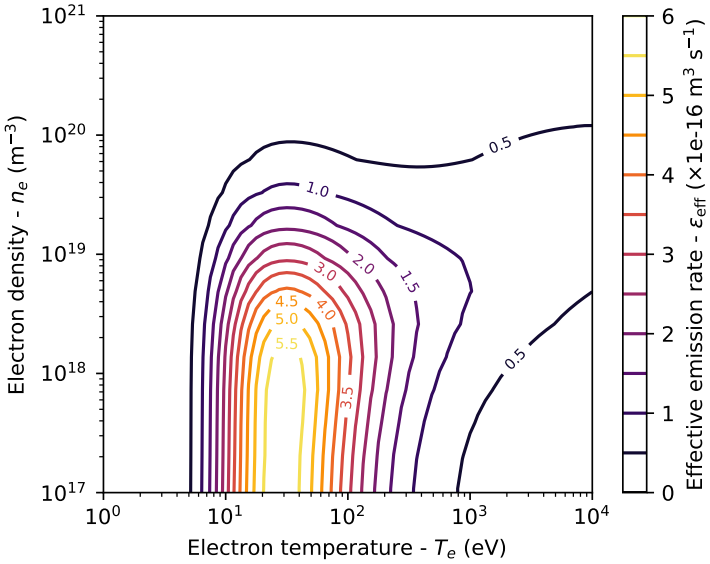

Figure 3.6: The effective emission rate, ε_{eff}, as calculated in refs. [85, 86] for the helium emission line with wavelength 587.6 nm.

3.3.3 Collisional radiative model

Now the electron density, electron temperature, and relative neutral density are known, the emission can be calculated. Equation (3.1), is rewritten here in terms of an *effective emission rate*, $\varepsilon_{\text{eff}} = f(n_e, T_e)/n_e$, calculated using the neutral transport Monte Carlo code DEGAS 2 [85, 86]. The values of ε_{eff} are shown in figure 3.6. With this, the local emission of each element in the domain can be calculated with

$$I = n_0 n_e \varepsilon_{\text{eff}} \, \mathrm{d}V \tag{3.6}$$

where $\mathrm{d}V$ is the volume of each element. Lines-of-sight from the lens' virtual location to the location in the tokamak of each pixel in the detector are calculated, and the emission from each location within the virtual domain will therefore contribute to the pixel who's line-of-sight it is closest to. Any location in the domain that is more than ≈ 1 mm away from a line-of-sight vector (i.e., those outside the view of the detector) does not contribute to the simulated GPI signal. 1 mm is chosen as this is about the smallest distance between adjacent pixels in the GPI view.

To account for the expansion of the gas cone as we move further away from the injection point, and hence a decrease in the neutral density, we assume neutral particle continuity

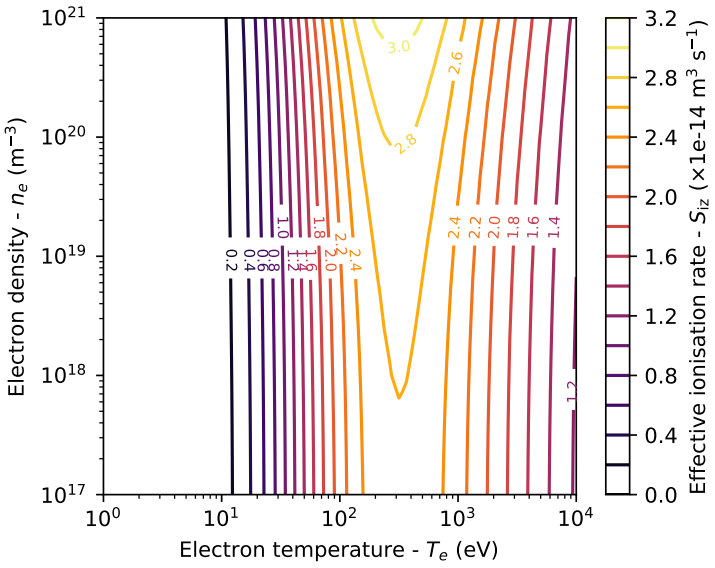

Figure 3.7: The effective electron impact ionisation rate, S_{iz}, as calculated in [85, 86], for atomic helium.

minus a number of particles due to ionisation moving from plane to plane in the $\hat{y}$ direction. Therefore, other than the ionised particles, we assume all the neutrals in plane y_i make it through to plane y_{i+1}, and the distribution of the neutral density uses a 2D Gaussian again but with an updated total and FWHM. The total rate of change of the neutral density is then given by

$$\frac{\mathrm{d}n_0}{\mathrm{d}t} = -n_0 n_e S_{\text{iz}} \tag{3.7}$$

where S_{iz} is the effective ionisation rate, as calculated in refs. [85, 86], plotted in figure 3.7. Solving equation (3.7) gives

$$n_0(t) = n_0(t=0)\exp\left(-n_e S_{\text{iz}} t\right) \tag{3.8}$$

where $n_0(t=0)$ is the constant of integration. Instead of solving for time, we solve through space, assuming any neutral gas lost through ionisation is replaced by neutral gas in the plane behind it. We here replace the time varying neutral density with the arbitrary total neutral density coefficient introduced in section 3.3.2, M, such that

$$M(y_{i+1}) = M(y_i)\exp\left(-n_e S_{\text{iz}} t\right). \tag{3.9}$$

A full treatment should include a term for the recombination rate in equation (3.7), but here has been neglected as at even the lowest temperatures and densities that could be applicable to tokmak SOLs the effective recombination rate coefficient is four orders of magnitude lower than S_{iz} ($n_e \approx 1 \times 10^{17}\,\mathrm{m}^3$, $T_e \approx 10\,\mathrm{eV}$) [85, 86]. In equation (3.6) the emission intensity is actually an emission rate, although the time dependence has been neglected as this has no effect other than to scale the emission profile everywhere by some coefficient. In equation (3.9), however, we do not have this luxury. As we are not solving particle transport against time, instead making some assumptions about the system in order to calibrate for the viewing angle and finite gas puff size, we must account for t. Increasing the time has the effect of moving the point of brightest emission closer to the injection point, and *vice versa* for decreasing t. Here t was chosen to be the time taken for a neutral helium atom with a thermal velocity at around room temperature ($T \approx 300\,\mathrm{K}$, $v_{\mathrm{th}} \approx 2000\,\mathrm{m/s}$) to move through the thickness of a plane in the simulation domain, 1 mm, giving a time of $\approx 5 \times 10^{-7}\,\mathrm{s}$.

A few examples of the reconstruction of the average gas puff emission with the simulated diagnostic are shown in figure 3.8. These discharges were chosen for their variation in the electron density values seen in the SOL. Each reconstruction uses the same value for the width of the gas puff cone, as calculated in section 3.3.2. The only difference between them is the values of the electron density and temperature throughout the modelling domain. In each example, the reconstruction manages to regain the overall shape of the average emission shape of the gas cloud. The location of the brightest emission point is also recovered to a good accuracy, to with $\approx 5\,\mathrm{mm}$ for all gas puffs. This lends evidence to our assumptions being valid, as nothing other than the density and temperature profiles were changed from one reconstruction to another, yet the overall emission rates and amount of ionisation was captured well enough to change the maximum brightness locations.

It is known that the backing pressure of the GPI gas chamber, as well as the voltage applied to the piezoelectric valve, can alter the gas puffing rate of the GPI diagnostic [81], and hence affect the density of neutrals in the gas puff cloud [19]. Whilst this has not been explicitly explored in this work, of the 28 different gas puffs that comprise of the data to be analysed as part of the experimental portion of this thesis in chapter 4, 23 had the same chamber pressure of 1.2 bar. This pressure applies to each of the examples in figure 3.8. In these examples, the simulated mean emission shape is different because of only changes to

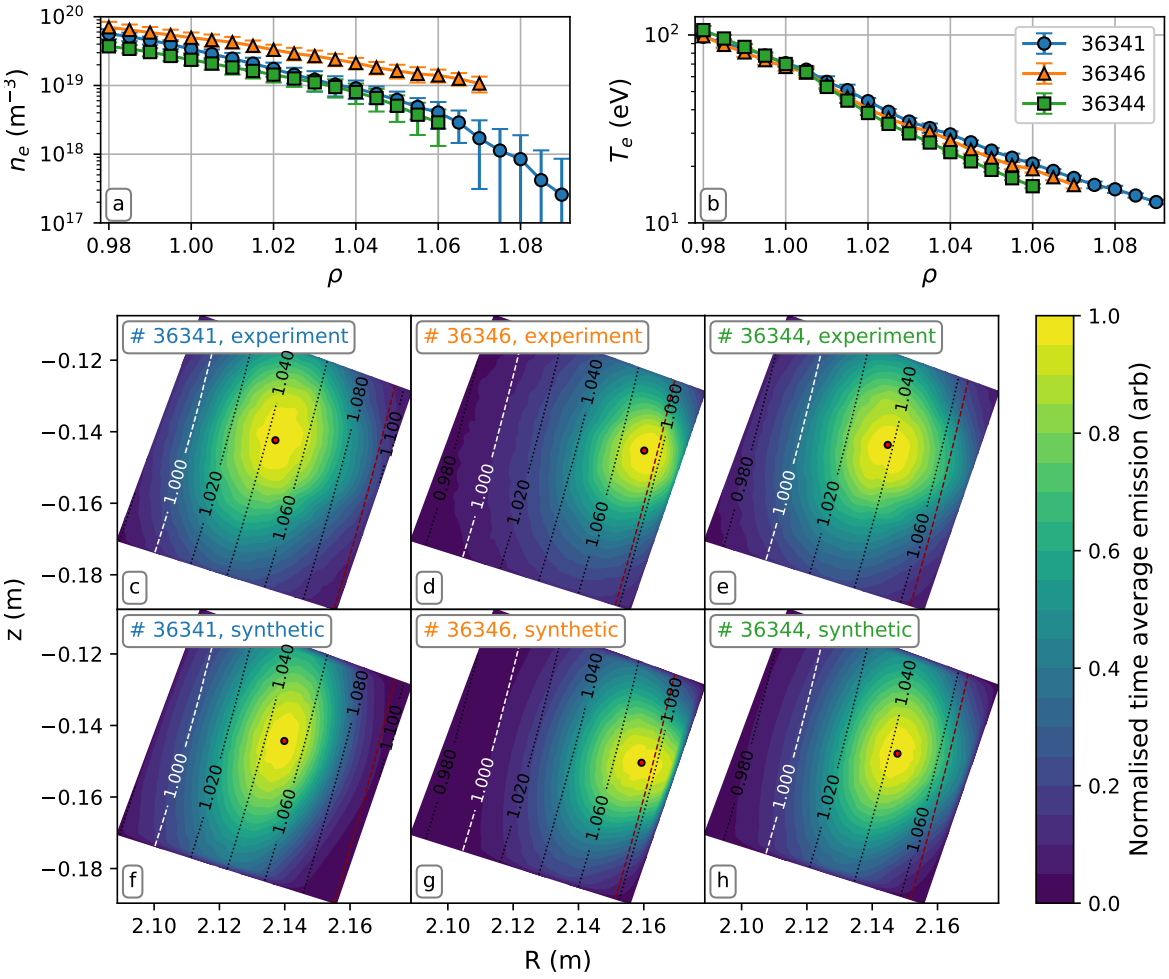

Figure 3.8: The electron density (a) and electron temperature (b) profiles for a selection of discharges during GPI gas puffs. The mean emission profiles for an H-mode discharge with 5 MW NBI heating (c); an H-mode discharge with 2.5 MW NBI-heating (d); and an L-mode discharge (e). The corresponding reconstructions with the simulated diagnostic without a filament (f-h). The differences in locations of the points of brightest emission (red circles) between the experimental and simulated gas puffs are 3.4 mm (c & f), 5.2 mm (d & g), and 5.2 mm (e & h). The separatrix (white) and limiter shadow (dark red) locations are added.

the electron density and temperature profiles. As such, rather than one synthetic model used for all gas puffs, the model has been run with enough different iterations to account for a variety of different profiles, as well as changes to the magnetic geometry, the importance of which will become apparent in section 3.3.4. Each time, the mean emission in the synthetic model is a good match to the experimental measure of the mean emission.

3.3.4 Adding filaments

Next, a filament is added into the virtual domain. A starting position is picked as one of the pixel locations in the GPI view and a second order Runge–Kutta (RK2) method [87] with step-size $\mathrm{d}l = 1\,\mathrm{mm}$ is used to trace the magnetic field from this position, in both directions, until outside the virtual domain – these positions define the centre of the filament, and its position, $\boldsymbol{r_b}(x, y, z)$. For a given blob diameter, δ_b, the positions of the domain, $\boldsymbol{r}(x, y, z)$ within the radius from the blob's position ($|\boldsymbol{r} - \boldsymbol{r_b}| \leq \delta_b/2$) are said to be part of the filament. We here make the assumption that the electron density inside the blob is equal to the electron density just inside the confined plasma, $n_{e,b} = n_e(\rho = 0.95)$. The electron temperature is left unchanged to the background as energy transport is much faster than mass transport.

Figure 3.9 shows the simulated diagnostic data for a blob with $\delta_b = 1\,\mathrm{cm}$ at $\rho = 1.04$. Three images are included. Figure 3.9a first gives an 'idealised' image for the viewing angle and toroidal gas puff extent we have where we imagine emission from only inside the blob itself ($I(|\boldsymbol{r} - \boldsymbol{r_b}| > \delta_b/2) = 0$), 3.9b shows the emission from the blob and the surrounding gas puff, which is how the signal would look in the raw GPI experimental data, and 3.9c after 3.9b has been normalised to the emission of the gas puff alone, which has the effect of removing the contribution of the neutral density, hence the large qualitative similarity between a and c. The smearing of the blob in the radial direction can clearly be seen, and should be expected as the angle in the radial direction between the local field line at the image plane and the diagnostic line-of-sight (i.e. $z = \text{const.}$ plane) contributes nearly all of the misalignment.

Scans for all the positions in the GPI detector for blob diameters from 0.2 cm to 3 cm have been performed for a variety of different shots, to cover a range of magnetic geometries in the SOL for different sets of n_e and T_e profiles. To calibrate from the measured sizes back to the estimated real sizes, the measured blobs positions is first identified. From this, the measured radial and poloidal diameters are used to determine the actual size from the virtual measurements at that location. A discussion of the error on the diameter measurements is given in section A.2.

3.3.5 Conclusion

In this chapter, the fundamentals of a gas puff imaging diagnostic have been explained. Specific details about the GPI on ASDEX-U have been detailed, and a simulated diagnostic

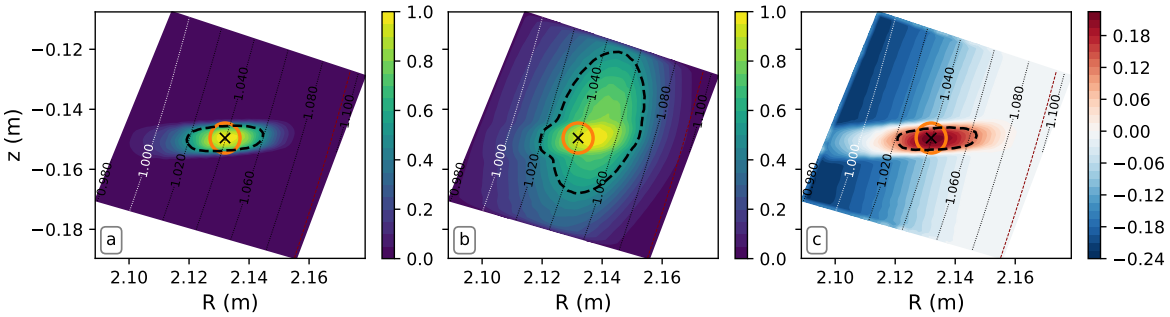

Figure 3.9: Normalised emission for a filament with $\delta_b = 1\,\text{cm}$ in the virtual domain neglecting emission from outside the filament (a) and including emission from outside the filament (b). The fluctuation emission, normalised to the gas puff emission without a filament (c). The starting position of the blob is plotted (black x), and the seperatrix (white) and limiter shadow (dark red) locations are added. The contour at half the maximum brightness (black dashed) denotes the blob edge, and a circle with diameter 1 cm is added for reference of the virtual blob diameter.

was constructed by measuring the mean size of the gas puff to counter for the limitations caused by the viewing position and curvature of the magnetic field. Filaments with a range of diameters were placed in various locations within the simulated gas puff, and the predicted emissions, and therefore 2D filament projections, were measured. These results can now be used to convert perceived filament sizes in the experimental GPI data to estimate the real radial and poloidal diameters of the filaments.

Chapter 4

Blob measurements in ASDEX Upgrade

4.1 The discharges

A total of 8 discharges were performed in ASDEX Upgrade that can be categorised into 4 different discharges types: L-mode, N_2 seeded L-mode, H-mode with 5 MW of NBI heating, and H-mode with 2.5 MW of NBI heating. Each of the discharges is in a lower single null configuration, with ion ∇B drift pointing downwards towards the x-point. They all have a toroidal magnetic field strength of $B_T = -2.5\,\mathrm{T}$, a plasma current $I_p = 0.8\,\mathrm{MA}$, and a safety factor of $q_{95} \approx 4.8$. The H-mode discharges have additional heating from electron cyclotron resonant heating (ECRH) of 1.2 MW, and 0.5 MW for the L-mode discharges. Ion cyclotron resonant heating (ICRH) was not used in any of these discharges.

4.2 ELM removal

In order to ensure a fair comparrison between each discharge type, ELMs must be correctly identified in the H-mode data and only the inter-ELM periods compared. A commonly used proxy of ELM activity in ASDEX Upgrade is the Ipolsola signal, which is the electrical shunt measuring the poloidal SOL current through two of the outer divertor tiles to the vessel structure [88]. An example of the signal can be seen in figure 4.1. Close to the seperatrix, ELMs can be seen in the GPI signal as large drops in signal intensity as the hot ELM filament propagates through the SOL and ionizes most of the injected neutral gas. In the far-SOL

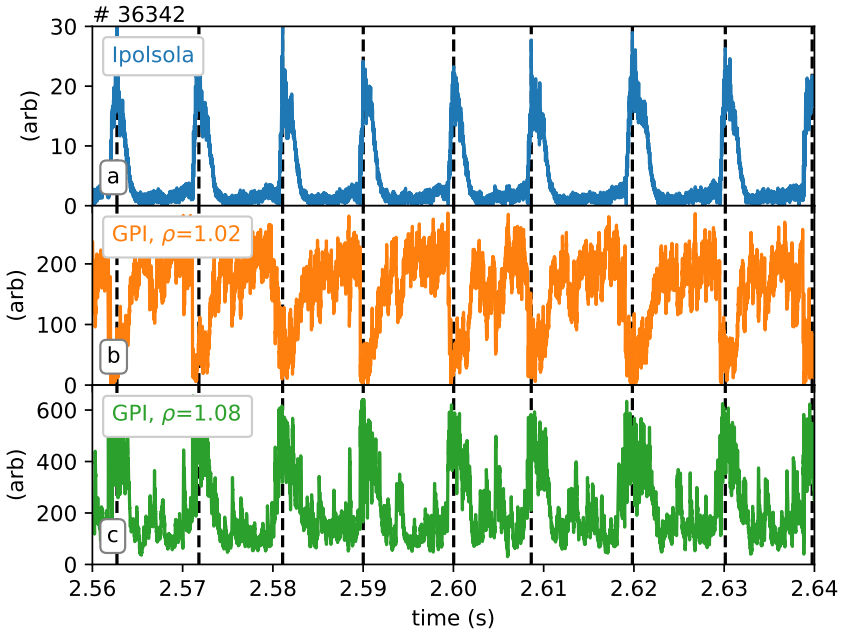

Figure 4.1: Example time traces of (a) the divertor shunt current signal, (b) GPI signal in the near-SOL, and (c) GPI signal in the far-SOL. The black dashed lines show estimated arrival times of the individual ELMs.

ambient temperatures and densities are lower than in the near SOL resulting in lower GPI intensities. Here, the ELM filament conversely causes a large increase in intensity. In the far SOL in particular it can be difficult to distinguish between ELM filaments and blob filaments as they have similar shapes in the 0D time signals, particularly with smaller ELMs, so the divertor current signal is used instead as the ELM events show obviously in the signal whilst the blob filaments show little to no feature in this signal.

To detect ELM filaments a wavelet transform is used [89]. The wavelet coefficient $C_\tau[n]$ for time t at time period τ is given by

$$C_\tau[n] = \frac{1}{N\sigma_M\sigma_I} \sum_{n=-(N/2)+1}^{N/2} (M[n,\tau] - \bar{M}[n,\tau]) * (I_p[n] - \bar{I}_p[n]) \tag{4.1}$$

where $M[n,\tau]$ is the chosen wavelet, $I_p[n]$ is the discrete-time signal of the IPOLSOLA current, $\bar{y}$ and σ_y donate the mean and standard deviation of quantity y, respectively, and N is the length of the wavelet and signal. The zero-centred Gaussian function was the chosen wavelet

in this work, given by

$$M[n,\tau] = \frac{1}{\tau\sqrt{2\pi}} \exp\left(-\frac{n^2}{2\tau^2}\right) \tag{4.2}$$

for $n \in -N/2 < n \leq N/2$. N was taken to be 1024 as using a power of 2 helps reduce cost computing the wavelet coefficients and was found to be long enough to provide a good measure of ELMs in ASDEX Upgrade. The IPOLSOLA signal has the same 200 kHz sample frequency as the GPI Phantom v711 detector, so 1024 time samples corresponds to 5.12 ms.

The normalisation of the wavelet and signal to the mean and standard deviation ensures $-1 \leq C_\tau[n] \leq 1$. Once a suitable wavelet width, τ, is chosen the wavelet coefficients are calculated and a value greater than a threshold of 0.5 is deemed to be caused by an ELM filament with that size. A wavelet width of $\tau = 100$ is well suited to detecting most ELMs, particularly larger ones similar to those shown in figure 4.1. Detecting smaller ELMs is more difficult, even with a smaller wavelet width. Figure 4.2 shows an example of smaller ELMs with wavelet coefficients for $\tau = 50$ and $\tau = 100$. This 80 ms snippet shows how a smaller wavelet width catches an extra 5 smaller ELM filaments, yet still demonstrates how the process is imperfect. Reducing the wavelet width any further showed no appreciative increase in detection rate, but even at $\tau = 50$ the coefficient stays above the 0.5 threshold for all of the longer duration large ELMs. In an attempt to catch a variety of ELM sizes, two wavelet widths were used, so the new wavelet coefficient is given by

$$C_{\max}[n] = \max\left\{C_{\tau=50}[n], C_{\tau=100}[n]\right\}. \tag{4.3}$$

To account for the sharp rise and slower decay of the ELM filament in the current, as well as to account for the propagation of the ELM through the SOL appearing in different GPI channels at different times, the ELM is defined to start 200 timesteps before and 600 timesteps after the wavelet coefficient crosses the 0.5 threshold, 1 ms and 3 ms at 200 kHz, respectively.

4.3 Data analysis

4.3.1 Data normalisation

The raw output from the GPI diagnostic contains data about not only the local electron density and and temperature, but also the local neutral density from the gas puff. A com-

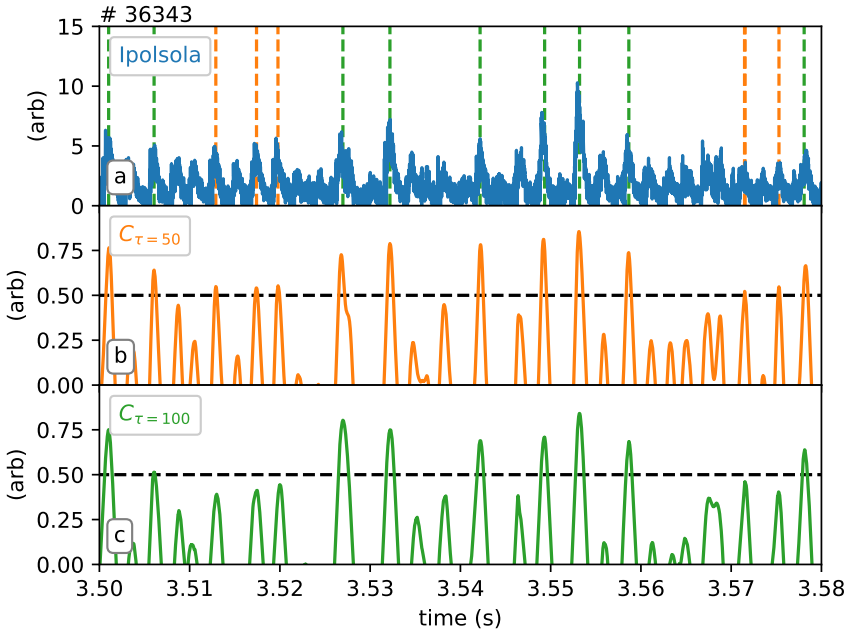

Figure 4.2: Time traces of: the divertor shunt current signal (a); wavelet coefficients for $\tau = 50$ (b); and wavelet coefficients for $\tau = 100$ (c). The orange vertical dashed lines show where ELMs are detected in the $C_{\tau=50}$ coefficients only, and the green vertical dashed lines are detected by both (a). The horizontal black lines represent the 0.5 threshold for ELM detection (b & c).

monly used analysis technique to study plasma fluctuations, whether with GPI [80, 90] or other diagnostics, such as BES [15,91] or Langmuir probes [46,57], is to normalise the signal to the signal mean, $\bar{I}$, such that the fluctuation data, $\tilde{I}$, is given by

$$\tilde{I} = \frac{I - \bar{I}}{\bar{I}}. \tag{4.4}$$

With gas puff imaging, a finite amount of time after an ELM filament passes is required for the local gas puff neutral density to regain a steady-state level and for the signal to reach a constant mean. In order to maximise the amount of usable data during a gas puff the fluctuation data are normalised to a lowpass filter of the signal instead of the mean, as showcased in figure 4.3. A comparison between the two normalisation techniques was made in a portion of L-mode data where the signal mean was not seen to vary much. The results showed qualitatively similar measurements of single point fluctuation PDFs, conditionally averaged waveforms, and filament size and velocity distributions. As such, the lowpass filter normalisation is used in this thesis.

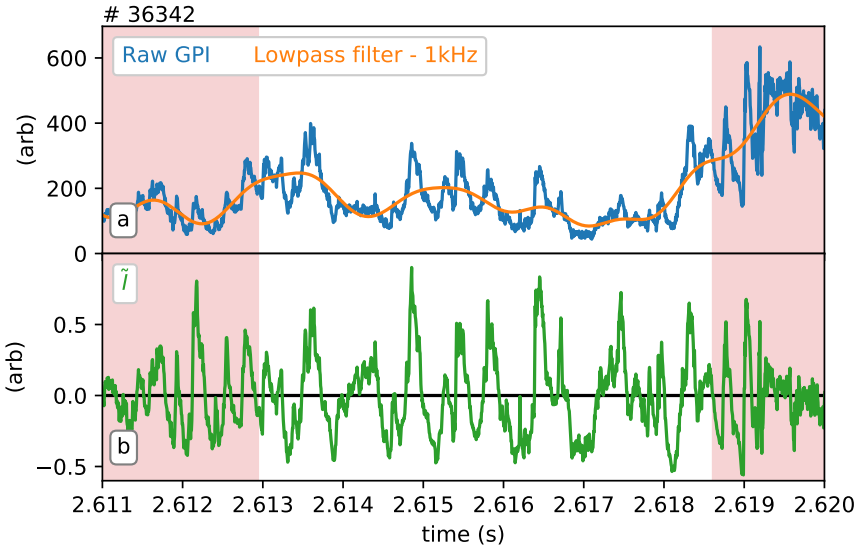

Figure 4.3: Time traces of: the raw GPI signal with the lowpass 1 kHz signal overlaid (a); and fluctuation signal (b), $\tilde{I}$, given by equation (4.4), with the $\tilde{I} = 0$ line included in black. Red shaded areas indicate a time during an ELM.

4.3.2 Blob detection

The filament detection method used here is commonly used throughout the field for a multitude of diagnostics [18, 43, 44, 57, 58, 63, 64]. A reference location is chosen in the GPI detector and the 1D time signal used - for an example, see figure 4.4. The signal is said to be contributed by a filament if it exceeds the threshold $\tilde{I}_{\text{blob}} \geq \mu + 2.5\sigma$, where μ and σ are the fluctuation signal mean and standard deviation, respectively. The blob's arrival time, t_i, is the maximum of the fluctuation signal above this threshold. Blob detections are said to be caused by the same filament if the signal does not decrease below 0 between detections. If multiple maxima are found in this duration, the largest is taken as the arrival time.

An example of the fluctuation signal with detected filaments is shown in figure 4.4. This shows one of the main limitations with using this threshold as a detection tool, in that only large amplitude filaments are included in the analysis. Although results show little variation in the conditionally averaged waveform for filaments with amplitudes above this threshold, seen in Alcator C-Mod with GPI [57], and TCV with Langmuir probes [62], as well as for filaments in discharges at different electron densities [92], given that some filament properties may change and depend on fluctuation amplitude (e.g., radial velocity) it must be noted that not all the filament-space is included in this analysis. A local intermittency measure has been

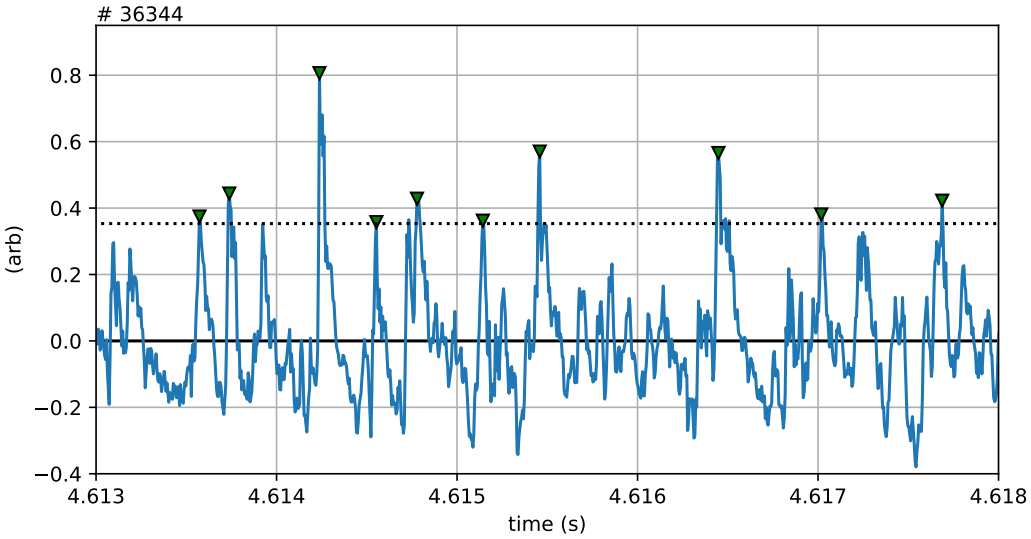

Figure 4.4: Example time trace of the fluctuation signal with filaments identified (green triangles). The detection limit of $\mu + 2.5\sigma$ is added (black dotted line).

Table 4.1: A table showing the total number of unique detected filaments for each discharge type.

Discharge type	L-mode	N_2 seeded	2.5 MW H-mode	5 MW H-mode
# blobs	396	337	300	262

used as a blob detection tool in previous works [6,93] that uses a wavelet transform to detect filaments in a time signal that is not immediately dependent on their amplitude, although this was found to return very few detected events when attempted on the data presented here. This is postulated to be due to a $\times 10$ lower temporal resolution in our diagnostic. An implementation of the deconvolution algorithm by Theodorsen *et al.* [50] (discussed in section 2.3), as well as full testing of filament detection with a wavelet transform, was outside the scope of this work. As such, the 2.5σ threshold is used. The total numbers of unique detected filaments for each discharge type are given in table 4.1.

Much of the literature stops here and defines this blob's position, $\mathbf{r}_i$, as that of the reference signal location, and the blob's amplitude, A_i, equal to the fluctuation signal at this position and time, $\tilde{I}(\mathbf{r}_i, t_i)$. This is a valid approach, particularly in diagnostics that can only sample one position in the plasma at a time, such as Langmuir probes, or in other imaging diagnostic systems with a low spatial resolution. The Phantom v711, however, has a nominal spatial resolution of $\approx 1\,\text{mm}$, with a blob often covering > 10 pixels in each direction, and

this method of describing a blob's amplitude and position becomes ineffective, particularly when tracking its motion through the SOL. Instead, this detection method is used here purely for detecting blobs, and their position and amplitude are measured separately. Two reference locations at a height of $z = -0.15\,\mathrm{mm}$, are used in each discharge. This is in the centre of the GPI frame, poloidally, and close to the centre of the gas puff, where the signal is strongest. The pixels closest to this height at $\rho = 1.04$ and $\rho = 1.06$ are used. The majority of detected events at $\rho = 1.02$ are too close to the separatrix to be a useful reference location, with some pixels corresponding the blob being in the confined plasma, and $\rho = 1.08$ to close to the limiter shadow in the H-mode discharges, and outside of the GPI view for L-mode discharges, to be used.

4.3.3 Blob amplitude and position

Turning to the 2D frame, F, at time t_i, where all pixels are normalised as described in section 4.3.1, all channels are considered to belong to blob i if their fluctuation amplitude is greater than half the current amplitude estimate, $F(\mathbf{r}_i, t_i) \geq A_i/2$, and they are connected to the reference channel by other channels above this threshold. The blob amplitude is then revised to be the maximum of these channels. Next, the limits of the blob are redefined using the revised amplitude, and some pixels which belonged to the blob previously will now lie outside the edges of blob. This ensures that the amplitude and size of the blob do not depend on the reference channel used for detection - it does require the starting location be close to the blob but does not require it to be within the limits of the blob, as is sometimes the case. An example blob is plotted in figure 4.5. The amplitude measured at the reference location is 0.436, where as the revised amplitude using the maxima of pixels in the blob is 0.580.

Once the amplitude is defined, the position of the blob can be calculated. The position is calculated as the centre of mass (CoM) using the intensity of all pixels inside the blob boundary. The CoM is given as

$$x_{\mathrm{CoM}} = \frac{\sum_i x_i \tilde{I}_i}{\sum_i \tilde{I}_i} \tag{4.5}$$

where x is the coordinate dimension to calculate the CoM for (i.e., R and z), and subscript i is each pixel belonging to the blob. The position of a filament's CoM is rarely the same as the reference location, or the location of the brightest blob pixel. Figure 4.5 shows how the blob's

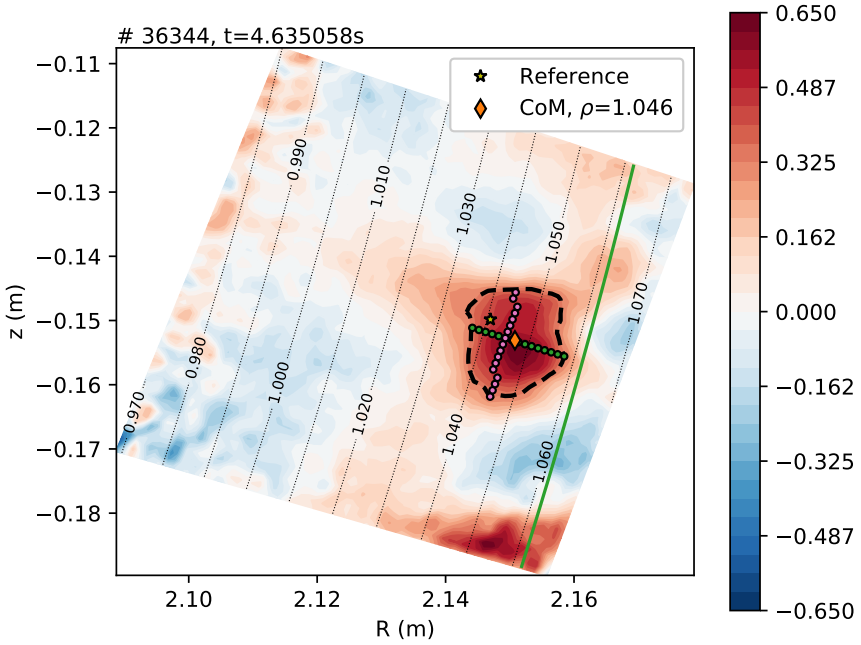

Figure 4.5: A frame showing an example of a blob measurement made in the far SOL. The blob position (orange diamond) has moved out and down from the reference location (yellow star), making the blob's position closer to ρ=1.05 than ρ=1.04. The flux surface and perpendicular pixels used to measure the blob poloidal (purple) and radial (green) diameters are shown.

position is 3 mm out and down from the reference location, which moves from a normalised radius of $\rho = 1.040$ to $\rho = 1.046$. By revising the blob's location and amplitude this way, the measurements do not depend on the reference location chosen to detect filaments.

4.3.4 Blob radial and poloidal size measurement

Once the filament's position and which pixels are considered to be part of the blob are identified, the radial and poloidal diameters, δ_r and δ_θ respectively, can be measured. Firstly, although the fibre-optic bundle was rotated to approximately line up with the minor radius and poloidal directions, the pixel positions are still given in terms of major radius and height (R and z), and the position of flux surfaces can vary from shot to shot, as well as through out the shot. As such, we start by measuring the angle the radial and poloidal direction vectors make to the $R - z$ plane, $\phi_{r,\theta}$, shown in figure 4.6.

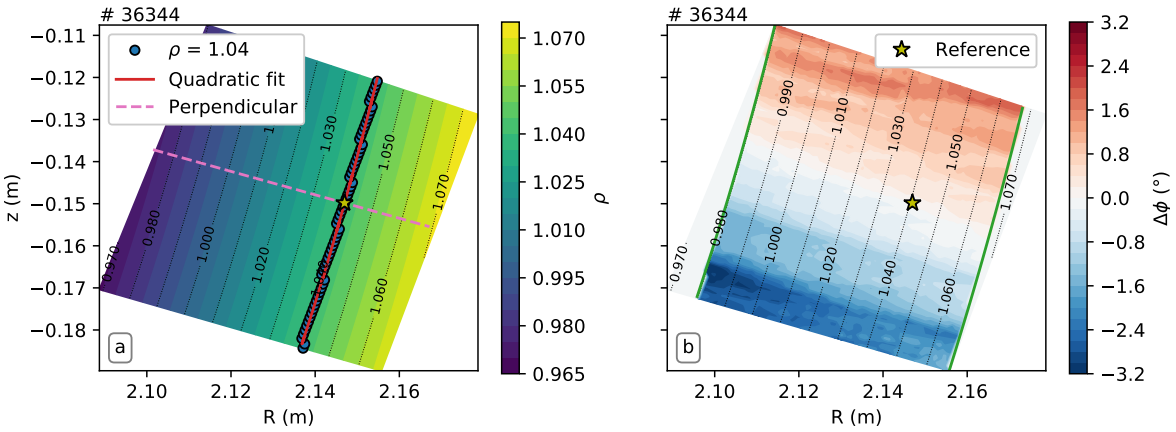

Figure 4.6: (a) Normalised radius values for the GPI view. Blue dots show the pixels used for the quadratic fit (red line) at the reference location (yellow star). The tangent at the reference location is found to calculate the poloidal direction vector (not shown), and the perpendicular used for the radial direction vector (pink dashed line). For this reference location and magnetic geometry, an angle of $\phi_{(r,\theta)} = -15.6°$ is found. (b) The difference between $\phi_{(r,\theta)}$ for each location minus and the reference location. The green lines show the limits where the value of ρ doesn't extend along the full poloidal extent of the GPI view. The maximum absolute difference in this region is 3.2°.

The pixel in each row* which is closest to the normalised radius in the reference location is chosen to locate the flux surface through the entire vertical extent of the GPI view. A quadratic function, $z = AR^2 + BR + C$, is fit to in order to locate the pixel height as a function of major radius for the $\rho = \text{const}$ surface. In the example shown in figure 4.6a the coefficient of determination [94] for the fit is $R^2 = 0.9962$, and is greater than 0.99 for all other reference locations in all shots and gas puffs. From this fit, the poloidal direction vector is defined as a tangent to the flux surface at the reference location, $\theta = 2AR_{\text{ref}} + B$, and perpendicular to this is the radial direction vector, $\mathbf{r} = -1/2AR_{\text{ref}}$, and the angle to transform from the $R - z$ plane to the $r - \theta$ plane is

$$\phi_{r,\theta} = \arctan\left(\frac{-1}{2AR_{\text{ref}}}\right). \tag{4.6}$$

For the example in figure 4.6, the specific quadratic fit parameters are given in table 4.2. Using these values gives the transform angle in this specific case as $\phi_{r,\theta} = -15.6 \pm 1.3°$. The

*Here a row refers to a line of pixels in the GPI view that extend approximately along the minor-radial direction, or almost horizontally in the plots.

Table 4.2: A table showing the parameters to a quadratic fit of the flux surface in the SOL.

Coefficient	Value	Error
A	28.5	5.9
B	-119	25
C	124	27

calculation of the error is discussed in section A.1.

The same transform angle is used for all blobs detected at a single reference location, and as they travel throughout the scrape-off layer, and is used when calculating the blob diameters and velocities. As such, the error from the fit can be less significant than the error from a changing transform angle in another part of the detector view. Figure 4.6b shows the difference between the transform angle calculated at each pixel position in the GPI view minus the angle found at the reference location, $\Delta\phi$. The size of the difference in the angles lies between -3.2–$2.0°$. The far edges of the view are not included beyond the limits of ρ at the top left and bottom right corners, as a flux surface cannot be traced over the whole poloidal view. The largest values of $\Delta\phi$ are found at the top and bottom of the frame, however most blobs cannot be tracked this close to the edge (section 4.3.5), so these larger differences in transform angle are unlikely. It was decided that, to air on the side of caution, a larger value of the error for the transform angle $\sigma_{\phi_{r,\theta}} = 3°$ would be used when performing error calculations through out the rest of this work.

To measure δ_θ, starting along the flux surface from the position where the blob's amplitude was recorded, the Euclidean distance between the top and bottom of the blob along the poloidal direction vector is measured, stopping when a pixel's intensity is $\tilde{I} < A_i/2$. This is repeated, moving the starting pixel along the row of pixels towards the separtrix until it is outside the blob, then repeated again in the opposite direction. The largest distance is attributed as the poloidal diameter of the blob at time t_i. Similarly for δ_r, starting from the location of maximum amplitude, but now the measurement is made along the radial direction vector, moving the starting position up and down the column of pixels, and the largest distance is the radial diameter for time t_i. For the example in figure 4.5 the blob's diameter is measured as $(\delta_r, \delta_\theta) = (1.49,1.67)$cm. The error on the diameter measurements is discussed in section A.2.

4.3.5 Blob velocity measurement

To measure the velocity of filaments, a tracking algorithm is implemented. Starting with the centre-of-mass position in the detected frame, $\mathbf{r}_{\mathrm{CoM}}(t_i)$, equation (4.5) is used to find the local centre-of-mass in a circle of radius 1 cm in the next frame, $F(t_i + \Delta t)$, where Δt is the time between frames which, for these experiments, is Δt=5 µs. A new circle with the same radius is used centred around the centre-of-mass found in the last step, and is repeated until it does not move. This has the effect of moving the centre-of-mass along the gradient of the intensity field in the frame, until an approximation of $\mathbf{r}_{\mathrm{CoM}}(t_i + \Delta t)$ is found. This location is used as the new 'reference location', and the blob's amplitude, location, and radial and poloidal diameters are measured, as described in sections 4.3.3 and 4.3.4. The velocity, in the $R - z$ plane is given by

$$v_x = \frac{x_{\mathrm{CoM}}(t + \Delta t) - x_{\mathrm{CoM}}(t)}{\Delta t}, \tag{4.7}$$

where x is the R or z direction, and x_{CoM} is given by equation (4.5). The transform into the $r - \phi$ plane uses the transform angle, $\phi_{r,\theta}$, and the velocity magnitude, and radial and poloidal velocities are given by

$$\begin{aligned} |\mathbf{v}| &= \sqrt{v_R^2 + v_z^2} \\ v_r &= |\mathbf{v}| \cos\alpha \\ v_\theta &= |\mathbf{v}| \sin\alpha. \end{aligned} \tag{4.8}$$

α is the angle that the velocity magnitude $|\mathbf{v}|$ makes with the radial direction vector, given by

$$\alpha = \arctan\left(\frac{v_z}{v_R}\right) - \phi_{r,\theta}. \tag{4.9}$$

The error calculations for v_r and v_θ are explained in appendix A.3.

4.4 Results

4.4.1 Single-point results

We begin by presenting results from analysis of single point time series data in the scrape-off layer, from a single pixel location in the gas puff imaging diagnostic. This can be directly

compared to analysis from diagnostics such as Langmuir probes, or other single-point analysis in other GPI systems, with the advantage of analysing and diagnosing multiple locations simultaneously.

4.4.1.1 Probability distribution functions

Here we demonstrate how the plasma fluctuations recorded by gas puff imaging at single locations in the SOL follow Gamma distributions, 2.3. The Gamma distribution function, shape parameter k, and scale parameter θ, are given by equations (2.9)-(2.11), respectively. Figure 4.7 shows the probability distribution functions for the fluctation data* at a range of locations in the SOL for each type of discharge. Each set of measured PDFs follow Gamma distribution functions, as shown by the dashed lines, which are not fits to the data points themselves, but instead are calculated from the input parameters of the Gamma distribution functions, k and θ, calculated from the mean and standard deviation of the fluctuation points alone. The L-mode discharges in particular (figures 4.7a and 4.7b) have PDFs of fluctuation amplitudes close to normal distributions in the near SOL which become more flattened with distance into the SOL, indicating a reduction in the smaller sized fluctuations and increases in the larger sized fluctuations and distance from the separatrix increases. The same Gamma distributions have been shown in Alcator C-Mod [57] [95], TCV [62], ASDEX Upgrade [96, 97], MAST [48], and NSTX [20]. Both with and without nitrogen seeding, the distribution functions remain approximately similar up to ρ=1.04, but for the far SOL, the PDF in the N_2 seeded discharges experiences a noticeable further broadening, with more fluctuations at higher values than without nitrogen.

Both types of H-mode discharge are similar to one another but both are markedly different to the L-mode. In H-mode the near-far SOL boundary (ρ=1.04,1.06) show similar distributions to the L-mode distribution (ρ=1.04), particularly when considering the input parameters for the distributions, as seen in table 4.3, and the far SOL (ρ=1.08) is very similar to the far SOL of L-mode without nitrogen (ρ=1.06). The similarity between L-mode and H-mode PDFs has been shown previously in ASDEX Upgrade [96]. Where the PDFs differ greatly is in the near SOL. At ρ=1.02 the distributions are again flattened similar to the far SOL, as opposed to becoming more Gaussian. Results from NSTX [20] using GPI

*Note that the Gamma distribution has a non-negative range, and as such cannot produce the exact single point PDFs shown here. Instead, when calculating the input parameters, $\tilde{I}+1$ is used, and the resulting PDFs are translated by +1 in the x-direction.

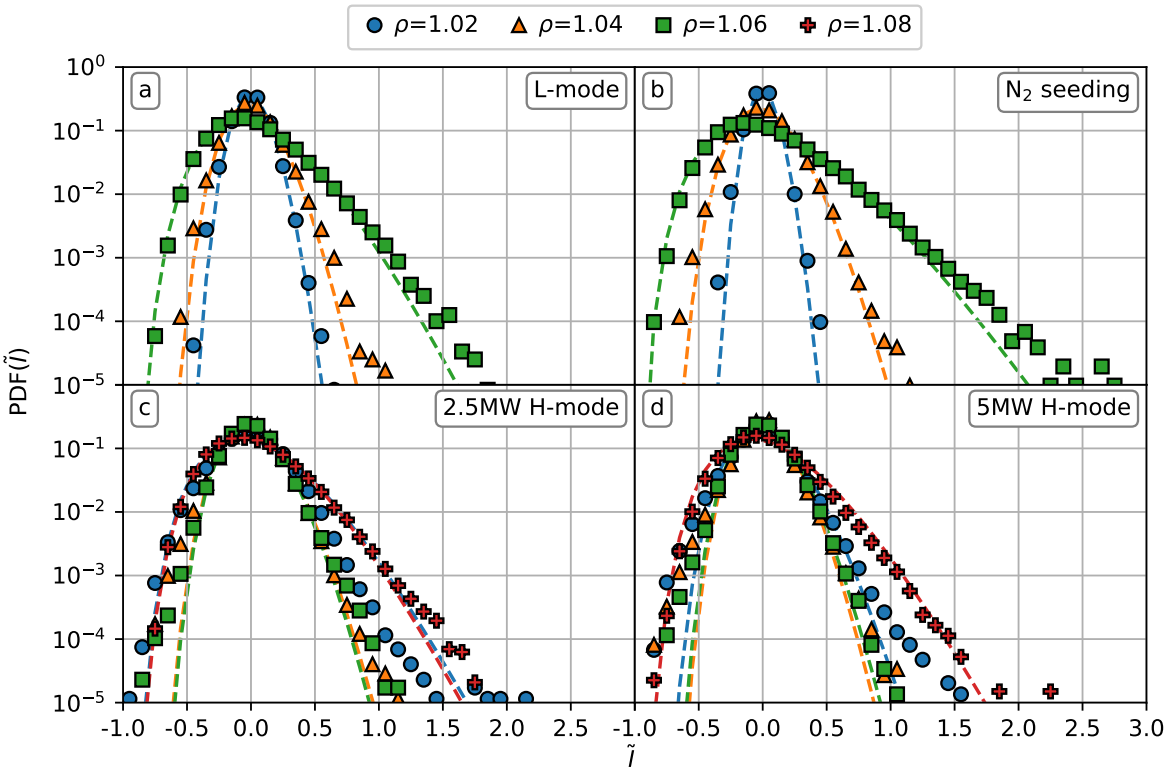

Figure 4.7: Probability distribution functions for different single locations in the SOL during (markers): L-mode (a); L-mode with N_2 seeding (b); H-mode with 2.5 MW of NBI heating (c); and H-mode with 5 MW of NBI heating (d), with the approximated Gamma distribution functions included (dashed lines).

show a PDF inside the LCFS in L-mode discharges with a similar slightly flattened shape presented here. This could indicate an error in the location of the LCFS, reconstructed with CLISTE [14,98]. Other potential sources of error are a reduction in signal strength far from the gas puff injection location as separatrix electron temperatures $\gtrsim 70\,\mathrm{eV}$, ionising most of the neutral gas puff, or a less than perfect removal of ELMs from the signal. The latter would be exacerbated near the separatrix with comparison with the far SOL, particularly for smaller ELMs.

4.4.1.2 Filament amplitudes

The literature widely reports the amplitudes of detected filaments to be exponentially distributed [56, 62, 63]. We investigated this in ASDEX Upgrade in figure 4.8 showing the complimentary cumulative distribution functions (CCDFs), which are equal to 1 minus the cumulative distribution functions (CDFs), for each discharge type for varying distances into

Table 4.3: A table showing the shape (k) and scale (θ) input parameters for the Gamma distribution function for different locations in the SOL for all types of discharges.

ρ	1.02		1.04		1.06		1.08	
Discharge type	k	θ	k	θ	k	θ	k	θ
L-mode	88.5	0.0113	42.6	0.0234	13.1	0.0761	-	-
N_2 seeded	139	0.00720	31.5	0.0317	8.59	0.116	-	-
2.5 MW H-mode	12.1	0.0824	32.8	0.0305	34.6	0.0288	12.62	0.0790
5 MW H-mode	26.1	0.0383	38.8	0.0258	35.0	0.0286	11.5	0.0863

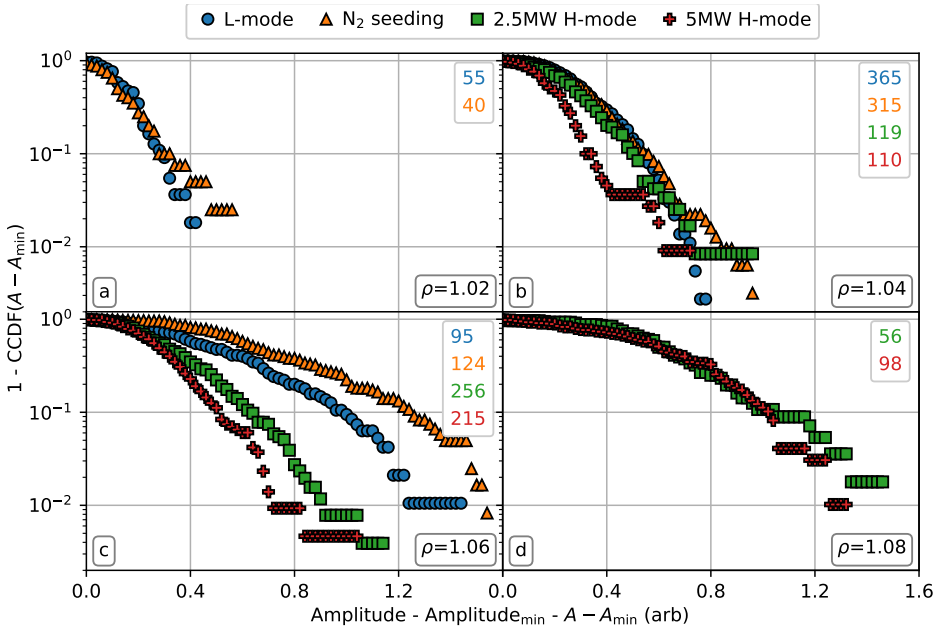

Figure 4.8: CCDFs for filament amplitudes at different radial locations, minus the minimum amplitude. The number of filaments is given in the legends.

the SOL. The CCDF is a measure of how the probability a randomly drawn variable X will be greater than some value x, $P(X > x)$. The CCDF for an exponential distribution is given by

$$F(x;\lambda) = \exp\left(\frac{-x}{\lambda}\right) \tag{4.10}$$

where λ is the mean value, or the mean amplitude in the case of the amplitude distribution, $\langle A \rangle$. Here, the amplitude minus the minimum detectable amplitude is presented. This has the effect of shifting the CCDF in the negative x direction without altering the shape.

When considering the CCDFs for each discharge type individually, it can be seen that the mean amplitude increases as distance into the SOL increases, as shown by the decrease of the gradients of the graphs. The L-mode discharges have no measurements as far into the

SOL as $\rho = 1.08$ and the number of blobs in H-mode successfully tracked back as close to the separatrix as $\rho = 1.02$ is very low, making direct comparisons between these discharges at these SOL locations difficult. At the near-far SOL boundary ($\rho = 1.04$) filament amplitudes are approximately equal, and continue to rise further into the SOL, and the N_2 seeded amplitudes are still equivalent to the H-mode amplitudes at each discharge types largest radii, with the unseeded L-mode discharge showing a clear amplitude reduction compared to all other discharges.

The measurements deviate from the ideal CCDFs, and here we explore why this may be. As explained in section 4.3.3, the way in which we define the blob amplitude and position varies slightly to the literature. This is likely to cause a systematic difference in measurement rather than the large deviation seen here. Instead the discrepancy is likely due to a lower than expected number of measurements for amplitudes near near $A_{\min}$. This could be due to smaller filaments appearing close to larger ones in time. As explained in the filament detection section (section 4.3.2), multiple local maxima are attributed to the same blob if the signal if the signal doesn't go below zero between the maxima, taking the largest to be the blob's arrival time, and discarding the smaller filament. It could also be caused by the different cut-off values used for each gas puff / inter-ELM period. The minimum amplitude subtracted is the minimum amplitude for the entire discharge type, and not for each period of measurement. As such, a shorter period with a low cut-off may be able to measure a small number of filaments with low amplitude, which cannot then be detected in the other measurement periods with a higher cut-off value.

This is demonstrated in figure 4.9. To test this hypothesis, an exponentially distributed set of numbers was randomly drawn with a mean of $\lambda = 0.25$ and its PDF measured. The PDF of the randomly generated data set deviates largely from the experimental PDF. Even when all randomly drawn values below some cut-off were excluded, the normalised PDF does not change if plotted against $x - x_{\min}$, and if normalised to the total number of values measured. Instead, we convolve the PDF with a weighting function, $\mathrm{WF}(x)$, defined as

$$\mathrm{WF}(x) = \begin{cases} y_0 + \left(\frac{1-y_0}{x0}\right) x & 0 \leq x < x_0 \\ 1 & x \geq x_0 \end{cases} \tag{4.11}$$

where, in this specific case, $x_0 = 0.5$ and $y_0 = 0.1$. This simulates detecting fewer events near

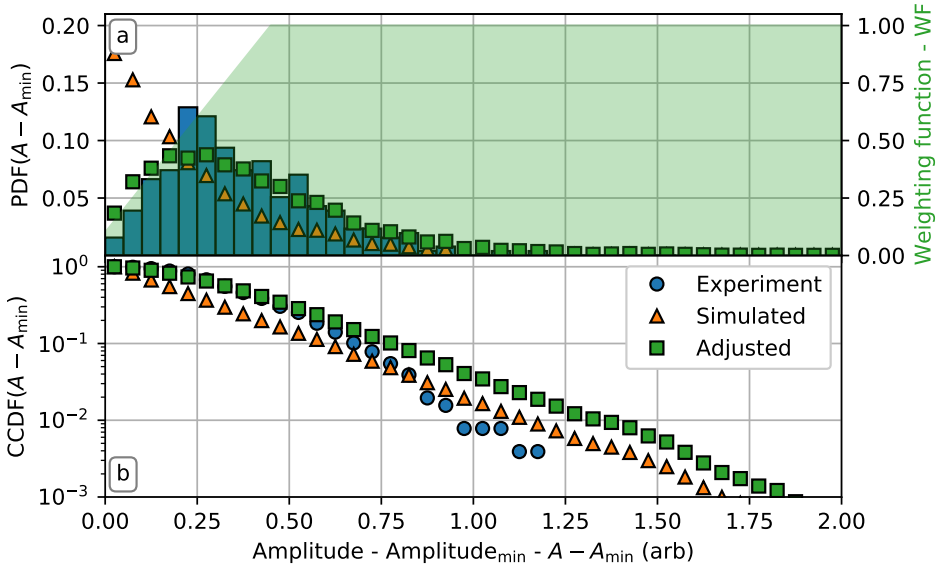

Figure 4.9: The PDF (a) and CCDF (b) for the 2.5 MW H-mode at $\rho = 1.06$ (blue, bar chart & circles). Measurements from an exponentially distributed random distribution with mean = 0.25 (orange, triangle). The adjusted variables (green, square) are calculated by convolving the simulated result with the weighting function with $x_0 = 0.5$ and $y_0 = 0.1$ (green, eq. (4.11)).

the $x_{\min}$ value. Even in this simplified example, the adjusted PDF shape qualitatively tends more closely towards the experimental one. The effect on the CCDF can also be seen. The adjusted CCDF decreases in gradient until x_0, where the gradient matches the simulated CCDF. This shows that the measurements presented here can be made consistent with an exponential distribution of filament amplitudes, given these kinds of assumptions about the measurement limitations.

4.4.1.3 Waiting times

Filaments are born through a Poisson process and as such the waiting time between filaments, given by the difference in arrival times $t_{w,i} = t_{i+1} - t_i$, section 4.3.2, should be exponential distributed by some constant average waiting time, $\langle t_w \rangle$ [6,56,57]. The waiting time CCDFs, equation (4.10), are measured for two reference locations in the SOL, $\rho = 1.04$ and $\rho = 1.06$. When calculating filament amplitudes, the blob was tracked before and after detection, and its precision of location and amplitude refined based on the 2D frame, but for the waiting time statistics, just the times and events detected in the single-point time series are used. This is to ensure we are comparing the waiting time statistics of a single point, rather than filaments that cross through the entire flux surface in the GPI view for any height, z. Any

Table 4.4: A table showing the average waiting times for $\rho = 1.04$ and $\rho = 1.06$ for each type of discharge. $\langle t_w \rangle$ is the measured mean of the waiting times, τ_w and σ_{τ_w} are the fit and error, respectively, from fitting an exponential function, $\exp\left(-t_w/\tau_w\right)$, to the CCDFs. Waiting times are given in milliseconds. R^2 is the coefficient of determination for those fits.

ρ	1.04				1.06			
Discharge type	$\langle t_w \rangle$	τ_w	σ_{τ_w}	R^2	$\langle t_w \rangle$	τ_w	σ_{τ_w}	R^2
L-mode	1.954	1.945	0.027	0.9973	5.737	5.582	0.098	0.9862
N_2 seeded	2.318	2.305	0.031	0.9973	5.23	5.37	0.14	0.9711
2.5 MW H-mode	1.890	1.912	0.065	0.9872	2.602	2.518	0.039	0.9955
5 MW H-mode	1.271	1.419	0.085	0.9806	1.332	1.368	0.072	0.9841

error introduced in the waiting times caused by using the arrival time in the 1D signal rather than the time the blob's CoM is at the exact normalised radius is negligible, as this would be only a few timesteps, where the GPI sampling period is 5 µs, and the bin size used is ten times larger at 0.05 ms.

Figure 4.10 shows the CCDFs for the waiting time between detected filaments. In each case, the average of the waiting times ($\langle t_w \rangle = \sum_i^N t_{w,i}/N$) agrees with τ_w, found by fitting the CCDFs with an exponential function within ±3 %, with the exception of the 5 MW H-mode where the number of waiting times is low, but still agrees to within ±10 %. The values for $\langle t_w \rangle$ and τ_w, as well as the error on the fits, σ_{τ_w}, and the coefficient of determination, R^2, are displayed in table 4.4. At $\rho = 1.04$ the difference between average waiting times across the discharge types is lower than in at $\rho = 1.06$, which would indicate a reduction in the percentage of filaments that make it that far into the SOL. For both locations, H-mode plasmas show a reduced average wait time compared with L-mode discharges, with the 5 MW discharge lower than the 2.5 MW discharges. H-mode shots have a reduced number of waiting times because only filaments in the same inter-ELM period are used to calculate a waiting time. This puts a maximum waiting time on the order of 10s of milliseconds, compared to ≈ 200 ms for L-mode and nitrogen seeding. Even taking this into account, the results suggest a change in the filament generation rate is seen as additional NBI heating power is used.

4.4.1.4 Average waveform & autocorrelation

The average waveform is a commonly used method for measuring the duration time, τ_d, of a filament past a location in the SOL. Whilst the literature is often inexplicit in how τ_d is

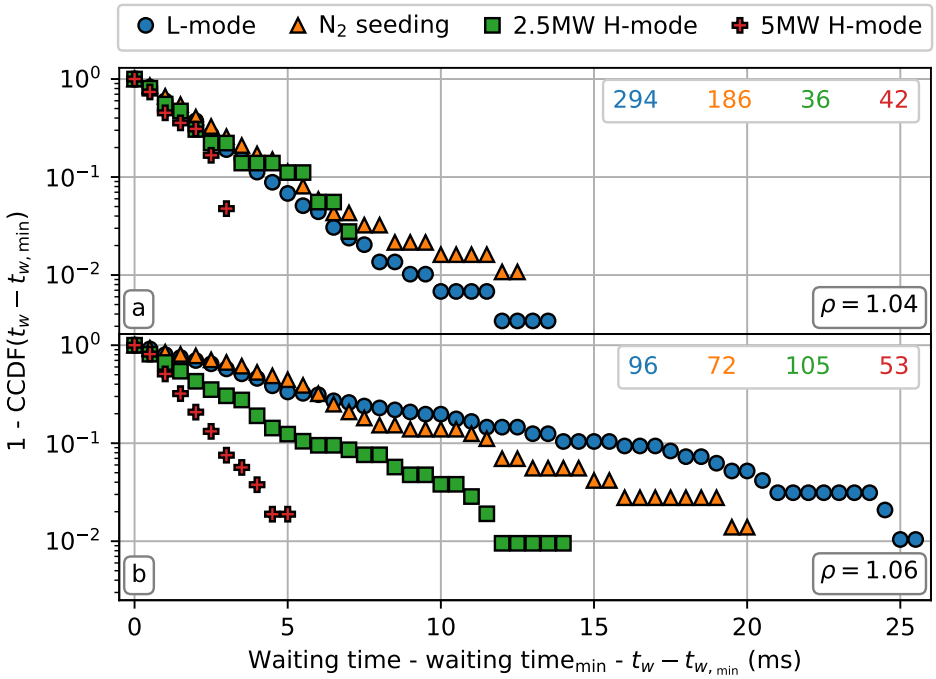

Figure 4.10: The CCDF for waiting times between filaments, taken at the reference locations $\rho = 1.04$ (a), and $\rho = 1.06$ (b). The number of waiting times is given in the legends.

defined, here we take it to be the amount of time the signal due to the filament is above $1/e$ of its amplitude value. Similarly to the waiting time distribution measurements, we take only the signal from the reference locations $\rho = 1.04$ and $\rho = 1.06$, not correcting for the position defined in 2D data. Each filament in the time series is centred to the arrival time, t_i, and normalised to its amplitude, $\tilde{I}(\mathbf{r}_{\text{ref}}, t_i)$ before the signals for each type of discharge are averaged, and the duration time of the averaged signals measured. The results are shown in figure 4.11.

The L-mode and N_2 seeded waveforms show the typical double-exponential shape, with a fast rise and slow decay at both reference locations. The duration time, shown in table 4.5, increases with distance into the SOL, as well with the addition of nitrogen seeding, suggesting either an increase in blob sizes, or a decrease in blob speeds. This increase with ρ is mirrored in the H-mode discharges, although the change for 2.5 MW heating is minimal, and a larger increase is seen for the 5 MW in the far SOL, despite them being equivalent in the near SOL. Interestingly, the H-mode waveform does not exhibit the same shape as L-mode for $\rho = 1.04$. Here, we measure the shortest duration times and the waveform now exhibits a slow rise and fast decay. The autocorrelation times, τ_{ac}, are also measured and shown in figure 4.12 and table 4.5. The autocorrelation is a measure of the how similar the

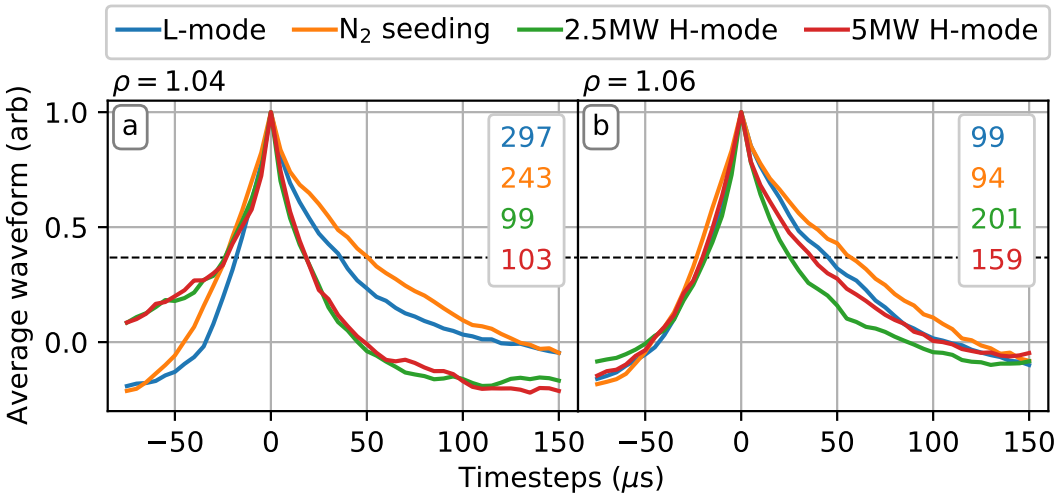

Figure 4.11: The conditionally averaged waveform taken at the reference locations $\rho = 1.04$ (a), and $\rho = 1.06$ (b). The number of filaments used is given in the legends. The $y = 1/e$ cut-off is added (black, dashed).

signal is with itself over some time lag. The autocorrelation function of signal X for time lag τ is given by

$$\mathrm{AC}_{X,X}(\tau) = \frac{1}{N\sigma_{X_n}\sigma_{X-\tau}} \sum_{n=-(N/2)+1}^{N/2} \big(X(n) - \bar{X}(n)\big) * \big(X(n-\tau) - \bar{X}(n-\tau)\big) \qquad (4.12)$$

where $\bar{X}$ and σ_X denote the signal mean and standard deviation, respectively, and the autocorrelation time, τ_{ac} is the time lag required for the autocorrelation function to fall below $1/e$. The only difference in τ_{ac} between discharges is seen in the nitrogen seeding, which is still larger than the L-mode and H-mode discharges, and any increase with ρ is also smaller in comparison to τ_d, with the standard L-mode discharge increasing the most. The data presented here was calculated using $n = 64$ data points, averaging over each the autocorrelation functions for each filament. Whilst changing the number of data points to $n = 32$ or $n = 128$ quantitatively changes the autocorrelation time, the qualitative differences and similarities between discharges and locations are unaltered.

What causes the differences between these conditional averages is not clear. The conditional average of filament waveforms is often performed for data from diagnostics such as Langmuir probes, where a single measurement at one point in space can be made. Whilst any differences between averages allows one to draw conclusions about some corresponding change to the filaments, the measurement is caused by a combination of the filaments' sizes

Table 4.5: A table showing the duration times, τ_d, and autocorrelation times, τ_{ac}, at $\rho = 1.04$ and $\rho = 1.06$ for each type of discharge.

Discharge type	τ_d (µs)		τ_{ac} (µs)	
	$\rho = 1.04$	$\rho = 1.06$	$\rho = 1.04$	$\rho = 1.06$
L-mode	55	65	30	38
N_2 seeded	74	80	40	43
2.5 MW H-mode	42	44	32	31
5 MW H-mode	42	57	31	35

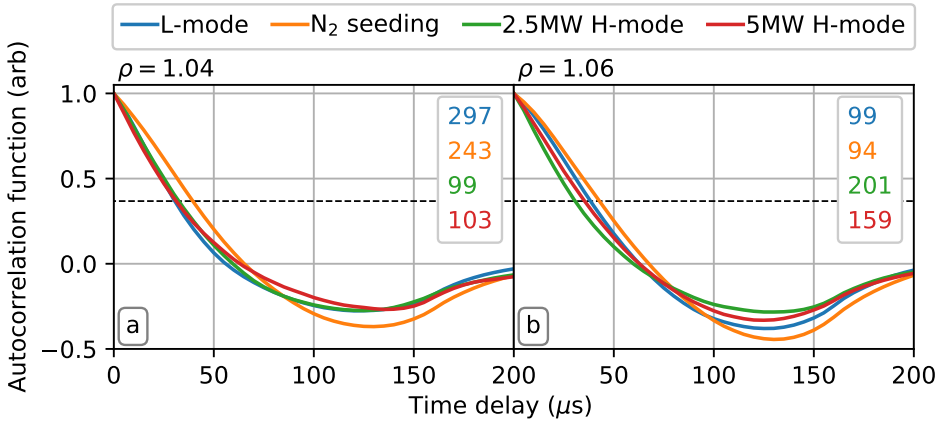

Figure 4.12: The average autocorrelation functions, using $n = 64$ data points, calculated at the reference locations $\rho = 1.04$ (a), and $\rho = 1.06$ (b). The number of filaments used is given in the legends. The $y = 1/e$ cut-off is added (black, dashed).

and velocities and as such we cannot say which of the quantities has changed. This will be addressed in section 4.4.2.

Previously, changes in the conditionally averaged waveform of the electron density of filaments has shown variation with distance from the separatrix [99], including both the reduction in duration time and the change in the ratio of the rise and decay times of the waveform moving closer to the separatrix, reported here. Multiple publications report no change to the average when altering the discharge density [57, 63], or when averaging for binned filament amplitudes [57,62]. There is evidence that increasing magnetic field strength causes a decrease in the duration time of the waveform [100], although any change in the magnetic field between the two measurement locations here is too small to have caused any appreciable difference in the average waveform.

4.4.2 Multi-point results

Here we present the results from analysis of 1D and 2D data, where a gas puff imaging diagnostic shows its strongest advantage over other diagnostic systems.

4.4.2.1 Profiles of statistical metrics

We start by measuring the first four statistical moments of a radial slice through the GPI detector at a constant height of $z = -0.15\,\mathrm{m}$ as this is in the centre of the Phantom view and has a good signal over most of the scrape-off layer near the middle of the gas puff. The results are shown in figure 4.13. (a) shows $I_{\mathrm{RMS}}/\bar{I}$, where I_{RMS} is the mean adjusted standard deviation of the signal and $\bar{I}$ is the mean of the signal, using the 1 kHz low-pass filtered signal. This is a measure of the size of the amplitude of the fluctuations in a signal relative to its mean, or the relative fluctuation size. An increase in $I_{\mathrm{RMS}}/\bar{I}$ is seen in all discharge types for increasing distance into the SOL, caused by an increase in the filament amplitude relative to the mean at these larger distances, also shown in the amplitude CCDFs in section 4.4.1.2. Figures (b) and (c) show the third and fourth statistical moments, the *skewness* and *kurtosis* given by equations (2.13) and (2.14), respectively. The skewness is a measure of the asymmetry of a distribution, where a value of zero would indicate a distribution equally centred around its mean value. Here, positive values of the skewness indicate distributions with the mean shifted to a value higher than the mode or median of the distributions, which increases with distance into the SOL. The result is mirrored by the PDFs shown in figure 4.7 which deviate from normal distributions near the separatrix to distributions with an exponential tail at higher fluctuation values. The kurtosis is a measure of the how much the higher (lower) value measurements contribute towards the distribution, with the kurtosis of the normal distribution equal to 3, by definition*. For example, a distribution with kurtosis greater than 3 would represent a PDF with a relatively higher peak and wider wings compared to a normal distribution with the same standard deviation.

Here, the kurtosis is shown to be around 3 through the edge, which strongly rises with increased distance into the far SOL, indicative of a signal with relatively few measurements far away from the mean. This again is seen in the PDFs in figure 4.7, where an increase in ρ sees a larger deviation from the normal distribution. Finally, figure 4.13 (d) shows the

*We here note that some publications refer to the *excess kurtosis* simply as the kurtosis, which is shifted down by 3, such that the kurtosis of the normal distribution is equal to zero. Throughout this work, unless otherwise specified, we use Pearson's non-adjusted kurtosis

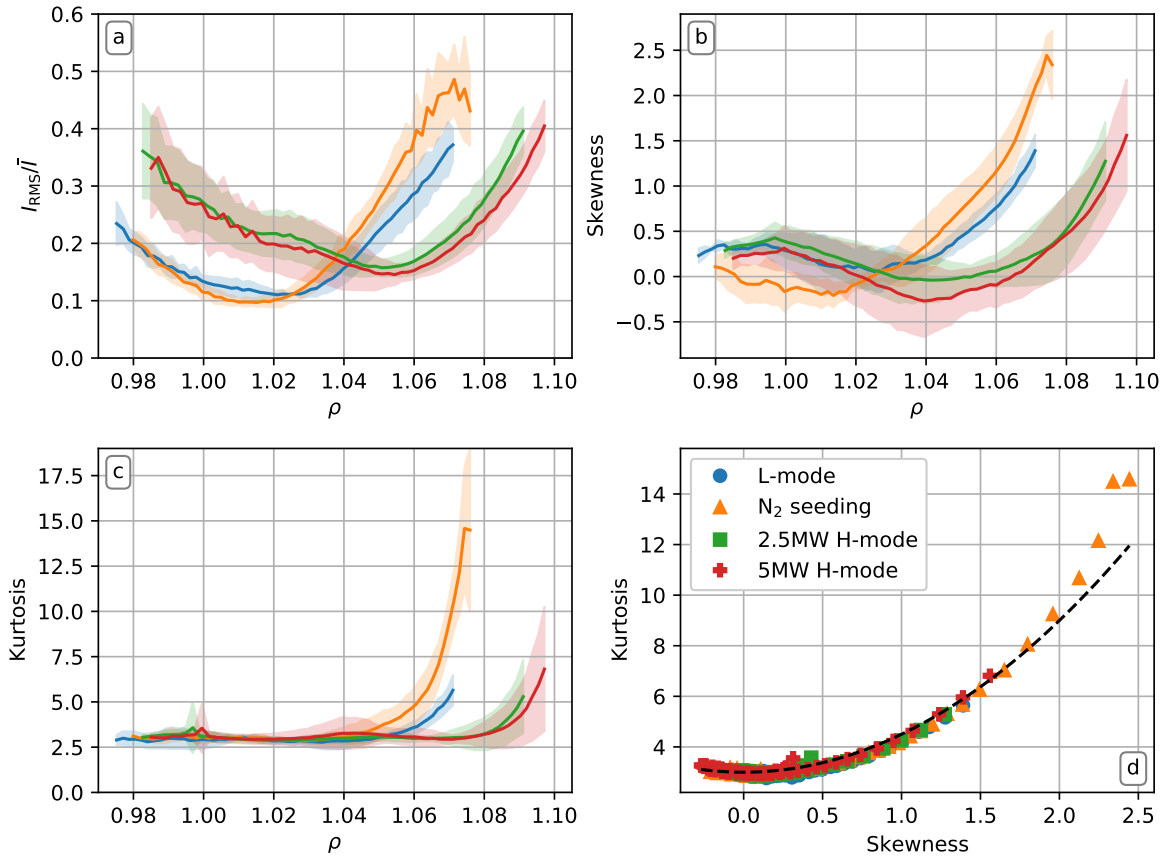

Figure 4.13: Profiles in the SOL for: the relative fluctuation levels (a); skewness (b); and kurtosis (c). The values of kurtosis against skewness are shown (d). The discharge types are L-mode (blue, circle), N_2 seeding (orange, triangle), 2.5 MW H-mode (green, square), and 5 MW H-mode (red, plus).

kurtosis of a signal plotted against its skewness. For the Gamma distribution, the skewness and kurtosis can be expressed solely in terms of the shape parameter, with $S = 2/\sqrt{k}$ and $K = 6/k + 3$, giving the quadratic dependence $K = 3S^2/2$. The measured skewness and kurtosis dependence match the theoretical quadratic scaling well, with each deviating by less than 10 %, with the mean square error for each discharge type being 7 % for L-mode, 6 % for N_2 seeding, 4 % for the 2.5 MW H-mode, and 3 % for the 5 MW H-mode. The points which deviate most from the quadratic scaling are either in the confined plasma at $\rho \lesssim 1.0$ where there is low signal due to most of the helium in the gas puff being ionised, or in the limiter shadow in the far SOL, where the signal is low due to low electron density and temperature.

These results agree well with theory and other results in the literature, but with some differences. Firstly, we discuss the difference in the relative fluctuation amplitudes between the L-mode and H-mode discharges, which was also present in the single point PDFs. The

location of the minima for L-mode and nitrogen seeded discharges is around, or just outside of, the separatrix, and agrees with other low density L-mode results using GPI [57], which show the steadily rising profile with distance into the SOL. The H-mode discharges instead show this minima to be much further out, showing a decrease until the mid-SOL and then the increase. Higher density L-mode discharges have shown a flattened fluctuation level profile, with no increase into the far SOL in Alcator C-Mod [101], and a similar minima near the near-far SOL boundary has also been recorded with ball-pen probe measurements in L-mode discharges in ASDEX Upgrade [99].

The skewness and kurtosis tell a similar story, with much of the literature reporting a minima near the separatrix, approximately 0 and 3 for the skewness and kurtosis, respectively, that increases radially into the SOL [57, 102]. Whilst the kurtosis results here match the literature reportings, the skewness has a similar shift of the minima into the scrape-off layer, not reported by Kube *et al.* [101], who reported the flattened relative amplitudes. Horacek *et al.* [99], who reported the minima further into the SOL, do not report results for skewness or kurtosis. Agostini *et al.* (with whom we compare the flattened PDFs near the separatrix with their values just inside the LCFS in section 4.4.1.1) report a similar local minima in the skewness profile in the vicinity of the separatrix which increases radially into the SOL. This leads us to believe that the position of our measurements is correct, but instead is likely caused by not completely filtering out all the ELM events in the signal, particularly for smaller ELMs, which may only be detected in the near SOL signals. This would explain why the skewness goes negative, due to a reduction in the signal strength as all the helium gas is ionised by the hot ELM filaments. This ELM activity is not seen in the kurtosis profile, as this doesn't measure which side of the mean the signal is contributing to, only how relatively far away from the mean it is.

4.4.2.2 Filament sizes

Similar to the average waveform, we can perform a 2D average of the filaments to get an average radial and poloidal diameter for filaments in each discharge at various positions in the SOL. The average waveform was only performed at the reference locations used in the blob detection, so each filament needed to be centred around its detection time, and normalised to the maxima at this time. Some normalisation and centring must be done in 2D conditional averages too. Here, each filament's frame is translated so as to position the

blobs' CoM position, equation (4.5), for a given flux surface on the pixel closest to the flux surface at a height of $z = -0.15\,\mathrm{m}$. This allows all blobs that are tracked through a given flux surface to be used in the average, regardless of their z coordinate. Before averaging, the frames are normalised to their total emission per area

$$F_{i,\mathrm{Norm}} = \frac{F_i}{\frac{\sum I_{\mathrm{blob}}}{\mathrm{Area}_{\mathrm{blob}}}}. \tag{4.13}$$

The results are displayed in figure 4.14 and table 4.6. The results for H-mode discharges are not included for $\rho = 1.02$ as only 4 and 6 filaments were successfully tracked this far back through the SOL for 2.5 MW and 5 MW, respectively. Both the L-mode and nitrogen discharges had the limiter shadow just after $\rho = 1.06$ and so data is unavailable at $\rho = 1.08$ for these discharge types.

Most 2D averages suggest a slight decrease to the blob's radial size with increasing distance into the SOL, however the decrease is small, close to within error. Therefore, the perceived radial size decrease is perhaps less than expected due to the smearing effect being more aggressive at smaller major radii. It is likely that any variation in the relative CoM positions inside the blobs will cancel one another out when averaging to give an averaged size less than the average of the individual sizes. The L-mode and N_2 seeded discharges show a similar unchanging poloidal diameter when moving through the SOL, where as both H-mode discharges have their largest averages closest to the separatrix at $\rho = 1.04$, larger than any of the other discharges or locations, that all decrease as they move to the wall. This increase in blob size from L-mode to H-mode discharges has previously been reported in ASDEX Upgrade with GPI by Fuchert *et al.* [80]. Their conditional average was performed just in-front of the limiter shadow ($\rho = 1.06$ and 1.08 for L-mode and H-mode here, respectively), reporting averages approximately half of what we measure here, albeit for densities 3-5 times smaller than here, although they are not explicit in how they define the measurement for the blob size, and the radius is a commonly used measure of the blob size. We here note that as the 2D conditionally averaged sizes are an average of multiple filaments that have been translated in the viewing plane so that their CoMs align with one another, the sizes quoted in table 4.6 have not been calibrated for the diagnostic's viewing geometry, as discussed in section 3.3.

For the poloidal and radial diameter measurements, as a blob's shape can fluctuate as it

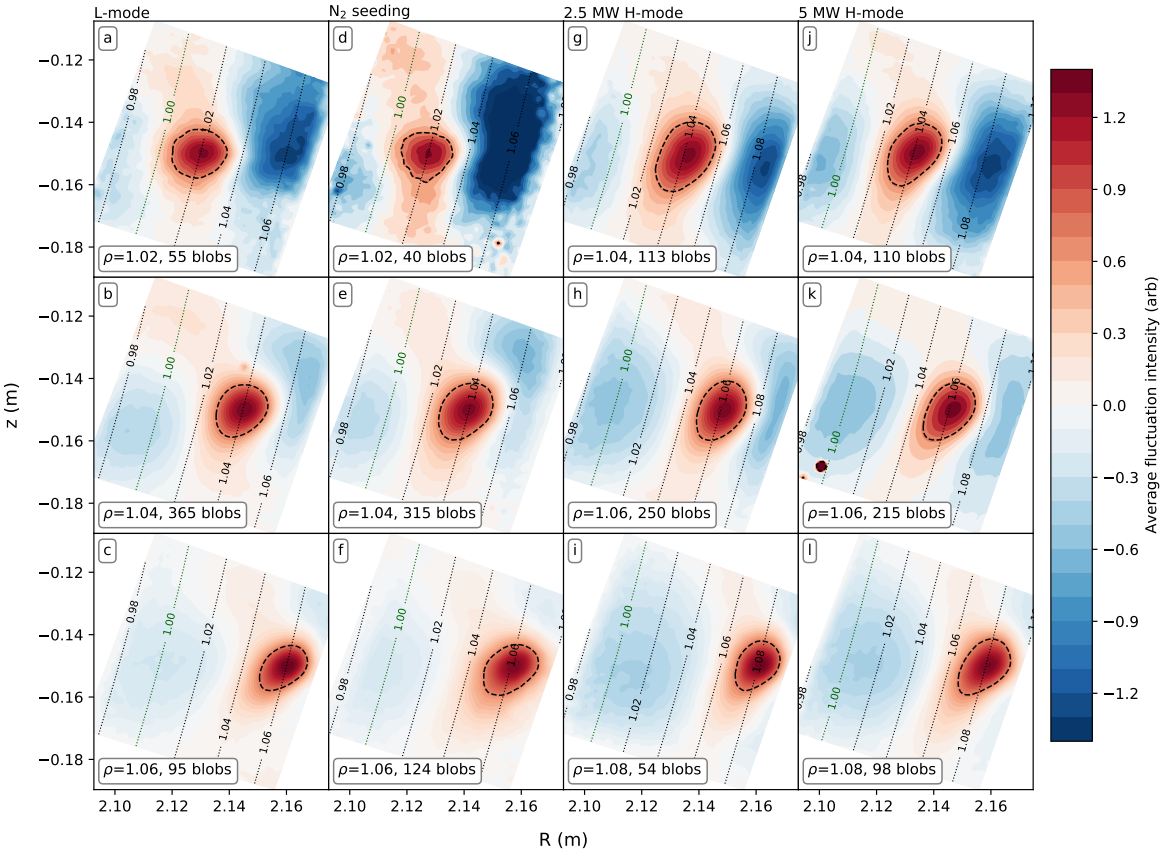

Figure 4.14: The 2D conditional average of filaments, normalised to intensity per area, and centred on their centre of mass. The averages are for $\rho \in [1.02, 1.04, 1.06]$ for L-mode (a-c) and N_2 seeding (d-f), and for $\rho \in [1.04, 1.06, 1.08]$ for 2.5 MW (g-i) and 5 MW (j-l) H-mode. The number of filaments used in the average is given in the bottom left corner.

Table 4.6: A table showing apparent size of the 2D average of filaments in the SOL in the radial and poloidal directions, r and θ (cm).

ρ	1.02		1.04		1.06		1.08	
Discharge type	δ_r	δ_θ	δ_r	δ_θ	δ_r	δ_θ	δ_r	δ_θ
L-mode	1.8	1.5	1.5	1.7	1.3	1.3	-	-
N_2 seeded	1.7	1.5	1.6	1.8	1.6	1.6	-	-
2.5 MW H-mode	-	-	1.6	2.2	1.5	1.9	1.3	1.6
5 MW H-mode	-	-	1.5	1.9	1.4	1.8	1.5	1.7

moves through the SOL, average size measurements are used in this section. The poloidal and radial diameters are averages over the individual measurements for the frames in which the filament's position is within $\rho_{\text{eavl}} \pm 0.005$ to account for any small variation of filament size and shape from frame to frame, where ρ_{eval} is the evaluation location. For example, for the measurements taken at the $\rho = 1.04$ location, whichever frames has the blob position as $1.035 \leq \rho < 1.045$ are used for the measurement of this one filament. Details on how this affects the error analysis are in section A.4. The sizes measured in each frame are individually adjusted to account for the viewing geometry of the diagnostic, as discussed in section 3.3, and the adjusted values are then averaged together.

Figures 4.15 and 4.16 show the poloidal and radial diameter probability distribution functions, respectively, with the quantitative measurements displayed in table 4.7. Each graph has the corresponding log-normal distribution added. The distribution is not a fit to the measured distribution but is instead constructed from the input parameters of the associated log-norm distribution. The log-normal distribution for randomly distributed variable x is given by

$$f(x;\sigma,\alpha) = \frac{1}{x\sqrt{2\pi}\sigma} \exp\left(\frac{-\ln^2\left(\frac{x}{\alpha}\right)}{2\sigma^2}\right) \tag{4.14}$$

where σ is the *shape parameter* and α is the *scale parameter*, calculated with the expectation/mean and the variance of the natural logarithm of x, $E[Y]$ and $V[Y]$, respectively, where $Y = \ln(X)$ and $y_i = \ln(x_i)$, by

$$\sigma = \sqrt{V[Y]} = \sqrt{\frac{1}{N}\sum_i^N (y_i - \bar{y})^2} \tag{4.15}$$

$$\alpha = \exp\big(E[Y]\big) = \exp\left(\frac{1}{N}\sum_i^N y_i\right). \tag{4.16}$$

L-mode and N_2 discharges show closely matching distributions for the poloidal diameter at $\rho = 1.02$ and $\rho = 1.04$, which also closely aligns with similar 2D averages, and only begin to deviate at the far SOL. Here a relative increase in the number of blobs above $\delta_\theta \approx 1.5\,\text{cm}$ can be seen, which is also mirrored in a slightly larger 2D average here. This indicates, along with the increased expected amplitude at this position, that blobs in N_2 seeded discharges lose their plasma more slowly than discharge without N_2. Both types of H-mode discharges give distributions with a higher spread of measured diameters, as well as a shift towards

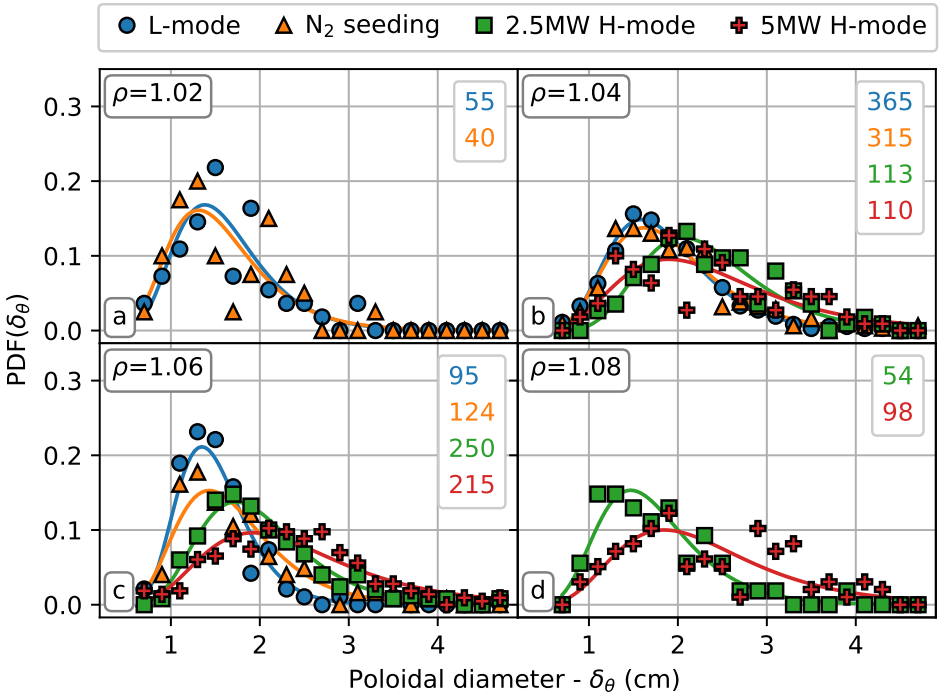

Figure 4.15: PDFs for the poloidal diameters of blobs at different positions in the SOL, with corresponding log-normal distribution functions. The number of filaments used is given in the legends.

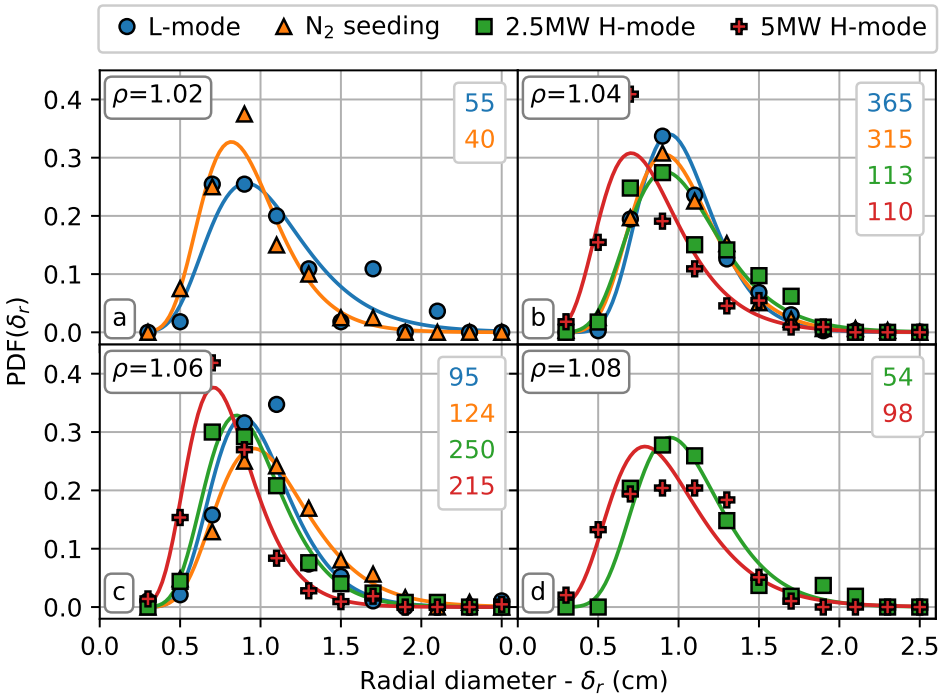

Figure 4.16: PDFs for the radial diameters of blobs at different positions in the SOL, with corresponding log-normal distribution functions. The number of filaments used is given in the legends.

Table 4.7: A table showing the shape, σ, and scale, α, input parameters for the log-normal distributions for blob radial, r, and poloidal, θ, diameters (cm).

ρ	1.02		1.04		1.06		1.08	
Discharge type	σ	α	σ	α	σ	α	σ	α
Poloidal diameter - δ_θ (cm)								
L-mode	0.326	1.53	0.320	1.77	0.270	1.45	-	-
N_2 seeded	0.355	1.49	0.338	1.82	0.344	1.61	-	-
2.5 MW H-mode	-	-	0.299	2.25	0.319	1.91	0.335	1.64
5 MW H-mode	-	-	0.406	2.24	0.398	2.26	0.399	2.16
Radial diameter - δ_r (cm)								
L-mode	0.324	1.01	0.242	0.999	0.265	0.958	-	-
N_2 seeded	0.286	0.888	0.275	0.985	0.294	1.04	-	-
2.5 MW H-mode	-	-	0.302	1.00	0.2749	0.917	0.279	0.917
5 MW H-mode	-	-	0.346	0.794	0.287	0.769	0.346	0.891

larger blobs at all radial locations, which is again consistant with the results of [80]. In the H-mode far SOL with more heating power, a larger relative number of large filaments was seen.

In the fluctuation frame data, filaments' radial sizes appear larger in the near SOL compared to the far SOL, although, once the correction for the GPI viewing angle and finite toroidal gas puff extent are applied, any differences due to location appear minimal. The radial sizes in the 5 MW H-mode, however, appear to be shifted to smaller radii, as compared to the other discharge types. This trend is also mirrored by the consistently lowered shape parameter, α. The difference between this discharge type and the others cannot be rectified by normalisation to the gyro-radius, ρ_s. The gyro-radius is given by

$$\rho_s = \frac{\sqrt{T_e} m_i}{eB} \tag{4.17}$$

where T_e is the electron temperature in eV, m_i is the ion mass, e is the elementary charge, and B is the magnetic field. The gyro-radii for each discharge as a function of radius are shown in figure 4.17. Normalising δ_r to ρ_s would increase the difference between the radial diameter distribution in the 5 MW H-mode as the gyro-radius is at a maximum for this discharge type. Only a difference of $\approx 2\,\%$ is seen between the two H-mode discharge types, and between 5–10 % between the H-mode and L-mode gyro-radii, which is not enough of a difference to bring the PDFs for the poloidal diameters between discharges in line with one

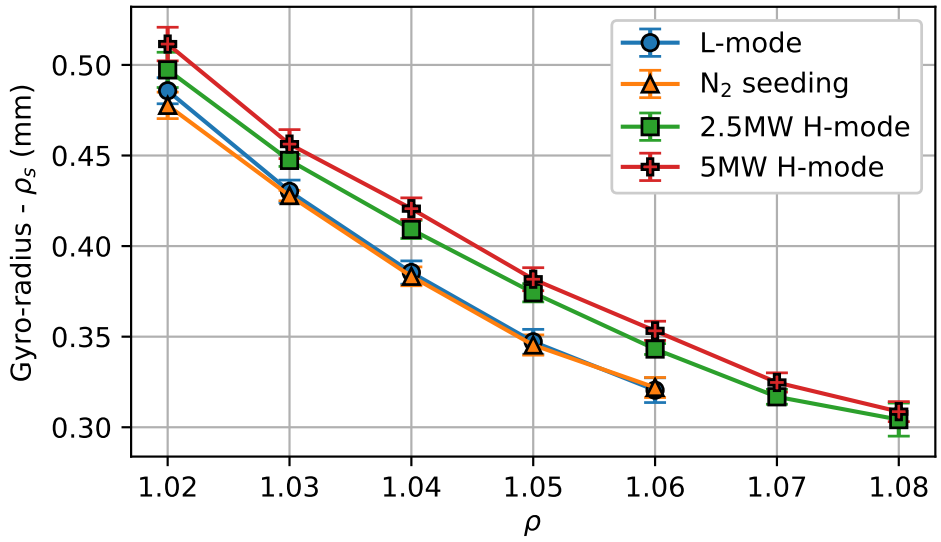

Figure 4.17: The ion gyro-radius, ρ_i, for each discharge type throughout the SOL, for temperature T_e.

another, so any difference we do measure is a real change in filament size.

4.4.2.3 Filament velocities

A filament's velocity measurement may also fluctuate as it moves through the SOL, similar to the blob diameter. As such, in this section we also evaluate the average filament velocity as it traverses the region spanned by $\rho_{\text{eval}} \pm 0.005$. This evaluation and the possible errors associated with it are discussed in section A.5. The distributions for the radial and poloidal filament velocities are shown in figures 4.18 and 4.19, respectively. The radial velocities have had log-normal distributions added, and the poloidal velocities have had normal distributions added: the input parameters for these distributions are given in table 4.8. The normal distribution is given by

$$f(x;\mu,\sigma) = \frac{1}{\sqrt{2\pi}\sigma} \exp\left(\frac{-(x-\mu)^2}{2\sigma^2}\right) \tag{4.18}$$

where μ and σ are the mean and standard deviation, respectively. Both the L-mode and N_2 discharges show a large reduction in radial velocity from $\rho = 1.02$ compared with the rest of the SOL, with this effect being more pronounced with the nitrogen seeding. This is similarly reflected in the scale parameters, although the large difference at $\rho = 1.02$ could be caused by the N_2 bin between 400–600 m/s, where a movement of a few measurements into the bins

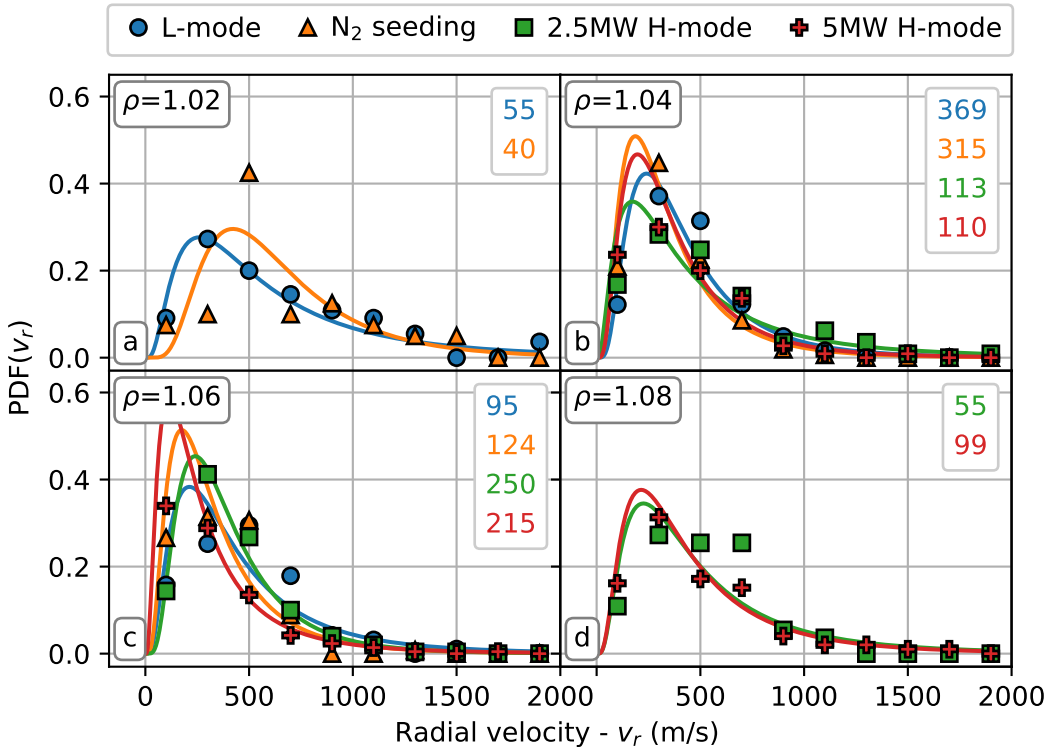

Figure 4.18: PDFs for the radial velocities of blobs at different positions in the SOL, with corresponding log-normal distribution functions. The number of filaments used is given in the legends.

either side would recreate the L-mode distribution perfectly. Except for at $\rho = 1.02$, the radial velocity distributions, which have been calibrated for the error in position from the viewing angle, match quite similarly to one another.

The poloidal velocity measurements are where the velocities vary the most. Both H-mode distributions appear approximately centred around $v_\theta \approx 0\,\mathrm{m/s}$ with very wide distributions, whilst L-mode and N_2 discharges have velocities that are mostly centred around $v_\theta \approx 200\,\mathrm{m/s}$. The near SOL, at $\rho = 1.02$, shows a reduction of the L-mode mean velocity by about half, whilst the N_2 distribution shows a slightly negative average, although the velocity measurements here do not match well to the predicted normal distribution. Care is taken to ensure that blob tracking stops just before any blob pixel is at a location of $\rho < 1.00$ (i.e., before the blob is connected to the main plasma), however the correction on blob location is only performed on the centre-of-mass location. Also, the chosen cut-off for a a pixel's intensity and whether or not it is considered part of the blob or not is half the blob amplitude, and not zero. These are two possible ways that blobs tracked back to $\rho = 1.02$

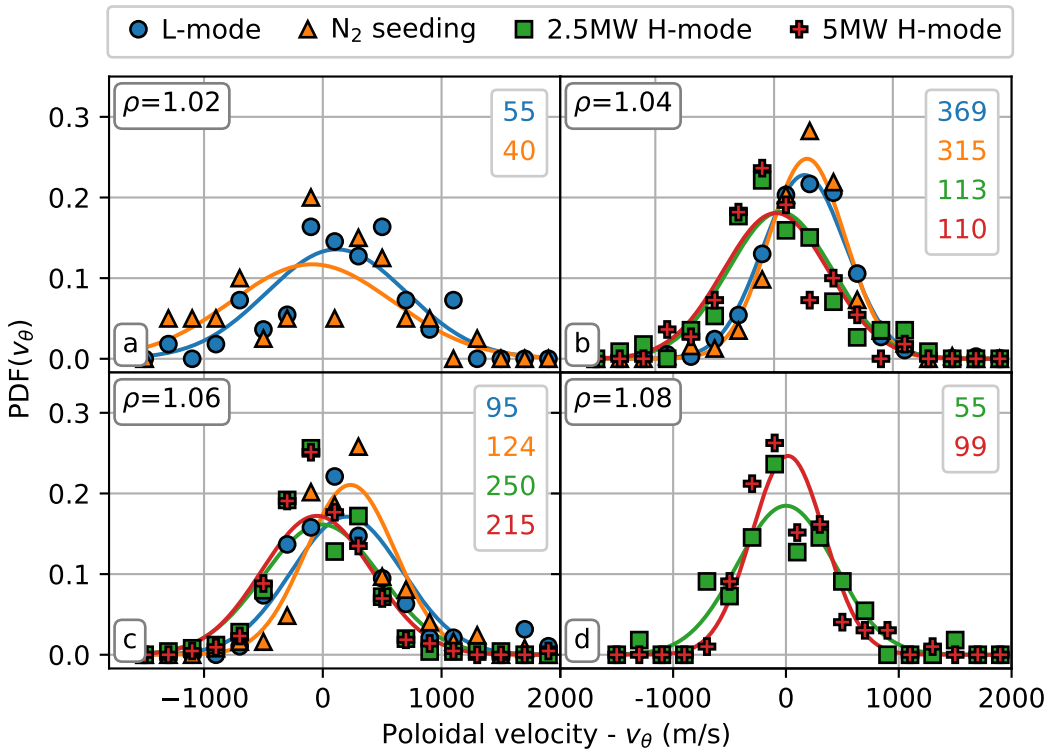

Figure 4.19: PDFs for the poloidal velocities of blobs at different positions in the SOL, with corresponding Gaussian distribution functions. The number of filaments used is given in the legends.

Table 4.8: A table showing the shape, σ, and scale, α, input parameters for the log-normal distributions for blob radial velocities, v_r, and the mean, μ, and standard deviation, σ, input parameters for the normal distributions for poloidal velocities, v_θ, (m/s).

ρ	1.02		1.04		1.06		1.08	
Radial velocity - v_r (m/s)								
Discharge type	σ	α	σ	α	σ	α	σ	α
L-mode	0.801	496	0.640	362	0.744	369	-	-
N_2 seeded	0.550	571	0.671	293	0.695	284	-	-
2.5 MW H-mode	-	-	0.876	373	0.609	348	0.765	405
5 MW H-mode	-	-	0.686	315	0.842	231	0.747	375
Poloidal velocity - v_θ (m/s)								
Discharge type	μ	σ	μ	σ	μ	σ	μ	σ
L-mode	116	588	257	350	203	466	-	-
N_2 seeded	-90.4	681	278	322	233	379	-	-
2.5 MW H-mode	-	-	51.6	438	-7.65	494	0.602	432
5 MW H-mode	-	-	15.6	442	-50.5	463	18.0	323

could still be connected to the confined plasma, and why the results from these locations may differ from the other locations.

In addition to the distributions of filament velocity, we also explore the scaling of radial velocity with poloidal diameter with respect to the sheath limited and inertial filament regimes, given by equations (2.3) and (2.4), respectively. The results are shown in figure 4.20. We first note that at each position and for each discharge type, over 95 % (in some cases, 100 %) of filaments detected have a poloidal size larger than the fundamental blob size, given by equation (2.5), with the exception of the L-mode and nitrogen seeded discharges in the very near SOL at ρ=1.02, where the number is only 51 % and 45 %*. Of those filaments with size larger than the fundamental blob size, most have corresponding radial velocity under the inertial regime velocity scaling, which is considered as an upper limit for the filament velocity [39, 103]. We point out a few exceptions to this. For the nitrogen seeded discharge at $\rho = 1.06$, figure 4.20d., a few of the larger filaments have larger velocities, although most are within error of the sheath limited regime scaling.

For the H-mode discharges, there are multiple filaments with velocities above the scaling which are now not just limited to the larger filaments. For example, in figures k. and l. for the far SOL in 5 MW H-mode discharge, filaments with velocities larger than the inertial scaling appear for a range of filament diameters above the fundamental blob size. This could be explained either as an effect due to warm ions [42], or as a shift into the resistive x-point regime, the top right of figure 2.2. This has the effect of increasing the velocity for a given filament size. Neither of these mechanisms is confirmed here as measurements of ion temperatures and divertor collisionality have not been made here.

All but a few filaments with poloidal diameters smaller than the fundamental blob size fall below the expected inertial regime velocity scaling (or resistive ballooning regime), although these are within estimated error on the velocity measurement. Similarly to before, inclusion of warm ions would increase the velocity for a given filament diameter, and easily include all smaller filaments. One consideration not made here is with respect to the connected ideal interchange regime, the bottom left of figure 2.2. Here, the velocity reduces due to the flattening parameter, ε_x, which is always < 1. As such, multiple filaments in L-mode and with nitrogen seeding at $\rho = 1.02$ would likely now be above the scaling velocity. This is in contrast to recent work on TCV [104] which estimates $\varepsilon_x \approx 0.3$, and benefited from

*Unfortunately, only 3 and 5 filaments are successfully tracked back this close to the separatrix for the 2.5 MW and 5 MW H-mode discharges, where 2 and 3 are above the funadamental blob size, respectively.

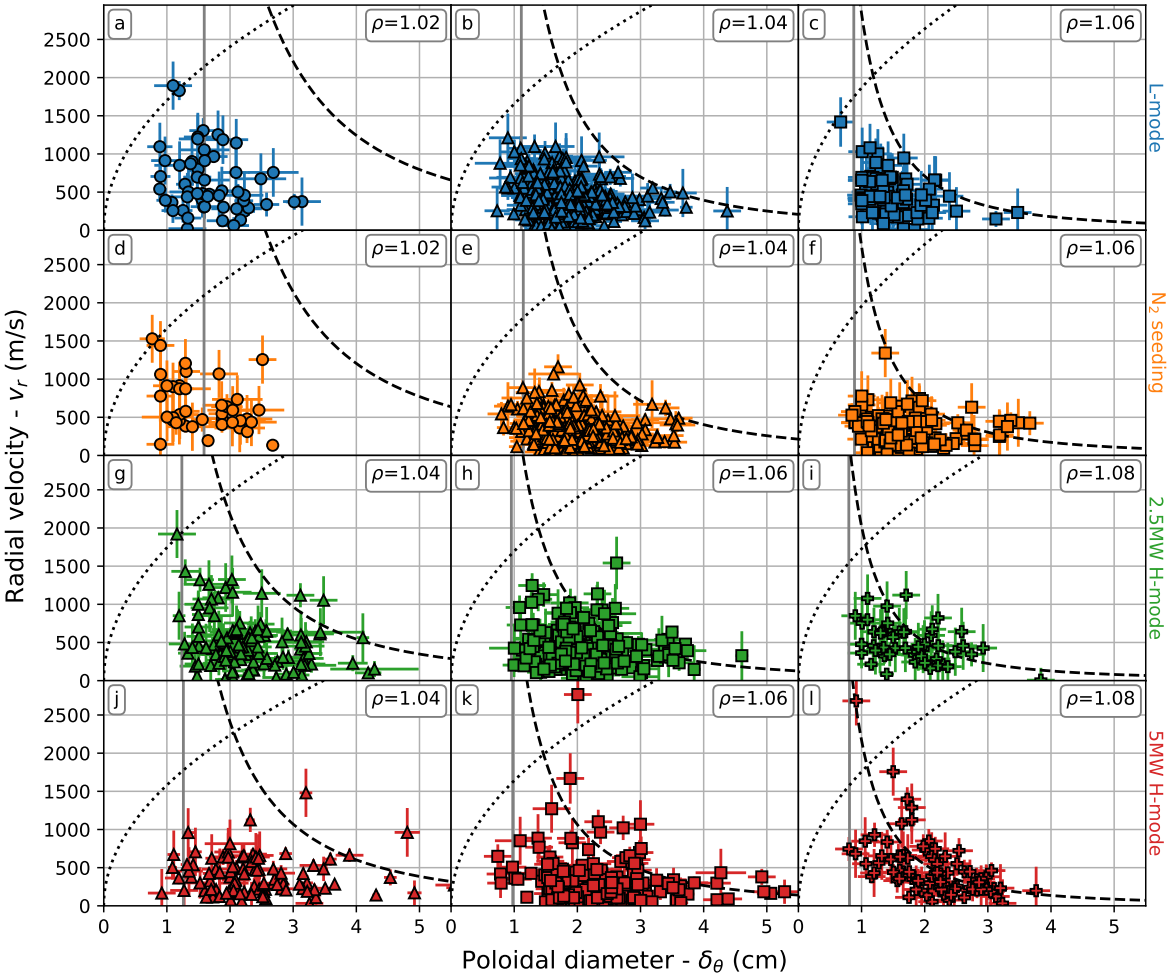

Figure 4.20: Scatter plots for the radial velocity of filaments against their poloidal diameter. The L-mode (top row, a-c, blue) and N_2 seeding (second top, d-f, orange) filaments are for positions ρ=[1.02,1.04,1.06] (circles, triangles, and squares, left to right), and the 2.5 MW H-mode (second bottom, g-i, green) and 5 MW H-mode (bottom row, j-l, red) filaments are for positions ρ=[1.04,1.06,1.08] (triangles, squares, and pluses, left to right). The sheath limited regime (black dashed, eq. (2.3)) and inertial regime (black dotted, eq. (2.4)) velocity scalings, have been overlaid in each plot, with the fundamental blob size (vertical grey, eq. (2.5)) included.

multi-diagnostics connected along field lines to deduce the average velocity of filaments is best described by the ideal interchange regime at low discharge densities.

4.4.2.4 Inter-filament flow velocities

We can compare the velocity of filaments with the background flow of the plasma in between filaments. Any data within ±100 time steps (±0.5 ms) of the blob arrival time, t_i, is defined to belong to the filament, and data outside of this time range is deemed as inter-filament data. This allows ample time for any effect in the wake of the filament to be minimised, allowing for even the longest tracked blobs. For the H-mode discharges, any data during an ELM is also not included in the inter-filament flow measurements. The inter-filament period is the any time in-between these periods, as well as any time that isn't attributed to an ELM in H-mode discharges. Here, the inter-blob plasma flow is measured using the dynamic time warping (DTW) algorithm [105–107]. The velocities shown here are averages for the entire inter-filament periods for each discharge. The means are then averaged along the poloidal direction, and the standard deviation of the means also calculated. Measurements from within 8 pixels at the edges of the detector are not included, as DTW is known to perform badly at the edges.

Figure 4.21 shows the inter-blob SOL flows. The radial inter-blob velocity show trends that all decrease with distance into the SOL. This matches with the decrease of velocities seen in the distributions at the near SOL for L-mode and N_2 seeded discharges, although the velocity reduction continues here through the entire SOL, tending to zero, with even some negative radial velocities recorded right in front of the limiter shadow, which was not seen with the filament velocities. The same radially decreasing profile is reported by Fuchert *et al.* in the SOL [80], although their measure does not limit itself to just the inter-filament periods. We cannot, however, rule out that no filaments are present during the inter-blob periods, as only larger blobs are detected, as discussed in section 4.3.2. We also note that the inter-blob mean flows shown here have not been corrected for the GPI viewing geometry, which should only scale the radial velocities rather than change the profile shape.

The SOL experiences a radial electric field, E_r, due to the temperature profile. Plasma flow along the field lines to the connecting solid surface is dictated by the plasma potential [108], and related to the electron temperature by $\phi(r) \approx 3T_e(r)$, where T_e is measured in eV. As the temperature decreases with r, so does the potential, and the resulting electric field is

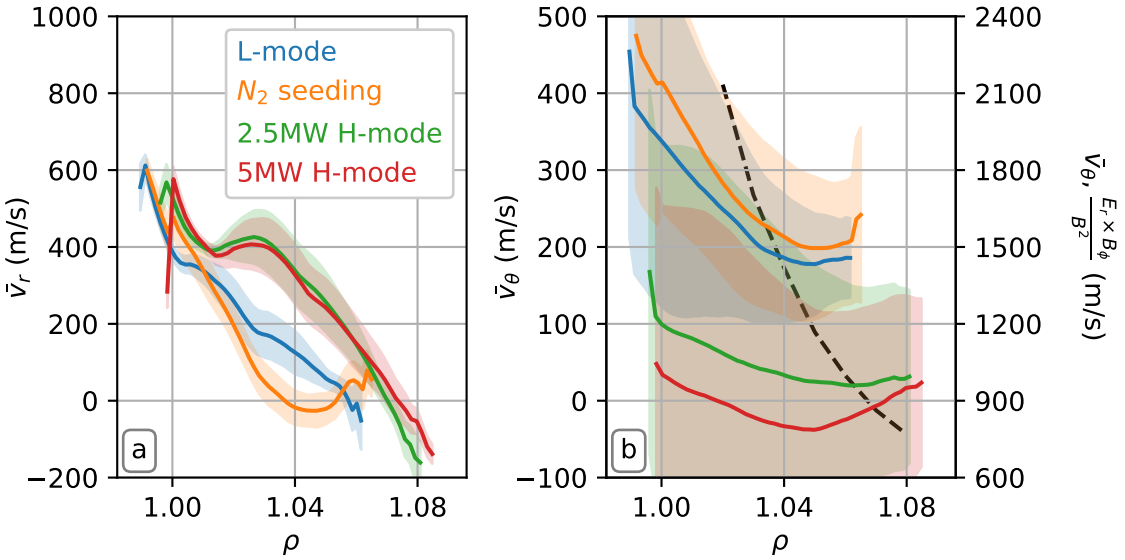

Figure 4.21: Inter-filament flows in the scrap-off layer in the radial direction, v_r, (a) and poloidal direction, v_θ, (b). The discharge types are: L-mode (blue); N_2 seeded (orange); 2.5 MW H-mode (green); and 5 MW H-mode (red). The predicted poloidal flow from the SOL electron temperature gradient is added (b, black dashed, right hand y-axis).

radially outward, $E_r = -\boldsymbol{\nabla}\phi$. The resulting poloidal $E \times B$ velocity is given by

$$v_\theta = \frac{E_r \times B_\phi}{B^2} \approx \frac{3T_e}{\lambda_{T_e} B_\phi}, \tag{4.19}$$

where λ_{T_e} is the electron temperature gradient length scale, and B_ϕ is the toroidal component of the magnetic field. Here, we have assumed no variation of temperature along a flux tube in the SOL, and the electron temperature is taken as an exponentially decaying profile as measured by the lithium beam diagnostic. For all discharges used here, the temperature profiles do not vary much, neither in magnitude nor gradient, and are well described by a single exponential decay length, $\lambda_{T_e} = 32.2 \pm 0.3$ mm, with an approximately equal predicted $v_{\theta,(E\times B)}$ for all shots, which is included in figure 4.21b, alongside the experimentally measured values. The poloidal inter-filament flow velocities have also not been corrected for the GPI geometry, but poloidal measurements require very little adjustment, and would be within the variance of measurements along the poloidal direction.

The predicted poloidal $E \times B$ flow decreases radially, dominated by the electron temperature profile, as the change in magnetic field over the SOL width is small. The L-mode and N_2 seeding poloidal flow profile match closely to one another, with the N_2 discharge slightly higher than without nitrogen, but both exhibiting a positive poloidal flow that decreases

with distance into the SOL. The measured flow is vastly under what is predicted by the T_e profile. The H-mode flows measured are even lower than those measured for L-mode. The 2.5 MW discharges still exhibit a slight decrease with distance, but is much flatter than predicted by T_e, and flows measured in L-mode. Something apparently changes when the NBI heating is doubled to 5 MW, as the measured poloidal flow decreases further, even exhibiting negative measurements around the near-far SOL boundary, although as the variance is large the poloidal flow could be close to zero and any change in sign could be within error. This change in poloidal flow is also measured in the filaments themselves, with the mean H-mode poloidal filament velocity ≈ 0 m/s, and ≈ 200 m/s in L-mode. Fuchert *et al.* [80] report a change in flow direction of filaments from positive to negative for L-mode and H-mode discharges, respectively. Our results here suggest a change in the radial electric field, causing some difference to the poloidal flow. The trend here would suggest some dependence on the amount of auxiliary heating power, however the result from [80] with 3 MW of auxiliary ECRH heating measure poloidal velocities of -100–-300 m/s, 0.7 MW less than the total heating power in the 2.5 MW H-mode experiments here. We cannot rule out that the type of heating may have an effect, as NBI heating could add a torque and resultant toroidal rotation that ECRH heating doesn't.

4.4.3 2D distribution functions

Next we explore the dependence of one blob property on another property. We start by investigating the amplitude dependence on the poloidal diameter. An example 2D distribution, with corresponding binned 1D amplitude distributions, for L-mode discharges at $\rho = 1.04$ are shown in figure 4.22. Any issues experienced with low numbers for good statistics in 1D PDFs can exacerbated with 2D distributions, but some meaningful conclusions can still be drawn. The 2D PDF shows the general upwards trend between the amplitude and poloidal diameter. The white dashed line added on to figure 4.22a is the mean filament amplitude for that diameter range, which is the only input parameter required for the exponential distribution, which the filament amplitudes are shown to follow in section 4.4.1.2. The 1D PDFs for a given diameter range are shown in figure 4.22b. Even with the modest number of measurements here, the distributions can be seen to shift towards higher amplitudes as the diameter range increases, following on from the mean measurement. It is worth noting that the measurements of amplitude here have not had the minimum amplitude removed,

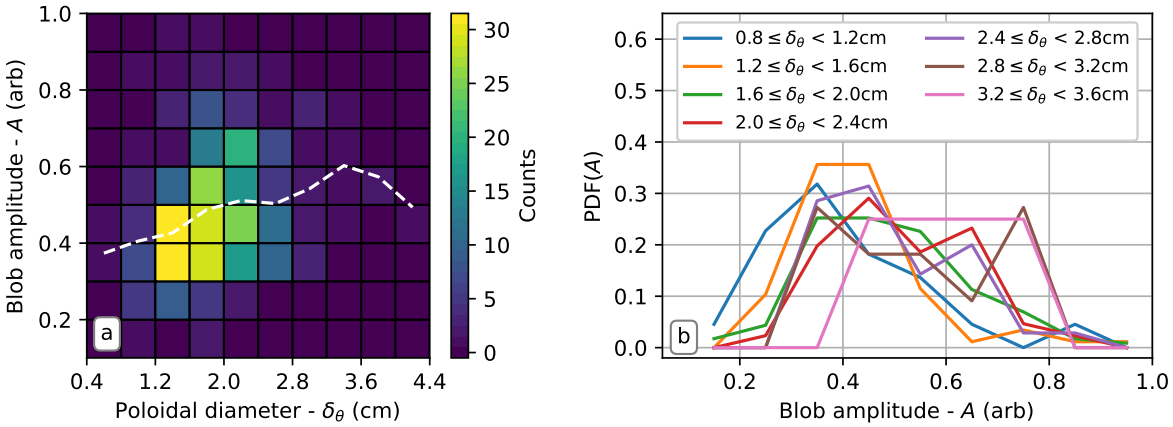

Figure 4.22: An example 2D PDF for blob amplitude and poloidal diameter for L-mode discharges at $\rho = 1.04$ (a) with mean amplitude for each poloidal diameter bin (white dashed). The 1D amplitude PDFs for each poloidal diameter bin (b). The first bin and last two bins have been omitted for clarity.

and the distributions exhibit the same adjustment from the ideal exponential distribution, as demonstrated in figure 4.9.

Figure 4.23 shows the binned average amplitude measurements for each discharge type at various radial locations. Firstly, we notice each average increases as a function of distance into the SOL, consistent with figures 4.8 and 4.13a. Next, the majority of lines agree with the example in figure 4.22a, showing an increase in mean amplitude with poloidal size. The trend is even more pronounced when data points with a low number of filament measurements are ignored. For example, the 2.5 MW discharge has < 10 measurements at $\rho = 1.02$. Similarly, from the example in figure 4.22a, and the poloidal diameter PDFs in figure 4.15 the number of measurements in the smallest and largest diameter ranges is usually very small. As such, the positive trend is more obvious if the outer most data points are not included. Finally, we note differences and similarities between the discharge types. Both H-mode discharges have a similar range of mean amplitudes as we move through the SOL. The range isn't too dissimilar for the L-mode cases, but the difference is over a domain of $1.02 \leq \rho \leq 1.06$, rather than $1.02 \leq \rho \leq 1.08$.

Similarly, we can look at the radial velocity dependence on the poloidal diameter. Figure 4.24 shows an example measurement for the L-mode discharges at $\rho = 1.05$. Here we see that the filaments with the largest poloidal diameters tend to give filaments with the smallest velocities. In particular, this is shown in the velocity PDFs for a given poloidal diameter range. The smallest diameter range shows a diffuse distribution, with the distributions be-

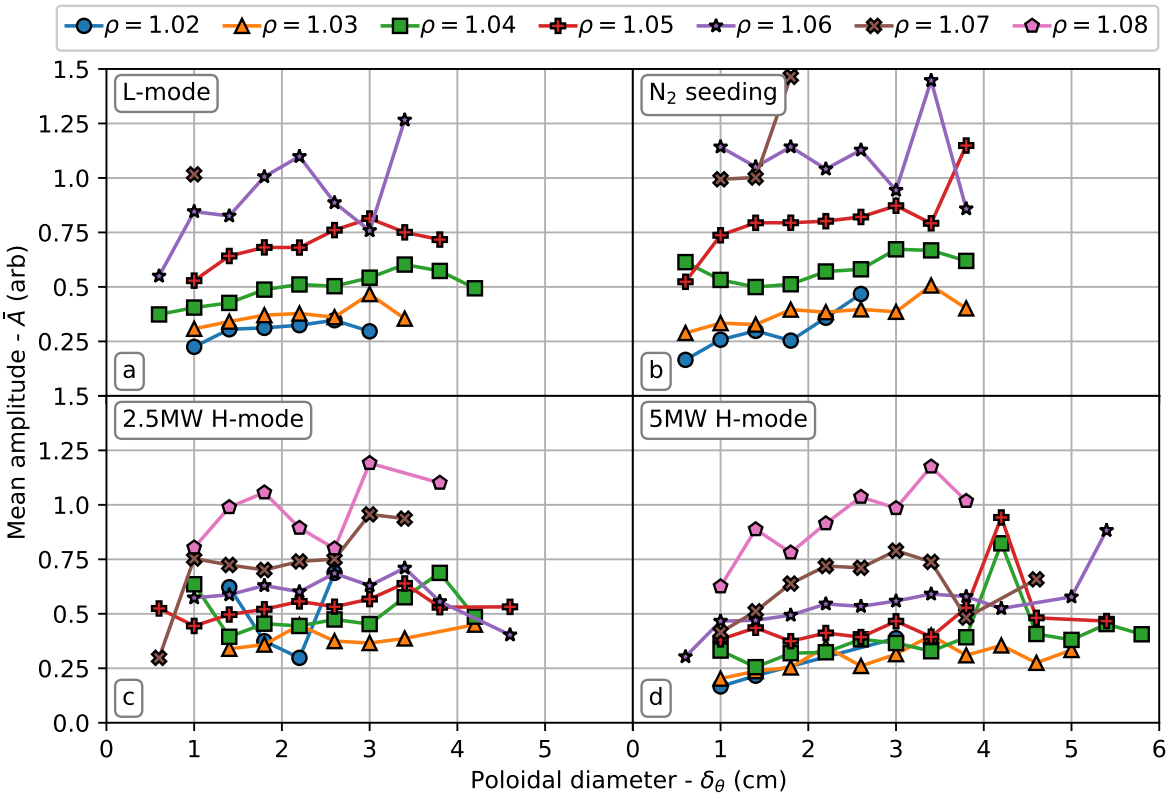

Figure 4.23: Amplitude averages for binned poloidal diameter size for all discharge types for various locations throughout the SOL.

coming narrower, and more centred at lower velocities as the diameter range increases. This is largely mirrored in the scale parameters, a good proxy for the means of the distributions, of the other discharges at other locations, figure 4.25. Each discharge type and for each location shows the decrease from smaller blob diameters at 1–2 cm. For larger diameters it is unclear if the relation ship still decreases or if the some minimum radial velocity is reached. For the nitrogen seeding, we also recover the larger velocities for the position closest to the separatrix, as in section 4.4.2.3. No clear trends are seen in the shape parameters, figure 4.26.

We can also see how the radial size depends on the poloidal diameter. The radial diameter scale parameter as a function of poloidal diameter is shown in figure 4.27. No variation is seen with SOL position, but a clear difference is seen between the L-modes and H-modes. In L-mode, with and without nitrogen, the radial diameters' scale parameters start at ≈ 1, and then increase slightly, up to ≈ 1.5 as the poloidal diameters go from 1–4 cm. For the 2.5 MW H-mode, α_{δ_r} starts just under 1 for small poloidal diameters, and goes just above

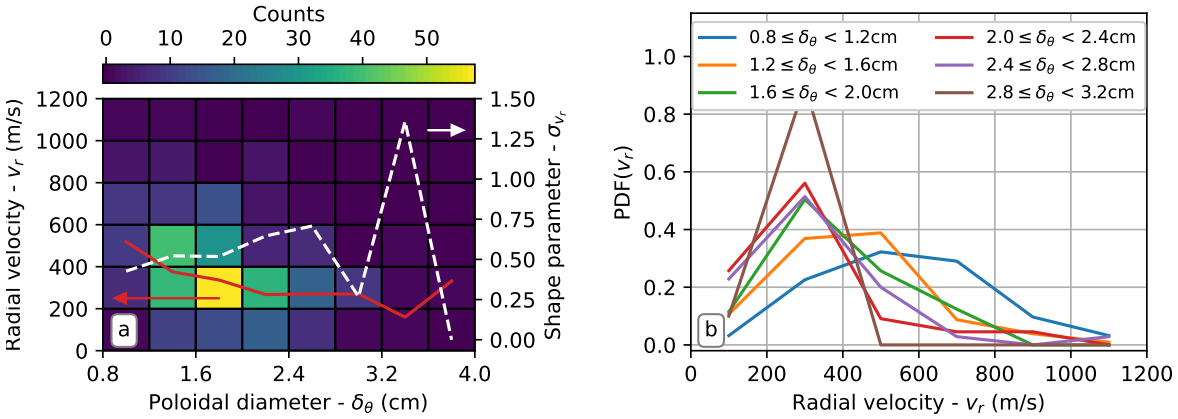

Figure 4.24: An example 2D PDF for radial velocity and poloidal diameter for L-mode discharges at $\rho = 1.05$ (a). The radial velocity shape (σ_{v_r}, dashed white, right axis) and scale (α_{v_r}, solid red, left axis) parameters for each poloidal range are added. The 1D radial velocity PDFs for each poloidal diameter range (b). The last two bins have been omitted for clarity.

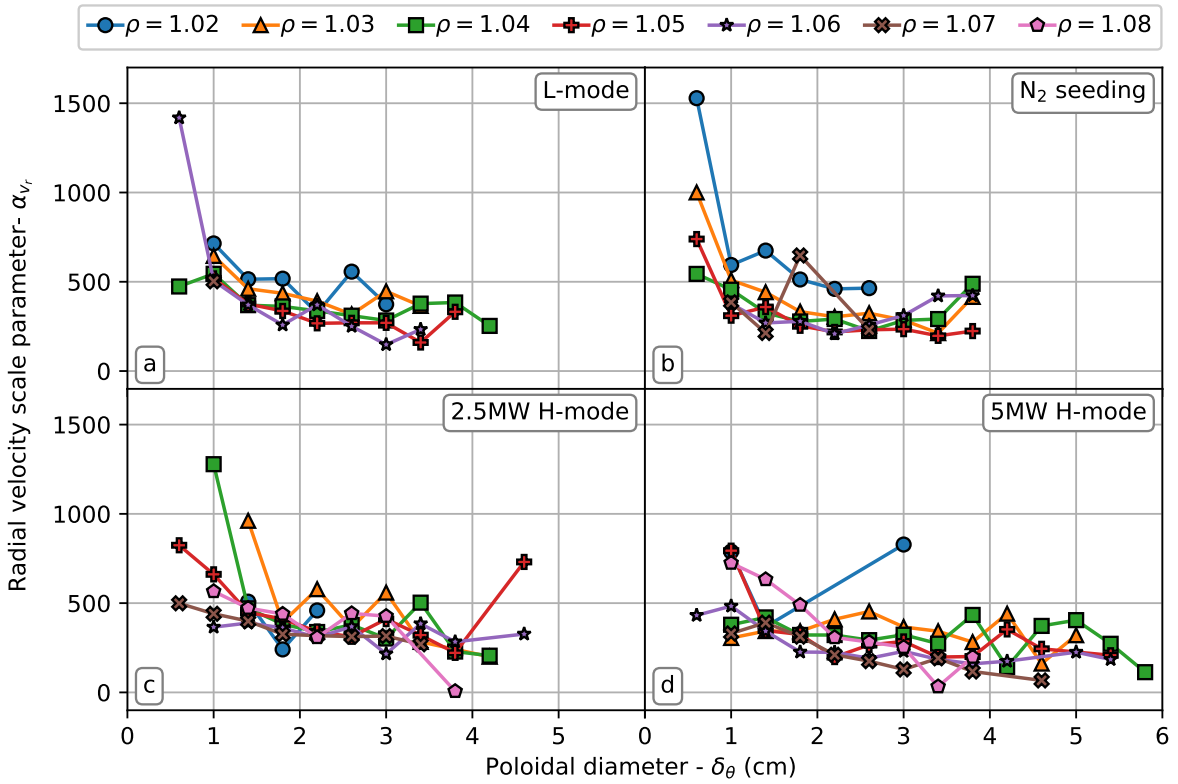

Figure 4.25: Radial velocity scale parameters for binned poloidal diameter size for all discharge types at various locations throughout the SOL.

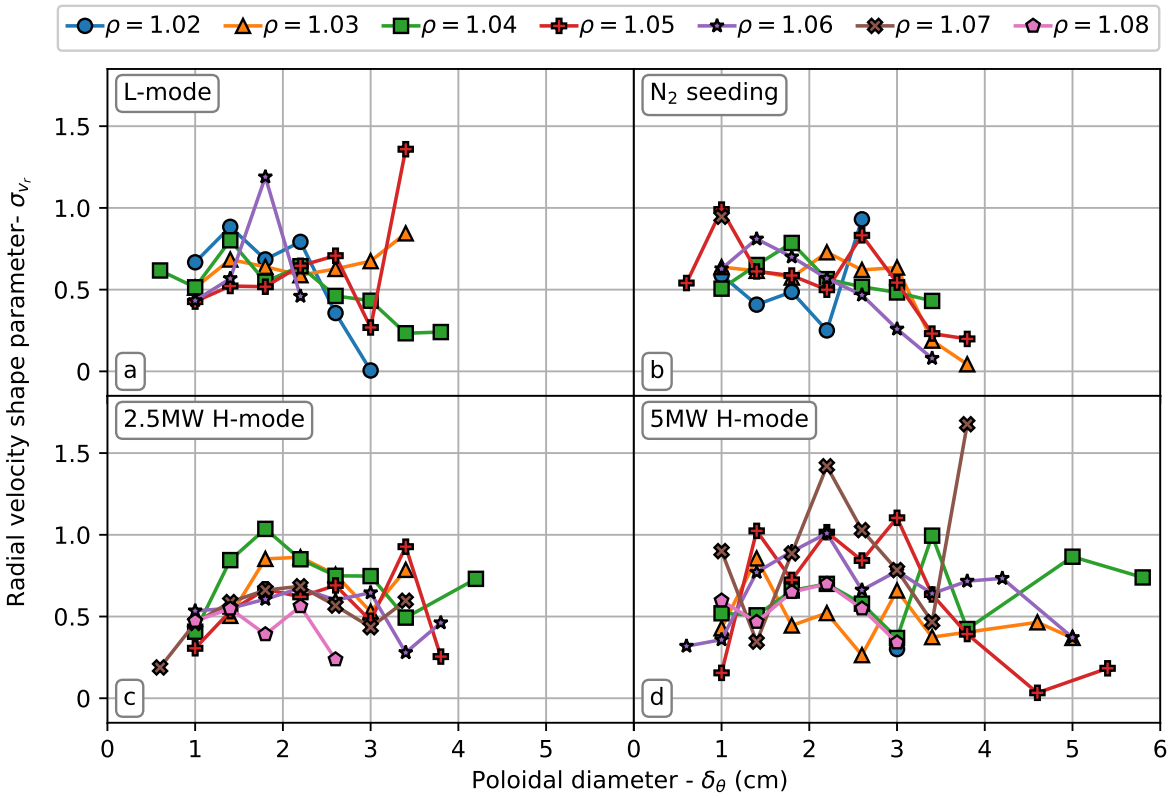

Figure 4.26: Radial velocity shape parameters for binned poloidal diameter size for all discharge types at various locations throughout the SOL.

1 for larger sizes, with the 5 MW H-mode showing a similar trend rise in scale parameter against poloidal diameter, but being slightly lower for all sizes. This trend is seen for all radial positions. No significant change or trend is seen in the shape parameters, which are ≈ 0.3 for all discharge types and SOL positions.

Whilst there is only a small change in electron gyro-radius between discharge types, reducing by ≈ 0.03 mm from H-mode to L-mode, shrinking from 0.5–0.3 mm from $\rho = 1.02$ to $\rho = 1.08$, see figure 4.17, the reduction in the scale parameter could be due to changes in the magnetic geometry between discharges, as flux surfaces are closer together in H-mode discharges than in L-mode, caused by a change in the poloidal magnetic field component. The gradient of the magnetic field changes from the near to far SOL, $R - R_{\text{min}} \approx 30$ mm (ρ ≈1.043–1.054), and the difference in $\partial_r B_\theta$ is seen in the near and far SOL between discharges. The poloidal magnetic field gradients are shown in table 4.9. It is known that magnetic shear can have an effect on filaments. For example, strong magnetic shear near the x-point can distort a filament enough to disconnect it from the target [17], and recent

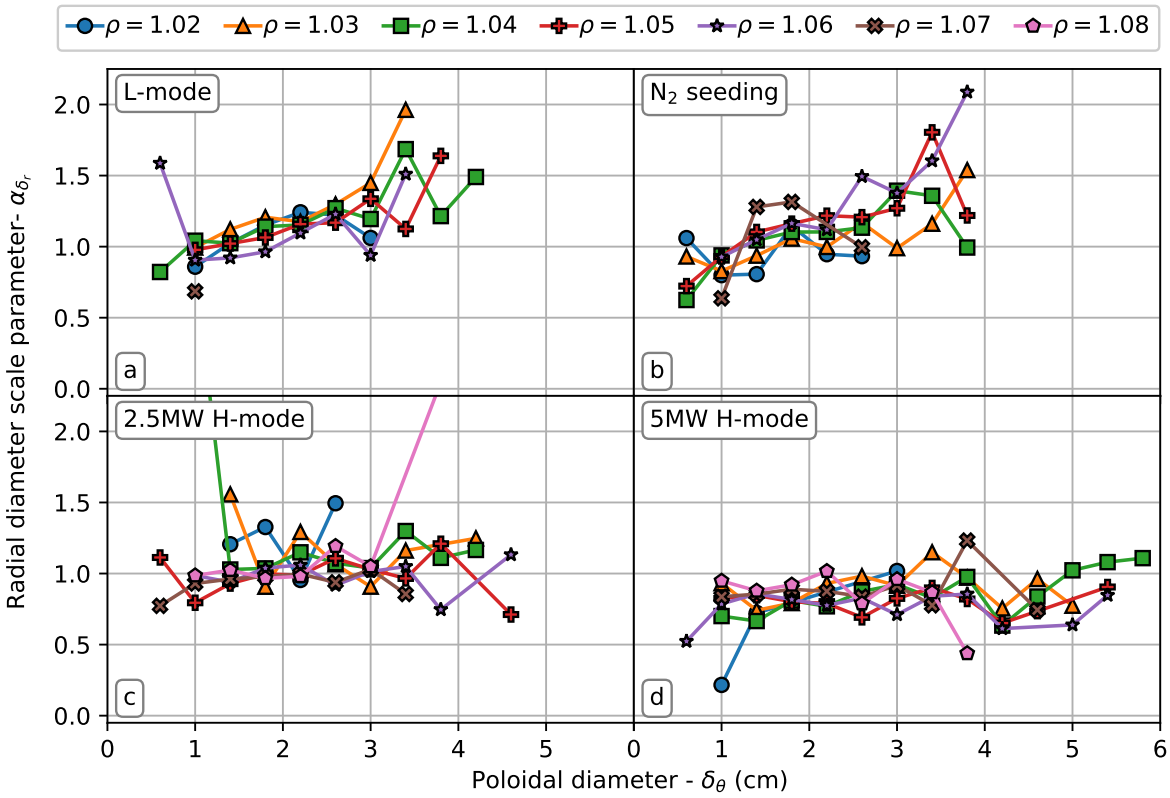

Figure 4.27: Radial diameter scale parameters for binned poloidal diameter size for all discharge types at various locations throughout the SOL.

3D fluid simulations have shown that magnetic shear can alter the density and potential distribution within a filament [109]. An increase in magnetic shear in the SOL could be responsible for the stretching of a blob in the poloidal direction, whilst also reducing its size in the radial direction, which is why we see lower scale parameters for the same poloidal diameter in discharges with the higher magnetic field gradient. Although the poloidal field gradient in the far SOL is comparable in H-mode to the near SOL in L-mode, the scale parameters for the radial diameters show no radial dependence in the H-mode case. The shear in the near SOL could already have limited the filament's radial size in the H-mode near SOL, and so to blobs are unable to recover to larger sizes in the far SOL.

The relationship between the radial velocity dependence on the blob's amplitude has been also examined. It shows similar reduction in the velocity as amplitude increases as it did for the radial velocity on poloidal diameter dependence up to a medium amplitude value, after which the velocities remain constant independent of the amplitude. This follows on from our previous conclusions that the amplitude has a dependence on the poloidal diameter

Table 4.9: A table showing poloidal magnetic field gradient, $\frac{\partial B_\theta}{\partial R}$ (T/m), in the near and far SOL for all discharge types, measured at the height of the magnetic axis.

Discharge type	Near SOL	Far SOL
L-mode	0.3813 ± 0.0059	0.2986 ± 0.0025
N_2 seeded	0.404 ± 0.026	0.3055 ± 0.0043
2.5 MW H-mode	0.4682 ± 0.0096	0.3424 ± 0.0081
5 MW H-mode	0.455 ± 0.014	0.3564 ± 0.0078

size, and any dependence the radial velocity may appear to have with amplitude can arise from the poloidal measurement. A 2D PDF measurement of the poloidal velocity and radial velocity has also been made, and no dependence has been seen, other than the change in mean velocity between discharge types, already explored in the 1D poloidal distributions in section 4.4.2.3.

4.5 Summary

This chapter describes the analysis techniques used to investigate the filaments in the ASDEX Upgrade scrape-off layer for a collection of different discharge types, and the subsequent results of this analysis. It also includes some analysis of the SOL as a whole, which includes some statistical descriptions of the SOL which include the inter-filament periods too (and inter-ELM periods, for H-mode discharges). This analysis was primarily on data from the gas puff imaging diagnostic.

Single-point PDF measurements of the SOL show the time-series of the fluctuations follow Gamma distributions which become more flattened at larger radii due to the intermittent appearance of filaments that propagate this far into the SOL. H-mode discharges showed a lower change in the intermittency of the signal between positions in the SOL than their L-mode counterparts as the near-SOL PDFs already showed a larger deviation from a normal distribution, with the N_2 seeded discharge showing the most intermittent signals. Radial profiles of higher order statistical moments also show that the nitrogen seeded discharges had the highest values of skewness and kurtosis in the far SOL when compared to the other discharge types. The nitrogen seeded discharges also had a larger range of relative fluctuation levels over the whole SOL. Each discharge types' time-series data also followed a skewness-squared scaling for the kurtosis, again expected for a random variable from a

Gamma distribution.

The CCDF of filament amplitudes also showed the largest filament amplitudes for the N_2 seeded discharge, adding further credence to the larger signal contributions in the SOL coming from filaments. This suggests the addition of neutral impurities in the divertor region has an effect on reducing how quickly the filaments' amplitudes reduce in the upstream SOL as they propagate through it, (such as through increased collisionality, for example). H-mode discharges also showed smaller average waiting times between filaments than L-mode, as well as a further reduction in the waiting time with increased auxiliary heating.

Filament size distributions have been measured at multiple locations in the SOL for each of the discharge types. L-mode and nitrogen seeded discharges have similar poloidal size distributions in the near SOL, with larger filaments seen in the very far SOL in the N_2 discharges, also reflected in 2D averages of the filaments. This increase in filament size, in conjunction with the increased amplitudes also seen in these discharges, further points to evidence for a change in parallel drainage times of filaments, and thus a change in how quickly they reduce in amplitude, with the additional seeding. H-mode discharges show even larger poloidal filament sizes, with additional NBI heating further increasing the filament sizes, as well as the poloidal size distributions increasing to larger sizes as α, the log-normal scale parameter, increases.

Radial velocity distributions for L-mode and N_2 seeded discharges show larger velocities at the very near SOL compared with all other locations and discharge types, although few to no filaments could be measured this close to the separatrix in H-mode, with little variation otherwise. Poloidal velocity measurements show H-mode filaments have a gaussian distribution around 0 m/s, with approximately equal numbers of filaments moving with positive and negative velocities. This changes for L-mode discharges which are centred around slightly positive poloidal values. Measurements of the radial velocity of filaments versus poloidal diameter shows the overwhelming majority of filaments to be above the fundamental blob size, and most of these filaments have velocities below the inertial regime velocity scaling, for all discharge types. For the $\rho = 1.02$ SOL location in L-mode and N_2 seeded discharges, approximately half of the filaments are instead found to have poloidal sizes smaller than the fundamental blob size and velocities under the inertial regime velocity scaling. As too few filament measurements were made at this location in H-mode discharges, we are unable to determine if half the filaments are under the fundamental blob size in these discharges as

well.

Inter-filament flow measurements also confirm a decrease in radial velocity as position increase through the SOL. A reduction in the mean poloidal flow velocity is also seen going from L-mode to H-mode with increasing power. A decrease in the poloidal velocity is seen with increased distance into the SOL, which is the trend expected from a decreasing radial electric field caused by a decreasing electron temperature profile, however the measured velocities are between 5 to 20 times lower than expected.

2D filament distributions have also been characterised, showing a general increase in filaments' amplitudes with poloidal diameter, with the average amplitude increasing with distance into the SOL for all poloidal sizes too. The largest poloidal diameters tend to go with filaments with the smallest radial velocities, and the smallest poloidal filaments have the largest range of radial velocities. It was also seen that radial diameter increases with poloidal diameter too, although this effect was less pronounced in H-mode filaments than L-mode or N_2 seeded, where a soft limit on the distribution mean is seen for large diameters. Whether this could be due to the increased poloidal magnetic shear present in H-modes was discussed.

Chapter 5

SOL simulations

In this chapter we use a theoretical model and simulations of the scrape-off layer to explore the relationship between the experimental measurements of filaments in the ASDEX Upgrade SOL and the SOL electron density profiles, namely if filaments can be used to explain the different mean density profile shapes we measure independently of the filaments, as well as to draw some conclusions about the required timescale of the parallel direction. Filament amplitudes, sizes, and velocities are generated randomly from the distributions measured in sections 4.4.2-4.4.3 and allowed to propagate through a simulated SOL domain. If the SOL profiles are determined by the filaments that propagate through them, then a time average over the simulated domain will provide a measure of the density profile.

In these simulations, the blobs remain invariant under translation - i.e., they do not change in size or shape as they propagate through the SOL, and if filaments cross one-another and occupy the same space, their contributions to the signal simply add together. As such, the filament properties are set at the birth of the filament and do not change with position in this model. We therefore choose the experimental distributions from the SOL location with the most measurements to help increase confidence in the statistics of the distributions measured. This is at $\rho = 1.04$ for the L-mode and N_2 seeded discharges, and $\rho = 1.06$ for the 2.5 MW and 5 MW H-mode discharges.

The 1D model used here is based off the theoretical framework as laid out by Militello and Omotani [110], as well as independently derived by Garcia *et al.* [111]. In this model, all filaments are generated with identical attributes (diameters, amplitudes, and velocities), as well as a single parallel timescale parameter, $\tau_{\|}$, which is a constant that describes how quickly a filament reduces in amplitude as it propagates through the SOL. Using identical

Table 5.1: A table showing the average filament attributes for each discharge type used in the single blob case.

Discharge type	δ_θ (cm)	δ_r (cm)	A (arb)	v_r (m/s)	v_θ (m/s)
L-mode	1.858	1.028	0.472	423.9	256.7
N_2 seeded	1.925	1.024	0.534	347.0	277.6
2.5 MW H-mode	2.016	0.954	0.626	-7.654	404.9
5 MW H-mode	2.437	0.803	0.530	-50.52	265.4

Table 5.2: A table showing the distribution inputs for filament attributes for each discharge type used in the independent case.

Discharge type	σ_θ	α_θ	σ_r	α_r	$\langle A \rangle$	σ_{v_r}	α_{v_r}	μ_{v_θ}	σ_{v_θ}
L-mode	0.320	1.766	0.242	0.999	0.472	0.640	361.8	256.7	350.1
N_2 seeded	0.338	1.817	0.275	0.985	0.534	0.671	282.6	277.6	321.7
2.5 MW H-mode	0.319	1.914	0.275	0.917	0.626	0.609	347.6	-7.654	493.9
5 MW H-mode	0.398	2.255	0.287	0.769	0.530	0.842	231.1	-50.52	463.3

parameters for all the filaments that remain constant throughout the SOL simplifies the initial derivation of the statistical profiles of the SOL, and also allows one to change filament characteristics independently of one another in a controlled way to investigate what effect they have on the profiles. We refer to this as the *single-filament Garcia-Militello (GM) model*. The filament attributes used are the means of the experimental measurements recorded in chapter 4, and are shown in table 5.1. This model is later expanded into 2D [112].

In addition to the single-filament GM model, we introduce a *distributed-filament GM model*, in which the filaments are generated with randomly selected attributes according to the experimental distributions measured in sections 4.4.2-4.4.3. Here, the attributes are drawn independently to other filament attributes. The filament diameters and radial velocity are sampled from log-normal distributions, whilst the amplitudes are drawn from exponential distributions, and in the case of 2D simulations, the poloidal velocities are drawn from normal distributions. The distributions used are displayed in table 5.2. In both the single-filament and distributed-filament models, the waiting times between filaments are always generated from an exponential distribution.

Here we note that some dependence on the filament poloidal diameter was found for the radial diameter, amplitude, and radial velocity in section 4.4.3. As such, simulations were also run where the poloidal diameters are randomly generated as in the distributed-

Table 5.3: A table showing the input parameter equation constants for each discharge type used in the dependent case for radial diameter and amplitude as functions of poloidal diameter.

Discharge type	$\sigma_r(\delta_\theta)$		$\alpha_r(\delta_\theta)$		$\langle A \rangle(\delta_\theta)$	
	m	c	m	c	m	c
L-mode	-0.00995	0.338	0.108	0.921	0.0749	0.332
N_2 seeded	0.0269	0.270	0.178	0.763	0.0734	0.415
2.5 MW H-mode	-0.00135	0.333	0.00676	0.979	0.0490	0.523
5 MW H-mode	-0.0875	0.513	0.00208	0.817	0.0561	0.397

Table 5.4: A table showing the input parameter equation constants for each discharge type used in the dependent case for radial velocity as functions of poloidal diameter.

Discharge type	$\sigma_{v_r}(\delta_\theta)$		$\alpha_{v_r}(\delta_\theta)$		
	m	c	A	L	C
L-mode	-0.0955	0.758	2821	0.4019	305.8
N_2 seeded	-0.0741	0.725	4503	0.318	270.2
2.5 MW H-mode	-0.0936	0.784	1582	0.460	316.3
5 MW H-mode	-0.0971	1.026	2272	0.488	194.4

filament GM model, and the size is used to determine the input parameters for the radial diameter, amplitude, and radial velocity distributions. Each distribution input follows a linear dependence ($m\delta_\theta + c$), except for the radial velocity scale parameter, which follows an exponential function ($A\exp\left(-\delta_\theta/L\right) + c$). The equation constants are given in tables 5.3 and 5.4. As the poloidal velocity was not seen to depend on the poloidal diameter, this was drawn independently, as in the distributed-filament GM model. It was found that no significant variation was found between the dependent and independent cases, and the same qualitative conclusions can be drawn for each. As such, the results for the distributed-filament GM models shown are from simulations where all the filament attributes are drawn independently of one another.

We will then go on to adjust the model three different ways. The first is a *dual timescale* model, or $\Delta\tau_\parallel$, which introduces a second parallel timescale so that the first part of the SOL has $\tau_{\parallel,1}$ up to some position, R_{ch}, and a second timescale, $\tau_{\parallel,2}$, from R_{ch} onwards. The second adjustment is a *dual velocity* model, or Δv_x instant, where a filament will have one radial velocity, $v_{x,1}$, for the first part of the SOL up to R_{ch}, and then a second velocity, $v_{x,2}$, thereafter. The third adjustment is a *finite acceleration* model, or Δv_x gradual, which

introduces a finite filament acceleration, a_x, between two SOL locations, $R_{\mathrm{ch},1}$ and $R_{\mathrm{ch},2}$. The single-filament and distributed-filament models for each of these model adjustments is explored in both 1D and 2D. In every simulation, the waiting time between filaments, τ_w, is kept constant, as this is later shown to have no effect on the trends of the simulated profiles when normalised to the separatrix values, only adjusting their absolute value. In 1D, $\tau_w = 10\,\mu\mathrm{s}$, and in 2D, $\tau_w = 0.1\,\mu\mathrm{s}$. This change is to account for the change in normalisation of the 2D model over the added dimension, and is justified in section 5.2.1.

When the various models are used, the simulated profiles that they generate are compared to the experimental profiles. This is done by changing input variables, detailed in the relevant section for that variation of the model, so that the fit to the resulting simulated profile best matches the fit to the corresponding experimental profile. The experimental electron density profiles are taken from measurements with the lithium beam emission spectroscopy diagnostic [33]. The profiles are averaged over the duration of a GPI gas puff (200 ms). For the H-mode profiles, only the inter-ELM periods are used. The profiles used here are only taken up to the position of the limiter shadow.

This chapter is organised as follows. We start in 1D, introducing the theoretical framework introduced in section 5.1. The single-filament GM model is derived and used in section 5.1.1, then the distributed-filament GM model is derived and used in section 5.1.2. As this is the first introduction of distributed filaments in this work, the different blob attributes will be introduced to the model individually to explore what change they have to the density profiles in isolation to one another, before combining them all at the end. These models are used with measurements of experimental density profiles that can be described with one exponential decay length.

In section 5.1.3 we will progress to the adjusted single-filament models, which are used for recreating profiles which require two exponential decay lengths to describe them. The single-filament $\Delta\tau_{\parallel}$ model is derived in section 5.1.3.1, the single-filament instant Δv_x model is derived in section 5.1.3.2, and the single-filament gradual Δv_x model is derived in section 5.1.3.3. The results from each of these three models is presented and compared in section 5.1.3.4. This is then repeated for the adjusted distributed-filament models in section 5.1.4, deriving the distributed-filament $\Delta\tau_{\parallel}$ model in section 5.1.4.1, the distributed-filament instant Δv_x model in section 5.1.4.2, and the distributed-filament gradual Δv_x model in section 5.1.4.3, before showing the results in section 5.1.4.4.

The 2D work is organised in the same manner, introducing the 2D theoretical framework in section 5.2, the 2D single-filament GM model in section 5.2.1, and the distributed-filament GM model in section 5.2.2. The adjusted single-filament models are in section 5.2.3, with the dual timescale model derived in section 5.2.3.1, the dual velocity model derived in section 5.2.3.2, and the finite acceleration model derived in section 5.2.3.3, with the results presentated and compared in section 5.2.3.4. Finally, the 2D distributed-filament models are in section 5.2.4. These include the $\Delta\tau_{\parallel}$ case in section 5.2.4.1, the instant Δv_x case in section 5.2.4.2, and the gradual Δv_x case in section 5.2.4.3, with the results to these extended distributed-filament models shown and discussed in section 5.2.4.4. A summary of all the results in this chapter is given at the end in section 5.3.

5.1 1D theoretical framework

We start by introducing the theoretical framework for the 1D simulations, as laid out by Militello and Omotani [110]. The 1-dimensional domain is aligned in the radial-direction, x, where the separatrix is located at $x = R - R_{\text{sep}} = 0$, and positive x values represent the SOL. An individual blob is represented by the equation

$$B_i(x,t) = A_{0,i}\Lambda\left(x - X(t), \delta_{x,i}\right) F_i(t) \tag{5.1}$$

where subscript i denotes the i-th filament being considered. $A_{0,i}$ is the starting amplitude of a filament at the separatrix, which here is taken to be a measure of the blob's density. Λ is a function defining the shape of the blob in 1D, X is the blob position*, given by

$$X(t) = \int_0^t v_{x,i}(t')\,\mathrm{d}t', \tag{5.2}$$

$v_{x,i}(t)$ is the radial velocity function of the filament, $\delta_{x,i}$ is the radial diameter of the filament, and $F_i(t)$ is a function describing the reduction of the filament's amplitude due to parallel losses as it traverses the SOL. Filaments i cross the separatrix at their arrival time, $t = t_{0,i}$.

*Here, the filaments' positions are given by the location of their maxima, rather than the CoM equation (4.5), used to define blob locations in section 4.3.3

An exponential function is used for the amplitude reduction function,

$$F_i(t) = \begin{cases} 1 & t < t_{0,i} \\ \exp\left(\frac{t_{0,i}-t}{\tau_\parallel}\right) & t \geq t_{0,i}. \end{cases} \tag{5.3}$$

Λ can be any well defined shape. A few good examples are: to replicate the double exponential waveform seen in experimental data [23, 57], section 4.4.1.4, given by

$$\Lambda(x,t) = \begin{cases} \exp\left(\frac{x-X(t)}{\delta_x^{\text{decay}}}\right) & x < X(t) \\ \exp\left(\frac{X(t)-x}{\delta_x^{\text{rise}}}\right) & x \geq X(t) \end{cases} \tag{5.4}$$

where $\delta_x^{\text{decay}} + \delta_x^{\text{rise}} = \delta_x$; to approximate the double exponential with a single exponential [110, 113] given by

$$\Lambda(x,t) = \exp\left(\frac{x - X(t)}{\delta_x}\right) H[X(t) - x] \tag{5.5}$$

where H is the Heaviside step function [114]; or a Gaussian function, as one would expect a radial slice through a 2D Gaussian to be [112], given by

$$\Lambda(x,t) = \exp\left(\frac{(x - X(t)^2}{\delta_x^2 \ln(2)/4}\right). \tag{5.6}$$

The factor of $\ln(2)/4$ in equation (5.6) ensures each waveform type has the same full width at half maximum. Examples of the waveforms with $A = 1$, $\delta_x = 15\,\text{mm}$, and $X(t) = 55\,\text{mm}$ are given in figure 5.1.

As we have assumed filaments do not interact with one another, a snapshot of the signal caused by these filaments, and thus the density in our domain*, $\theta(x,t)$, can be calculated by summing over all filaments

$$\theta(x,t) = \sum_i^\infty B_i(x, t - t_{0,i}). \tag{5.7}$$

An example of the time signals generated at different locations in the scrape-off layer for the Heaviside approximation using equation (5.5) is shown in figure 5.2. The form of the equations are setup to guarantee invariance of the filament as they propagate, so a filament

*This is density because we choose our amplitude term $A_{0,i}$ to have the units of density, although this model could be used to account for fluctuations in other thermodynamic quantities, such as temperature, pressure, etc.

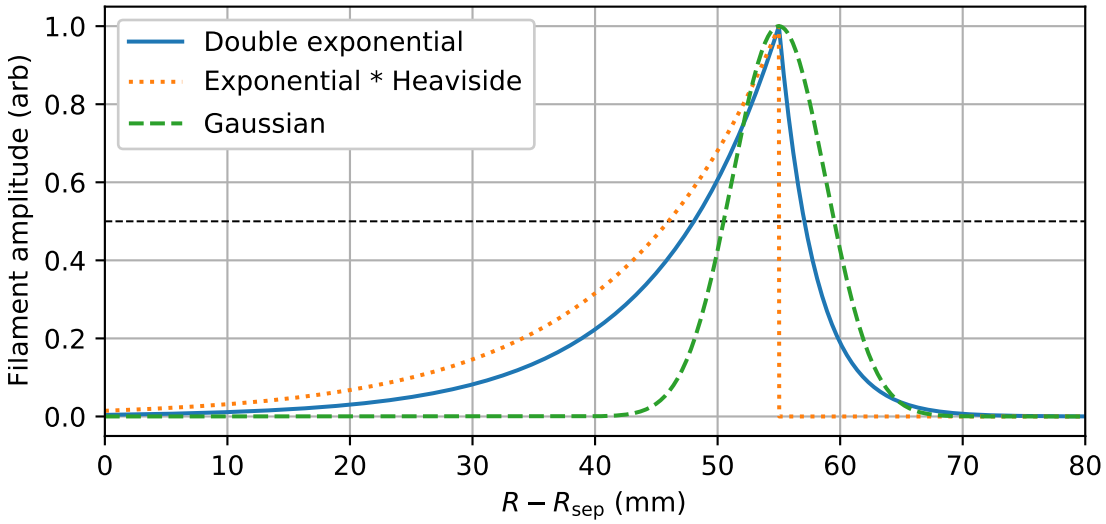

Figure 5.1: Example waveforms for equations (5.4) (blue, solid), (5.5) (orange, dotted), and (5.6) (green, dashed). All filaments have amplitude $A = 1$, $X = 55\,\text{mm}$, and $\delta_x = 1.5\,\text{cm}$ (the double exponential waveform has $\delta_x^{\text{rise}} = 0.3\,\text{cm}$ and $\delta_x^{\text{decay}} = 1.2\,\text{cm}$.)

does not change its shape and just reduces its amplitude, simulating parallel losses in the filament whilst moving through the SOL.

The density profile, $\Theta(x)$, can be obtained by taking the time average of our SOL signal

$$\begin{aligned}\Theta(x) &= \overline{\sum_i^{\infty} B_i(x, t - t_{0,i})} \\ &= \lim_{T\to\infty} \frac{1}{T} \int_0^T \sum_i^{\infty} B_i(x, t - t_{0,i})\,\mathrm{d}t.\end{aligned} \tag{5.8}$$

Here, the bar notes a time average, so $\overline{\ldots} \equiv \lim_{T\to\infty} T^{-1} \int_0^T \ldots \mathrm{d}t$. In practice, the time period is not infinite, but as long as the finite time T is large enough to allow the system to converge to a statistical average, then the above equation holds. This also means we do not sum an infinite number of filaments, but instead a finite number, K. As the system has been set up with independence between filaments generated with a constant average time between them, τ_w, K will itself be a random variable from the Poisson distribution, given by

$$f(k;\lambda) = \frac{\lambda^k \mathrm{e}^{-\lambda}}{k!} \tag{5.9}$$

where λ is the rate parameter, given by the expected number of events in a given time interval, T/τ_w, and the arrival times of filaments are uniformly distributed over time T with

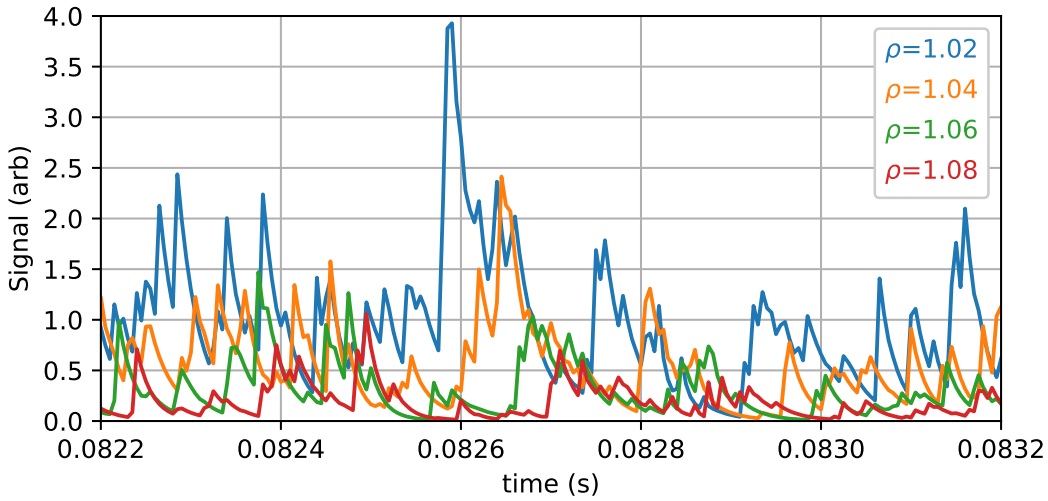

Figure 5.2: Example signals from the simple 1D model with the Heaviside approximation of the blob at various locations in the SOL.

a constant average waiting time between filaments, τ_w. Equation (5.8) can then be re-written as

$$\Theta_T(x) = \frac{1}{T}\int_0^T \sum_i^K B_i(x, t - t_{0,i})\,\mathrm{d}t. \tag{5.10}$$

As this system is ergodic by design, Campbell's theorem can be used to show the time-average of the system is equivalent to the ensemble average over the possible statistical outcomes [110, 115], and equation (5.10) becomes

$$\begin{aligned}\Theta_T(x) &= \langle\theta(x,t)\rangle \\ &= \int_0^\infty P_{A_0}\,\mathrm{d}A_{0,i}\int_0^\infty P_{\delta_x}\,\mathrm{d}\delta_{x,i}\sum_{K=1}^\infty P_K\sum_i^K\int_0^T P_{t_{0,i}}B_i(x,t-t_{0,i})\,\mathrm{d}t\end{aligned} \tag{5.11}$$

where $\langle ...\rangle$ denotes the ensemble average, and P_X is the probability distribution function for filament attribute X. We will explore how changing P for certain filament attributes affects the radial statistical moments calculated in this model, however the number of events, K, is always Poisson distributed, so P_K is given by equation (5.9), and the arrival times are always uniformly distributed, $P_{t_{0,i}} = 1/T$, which is the equivalent as exponentially distributed waiting times between events t_i and t_{i+1}, as shown in section 4.4.1.3. For the system here it can be shown [115] that as $T \to \infty$, $\sum_{K=1}^\infty P_K \sum_i^K \int_0^T P_{t_{0,i}} B_i(x, t - t_{0,i})\,\mathrm{d}t = 1/\tau_w \int_{-\infty}^\infty B_i(t)\,\mathrm{d}t$,

and we re-write equation (5.11) as

$$\begin{aligned}\Theta_T(x) &= \{B(x,t)\} \\ &= \frac{1}{\tau_w}\int_{-\infty}^{\infty}\mathrm{d}t\int_0^{\infty}\mathrm{d}A_0\int_0^{\infty}\mathrm{d}\delta_x\left[B(x,t)P_{A_0}P_{\delta_x}\right]\end{aligned} \tag{5.12}$$

where the curly brackets denote the expectation value operator. Higher order statistical moments can similarly be found, such as the variance, $\sigma(x) = \{B(x,t)^2\}$, the skewness, $S(x) = \{B(x,t)^3\}/\{B(x,t)^2\}^{3/2}$, and the kurtosis, $K(x) = \{B(x,t)^4\}/\{B(x,t)^2\}^2$, where

$$\{B(x,t)^n\} = \frac{1}{\tau_w}\int_{-\infty}^{\infty}\mathrm{d}t\int_0^{\infty}\mathrm{d}A_0\int_0^{\infty}\mathrm{d}\delta_x\left[B(x,t)P_{A_0}P_{\delta_x}\right]^n. \tag{5.13}$$

5.1.1 Single-filament Garcia-Militello model

We first begin by making comparisons to an experimentally measured electron density profile that can be fully described by an exponential function with a single decay length throughout the whole of the SOL. For this, we use a *base case* of parameters, based off the mean of the measurements from 5 MW H-mode discharge # 36342 for $t \in [4.5, 4.7]$s. The profile decay length is measured as $L = 20.26 \pm 0.53$ mm, with the experimental profile shown in figure 5.3.

In this single filament model, we start by allowing each filament produced to be of the same size, amplitude, and velocity, allowing us to exactly control the changes in the inputs to measure the effect this has on the simulated profiles. This has the effect of replacing P_X in equation (5.12) with the *Dirac delta function*

$$P_X = \delta(X - x) = \begin{cases} 1 & X = x \\ 0 & X \neq x \end{cases} \tag{5.14}$$

where x is attribute X's mean value given in table 5.1. In order to match the simulated profile to the experimental profile, a parallel timescale of $\tau_{\parallel} = 76\,\mu$s, to the nearest 1 µs, is needed for the base case to give a profile decay length of $L = 20.1713 \pm 0.0025$ mm and has been added into figure 5.3.

By doubling the radial velocity of the filaments for a fixed parallel timescale they are able to propagate twice as far into the SOL for a given reduction in their amplitude, causing

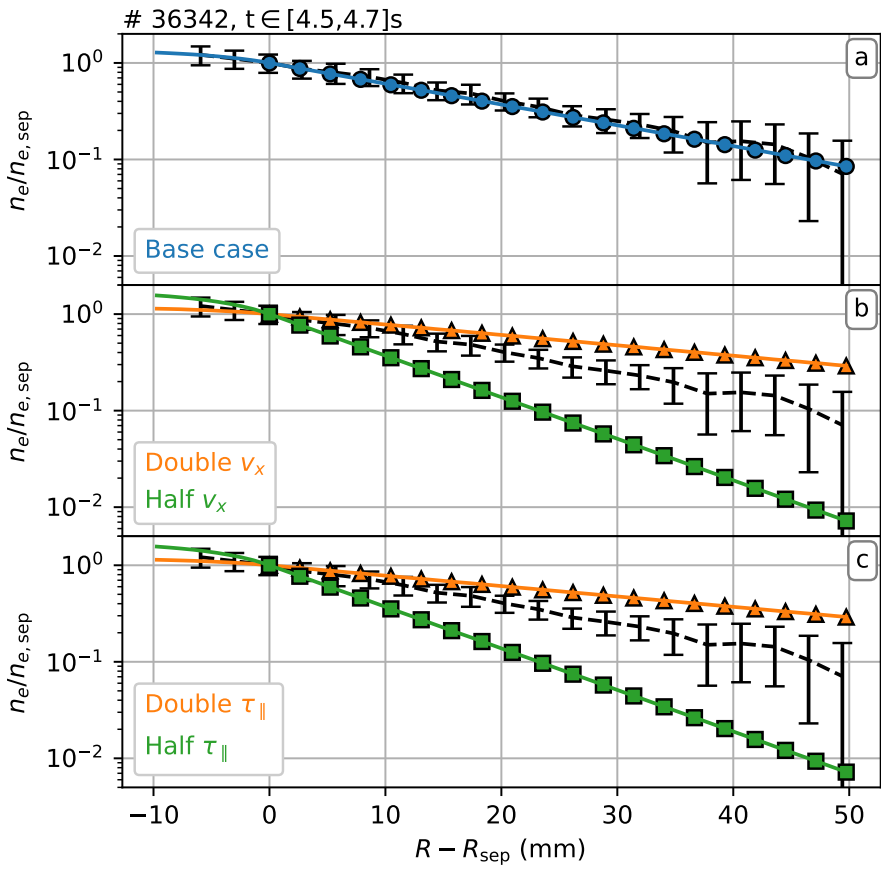

Figure 5.3: Density profile for the 5 MW H-mode experimental discharge # 36342, for $t \in [4.5, 4.7]$s (black dashed). The simulated profiles (coloured lines) from the 1D single blob case are: the base case (a); changing v_x (b); and changing $\tau_\parallel$ (c). The outputs from the statistical framework (shapes) are included.

larger densities at larger radii. This has the effect of doubling the decay length of the density profile. Conversely, halving the radial velocity has the effect of halving the decay length of the profile. The same effect can be seen by changing the parallel timescale, $\tau_\parallel$. If the parallel timescale doubles, then the filaments take twice as long to decay, so larger densities can be seen at larger radii, and if $\tau_\parallel$ is halved then the profile decay length is halved too. These profiles are all included in figure 5.3. The profile changes caused by doubling the parallel timescale are indistinguishable from the one caused by doubling the radial velocity (within error), and as such, doubling the radial velocity whilst halving the parallel timescale cancel each other out in the profiles to reproduce the base case. Exact measurements of the profile decay length are given in table 5.5. We here reiterate that the examples shown are normalised to the separatrix density, so the profiles do differ from another when looking at them in absolute values. This would then have an effect of changing the amount of flux

Table 5.5: A table showing the profile decay length for 1D simulations, using the Heaviside approximation, by varying v_x and $\tau_\parallel$. For each case, $1v_x = 265.4\,\mathrm{m/s}$ and $1\tau_\parallel = 76\,\mu\mathrm{s}$.

v_x (arb)	$\tau_\parallel$ (arb)	L (mm)
1	1	20.1713 ± 0.0025
2	1	40.339 ± 0.018
0.5	1	$10.085\,61 \pm 0.000\,54$
1	2	40.3427 ± 0.0087
1	0.5	$10.085\,67 \pm 0.000\,83$
2	0.5	20.1702 ± 0.0051
0.5	2	20.1719 ± 0.0016

further into the SOL.

The other parameters also investigated were the radial filament size, δ_x, the filament amplitude, A, and the filament waiting time, τ_w. These have no effect on the profile decay length, however changing A and τ_w change the value of the profile at $x = 0$. As all profiles are normalised to the separatrix value, this has no effect. The filament waveform was also changed to the double exponential and Gaussian, which modified the decay lengths slightly to $20.399 \pm 0.047\,\mathrm{mm}$ and $20.388 \pm 0.057\,\mathrm{mm}$, respectively.

We now check the fitted decay lengths against the model by solving equation (5.12). In the single filament case, no filament attribute depends on another and the order of integration does not matter. For a Dirac delta function as the distribution function, the integral over all space returns the point around which the function is centred, namely

$$\int_0^\infty x\delta(X - x)\,\mathrm{d}X = x, \tag{5.15}$$

and the distributions are simply replaced with the single attribute value. Equation (5.12) then becomes

$$\begin{aligned}\Theta(x) &= \frac{A_0}{\tau_w}\int_{-\infty}^{\infty} \exp\left(\frac{x - X(t)}{\delta_x}\right) H[X(t) - x] \exp\left(\frac{-t}{\tau_\parallel}\right)\mathrm{d}t \\ &= \frac{A_0}{\tau_w}\exp\left(\frac{x}{\delta_x}\right)\int_{X^{-1}(x)}^{\infty} \exp\left(\frac{-t}{\tau_\parallel} - \frac{X(t)}{\delta_x}\right)\mathrm{d}t\end{aligned} \tag{5.16}$$

where $X^{-1}(x)$ is the inverse function of the position function $X(t)$, equation (5.2). For a constant filament velocity, v_x, $X(t) = v_x t$ and $X^{-1}(x) \equiv t = x/v_x$. Therefore, the profile is

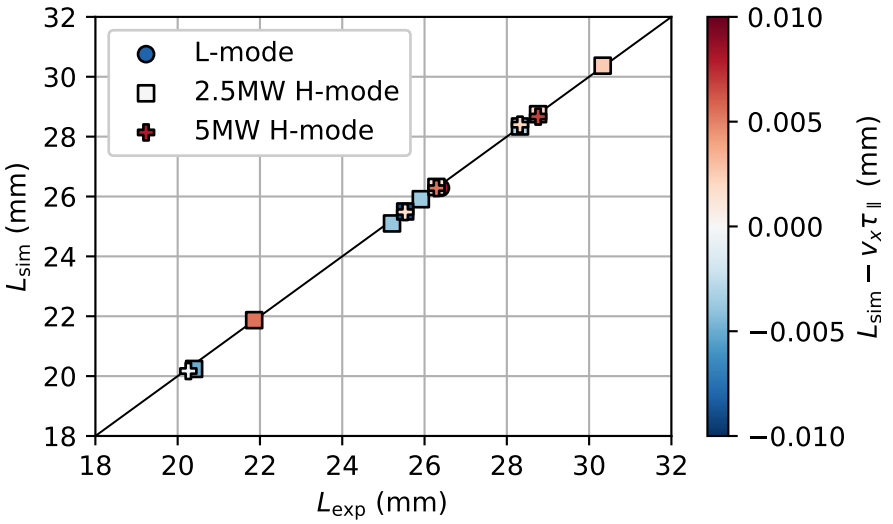

Figure 5.4: Simulated profile decay lengths against the experimental decay lengths during gas puffs where the profile is described by one decay constant. The difference between the decay length of the simulation, L_{sim}, and the product of $v_x\tau_{\parallel}$ used in the simulation is represented by the colourbar.

given by

$$\begin{aligned}\Theta(x) &= \frac{A_0}{\tau_w}\exp\left(\frac{x}{\delta_x}\right)\int_{\frac{x}{v_x}}^{\infty}\exp\left(-\frac{t}{\tau_{\parallel}}\left(1+\frac{v_x\tau_{\parallel}}{\delta_x}\right)\right)\mathrm{d}t \\ &= \frac{A_0}{\tau_w}G_0\exp\left(-\frac{x}{v_x\tau_{\parallel}}\right)\end{aligned} \tag{5.17}$$

where

$$G_0 = \frac{\tau_{\parallel}}{\left(1+\frac{v_x\tau_{\parallel}}{\delta_x}\right)}. \tag{5.18}$$

From equation (5.17), it can be seen that the profile decay length is exponential, and given by the product $v_x\tau_{\parallel}$, confirming the results of Garcia and Militello [110, 111]. For the base case with $v_x = 265.4\,\text{m/s}$ and $\tau_{\parallel} = 76\,\mu\text{s}$, the 1D GM model predicts a decay length of 20.1704 mm. Figure 5.4 shows the simulated profile decay lengths against the experimental decay lengths for gas puff durations where the density profiles are described by one decay length only, with the difference between the model estimated decay length and the simulated decay length shown by the colours. All simulated profile decay lengths are within the estimated error from the fit of the expected analytical decay length, within $\pm 0.01\,\text{mm}$. From this, we conclude that the profile decay length is directly proportional to the filament radial velocity and parallel timescales. This will be explored in further detail in section 5.1.2.

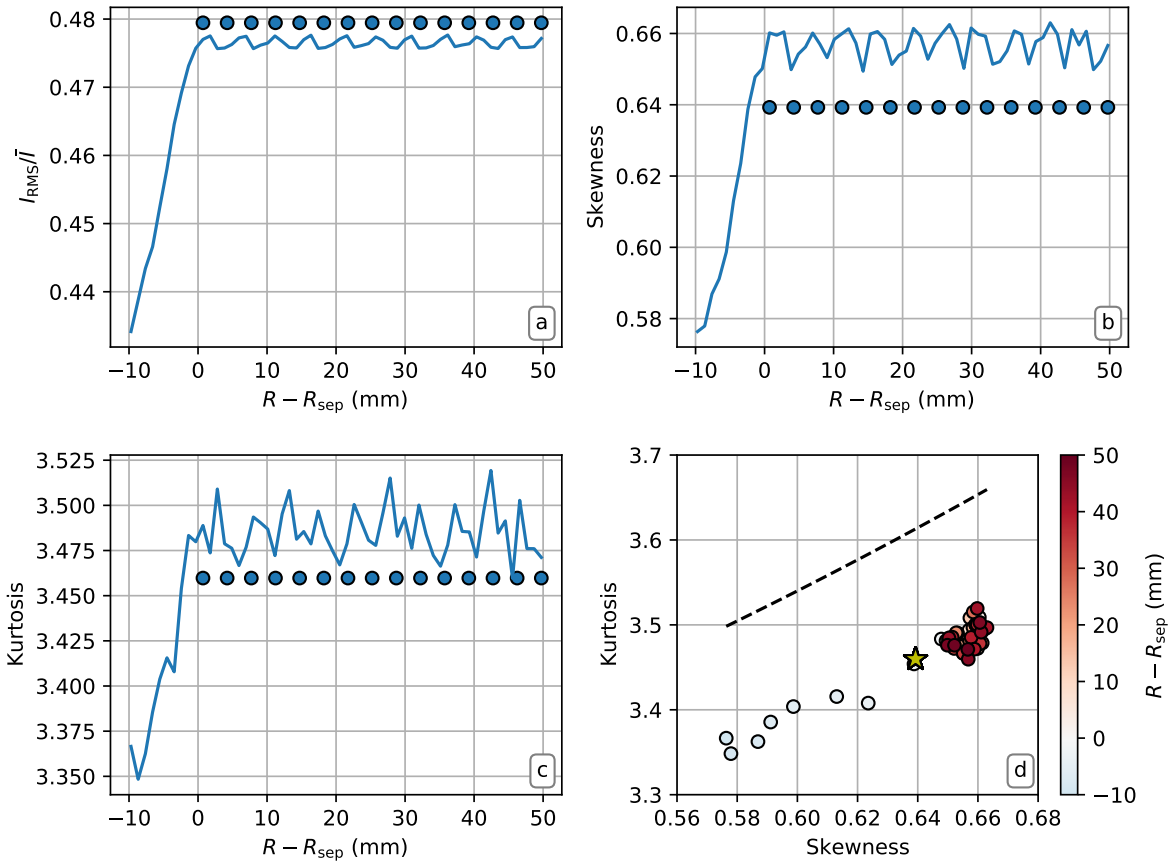

Figure 5.5: Profiles in the simulated SOL for the 1D single blob case (solid lines) for shot # 36342, $t \in [4.5, 4.7]$s for: the relative fluctuation levels (a); skewness (b); and kurtosis (c). The values of kurtosis against skewness are shown (d) with the theoretical $K = 3S^2/2 + 3$ relation added (black dashed). The theoretical values are added (blue circles, yellow star).

We now turn to the higher order statistical moments. Figure 5.5 shows an example of these measurements for the single filament case using the Heaviside waveform. Similarly to how we derived the expression for the profile, we can replace the integration over the amplitude and size distributions with the relevant values. The variance then becomes

$$\begin{aligned}
\sigma(x) &= \{B(x,t)^2\} \\
&= \frac{1}{\tau_w}\int_{-\infty}^{\infty}\left[A_0 \exp\left(\frac{x - X(t)}{\delta_x}\right) H[X(t) - x] \exp\left(\frac{-t}{\tau_\parallel}\right)\right]^2 \mathrm{d}t \\
&= \frac{A_0^2}{\tau_w}\exp\left(\frac{2x}{\delta_x}\right)\int_{\frac{x}{v_x}}^{\infty}\exp\left(-\frac{2t}{\tau_\parallel}\left(1 + \frac{v_x\tau_\parallel}{\delta_x}\right)\right)\mathrm{d}t \\
&= \frac{A_0^2}{2\tau_w}G_0 \exp\left(-\frac{2x}{v_x\tau_\parallel}\right),
\end{aligned} \tag{5.19}$$

which in turn gives the relative fluctuations as

$$\frac{I_{\mathrm{RMS}}}{\bar{I}} = \frac{\sqrt{\sigma(x)}}{\Theta(x)} = \frac{\sqrt{2}}{2}\sqrt{\frac{\tau_w}{G_0}}. \tag{5.20}$$

For the inputs of the base case this gives $\sqrt{\sigma(x)}/\Theta(x) = 0.479$, a slight overestimate of the average of the simulated SOL of 0.477. Neither equation (5.20) nor figure 5.4a show any variation with distance into the SOL, in contrast to the experimental relative fluctuation levels seen in figure 4.13a. This is not a special case for the base case, nor for any of the other shots included in figure 5.4, and is instead caused by all filaments being generated with the same size, amplitude and velocity.

In general, for the single filament case with a Heaviside waveform, we can write

$$\begin{aligned}\{B(x,t)^n\} &= \frac{A_0^n}{\tau_w}\exp\left(\frac{nx}{\delta_x}\right)\int_{\frac{x}{v_x}}^{\infty}\exp\left(-\frac{nt}{\tau_\parallel}\left(1+\frac{v_x\tau_\parallel}{\delta_x}\right)\right)\mathrm{d}t \\ &= \frac{A_0^n}{n\tau_w}G_0\exp\left(-\frac{nx}{v_x\tau_\parallel}\right),\end{aligned} \tag{5.21}$$

and the skewness and kurtosis* are

$$S = \frac{\{B(x,t)^3\}}{\{B(x,t)^2\}^{3/2}} = \frac{2\sqrt{2}}{3}\sqrt{\frac{\tau_w}{G_0}} \tag{5.22}$$

and

$$K = \frac{\{B(x,t)^4\}}{\{B(x,t)^2\}^2} = \frac{\tau_w}{G_0}, \tag{5.23}$$

respectively. These also do not increase with distance into the SOL, as in the examples in figure 4.13, which is also caused by the identical filaments. The kurtosis also deviates from the theoretical $K = 3S^2/2$ dependence, both in the sense that the simulation results do not follow this trend, figure 5.3d, and, using equations (5.22)-(5.23), $K \neq 3/2S^2$, but instead suggests a $K = 9/8S^2$ scaling.

Finally, we study the single point probability distribution functions, like in section 4.4.1.1, for the simulated signal fluctuations, given by equation (4.4), to see if they still follow a Gamma distribution, equation (2.9). Figure 5.6 shows the PDFs for the base single blob case. Here we see how each location in the SOL has a nearly identical PDF, with no variation

*This derivation of the kurtosis gives the *excess kurtosis*, and all values shown in the graphs, both the derived values and measurements of the simulated data, are the unadjusted Pearson's kurtosis, as in section 4.4.2.1.

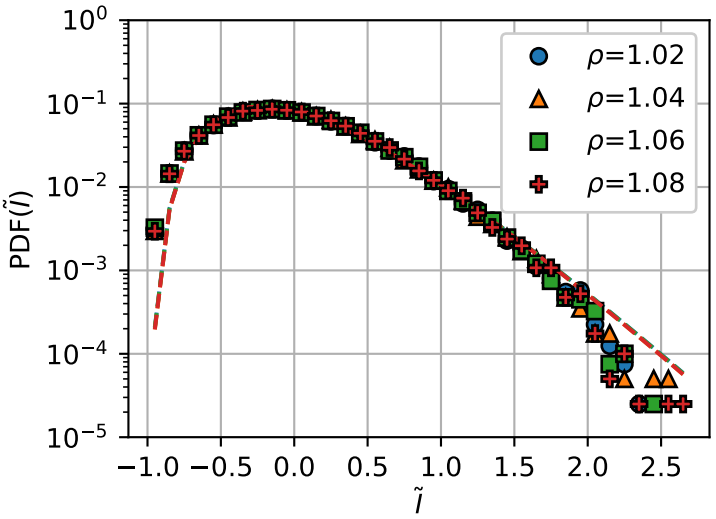

Figure 5.6: Probability distribution functions for different single locations in the SOL for the 1D single blob case (coloured markers) for shot # 36342, $t \in [2.5, 2.7]$s. The Gamma functions calculated from the input parameters, k and θ, are included (dashed lines). The ρ positions are at $R - R_{\text{sep}} = [12, 23, 35, 46]$mm.

with location. This follows the same trend as the higher order moments also having no radial variation, in contrast to the experimental results presented in figure 4.7. We do still see that the fluctuations closely follow Gamma distributions, even without the radial change, as each PDF has approximate input parameters of $k = 4.40 \pm 0.02$ and $\theta = 0.227 \pm 0.001$, with any variation due to the finite temporal resolution of the data. The other single blob cases' PDFs from figure 5.3 were also checked, each still showing no variation with x, although the values of the Gamma input parameters do change, so each case has a different shape parameter.

We here note how the inputs to the Gamma distribution relate to the first two statistical moments.* The equations for k and θ are given by equations (2.10) and (2.11), respectively, using the signal fluctuation, where as the statistical moments are calculated on the raw signal. If the fluctuation signal is just a scaling of the raw signal to the signal's mean, then we can rewrite the expectation value and variance of $\tilde{I}$ in terms of I, and as such the Gamma distribution inputs of $\tilde{I}$ in terms of the lower statistical moments of I. This simply gives $k_{\tilde{I}} = E[X]^2/V[X] \equiv k_I$, so the shape parameter is unchanged by the change in variable, and $\theta_{\tilde{I}} = V[X]/E[X]^2 = \theta_y$, in which θ_y is the square of the relative fluctuation amplitude, the radial profile of which is shown in figure 5.3a. As such, radial behaviour of the relative

*As in section 4.4.1.1, we note that because the Gamma distribution is defined for a positive domain, when calculating the input parameters, $\tilde{I} + 1$ is used instead of equation (4.4), and the resulting PDFs are translated by $+1$ in the x-direction.

fluctuation amplitude, or lack thereof, informs us of the radial changes we should expect to see in the single point probability distribution functions. Similarly, Garcia shows [56, 111] how the inputs to the Gamma distribution are expressed as $k = \tau_d/\tau_w$ and $\theta = A_0$, where in his work τ_d is a combination of $\tau_\parallel$ and δ_x/v_x. In the model shown here, these variables do not vary over the SOL, and as such the single-point PDFs do not vary with position.

5.1.2 Distributed-filament Garcia-Militello model

In order to investigate the effect of all filaments having the same attributes in the previous section, we now introduce the distributions to randomly draw filament attributes from, starting with the 5 MW discharge # 36342 base case. The PDF input parameters introduced in this section are for the blob amplitude, radial diameter, and radial velocity, each introduced individually. They are used in isolation to one another, with the other attributes kept constant, as in the previous section, as well as an instance of all three together. The distribution inputs are given in table 5.2 and are all used independently to one another, taken directly from the experimental measurements in section 4.

The simulated density profiles from these examples are shown in figure 5.7, and the profile decay lengths are given in table 5.6. These were achieved by altering $\tau_\parallel$ to a precision of 1 mm. This was also repeated for the dependent case. In this instance, the filament poloidal sizes are generated first and the rest of the filament attributes generated afterwards using the coefficients given in tables 5.3 and 5.4.*. The measured decay lengths change quantitatively, but not qualitatively, and are within error on the fits to the profiles. Any small changes are likely due to the minute differences in the individual blobs generated. As such, the profiles are not included, but the measured decay lengths are also included in table 5.6.

Following on from the conclusion of section 5.1.1, we can here see how it is the radial velocity that has the largest effect on the density profile. In both the dependent and independent cases, adding in the radial or amplitude distributions affected the profile decay length by less than 0.1 % (< 0.01 mm) when compared with the single-filament profile, and is well within the error for the fit to the profiles. The expression for Θ remains unchanged in these cases from equation (5.17) with the exception of swapping either A_0 or δ_x with the expectation value of the relevant distribution. The radial velocity profiles however are very

*The poloidal sizes themselves are not required in the 1D simulations, but they are still generated first to allow direct comparison with the 2D simulations, section 5.2

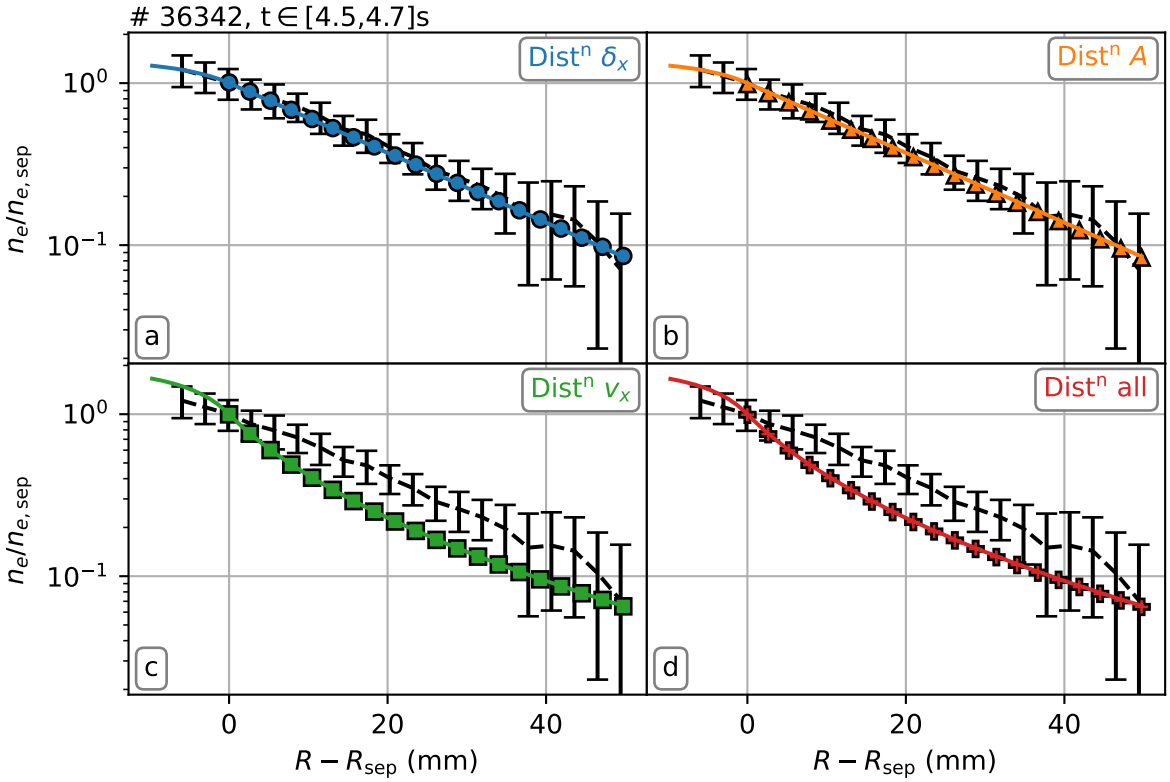

Figure 5.7: Profiles measured from 1D simulations adding in independent distributions for some blob attributes, using the Heaviside approximation (coloured lines) and the 5 MW H-mode experimental discharge # 36342, for $t \in [4.5, 4.7]$s (black dashed). The outputs from the statistical framework (shapes) are included.

Table 5.6: A table showing the profile decay length for 1D simulations, using the Heaviside approximation, with distributions for different blob attributes, in the independent and dependent cases.

Attribute from dist.	$L_{\text{ind.}}$ (mm)	$L_{\text{dep.}}$ (mm)
Radial diameter	20.1720 ± 0.0026	20.1709 ± 0.0025
Amplitude	20.1789 ± 0.0033	20.1638 ± 0.0031
Radial velocity	19.14 ± 0.41	19.08 ± 0.39
All	19.17 ± 0.52	18.84 ± 0.37

different. Firstly, by just looking at the absolute values of the decay lengths, a decrease of 1 mm (5 %) is seen, although much of the difference between the profiles is obscured by studying the decay lengths alone. The profile, seen in figure 5.7, can now seen to be deviating from an exponential profile quite largely, starting with a steeper profile near the separatrix with a decay length that increases with distance into the SOL. As such, the metric of a single decay length, used to define a normalised exponential function, may not be so appropriate to describe this profile.

The radial velocity distribution must be accounted for when calculating the expressions for Θ. Equation (5.12) has no information about the velocity distribution, but there is the $X^{-1}(x) = x/v_x$ term in the limit of the time integration itself in equation (5.16). We make the following argument for a derivation of the expression for the mean profile. In the case where each filament has the same velocity, then each filament contributes the same signal to the average, and we arrive at equation (5.17). In a simplified case where filaments can take on either one of two velocities, v_1 or v_2, with equal probability, then half the filaments would would contribute to the signal in one way, and the remaining filaments in another way. As such, we could rewrite equation (5.17) as

$$\Theta(x) = \frac{1}{2}\frac{A_0}{\tau_w}\left[G_{v_1}\exp\left(-\frac{x}{v_1\tau_\parallel}\right) + G_{v_2}\exp\left(-\frac{x}{v_2\tau_\parallel}\right)\right]. \tag{5.24}$$

Here, G_{v_i} is equation (5.18) with v_x swapped for v_i. A similar approach could be taken using more than two velocities, each with equal probability, or using two velocities, but with different probabilities. In the case of the former, the factor of $1/2$ would be replaced with $1/n_{v_x}$, where n_{v_x} was the number of different velocities the filament could have. For the latter scenario, the brackets would need expanding and each term would need a normalised coefficient representing the probability of that velocity.

This is what we have in the case of a well defined velocity distribution for an increasingly large number of velocities. Here we have used log-normally distributed radial velocities and so the relative fraction of filaments with velocity $v_{x,i}$ is given by the log-normal PDF. This gives the equation for the profile as

$$\Theta(x) = \sum_i^I \frac{1}{v_{x,i}\sqrt{2\pi}\sigma_{v_x}}\exp\left(-\frac{\ln\left(\frac{x}{\alpha_{v_x}}\right)^2}{2\sigma_{v_x}^2}\right)\frac{A_0}{\tau_w}G_{v_i}\exp\left(-\frac{x}{v_{x,i}\tau_\parallel}\right) \tag{5.25}$$

where i and I represent the smallest and largest velocities drawn from the distribution. In the simulations the velocities are a continuous random variable between the limits of $v_x \in [0, \infty]$. As such, equation (5.25) tends towards the analytical solution for the problem as the number of discrete $v_{x,i}$ values is increased, or by replacing the sum with an integral as $v_{x,i+1} - v_{x,i} \to 0$. This expression, however, has no analytical solution, and we instead calculate equation (5.25) for the smallest and largest v_x randomly drawn in the simulation with a $v_{x,i+1} - v_{x,i} = 1\,\mathrm{m/s}$ which gives good approximations for the radial statistical moments.

Changing the filament waveform from the Heaviside approximation to either the double exponential or Gaussian had a small effect on the absolute value of the decay length by slightly deviating from a perfect exponential near the separatrix, but was otherwise unchanged. This slight difference is attributed to the relative change between how we define the filaments' positions compared to their centre-of-mass. In the Heaviside approximation when a filament is positioned at the separatrix all of the filament contributes to signal before the separatrix only. As the filaments have a constant amplitude up to this point before they decay exponentially and this gives the non-exponential for $x < 0$ for the profiles in figure 5.7. As the other two waveform types have some non-zero signal for $x > 0$ when at the separatrix, this effect is shifted to slightly higher x. As such, the difference in the profiles due to a change in the filament waveform can be disregarded.

We also investigate the higher order moments of the signals, shown in figure 5.8. Similar to the mean profile, adding in the radial diameter and amplitude distributions has no effect on the profile shape for the relative fluctuation amplitude, skewness, or kurtosis. In fact, when adding in the radial diameter distribution, the equations for the mean, standard deviation, skewness, and kurtosis, do no change from those given in equations (5.17)–(5.23), except the radial diameter term is swapped for the expected value of the distribution. Because we used the mean value in the single blob case, the addition of the radial diameter distributions doesn't change any of the moments in relation to the base case. For the case with the amplitude distribution included, the A_0^n term is replaced in the n-th statistical moment with the corresponding n-th moment of the exponential distribution function,

$$\begin{aligned} I_n &= \int_0^\infty \frac{x^n}{A_0} \exp\left(-\frac{x}{A_0}\right) \mathrm{d}x \\ &= n! A_0^n. \end{aligned} \tag{5.26}$$

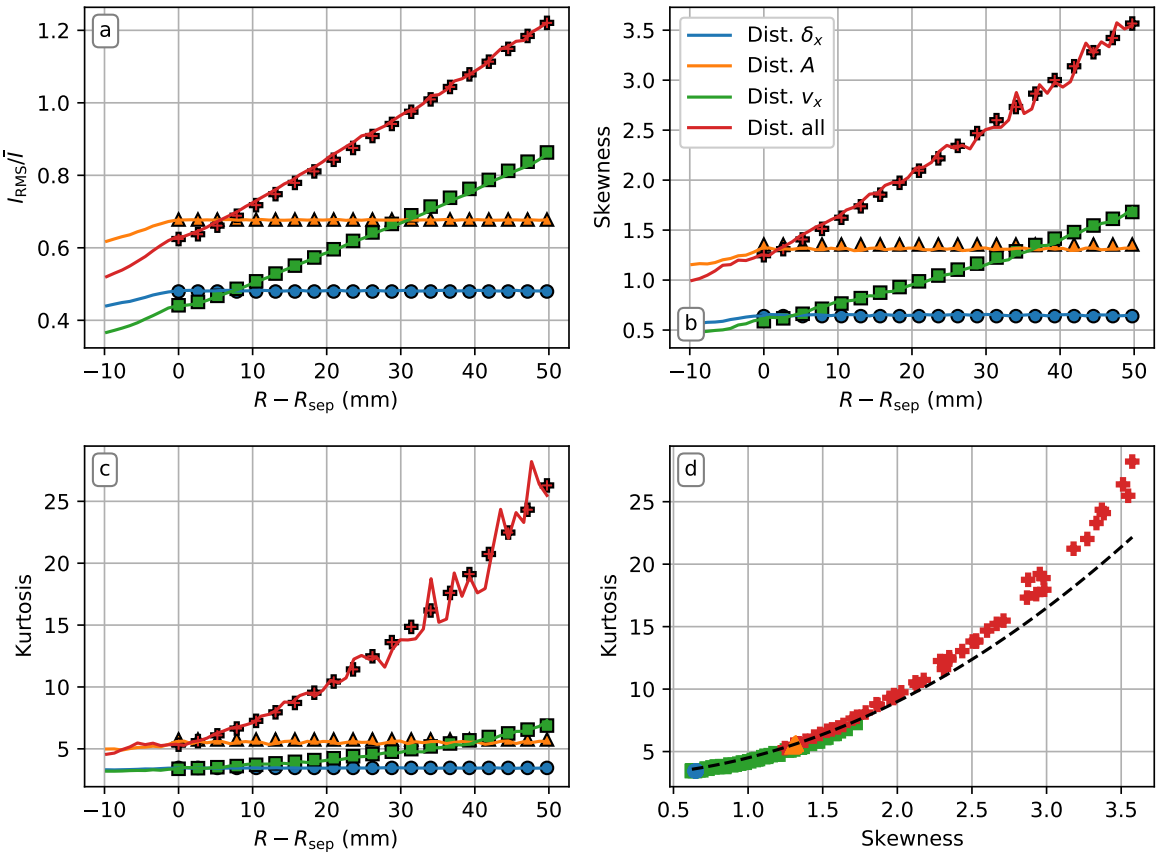

Figure 5.8: Profiles in the simulated SOL for the 1D independent blob case (solid lines) for shot # 36342, $t \in [4.5, 4.7]$s for: the relative fluctuation levels (a); skewness (b); and kurtosis (c). The values of kurtosis against skewness are shown (d) with the theoretical $K = 3S^2/2+3$ relation added (black dashed). The expected values derived from the model are included as symbols in (a–c).

The form of equations (5.20)–(5.23) do not change, i.e., there is still no dependence on x and the profiles remain flat, but now the coefficients change. The general case with exponentially distributed amplitudes is

$$\{B(x,t)^n\} = \frac{(n-1)!A_0^n}{\tau_w} G_0 \exp\left(-\frac{nx}{v_x \tau_\parallel}\right) \tag{5.27}$$

and specifically for the relative fluctuation level, skewness, and kurtosis,

$$\frac{\sqrt{\sigma(x)}}{\Theta(x)} = \sqrt{\frac{\tau_w}{G_0}}, \tag{5.28}$$

$$S = 2\sqrt{\frac{\tau_w}{G_0}} \tag{5.29}$$

and

$$K = 6\frac{\tau_w}{G_0}, \tag{5.30}$$

respectively. Note, that here we now recover the $K = 3/2S^2$ scaling expected for a signal described by a Gamma distribution, although radial variation of the moments is still not seen.

Again, it is the radial velocity distribution that brings about the largest change. We now see, for the first time, the increase in relative fluctuation amplitude, skewness, and kurtosis, with distance into the SOL, as recorded in the experimental data, figure 4.13. A similar method for obtaining expressions for the higher order moments can be used here as it was for the profile. The modified version of the n-th order expectation value becomes

$$\{B(x,t)^n\} = \frac{A_0^n}{n\tau_w}\sum_i^I \frac{1}{v_{x,i}\sqrt{2\pi}\sigma_{v_x}} \exp\left(-\frac{\ln\left(\frac{v_{x,i}}{\alpha_{v_x}}\right)^2}{2\sigma_{v_x}^2}\right) G_{v_i} \exp\left(-\frac{nx}{v_{x,i}\tau_\parallel}\right) \tag{5.31}$$

and approximations for the relative fluctuations, skewness, and kurtosis can be found. These have been added into figure 5.8 and agree will with the simulated values, giving an increase with all quantities into the SOL. Previously, all $\exp\left(-nx/v_x\tau_\parallel\right)$ terms cancelled, giving no radial variation, but now the velocity distribution terms mean the exponential terms cannot cancel, retaining the radial dependence in the statistical moments. From this we can conclude that, in the single-blob case, a distribution of radial velocities is necessary to reproduce the increasing relative fluctuations, skewness, and kurtosis values with distance into the scrape-off layer consistent with experimental results. Equation (5.31) can be modified for the moments for the independent blob scenario, when the amplitudes, radial sizes, and radial velocities, are all randomly generated, by replacing δ_x with the expectation value of the radial size distribution, and replacing the A_0^n term with the result of equation (5.26).

We now investigate the single point probability distribution functions for the 1D independent blob case, shown in figure 5.9. The corresponding Gamma PDF input parameters are included in table 5.7. As shown in the previous section, no radial variation in the relative fluctuation levels again translates to no change in the PDFs for the simulations with the added radial diameter and or amplitude distributions, but we do here directly show how the change in the the value of the fluctuations between the two cases directly leads to the change in the shape of the distributions. For the radial diameters, which does not deviate much

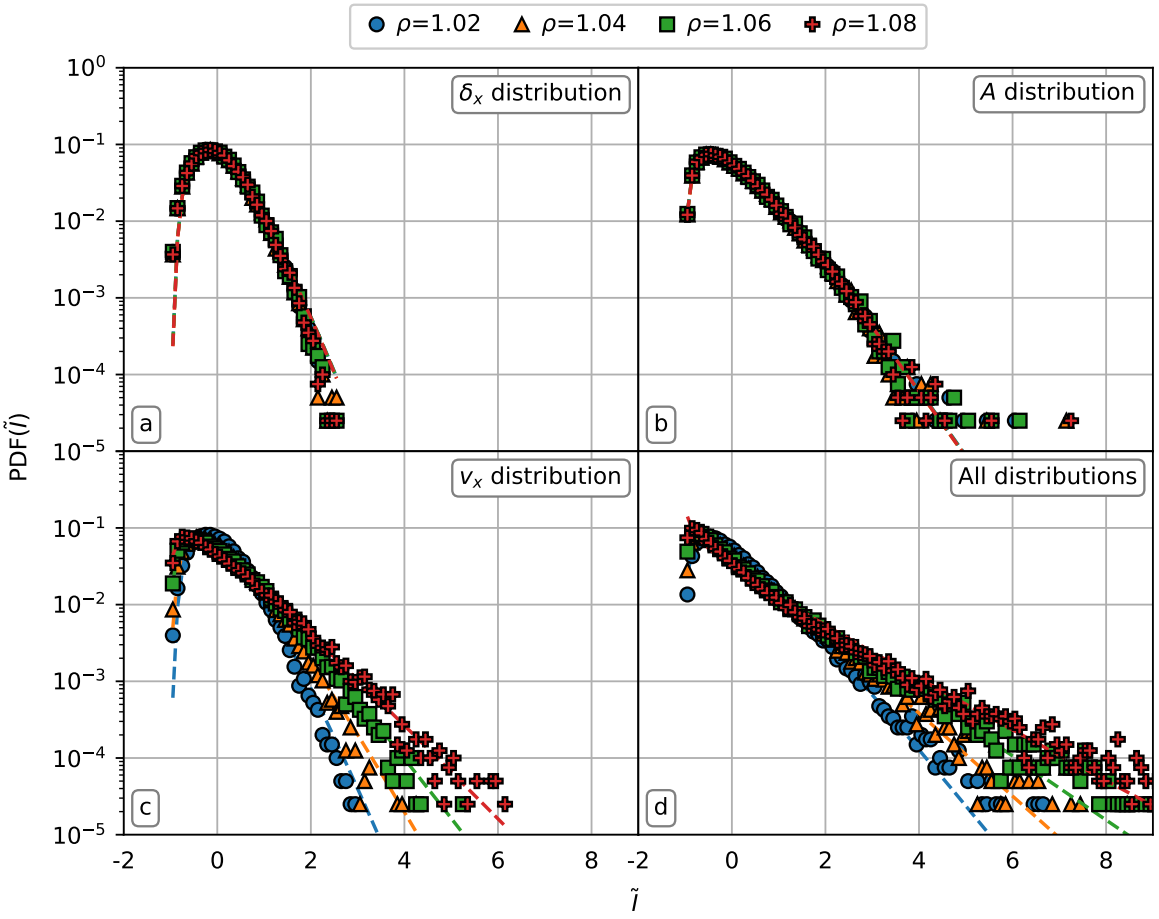

Figure 5.9: Probability distribution functions for different single locations in the SOL for the 1D independent blob case (coloured markers) for shot # 36342, $t \in [4.5, 4.7]$s. The Gamma functions calculated from the input parameters, k and θ, are included (dashed lines). The ρ positions are at $R - R_{\text{sep}} = [12, 24, 36, 48]$mm.

with respect to the single blob base case (both the relative fluctuations and the Gamma input parameters vary less than 5 %), the PDF is also very similar to the PDF in the base case, whilst the PDF with the amplitude distribution shows exhibits a larger positive tail, consistent with an increased scale parameter (or relative fluctuation level).

The radial variation seen in the statistical profiles when introducing the radial velocity distributions is recovered in the single point PDFs too. Now, as we increase our distance from the separatrix, the shape parameters decrease and the scale parameters increase. Previously, with a constant equal velocity for all filaments, the blobs moved together, so that any initial distance between filaments would remain the same throughout the entirety of their propagation. Even if filaments had different amplitudes and radial extents they were still similar, and the signal was still similar from position (x,t) to position $(x + v\Delta t, t + \Delta t)$, so

Table 5.7: A table showing the shape (k) and scale (θ) input parameters for the Gamma distribution function for different locations in the SOL for the four 1D independent blob case simulation shown in figure 5.9.

ρ	1.02		1.04		1.06		1.08	
Distribution added	k	θ	k	θ	k	θ	k	θ
Radial diameter	4.29	0.233	4.32	0.231	4.30	0.233	4.32	0.231
Amplitude	2.17	0.460	2.19	0.457	2.18	0.459	2.19	0.457
Radial velocity	3.83	0.261	2.71	0.370	1.96	0.509	1.48	0.675
All three	1.84	0.545	1.29	0.773	0.96	1.046	0.73	1.374

the PDFs would be the same. Now with varying filament velocities, this similarity no longer holds and we see a radial variation in the PDFs. It is this non-similarity that gives a radial dependence in the statistical moments, $B(x,t)^n$, and is therefore responsible for the change in the PDF input parameters.

5.1.3 Adjusted single-filament models

Here we explore how we can amend the single-filament GM model from section 5.1.1 to recreate density profiles that do no follow one exponential decay length. We consider two base cases: the first is the 5 MW H-mode discharge # 36342 for $t \in [2.5, 2.7]$s, where the density decay length decreases in the far SOL, shown in figure 5.10; and the L-mode discharge # 36344 for $t \in [2.5, 2.7]$s, where the density decay length increases in the far SOL, shown in figure 5.11. In these examples, the profiles cannot be described by a single exponential function, and instead a piecewise function of two exponentials is used, given by

$$y(x) = \begin{cases} y_0 \exp\left(\frac{x-x_0}{L_1}\right) & x \leq x_0 \\ y_0 \exp\left(\frac{x_0-x}{L_2}\right) & x > x_0 \end{cases} \tag{5.32}$$

where (x_0, y_0) are the coordinates of the point where the two exponentials meet, and L_1 and L_2 are the decay lengths of the profile in the SOL nearest to the separatrix and furthest from the separatrix, respectively. As the profiles are still normalised to the separatrix value, the y_0 variable is of no interest to us in these experiments but is required to ensure continuity between the two regions of the profile. It should be noted that the filament input parameters for the two base cases are different because of the different discharge types. Whilst this may

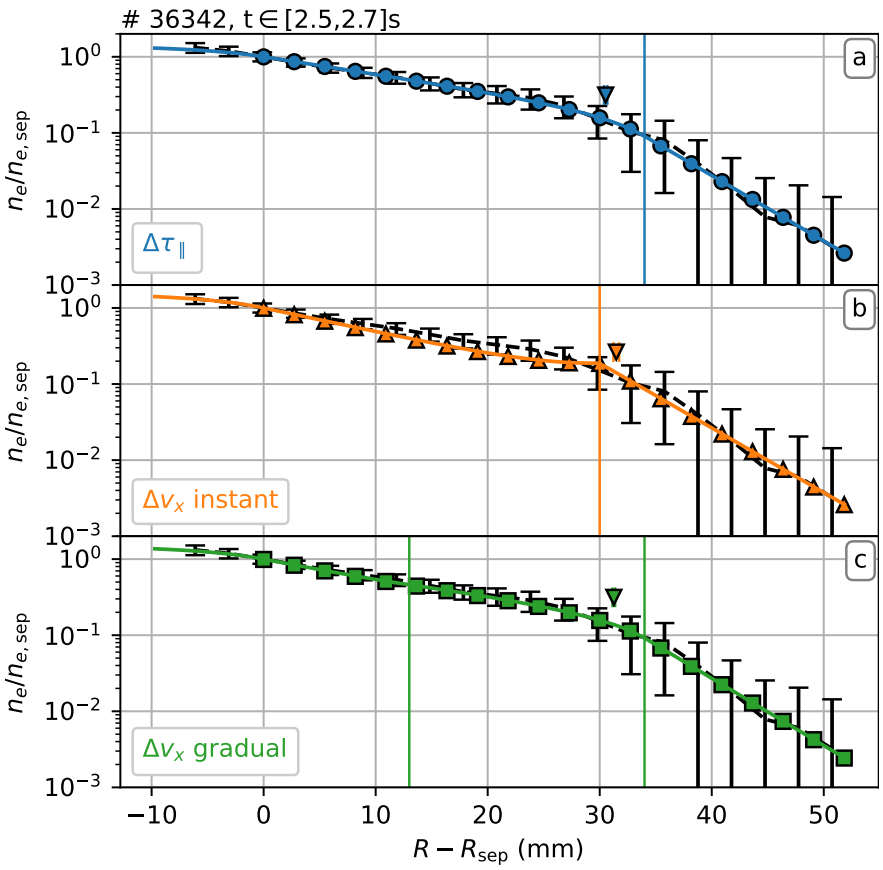

Figure 5.10: Electron density profile for the 5 MW H-mode discharge # 36342 (black dashed). Three simulation profiles from the 2D single blob case are included: changing $\tau_\parallel$ (a, blue); instantaneously changing v_x (orange); and gradually changing v_x (green). The x_0 parameters (coloured triangles), R_{ch} values (coloured vertical lines), and the outputs from the statistical framework (coloured shapes) are included.

quantitatively change the required parameters (for e.g., as v_x has changed, a different $\tau_\parallel$ would be required for the same L decay length) the analysis and conclusions are still valid. The fit parameters for the experimental profiles are given in table 5.8.

5.1.3.1 Single-filament dual timescale model

In this section, the single-filament GM model is extended by introducing a second parallel timescale in the scrape-off layer, simulating a change in collisionality, connection length, etc., as we move through the SOL, and upstream is now connected (or disconnected) to a different part of the divertor, or, more generally, a different part of the first wall. This changes the

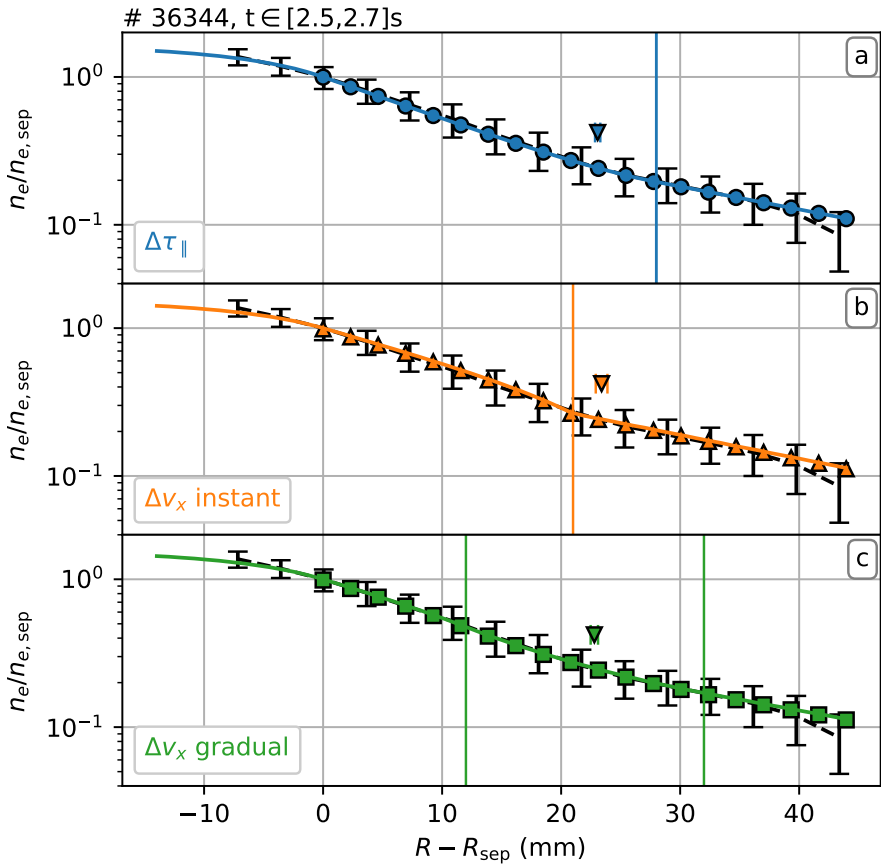

Figure 5.11: Electron density profile for the L-mode discharge # 36344 (black dashed). Three simulation profiles from the 1D single blob case are included: changing $\tau_{\parallel}$ (a, blue); instantaneously changing v_x (orange); and gradually changing v_x (green). The x_0 parameters (coloured triangles), R_{ch} values (coloured vertical lines), and the outputs from the statistical framework (coloured shapes) are included.

Table 5.8: A table showing the fit parameters for the base case non-exponential experimental profiles, and the profiles generated in the 1D single blob case using the Heaviside approximation. For the 5 MW H-mode discharge, when $x = 31$ mm, $\rho \approx 1.052$, and $x = 23$ mm, $\rho \approx 1.032$ in the L-mode discharge.

Profile type		x_0 (mm)	L_1 (mm)	L_2 (mm)
H-mode	Experimental	30.76 ± 0.89	17.1 ± 1.2	5.11 ± 0.20
	$\Delta\tau_{\parallel}$	30.53 ± 0.15	16.98 ± 0.20	5.115 ± 0.032
	Δv_x instant	31.48 ± 0.25	16.84 ± 0.32	4.953 ± 0.027
	Δv_x gradual	31.26 ± 0.12	16.93 ± 0.17	4.953 ± 0.027
L-mode	Experimental	23.15 ± 0.32	15.888 ± 0.087	27.49 ± 0.59
	$\Delta\tau_{\parallel}$	23.07 ± 0.22	16.092 ± 0.073	27.48 ± 0.26
	Δv_x instant	23.40 ± 0.49	16.06 ± 0.15	27.08 ± 0.54
	Δv_x gradual	22.79 ± 0.31	15.88 ± 0.11	27.40 ± 0.34

equation for the parallel drainage function, equation (5.3) to

$$F_i(t) = \begin{cases} 1 & t < t_{0,i} \\ \exp\left(\frac{t_{0,i}-t}{\tau_{\parallel,1}}\right) & t_{0,i} \leq t < t_{\mathrm{ch}} + t_{0,i} \\ \exp\left(\frac{-t_{\mathrm{ch}}}{\tau_{\parallel,1}} + \frac{t_{\mathrm{ch}}+t_{0,i}-t}{\tau_{\parallel,2}}\right) & t \geq t_{\mathrm{ch}} + t_{0,i} \end{cases} \tag{5.33}$$

where $t_{\mathrm{ch}} = R_{\mathrm{ch}}/v_x$, and R_{ch} is the x-position at which the parallel drainage times change.

By substituting the above expression for $F_i(t)$ into equation (5.1), we follow the same steps up to equation (5.12) as in the single-filament GM model. The dual timescale model equivalent of equation (5.16) for the n-th order statistical moment is then given by

$$\{B(x,t)^n\} = \begin{cases} \frac{A_0 \exp\left(\frac{nx}{\delta_x}\right)}{\tau_w} \left[\int\limits_{X^{-1}(x)}^{t_{\mathrm{ch}}} \exp\left(-\frac{nt}{\tau_{\parallel,1}}\right) \exp\left(-\frac{nX(t)}{\delta_x}\right) \mathrm{d}t \right. \\ \quad \left. + \int\limits_{t_{\mathrm{ch}}}^{\infty} \exp\left(-\frac{nt_{\mathrm{ch}}}{\tau_{\parallel,1}} - \frac{n(t-t_{\mathrm{ch}})}{\tau_{\parallel,2}}\right) \exp\left(-\frac{nX(t)}{\delta_x}\right) \mathrm{d}t \right] & x < R_{\mathrm{ch}} \\ \frac{A_0^n \exp\left(\frac{nx}{\delta_x}\right)}{\tau_w} \int\limits_{X^{-1}(x)}^{\infty} \exp\left(-\frac{nt_{\mathrm{ch}}}{\tau_{\parallel,1}} - \frac{n(t-t_{\mathrm{ch}})}{\tau_{\parallel,2}}\right) \exp\left(-\frac{nX(t)}{\delta_x}\right) \mathrm{d}t & x \geq R_{\mathrm{ch}} \end{cases} \tag{5.34}$$

where the velocity is constant so that $X(t) = v_x t$ and $X^{-1}(x) = x/v_x$. This can be solved to give general equation

$$\{B(x,t)^n\} = \begin{cases} \frac{A_0^n}{n\tau_w} G_{\tau_1} \left[1 + \exp\left(\frac{n(x-R_{\mathrm{ch}})}{v_x \tau_{\parallel,1}} + \frac{n(x-R_{\mathrm{ch}})}{\delta_x}\right)\left(\frac{G_{\tau_2}}{G_{\tau_1}} - 1\right)\right] \exp\left(-\frac{nx}{v_x \tau_{\parallel,1}}\right) & x < R_{\mathrm{ch}} \\ \frac{A_0^n}{n\tau_w} G_{\tau_2} \exp\left(\frac{nR_{\mathrm{ch}}}{v_x \tau_{\parallel,2}}\left[1 - \frac{\tau_{\parallel,2}}{\tau_{\parallel,1}}\right]\right) \exp\left(-\frac{nx}{v_x \tau_{\parallel,2}}\right) & x \geq R_{\mathrm{ch}} \end{cases} \tag{5.35}$$

used to find the profile, relative fluctuation level, skewness, and kurtosis. G_{τ_i} is given by equation (5.18) with $\tau_\parallel$ swapped for $\tau_{\parallel,i}$. If $\tau_{\parallel,2} = \tau_{\parallel,1}$, then $G_{\tau_2}/G_{\tau_1} = 1$, and equation (5.35) returns to equation (5.21), as expected. To match the simulated profile to the experimental profile, the input variables that can be changed are R_{ch}, $\tau_{\parallel,1}$, and $\tau_{\parallel,2}$. These are changed to a precision of 1 mm, 1 µs, and 1 % of $\tau_{\parallel,1}$, respectively.

5.1.3.2 Single-filament dual velocity model

In this section, the single-filament GM model is extended by the introduction of a second radial velocity, so that the blobs undergo a velocity change at some position, R_{ch}, with a

constant $\tau_\parallel$ through all of the SOL. They therefore have a velocity of $v_{x,1}$ for $x < R_{\text{ch}}$ and velocity $v_{x,2}$ for $x \geq R_{\text{ch}}$. This changes the blob's position equation to be*

$$X(t) = \begin{cases} X_1(t) = \int_0^t v_{x,1}(t')\,\mathrm{d}t' & t < t_{\text{ch}} \\ X_2(t) = \int_0^{t_{\text{ch}}} v_{x,1}(t')\,\mathrm{d}t' + \int_{t_{\text{ch}}}^t v_{x,2}(t')\,\mathrm{d}t' & t \geq t_{\text{ch}} \end{cases} \tag{5.36}$$

where $t_{\text{ch}} = R_{\text{ch}}/v_{x,1}$, which makes $\int_0^{t_{\text{ch}}} v_{x,1}(t')\,\mathrm{d}t' = R_{\text{ch}}$.

$\{B(x,t)^n\}$ can again be calculated for the double velocity case with the original parallel drainage term, equation (5.3), substituting equation (5.36) in place for equation (5.2) and treating the two parts of the SOL separately. This gives us our starting equation as

$$\{B(x,t)^n\} = \begin{cases} \frac{A_0^n \exp\left(\frac{nx}{\delta_x}\right)}{\tau_w} \left[\int\limits_{\frac{x}{v_{x,1}}}^{t_{\text{ch}}} \exp\left(-\frac{nt}{\tau_\parallel}\right) \exp\left(-\frac{nX_1(t)}{\delta_x}\right) \mathrm{d}t \right. \\ \left. \quad + \int\limits_{t_{\text{ch}}}^{\infty} \exp\left(-\frac{nt}{\tau_\parallel}\right) \exp\left(-\frac{nX_2(t)}{\delta_x}\right) \mathrm{d}t \right] & x < R_{\text{ch}} \\ \frac{A_0^n \exp\left(\frac{nx}{\delta_x}\right)}{\tau_w} \int\limits_{t_{\text{ch}}+\frac{x-R_{\text{ch}}}{v_{x,2}}}^{\infty} \exp\left(-\frac{nt}{\tau_\parallel}\right) \exp\left(-\frac{nX_2(t)}{\delta_x}\right) \mathrm{d}t & x \geq R_{\text{ch}} \end{cases} \tag{5.37}$$

where equation (5.36) is solved to yield $X_1(t) = v_{x,1}t$ and $X_2(t) = R_{\text{ch}} + v_{x,2}(t - t_{\text{ch}})$ for constant velocities. The general equation for the radial statistical moments is then given by

$$\{B(x,t)^n\} = \begin{cases} \frac{A_0^n}{n\tau_w} G_{v_1} \left[1 + \exp\left(\frac{n(x-R_{\text{ch}})}{v_{x,1}\tau_\parallel} + \frac{n(x-R_{\text{ch}})}{\delta_x}\right)\left(\frac{G_{v_2}}{G_{v_1}} - 1\right)\right] \exp\left(-\frac{nx}{v_{x,1}\tau_\parallel}\right) & x < R_{\text{ch}} \\ \frac{A_0^n}{n\tau_w} G_{v_2} \exp\left(\frac{nR_{\text{ch}}}{v_{x,2}\tau_\parallel}\left[1 - \frac{v_{x,2}}{v_{x,1}}\right]\right) \exp\left(\frac{-nx}{v_{x,2}\tau_\parallel}\right) & x \geq R_{\text{ch}} \end{cases} \tag{5.38}$$

where G_{v_i} is given by equation (5.18) with v_x swapped for $v_{x,i}$. If $v_{x,2} = v_{x,1}$, then $G_{v_2}/G_{v_1} = 1$ and equation (5.38) returns to equation (5.21), just like the $\Delta\tau_\parallel$ model. Here, R_{ch} and $\tau_\parallel$ are again changed to 1 mm and 1 µs, respectively, the same precision as in section 5.1.3.1, but now $v_{x,2}$ is changed to within 1 % of $v_{x,1}$.

5.1.3.3 Single-filament finite acceleration model

Because of some of the results of the instantaneous dual velocity model, that we will go on to show in section 5.1.3.4, a gradual Δv_x model was implemented and tested. Here a

*The i subscript has been removed for legibility.

constant $\tau_\parallel$ is used across the SOL, and the filaments begin with velocity $v_{x,1}$, as before. In this model, there is a region in the SOL over which the filament undergoes a constant, and finite, acceleration, a_x, starting at $R_{\mathrm{ch},1}$ and ending at $R_{\mathrm{ch},2}$. This alters the equation for the filament position to

$$X(t) = \begin{cases} X_1(t) = \int_0^t v_{x,1}(t')\,\mathrm{d}t' & t < t_{\mathrm{ch},1} \\ X_2(t) = \int_0^{t_{\mathrm{ch},1}} v_{x,1}(t')\,\mathrm{d}t' + \int_{t_{\mathrm{ch},1}}^t \left(v_{x,1} + \int_{t_{\mathrm{ch},1}}^t a_x(t')\,\mathrm{d}t'\right)\mathrm{d}t' & t_{\mathrm{ch},1} \le t < t_{\mathrm{ch},2} \\ X_3(t) = \int_0^{t_{\mathrm{ch},1}} v_{x,1}(t')\,\mathrm{d}t' & \\ \quad + \int_{t_{\mathrm{ch},1}}^{t_{\mathrm{ch},2}} \left(v_{x,1} + \int_{t_{\mathrm{ch},1}}^t a_x(t')\,\mathrm{d}t'\right)\mathrm{d}t' + \int_{t_{\mathrm{ch},2}}^t v_{x,2}(t')\,\mathrm{d}t' & t \ge t_{\mathrm{ch},2} \end{cases} \tag{5.39}$$

where a_x is a constant acceleration between $t_{\mathrm{ch},1}$ and $t_{\mathrm{ch},2}$ and 0 for all other time. We prescribe a_x, $v_{x,1}$, $R_{\mathrm{ch},1}$, and $R_{\mathrm{ch},2}$, so other terms can be calculated before hand. As such, $t_{\mathrm{ch},1} = R_{\mathrm{ch},1}/v_{x,1}$ as previously, $v_{x,2} = \sqrt{v_{x,1}^2 + 2a_x(R_{\mathrm{ch},2} - R_{\mathrm{ch},1})}$, and $t_{\mathrm{ch},2} = \left(v_{x,2} - v_{x,1}\right)/a_x + t_{\mathrm{ch},1}$. As such, equation (5.39) can be simplified to $X_1(t) = v_{x,1}t$, $X_2(t) = v_{x,1}t + a_x(t - t_{\mathrm{ch},1})^2/2$, and $X_3(t) = R_{\mathrm{ch},2} + v_{x,2}(t - t_{\mathrm{ch},2})$.

In deriving an expression for the radial statistical moments, the SOL must be split into three regions using equation (5.39) for the filaments position. The n-th expectation value is then given by

$$\{B(x,t)^n\} = \begin{cases} \frac{A_0^n \exp\left(\frac{nx}{\delta_x}\right)}{\tau_w} \left[\int\limits_{\frac{x}{v_{x,1}}}^{t_{\mathrm{ch},1}} \exp\left(-\frac{nt}{\tau_\parallel}\right) \exp\left(-\frac{nX_1(t)}{\delta_x}\right) \mathrm{d}t \right. & \\ \quad + \int\limits_{t_{\mathrm{ch},1}}^{t_{\mathrm{ch},2}} \exp\left(-\frac{nt}{\tau_\parallel}\right) \exp\left(-\frac{nX_2(t)}{\delta_x}\right) \mathrm{d}t & \\ \quad \left. + \int\limits_{t_{\mathrm{ch},2}}^{\infty} \exp\left(-\frac{nt}{\tau_\parallel}\right) \exp\left(-\frac{nX_3(t)}{\delta_x}\right) \mathrm{d}t \right] & x < R_{\mathrm{ch}} \\ \frac{A_0^n \exp\left(\frac{nx}{\delta_x}\right)}{\tau_w} \left[\int\limits_{X_2^{-1}(x)}^{t_{\mathrm{ch},2}} \exp\left(-\frac{nt}{\tau_\parallel}\right) \exp\left(-\frac{nX_2(t)}{\delta_x}\right) \mathrm{d}t \right. & \\ \quad \left. + \int\limits_{t_{\mathrm{ch},2}}^{\infty} \exp\left(-\frac{nt}{\tau_\parallel}\right) \exp\left(-\frac{nX_3(t)}{\delta_x}\right) \mathrm{d}t \right] & R_{\mathrm{ch},1} \le x < R_{\mathrm{ch},2} \\ \frac{A_0^n \exp\left(\frac{nx}{\delta_x}\right)}{\tau_w} \int\limits_{t_{\mathrm{ch},2} + \frac{x - R_{\mathrm{ch},2}}{v_{x,2}}}^{\infty} \exp\left(-\frac{nt}{\tau_\parallel}\right) \exp\left(-\frac{nX_3(t)}{\delta_x}\right) \mathrm{d}t & x \ge R_{\mathrm{ch},2} \end{cases} \tag{5.40}$$

where the integral limit $X_2^{-1}(x)$ is the inverse function of $X_2(t)$ in equation (5.39), given by $t_{\mathrm{ch},1} + \left(\sqrt{v_{x,1}^2 + 2a_x(x - R_{\mathrm{ch},1})} - v_{x,1}\right)/a_x$.

This is solved to give the general form for the gradual Δv_x case as

$$\{B(x,t)^n\} = \begin{cases} \frac{A_0^n}{n\tau_w}\left\{G_{v_1}\left[1 - \exp\left(\frac{n(x-R_{\mathrm{ch},1})}{v_{x,1}\tau_\parallel} + \frac{n(x-R_{\mathrm{ch},1})}{\delta_x}\right)\right]\right. & \\ \quad \times \exp\left(-\frac{nx}{v_{x,1}\tau_\parallel}\right) + \sqrt{\frac{n\pi\delta_x}{2a_x}}E & \\ \quad \times \left[\mathrm{erf}\left(\sqrt{\frac{n}{2a_x\delta_x\tau_\parallel^2}}T_2\right) - \mathrm{erf}\left(\sqrt{\frac{n}{2a_x\delta_x\tau_\parallel^2}}T_1\right)\right] & \\ \quad \left. + G_{v_2}\exp\left(\frac{n(x-R_{\mathrm{ch},2})}{\delta_x} - \frac{nt_{\mathrm{ch},2}}{\tau_\parallel}\right)\right\} & x < R_{\mathrm{ch},1} \\ \frac{A_0^n}{n\tau_w}\left\{\sqrt{\frac{n\pi\delta_x}{2a_x}}E\right. & \\ \quad \times \left[\mathrm{erf}\left(\sqrt{\frac{n}{2a_x\delta_x\tau_\parallel^2}}T_2\right) - \mathrm{erf}\left(\sqrt{\frac{n}{2a_x\delta_x\tau_\parallel^2}}T_{X_2}\right)\right] & \\ \quad \left. + G_{v_2}\exp\left(\frac{n(x-R_{\mathrm{ch},2})}{\delta_x} - \frac{nt_{\mathrm{ch},2}}{\tau_\parallel}\right)\right\} & R_{\mathrm{ch},1} \le x < R_{\mathrm{ch},2} \\ \frac{A_0^n}{n\tau_w}G_{v_2}\exp\left(\frac{nR_{\mathrm{ch},2}}{v_{x,2}\tau_\parallel} - \frac{nt_{\mathrm{ch},2}}{\tau_\parallel}\right)\exp\left(-\frac{nx}{v_{x,2}\tau_\parallel}\right) & x \ge R_{\mathrm{ch},2} \end{cases} \tag{5.41}$$

where

$$E = \exp\left(\frac{n(a_x t_1\tau_\parallel - v_{x,1}\tau_\parallel - \delta_x)^2}{2a_x\delta_x\tau_\parallel^2} + \frac{n(2x - a_x t_1^2)}{2\delta_x}\right), \tag{5.42}$$

$T_1 = v_{x,1}\tau_\parallel + \delta_x$, $T_2 = a_x\tau_\parallel(t_{\mathrm{ch},2} - t_{\mathrm{ch},1}) + v_{x,1}\tau_\parallel + \delta_x$, and $T_{X_2} = a_x\tau_\parallel(X_2^{-1}(x) - t_{\mathrm{ch},2}) + v_{x,1}\tau_\parallel + \delta_x$. For this model, $R_{\mathrm{ch},1}$ and $R_{\mathrm{ch},2}$ are each changed to the nearest 1 mm, $\tau_\parallel$ is changed to within 1 µs, and a_x is changed to within 2 significant figures.

5.1.3.4 Adjusted single-filament model results

The dual timescale model was applied to the H-mode single blob base case with parameters $R_{\mathrm{ch}} = 34\,\mathrm{mm}$, $\tau_{\parallel,1} = 71\,\mu\mathrm{s}$, and $\tau_{\parallel,2} = 19\,\mu\mathrm{s} \approx 0.27\tau_{\parallel,1}$, and the L-mode single blob case with $R_{\mathrm{ch}} = 28\,\mathrm{mm}$, $\tau_{\parallel,1} = 36\,\mu\mathrm{s}$, and $\tau_{\parallel,2} = 66\,\mu\mathrm{s} \approx 1.83\tau_{\parallel,1}$, both with the Heaviside waveform. This can be seen in figures 5.10a and 5.11a. The evaluations from equation (5.35) are included as blue circles, and the simulated profiles are shown with solid blue lines, with the fit parameters in table 5.8. The prediction of the model is found to accurately predict the simulated profiles in both cases, and agrees with the general conclusion of section 5.1.1 - namely that in order for the far SOL to decrease the parallel timescale must decrease

($\tau_{\parallel,2} < \tau_{\parallel,1}$) and *vice versa*.

Next, we notice the R_{ch} position used in the simulations is set about 3.5 mm and 5 mm further than the x_0 position of the profile fit for each of the two discharges. This is likely an artefact of how the position of the blob with the Heaviside approximation is calculated, as explored in section 5.1.2. When changing for the double exponential or Gaussian waveform, then the R_{ch} moves closer to the x_0 fit, becoming 31 mm and 30 mm, respectively, as the defined positions of these waveforms moves towards the centre-of-mass position. The $\tau_{\parallel}$ parameters also decrease slightly with these two waveforms, but each is less than 10 % and doesn't affect the qualitative outcome of the results.

The simulated profiles for the H-mode and L-mode profiles are shown as an orange solid line in figures 5.10b and 5.11b, respectively, with the fit parameters for the profiles displayed in table 5.8. Here, the simulation parameters required were $\tau_{\parallel} = 52\,\mu\text{s}$, $R_{\text{ch}} = 30\,\text{mm}$, and $v_{x,2} = 0.37 v_{x,1} \approx 98.2\,\text{m/s}$ for the decreasing decay length profile, and $\tau_{\parallel} = 45\,\mu\text{s}$, $R_{\text{ch}} = 21\,\text{mm}$, and $v_{x,2} = 1.42 v_{x,1} \approx 602\,\text{m/s}$ for the increasing decay length profile. Here R_{ch} was set a few mm in-front of the x_0 position of the profile, opposite to the dual parallel timescale scenario, but we still see the same dependence on the decay length with the radial velocity, namely that a decreased velocity can reduce the decay length past the R_{ch} position, and an increased velocity can increase the decay length.

If we look at how the profile shape is altered, we see a deviation from an exponential up to x_0 in both examples. When the velocity decreases, the near SOL decay length starts to increase as we approach R_{ch}. As such a smaller $\tau_{\parallel}$, compared to a single exponential with one velocity with this decay length, is required. This is caused by the relative increase in the signal contribution from filaments that have slowed down since passing the R_{ch} position. As their velocity has decreased, they are at a smaller x position for a given t', and hence for a given amplitude. In some cases, if the ratio of $v_{x,2}/v_{x,1}$ is too small this flattening can increase so much as to give an increase of density profile with increasing x in the middle of the SOL, which has never been recorded in experiment. This could be exacerbated by the instantaneous change in the filaments' velocities, which would require some instantaneous and infinite force to act on them. An attempt to alleviate this issue slightly is explored later in this section. In the opposite situation where the decay length increases in the far SOL, necessitating an increasing filament velocity, the near decay length now decreases as it approaches x_0, and a comparatively larger $\tau_{\parallel}$ is required in this part of the SOL.

The estimations for the dual velocity model from equation (5.38) have been added to figures 5.10b and 5.11b as orange triangles, and accurately follow the simulations' profiles, even accurately recreating the small increase before R_{ch} in the decreasing decay length example. This can be explicitly seen in equation (5.38). For example, in the case of a decreasing profile decay length, $v_{x,1} > v_{x,2}$, and therefore the ratio $G_{v_2}/G_{v_1} > 1$. As such, the coefficient in front of the first exponential term is positive, leading to an addition of the profile as a function of x up to R_{ch} when compared to the single velocity / decay length example.

The simulated profiles for the finite acceleration H-mode and L-mode experiments are added to figures 5.10c and 5.11c, respectively, as solid green lines green line, with the fit parameters included in table 5.8. The H-mode profile used $\tau_{\parallel} = 57\,\mu\text{s}$, $R_{\text{ch},1} = 13\,\text{mm}$, $R_{\text{ch},2} = 34\,\text{mm}$, and $a_x = -1.5 \times 10^6\,\text{m/s/s}$ (which gives $v_{x,2} = 86.2\,\text{m/s} \approx 0.32 v_{x,1}$), and the L-mode profile required $\tau_{\parallel} = 44\,\mu\text{s}$, $R_{\text{ch},1} = 12\,\text{mm}$, $R_{\text{ch},2} = 32\,\text{mm}$, and $a_x = 6.7 \times 10^6\,\text{m/s/s}$ (so $v_{x,2} = 669\,\text{m/s} \approx 1.58 v_{x,1}$). In each case, the simulated near SOL profile is brought closer to an exponential. This is particularly important in the H-mode profile, with a decreasing far SOL decay length. The ratio between $v_{x,2}$ and $v_{x,1}$ can now be reduced further, without the profile in front of R_{ch} increasing too much, by increasing the distance over which the filaments decelerate. Again, as with the instant Δv_x case, the reduction of the velocity produces a reduced decay length, and *vice versa*.

The estimates for the finite acceleration model from equation (5.41) are also included in figures 5.10c and 5.11c as green squares and accurately predict the simulated profiles. Whilst this form of the equations in this model are more complicated than the instantaneous Δv_x model equivalent of equation (5.38), it does help to match the near SOL profile shape more accurately, particular in the H-mode example.

For each of the three cases we study the higher order moments of each of these signals, starting with the H-mode base case, with the decreasing decay length, shown in figure 5.12. For the dual $\tau_{\parallel}$ case, each of the higher order profiles increases with distance into the SOL up to R_{ch}, after which they are a constant value. Conversely, the profiles decrease for both changing velocity cases, up to R_{ch} where they are again constant. In each case, the values of the radial statistics match closely to those predicted by the model, which are included in the figure. The gradual change of the profiles up to the flatter far SOL region is due to the finite extent of the blob. The model accurately predicts the rise/decline of the statistic

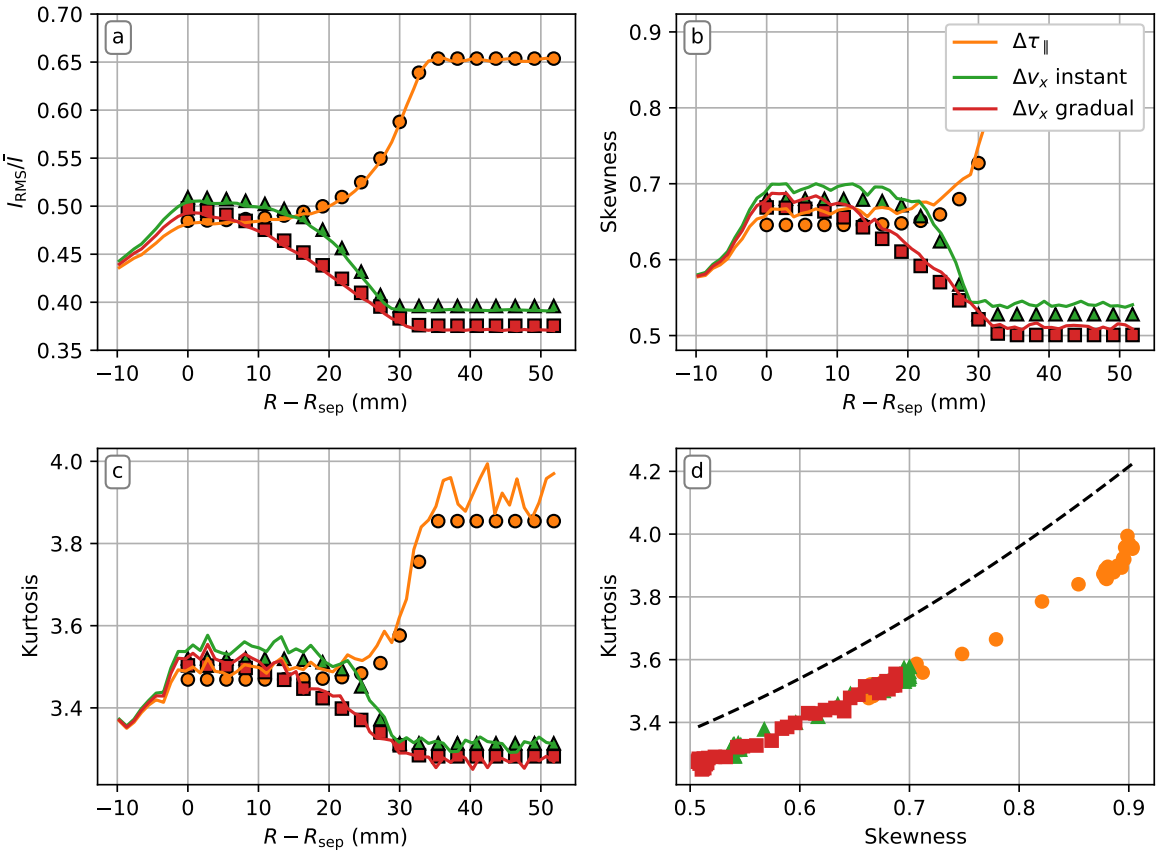

Figure 5.12: Profiles in the simulated SOL for the 1D single blob case (solid lines) for shot # 36342, $t \in [2.5, 2.7]$s for: the relative fluctuation levels (a); skewness (b); and kurtosis (c). The values of kurtosis against skewness are shown (d) with the theoretical $K = 3S^2/2 + 3$ relation added (black dashed). The expected values derived from the model are included as symbols in (a–c).

with distance into the SOL with the inclusion of the first exponential term inside equations (5.34), (5.37) and (5.41) (as well as the weak x dependence in the T_{X_2} term in the latter). It also captures the flat far SOL statistic for each case, as all x dependence cancels out in this region without the inclusion of filament velocity distributions.

Whilst the increase of the higher order statistics profiles in the near SOL, caused by the dual parallel timescale model with $\tau_{\parallel,2} < \tau_{\parallel,1}$, gives the trend seen in the experimental results reported in section 4.4.2.1, the flat part of the profiles in the far SOL does not match this trend. This is even worse for the case where a decreasing velocity is used, as a decrease in relative fluctuation level, skewness, and kurtosis is not observed experimentally. It is difficult to tell what the behaviour of the higher order statistical profiles will be from the equations for $\{B^n\}$ in the regions $x < R_{\text{ch}}$ ($x < R_{\text{ch},2}$ for the gradual Δv_x case), as the terms in the

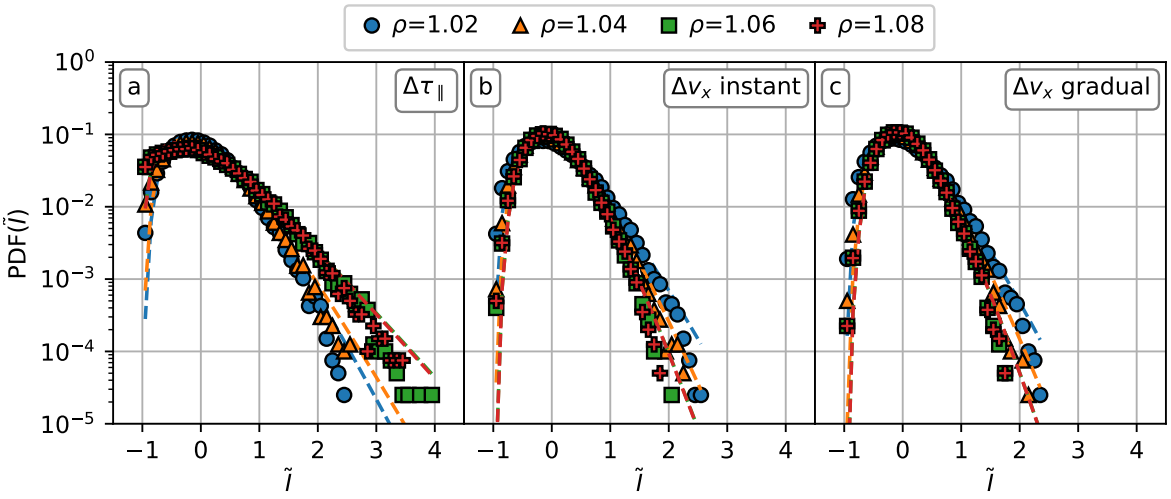

Figure 5.13: Probability distribution functions for different single locations in the SOL for the 1D single blob case (coloured markers) for shot # 36342, $t \in [2.5, 2.7]$s. The Gamma functions calculated from the input parameters, k and θ, are included (dashed lines). The ρ positions are at $R - R_{\text{sep}} = [11, 24, 36, 49]$mm.

equation do not cancel to give elegant expressions. However, for the far SOL region, $x > R_{\text{ch}}$ ($R_{\text{ch},2}$), they do. For example, for the $\Delta\tau_{\parallel}$ case in the far SOL, using equation (5.35) with $n = 2$, 3, and 4 to obtain expressions for the skewness and kurtosis where $x \geq R_{\text{ch}}$ are $2\sqrt{2}\tau_w/3G_{\tau_2}$ and τ_w/G_{τ_2}, respectively, with no variation in or dependence on x. This gives the flat $K = 9/8S^2$ scaling recovered in section 5.1.1, seen in figure 5.12d, rather than the experimentally measured $3S^2/2$. We can again conclude that the single blob case is unable to correctly reconstruct the experimentally measured statistics in the SOL.

We can also tentatively make the assumption that a decrease in the velocity is unlikely to be the cause of the deviation from an exponential profile when the far SOL decay length decreases, due to the adverse effect this has on the statistical profiles, and instead *is most likely caused by a decrease in the parallel timescales.* It is also noted that here, changing from the Heaviside approximation to the Gaussian waveform of the 1D blob alters the effect of the radial profiles for the dual $\tau_{\parallel}$ case. Rather than the increase in each of the moments, the symmetry of the blob shape means here we do not see an increase in any of the higher order moments, even though the mean (profile) still decreases for $x > R_{\text{ch}}$. The relative fluctuation level remains approximately equal, and the skewness and kurtosis both decrease slightly. This is explored in further detail in the 2D case, section 5.2.4 which uses a 2D Gaussian for the blobs' waveforms.

We also study the single point PDFs for each of the three single-blob cases described in

Table 5.9: A table showing the shape (k) and scale (θ) input parameters (from the 5 MW H-mode discharge # 36342, $t \in [2.5, 2.7]$s) for the Gamma distribution functions for different locations in the SOL for three 1D single blob case simulations with radial variation in $\tau_{\|}$ or v_x. The PDFs are shown in figure 5.13.

ρ	1.02		1.04		1.06		1.08	
Simulation type	k	θ	k	θ	k	θ	k	θ
$\Delta\tau_{\|}$	4.23	0.236	3.76	0.266	2.34	0.428	2.36	0.424
Δv_x instant	4.02	0.249	5.27	0.190	6.51	0.154	6.53	0.153
Δv_x gradual	4.51	0.222	5.97	0.168	7.27	0.138	7.28	0.137

table 5.9, which also gives the Gamma input parameters. The single point PDFs are shown in figure 5.13. As we now have radial variation in either $\tau_{\|}$ or v_x, the PDFs are no longer identical and retain some variation with distance into the SOL. However, as with the relative fluctuation levels, which we have shown the Gamma PDFs to follow, it is only the dual $\tau_{\|}$ case that results in Gamma distributions deviating further from normal distributions with distance into the SOL, in agreement with experimental results as k decreases with distance into the scrape-off layer. This lends further evidence towards a decrease in filament velocity not being the cause of the change in profile shape in this single blob case, but instead is caused by a decrease in the parallel timescale, consistent with the experimental results from Wynn *et al.* [77]. It is also noted that as the $\rho = 1.06$ and $\rho = 1.08$ positions are at a radius larger than R_{ch} in all cases, the PDFs at these two locations are almost identical in the single blob case.

A similar analysis was performed using the measurements from the L-mode discharge # 36344. The radial profiles for the higher order moments for each simulation type in the 1D single blob case using the L-mode parameters are also evaluated and displayed in figure 5.14. Each profile shows the opposite behaviour in the far SOL now the second decay length has increase, with each moment decreasing for the increased $\tau_{\|}$ case, and decreasing for the increased v_x cases. Each profile is flat throughout the far SOL where $x \geq R_{\text{ch}}$, and each falls short of the $K = 3S^2/2$ scaling expected for Gamma distributed signals, showing how the single blob case is unable to accurately recreate experimental signals and requires the velocity distribution and amplitude distribution to correct these shortcomings. In the single blob model however, we might conclude that in this case, the flattening of the far SOL profile cannot be caused by an increase in the parallel timescale, as this causes an uncharacteristic

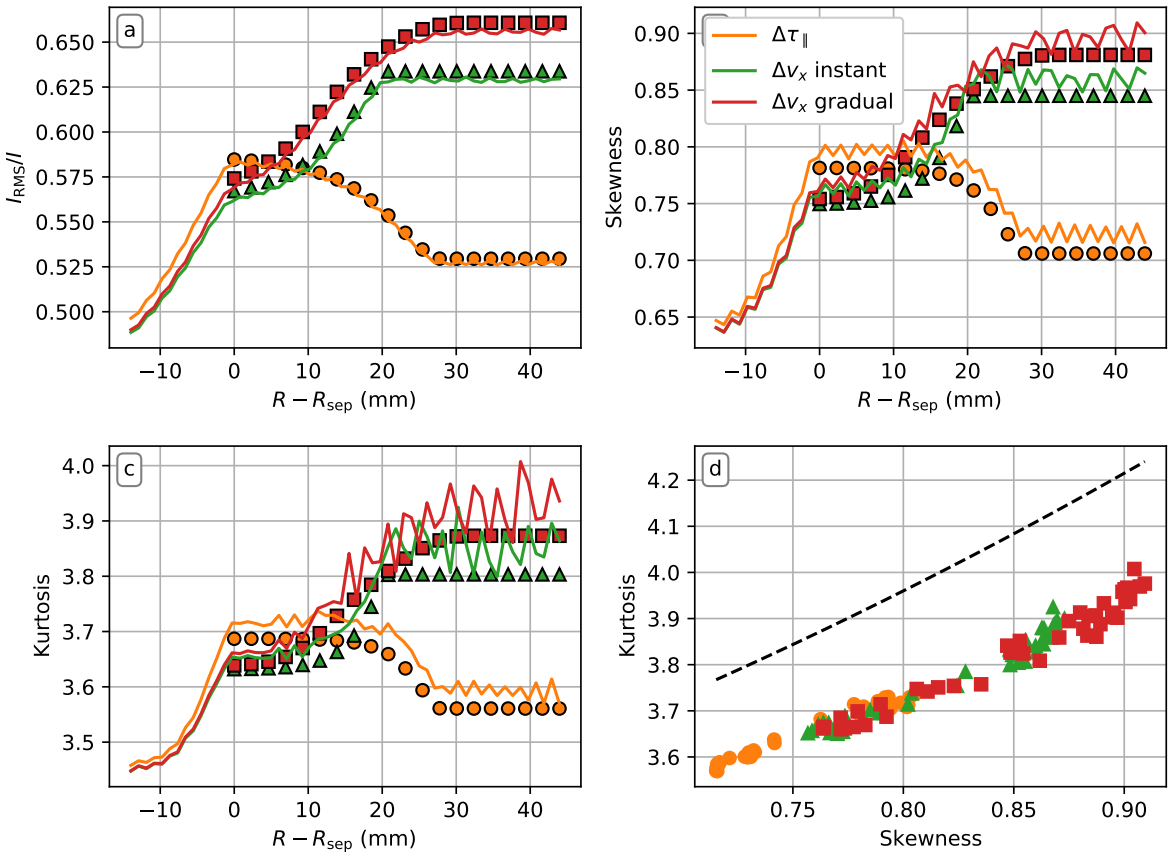

Figure 5.14: Profiles in the simulated SOL for the 1D single blob case (solid lines) for shot # 36344, $t \in [2.5, 2.7]$s for: the relative fluctuation levels (a); skewness (b); and kurtosis (c). The values of kurtosis against skewness are shown (d) with the theoretical $K = 3S^2/2 + 3$ relation added (black dashed). The expected values derived from the model are included as symbols in (a–c).

decrease in the higher order statistical moments, but an increase in the radial velocity could be the cause, as this also causes the moments to increase with distance into the scrape-off layer.

The radial behaviour of the statistics is also reflected in the single point PDFs, figure 5.15, with the input parameters shown in table 5.10. Firstly, we note how all the PDFs show a more intermittent and flattened profile shape than in figure 5.13 due to the relative decrease in k and increase in θ, likely due to the relative decrease in the duration time of the filaments, τ_d, which is proportional to the filaments' size and inversely proportional to the velocity (τ_w was kept constant at 10 µs between all 1D simulations). Whilst the PDFs appear more flattened than compared with experimental results, this can be tweaked by changing τ_w, which has no effect on any of the radial profile shapes, only their absolute

Table 5.10: A table showing the shape (k) and scale (θ) input parameters (from the L-mode discharge # 36344) for the Gamma distribution functions for different locations in the SOL for three 1D single blob case simulations with radial variation in $\tau_{\parallel}$ or v_x. The PDFs are shown in figure 5.15.

ρ	1.02		1.04		1.06	
Simulation type	k	θ	k	θ	k	θ
$\Delta\tau_{\parallel}$	3.08	0.324	3.61	0.277	3.61	0.277
Δv_x instant	2.81	0.356	2.53	0.395	2.52	0.396
Δv_x gradual	2.61	0.383	2.33	0.428	2.32	0.431

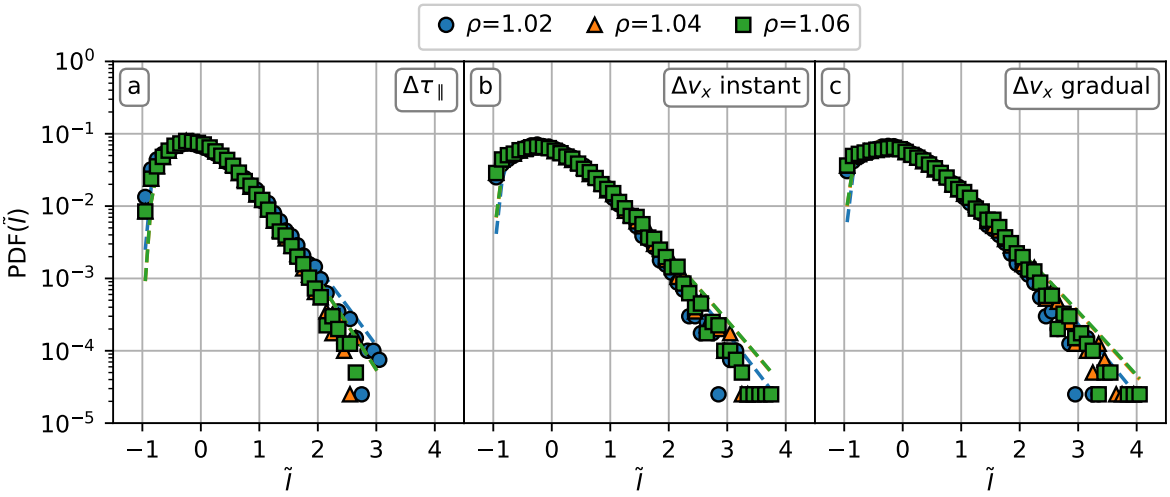

Figure 5.15: Probability distribution functions for different single locations in the SOL for the 1D single blob case (coloured markers) for shot # 36344, $t \in [2.5, 2.7]$s. The Gamma functions calculated from the input parameters, k and θ, are included (dashed lines). The ρ positions are at $R - R_{\text{sep}} = [14, 29, 43]$mm.

values. Whether this assumption holds in experiment due to larger filament numbers that this would produce in the scrape-off layer, which in turn alters the amount of plasma-wall interaction, or plasma-neutral recycling, for example, is out of the scope of this model.

Next, the changing velocity cases show a flattening of the PDFs for higher radial positions reflecting the increase in the relative fluctuation levels, contrasted with the decreasing relative fluctuation level in the dual $\tau_{\parallel}$ case, which results in the flatter PDFs at lower radial positions. This further shows how, in the single blob case, an increased density profile decay length cannot be caused by an increase in parallel timescales alone.

Table 5.11: A table showing the fit parameters for the base case non-exponential experimental profiles, and the profiles generated in the 1D independent blob case using the Heaviside approximation. For the 5 MW H-mode discharge, when $x = 31\,\text{mm}$, $\rho \approx 1.052$, and $x = 23\,\text{mm}$, $\rho \approx 1.032$ in the L-mode discharge.

Profile type		x_0 (mm)	L_1 (mm)	L_2 (mm)
H-mode	Experimental	30.76 ± 0.89	17.1 ± 1.2	5.11 ± 0.20
	$\Delta\tau_{\|\|}$	30.58 ± 0.37	17.17 ± 0.53	5.116 ± 0.080
	Δv_x instant	30.97 ± 0.98	17.0 ± 1.3	5.16 ± 0.22
	Δv_x gradual	30.20 ± 0.92	17.6 ± 1.4	5.12 ± 0.20
L-mode	Experimental	23.15 ± 0.32	15.888 ± 0.087	27.49 ± 0.59
	$\Delta\tau_{\|\|}$	21.86 ± 0.58	16.01 ± 0.21	27.97 ± 0.67
	Δv_x instant	23.21 ± 0.28	16.035 ± 0.092	27.57 ± 0.33
	Δv_x gradual	23.51 ± 0.41	15.89 ± 0.13	27.39 ± 0.49

5.1.4 Adjusted distributed-filament models

In this section, we re-introduce the distributed filament attributes to the simulations for the same non-exponential profiles as in section 5.1.3. The input parameters to the relevant distributions for the independent blob case are given in table 5.2. Again, it was tested adding in each filament attribute distribution independently, and the same conclusion as the one in section 5.1.2 was reached; namely that introducing distributions for the radial size and amplitude did not change the normalised profile outside the error of the fits. It was also seen again that the normalised profile did not change between adding in the radial velocity distribution in isolation when compared with adding in all three filament attribute distributions independent to one another. Finally, the difference between the profiles in the dependent and independent cases were also within error of the fit. As such, only the experimental profile and the results from the independent blob case with all three filament attributes randomly drawn from distributions are included in this section, for both double decay length discharge examples (5 MW H-mode # 36344 and L-mode # 36342). The fit parameters for the simulated profiles in each of the models in this section are shown in table 5.11.

In order to derive the equations for the radial profile and higher order statistics, we take the same approach as in section 5.1.2. Including the radial diameter distribution doesn't change the form of the equations for $\{B(x,t)^n\}$, the exponentially distributed filament amplitudes requires the result of equation (5.26) to be included, and including the radial velocity

distribution introduces the sum over the relevant velocities and the equation for the lognormal distribution, equation (4.14).

5.1.4.1 Distributed-filament dual timescale model

For the distributed-filament dual timescale model, we start with equation (5.34), and get

$$\{B(x,t)^n\} = \begin{cases} \frac{A_0^n(n-1)!}{\tau_w} \sum_{v_{x,\min}}^{v_{x,\max}} \frac{1}{v_x\sqrt{2\pi}\sigma_{v_x}} \exp\left(-\frac{\ln\left(\frac{v_x}{\alpha_{v_x}}\right)^2}{2\sigma_{v_x}^2}\right) G_{\tau_1} \\ \quad \times \left[1 + \exp\left(\frac{n(x-R_{\rm ch})}{v_x\tau_{\parallel,1}} + \frac{n(x-R_{\rm ch})}{\delta_x}\right)\left(\frac{G_{\tau_2}}{G_{\tau_1}} - 1\right)\right] \exp\left(-\frac{nx}{v_x\tau_{\parallel,1}}\right) & x < R_{\rm ch} \\ \frac{A_0^n(n-1)!}{\tau_w} \sum_{v_{x,\min}}^{v_{x,\max}} \frac{1}{v_x\sqrt{2\pi}\sigma_{v_x}} \exp\left(-\frac{\ln\left(\frac{v_{x,1}}{\alpha_{v_x}}\right)^2}{2\sigma_{v_x}^2}\right) G_{\tau_2} \\ \quad \times \exp\left(\frac{nR_{\rm ch}}{v_x\tau_{\parallel,2}}\left[1 - \frac{\tau_{\parallel,2}}{\tau_{\parallel,1}}\right]\right) \exp\left(-\frac{nx}{v_x\tau_{\parallel,2}}\right) & x \geq R_{\rm ch} \end{cases} \tag{5.43}$$

for n-th order expectation value of the profiles. The input variables to the simulations are $R_{\rm ch}$, $\tau_{\parallel,1}$ and $\tau_{\parallel,2}$, varied to the nearest 1 mm, 1 µs, and 1 % of $\tau_{\parallel,1}$.

5.1.4.2 Distributed-filament dual velocity model

For the distributed filament dual velocity model, the starting equation of (5.37) for the single-filament equivalent is used. Including the changes for the amplitude and velocity distributions gives

$$\{B(x,t)^n\} = \begin{cases} \frac{A_0^n(n-1)!}{\tau_w} \sum_{v_{x,1,\min}}^{v_{x,1,\max}} \frac{1}{v_{x,1}\sqrt{2\pi}\sigma_{v_x}} \exp\left(-\frac{\ln\left(\frac{v_{x,1}}{\alpha_{v_x}}\right)^2}{2\sigma_{v_x}^2}\right) G_{v_1} \\ \quad \times \left[1 + \exp\left(\frac{n(x-R_{\rm ch})}{v_{x,1}\tau_{\parallel}} + \frac{n(x-R_{\rm ch})}{\delta_x}\right)\left(\frac{G_{v_2}}{G_{v_1}} - 1\right)\right] \exp\left(-\frac{nx}{v_{x,1}\tau_{\parallel}}\right) & x < R_{\rm ch} \\ \frac{A_0^n(n-1)!}{\tau_w} \sum_{v_{x,1,\min}}^{v_{x,1,\max}} \frac{1}{v_{x,1}\sqrt{2\pi}\sigma_{v_x}} \exp\left(-\frac{\ln\left(\frac{v_{x,1}}{\alpha_{v_x}}\right)^2}{2\sigma_{v_x}^2}\right) G_{v_1} \\ \quad \times \exp\left(\frac{nR_{\rm ch}}{v_{x,2}\tau_{\parallel}}\left[1 - \frac{v_{x,2}}{v_{x,1}}\right]\right) \exp\left(-\frac{nx}{v_{x,2}\tau_{\parallel}}\right). & x \geq R_{\rm ch} \end{cases} \tag{5.44}$$

In these simulations, the input variables are $R_{\rm ch}$, $\tau_{\parallel}$, and $v_{x,2}$, changed to within 1 mm, 1 µs, and 1 % of $v_{x,1}$, respectively.

5.1.4.3 Distributed-filament finite acceleration model

For the last 1D simulation type, the expression for the distributed-filament finite acceleration model is given by taking the result of the single-filament analogue, equation (5.41). The result is given by

$$\{B(x,t)^n\} = \begin{cases} \frac{A_0^n(n-1)!}{\tau_w} \sum_{v_{x,1,\min}}^{v_{x,1,\max}} \frac{1}{v_{x,1}\sqrt{2\pi}\sigma_{v_x}} \exp\left(-\frac{\ln\left(\frac{v_{x,1}}{\alpha_{v_x}}\right)^2}{2\sigma_{v_x}^2}\right) \{G_{v,1} \\ \quad \times \left[1 - \exp\left(\frac{n(x-R_{\mathrm{ch},1})}{v_{x,1}\tau_\parallel} + \frac{n(x-R_{\mathrm{ch},1})}{\delta_x}\right)\right] \exp\left(-\frac{nx}{v_{x,1},\tau_\parallel}\right) \\ \quad + \sqrt{\frac{n\pi\delta_x}{2a_x}} E \left[\mathrm{erf}\left(\sqrt{\frac{n}{2a_x\delta_x\tau_\parallel^2}} T_2\right) - \mathrm{erf}\left(\sqrt{\frac{n}{2a_x\delta_x\tau_\parallel^2}} T_1\right)\right] \\ \quad + G_{v_2} \exp\left(\frac{n(x-R_{\mathrm{ch},2})}{\delta_x} - \frac{nt_{\mathrm{ch},2}}{\tau_\parallel}\right)\Big\} & x < R_{\mathrm{ch},1} \\ \frac{A_0^n(n-1)!}{\tau_w} \sum_{v_{x,1,\min}}^{v_{x,1,\max}} \frac{1}{v_{x,1}\sqrt{2\pi}\sigma_{v_x}} \exp\left(-\frac{\ln\left(\frac{v_{x,1}}{\alpha_{v_x}}\right)^2}{2\sigma_{v_x}^2}\right) \Big\{E\sqrt{\frac{n\pi\delta_x}{2a_x}} \\ \quad \times \left[\mathrm{erf}\left(\sqrt{\frac{n}{2a_x\delta_x\tau_\parallel^2}} T_2\right) - \mathrm{erf}\left(\sqrt{\frac{n}{2a_x\delta_x\tau_\parallel^2}} T_{X_2}\right)\right] \\ \quad + G_{v_2} \exp\left(\frac{n(x-R_{\mathrm{ch},2})}{\delta_x} - \frac{nt_{\mathrm{ch},2}}{\tau_\parallel}\right)\Big\} & R_{\mathrm{ch},1} \le x < R_{\mathrm{ch},2} \\ \frac{A_0^n(n-1)!}{\tau_w} \sum_{v_{x,1,\min}}^{v_{x,1,\max}} \frac{1}{v_{x,1}\sqrt{2\pi}\sigma_{v_x}} \exp\left(-\frac{\ln\left(\frac{v_{x,1}}{\alpha_{v_x}}\right)^2}{2\sigma_{v_x}^2}\right) G_{v_2} \\ \quad \times \exp\left(\frac{nR_{\mathrm{ch},2}}{v_{x,2}\tau_\parallel} - \frac{nt_{\mathrm{ch},2}}{\tau_\parallel}\right) \exp\left(-\frac{nx}{v_{x,2}\tau_\parallel}\right) & x \ge R_{\mathrm{ch},2} \end{cases} \tag{5.45}$$

for $a_x > 0$, where where E is given by equation (5.42), and T_1, T_2, and T_{X_2} are as defined in section 5.1.3.3. In this model, $R_{\mathrm{ch},1}$ and $R_{\mathrm{ch},2}$ are each changed to the nearest 1 mm, $\tau_\parallel$ is changed to within 1 µs, and a_x is changed to within 2 significant figures.

Equation (5.45) is only defined for positive accelerations. In the case of $a_x < 0$, the scenario had to be changed slightly. In the single-filament finite acceleration case, it was simple to calculate what the final velocity would be for all the filaments once they had undergone acceleration a_x through a displacement $R_{\mathrm{ch},2} - R_{\mathrm{ch},1}$. Now that a distribution of velocities is included, some filaments would undergo a direction change if their starting velocity was sufficiently low, causing them to change direction and propagate back towards the separatrix, which has never been seen in experiments performed in the low-field side scrape-off layer. Rather than place a minimum radial velocity, $v_{x,\min}$, of zero which would cause slower blobs to stop at some position in the SOL, a minimum velocity of $v_{x,\min} = 0.1v_{x,1}$

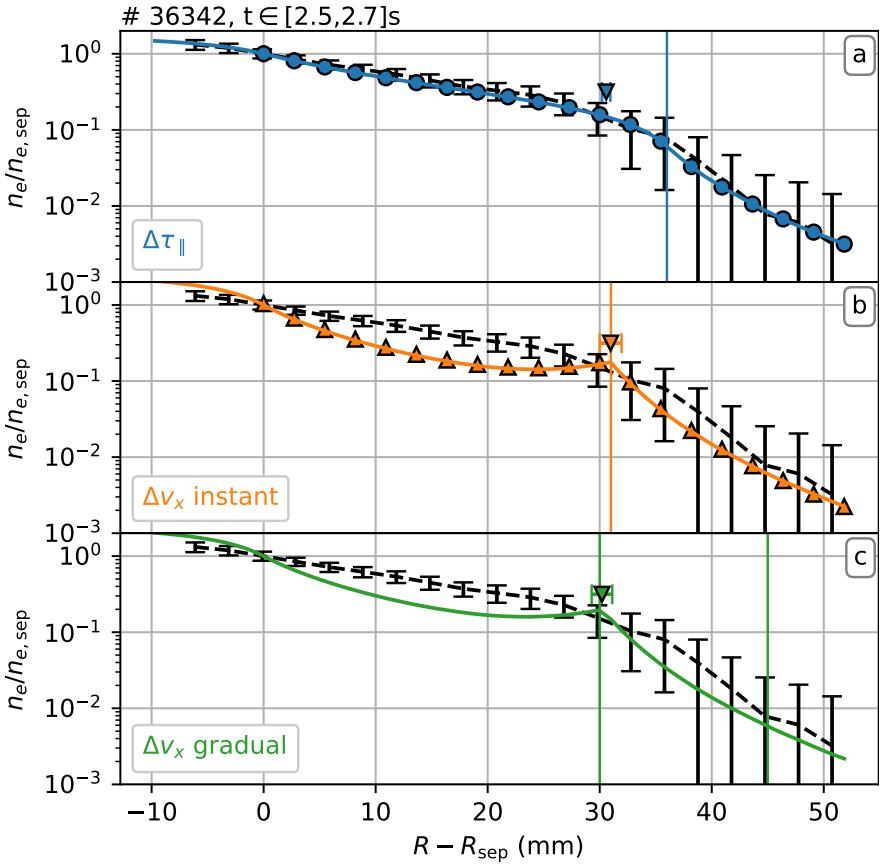

Figure 5.16: Electron density profile for the 5 MW H-mode discharge # 36342 (black dashed). Three simulation profiles from the 1D independent blob case are included: changing $\tau_\parallel$ (a, blue); instantaneously changing v_x (orange); and gradually changing v_x (green). The x_0 parameters (coloured triangles), R_{ch} values (coloured vertical lines), and the outputs from the statistical framework (coloured shapes) are included.

is used instead so that all filaments continue to propagate with some small, finite velocity. This means that an analytical expression for the statistical moments cannot be found when $a_x < 0$.

5.1.4.4 Adjusted distributed-filament model results

The simulated profiles for the 5 MW H-mode discharge with the decreasing profile decay legnth are shown in figure 5.16 with the fit parameters in table 5.11. For the dual $\tau_\parallel$ case $\tau_{\parallel,1} = 110\,\mu\mathrm{s}$, $\tau_{\parallel,2} = 10\,\mu\mathrm{s} \approx 0.091\tau_{\parallel,1}$, and $R_{\mathrm{ch}} = 36\,\mathrm{mm}$. For the instantly changing velocity case, $\tau_\parallel = 43\,\mu\mathrm{s}$, $v_{x,2} = 0.12v_{x,1}$, and $R_{\mathrm{ch}} = 31\,\mathrm{mm}$. For the gradually changing velocity scenario, the acceleration used was $a_x = -4 \times 10^8\,\mathrm{m/s/s}$ between $R_{\mathrm{ch},1} = 30\,\mathrm{mm}$ and $R_{\mathrm{ch},2} = 45\,\mathrm{mm}$, and $\tau_\parallel = 45\,\mu\mathrm{s}$.

We find that the overall result of the single blob case applies once the filament distributions are introduced. This is that a reduction in either $\tau_{\|}$ or v_x is required at some point in the SOL to counter the natural flattening of the profiles caused by the introduction of the velocity distribution, as well as a longer $\tau_{\|}$ required. Of the three profiles, the one from the $\Delta\tau_{\|}$ case matches the experimental profiles more closely than either of the Δv_x cases. By using two $\tau_{\|}$ values in the SOL, the simulated profile in the independent blob case can again be matched to the experimental one closely, especially in the near SOL where the flattening effect from the introduction of the radial velocity, seen in section 5.1.2, is balanced by the decreasing effect up to R_{ch} caused by the decrease in $\tau_{\|}$. In the far SOL, the flattening caused by the velocity distribution is more pronounced, with no third timescale to counter it.

In the distributed filament dual velocity case, the reduction in velocity was larger than in the single blob case and the natural profile flattening was more pronounced, leading to a rise in the profiles just before the x_0 position. For a reduction in $\tau_{\|}$, such as through a reduction in the connection length, this does not happen, although the natural flattening in the far SOL profile can be seen here. For the changing velocity cases, the second velocity and velocity distribution reinforce one another in the profile before x_0. The only way to recreate the much shorter decay length in the far SOL is to have a large reduction in velocity, which results in a more increased flattening in the near SOL, and here even an increase in the profile just before x_0. This is not a feature seen in experimental profiles, and as such we would conclude that such a large reduction of filament velocity is unlikely to be the cause of the profile decay length decrease. A gradually changing velocity was not able to reduce the flattening effect, as it did in section 5.1.2, due to the large reduction in velocity required by the large decrease in decay length. With the specific acceleration, velocity distribution, and displacement over which the acceleration is applied, only filaments with a $v_{x,1} \gtrapprox 3482\,\text{m/s}$ finish with $v_{x,2} > 0.1 v_{x,1}$, which, for the given log-normal distribution of velocities, is $\approx 0.05\,\%$. From these observations, it is unlikely that a velocity reduction of the filaments is responsible for causing such a large decrease in the plasma density profile in the far SOL, and is more likely caused by the reduction in the parallel timescale.

Studying the higher order statistical moments, figure 5.17 we now see that each of the profiles rise with increasing distance into the SOL for each of the simulation types with the introduction of the velocity distributions. We also see that each of the simulations now follows

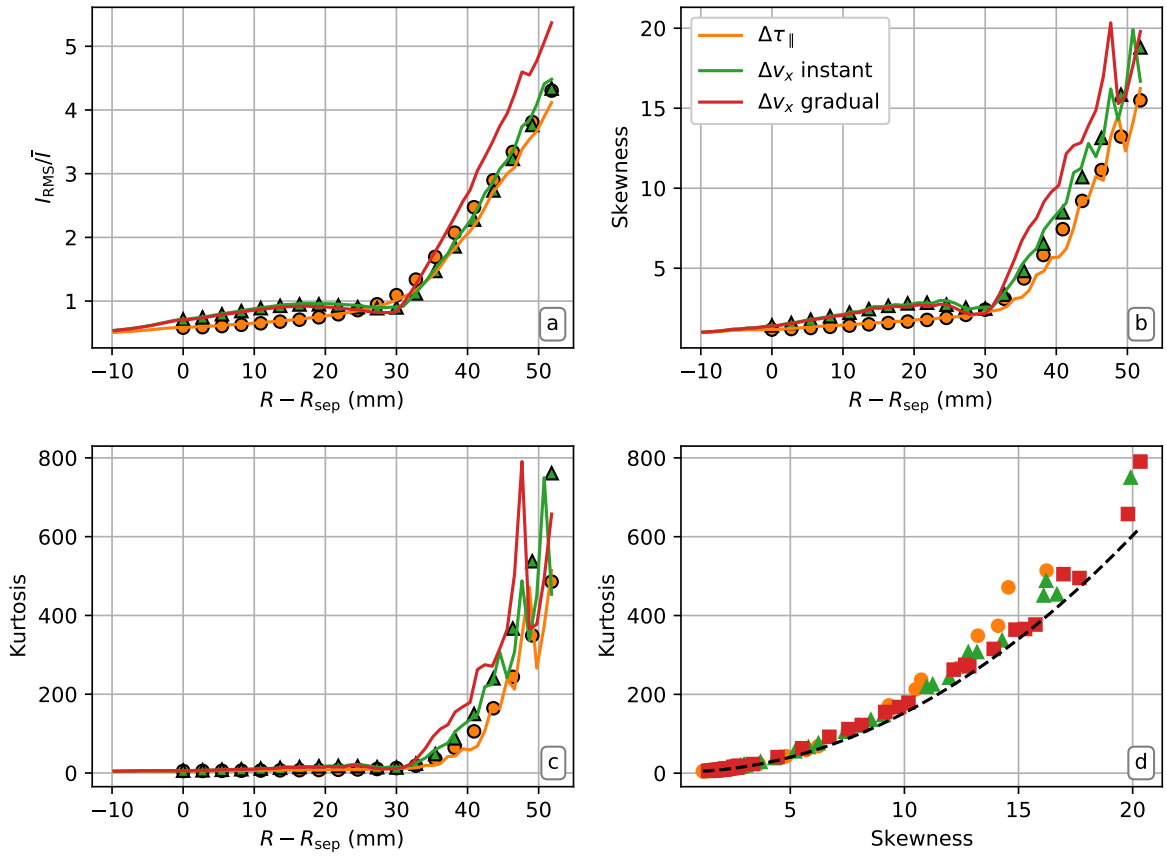

Figure 5.17: Profiles in the simulated SOL for the 1D independent blob case (solid lines) for shot # 36342, $t \in [2.5, 2.7]$s for: the relative fluctuation levels (a); skewness (b); and kurtosis (c). The values of kurtosis against skewness are shown (d) with the theoretical $K = 3/2S^2 + 3$ relation added (black dashed). The expected values derived from the model are included as symbols in (a–c).

the expected $K = 3S^2/2$ scaling now the amplitude distributions are included. The main difference between the profiles is that the dual $\tau_{\parallel}$ case continuously rises from the separatrix all the way through the SOL, whereas both the double v_x cases exhibit a slight decrease just before $x \approx 30\,\text{mm}$, the R_{ch} position, which reflects the increase in the density profiles seen in these simulations. This is seen in both the simulated profiles, and the expected profile from the model's equations. Now we see that the velocity distribution causes the rise in the higher order moments and it is strong enough to overcome the reduction in the velocity that would be needed to cause the reduction in the profile decay length. As expected, the single point PDFs also show a further deviation from the normal distribution with increasing distance into the SOL, following the increase in the relative fluctuation levels. These are shown in figure 5.18, with the k and θ input parameters in table 5.12. In the single blob case, it was

Table 5.12: A table showing the shape (k) and scale (θ) input parameters (from the 5 MW H-mode discharge # 36342, $t \in [2.5, 2.7]$s) for the Gamma distributions functions for different locations in the SOL for three 1D independent blob case simulations with radial variation in $\tau_{\parallel}$ or v_x. The PDFs are shown in figure 5.18.

ρ	1.02		1.04		1.06		1.08	
Simulation type	k	θ	k	θ	k	θ	k	θ
$\Delta\tau_{\parallel}$	2.26	0.442	1.46	0.687	0.420	2.38	0.0798	12.5
Δv_x instant	1.24	0.809	1.14	0.880	0.384	2.61	0.0679	14.7
Δv_x gradual	1.31	0.763	1.32	0.759	0.273	3.67	0.0483	20.7

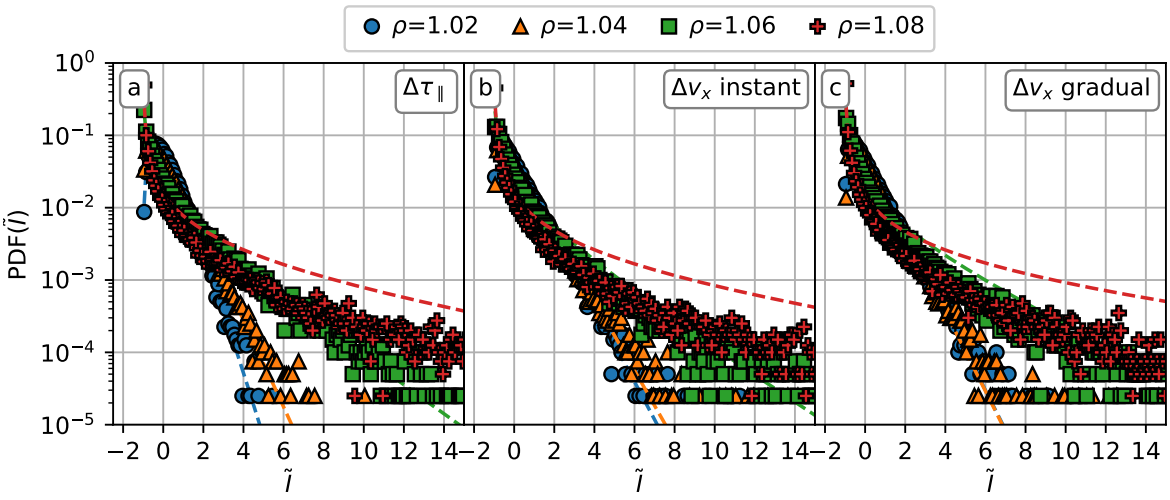

Figure 5.18: Probability distribution functions for different single locations in the SOL for the 1D independent blob case (coloured markers) for shot # 36342, $t \in [2.5, 2.7]$s. The Gamma functions calculated from the input parameters, k and θ, are included (dashed lines). The ρ positions are at $R - R_{\text{sep}} = [11, 24, 36, 49]$mm.

only the dual $\tau_{\parallel}$ scenario that reported this increase, but now the far SOL sees an increased intermittency, with only the fastest of the filaments able to propagate this far into the SOL to contribute to very high $\tilde{I}$ contributions to the PDFs. In experiment, PDFs this positively skewed are not seen. This can be counteracted in the simulations by increasing τ_w, having no effect on the shapes of any of the statistical profiles, only changing their absolute values. However, increasing τ_w does increase the computation time of the simulations, as this scales with the number of filaments generated.

Finally, we perform the same 1D Heaviside simulation experiments introducing the filaments' distributions for each attribute on the L-mode discharge # 36344, $t \in [2.5, 2.7]$s, to show that the model can still be used with filament distributions when the far SOL decay

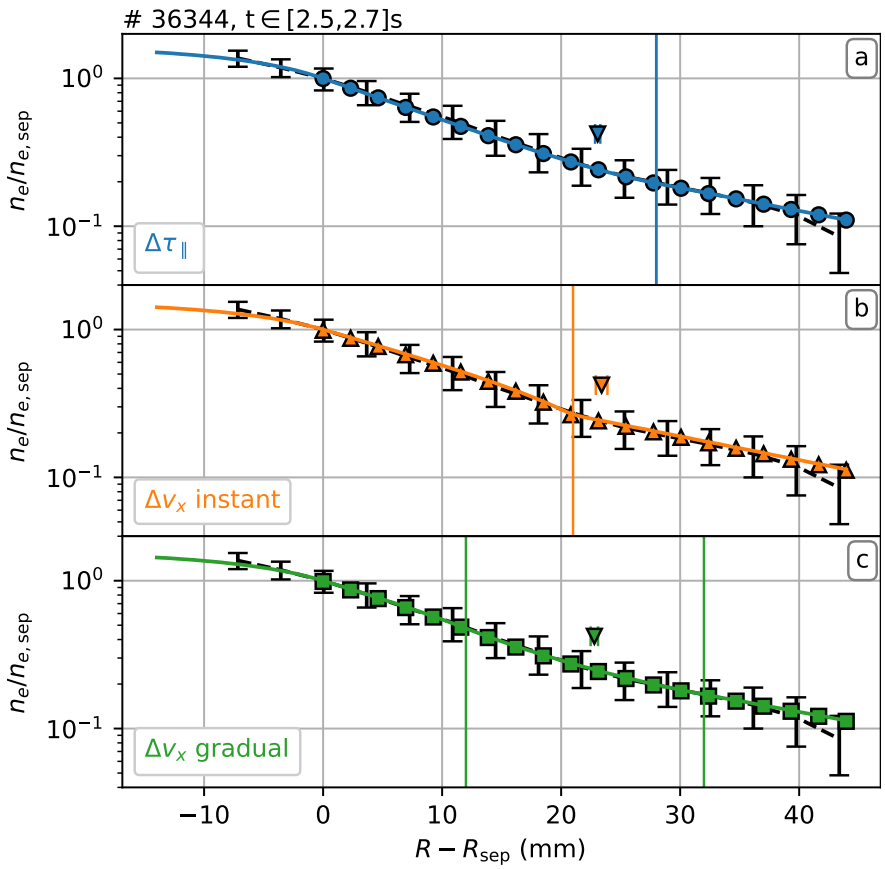

Figure 5.19: Electron density profile for the L-mode discharge # 36344 (black dashed). Three simulation profiles from the 1D independent blob case are included: changing $\tau_\parallel$ (a, blue); instantaneously changing v_x (orange); and gradually changing v_x (green). The x_0 parameters (coloured triangles), R_{ch} values (coloured vertical lines), and the outputs from the statistical framework (coloured shapes) are included.

length increases instead of decreases. We again saw no deviation between the profiles' shapes with no distributions added as we did when the amplitude and radial diameter distributions were added in independently; nor any deviation with only the radial velocity distribution included and all the distributions included; nor any significant difference between the independent and dependent case, other than changes in the absolute values of the profiles. As such, only the independent cases with all distributions included are presented. The profiles of the simulations are shown in figure 5.19, and the fit parameters included in table 5.11. The dual timescale scenario required $\tau_{\parallel,1} = 51\,\mu\mathrm{s}$, $\tau_{\parallel,2} = 70\,\mu\mathrm{s}$ and $R_{\mathrm{ch}} = 34\,\mathrm{mm}$; the instant velocity change case used $\tau_\parallel = 56\,\mu\mathrm{s}$, $v_{x,2} = 1.18 v_{x,1}$, and $R_{\mathrm{ch}} = 23\,\mathrm{mm}$; and the gradually changing velocity scenario needed $a_x = 2.6 \times 10^6\,\mathrm{m/s/s}$ between $R_{\mathrm{ch},1} = 19\,\mathrm{mm}$ and $R_{\mathrm{ch},2} = 39\,\mathrm{mm}$, and $\tau_\parallel = 55\,\mu\mathrm{s}$.

In this example, all the decay lengths and x_0 parameters measured in the simulations are within error of the fits to the experimental profile, and from the profiles alone it is difficult to conclude whether the changing profile could be caused by the change in $\tau_{\|}$ or v_x from using the profile alone. The effects of the velocity distribution increasing the decay length are countered by the increase in v_x which causes a decrease in the decay length, and the near SOL fits much more closely to double exponential form of equation (5.32), especially compared with the changing velocity cases in figure 5.19. Each of the higher order statistical moments, shown in figure 5.20*, increase as distance into the SOL increase, in agreement with experimental measurements, conversely to the single blob case, as in figure 5.14. We again see that the addition of the velocity distribution is responsible for each of these increasing with distance, even in the dual $\tau_{\|}$ scenario where we previously recorded a decrease in these quantities. This again makes it difficult to determine whether it is the change in velocity or the change in parallel timescale responsible for the change in profile decay length. The kurtosis $3S^2/2$ scaling is also reintroduced with the inclusion of the amplitude distribution in each of the three simulation types.

We also study the single point PDFs, shown in figure 5.21, with the input parameters in table 5.13. They all show an increased flattening with distance into the SOL, as expected from the relative fluctuation level measurements, or θ. As in the previous example, they start from a much more flattened distribution at the lowest ρ than the same scenario without the velocity distributions, and can be altered by changing the τ_w parameter of the simulations without affecting the shapes of the profiles. As the velocities are drawn from log-normal distributions, and the mean of the log-normal distribution, $\alpha \exp\left(\sigma^2/2\right)$, is always larger than the distribution's median, α, then more than half the filaments generated will always have a velocity lower than the mean, the value used in the single blob case. This means that, for the same density profile, more than half the velocities *always* have a velocity lower than the mean velocity, so the k and θ input parameters to the Gamma distribution will always be lower and higher, respectively, than compared to the single blob case.

As it is thought that the divertor collisionality can play a role in changes to upstream density profiles, we investigate where the R_{ch} position connects along magnetic field lines from the outboard midplane to the divertor in each of the two non-exponential profiles

*In the gradual Δv_x case, the model was unable to correctly predict the profiles for $R_{\text{ch},1} \leq x < R_{\text{ch},2}$, thought to be caused by the rounding errors introduced when calculating $\text{erf}(T_0)$ and $\text{erf}(T_2)$ in equation (5.45).

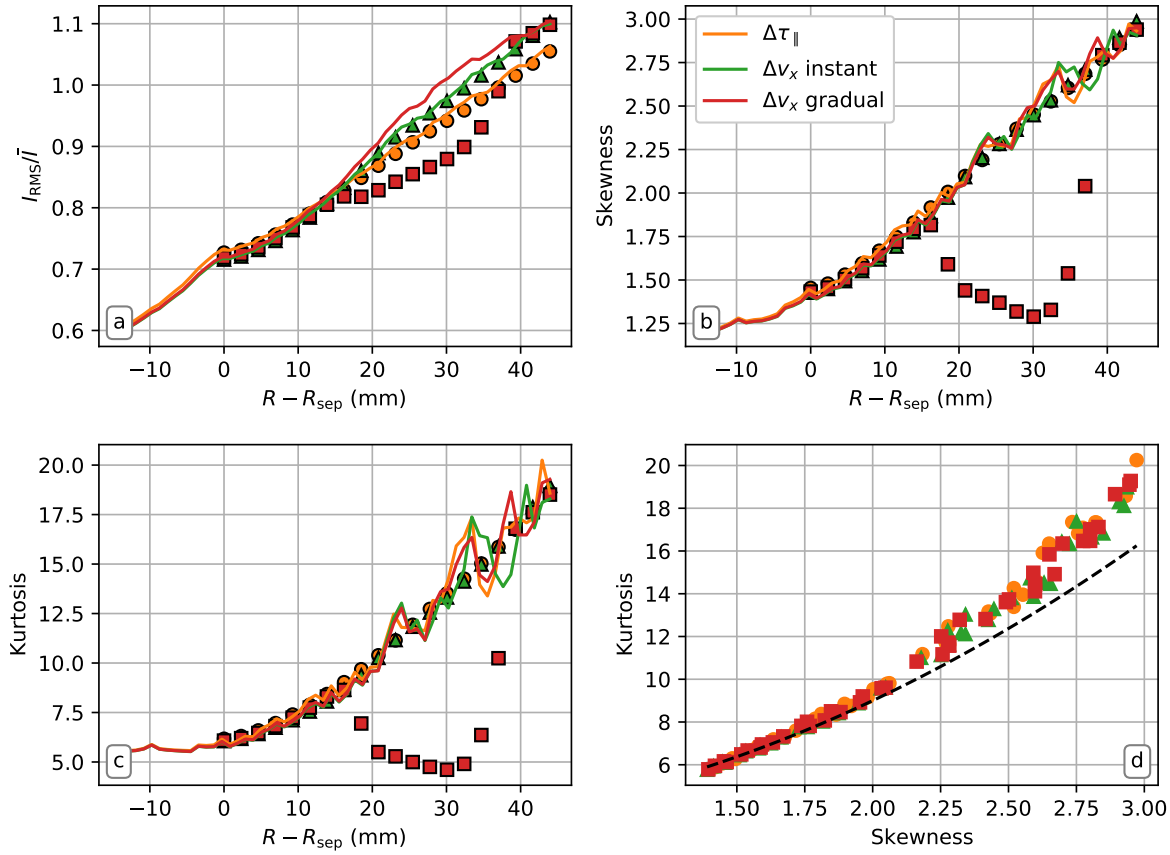

Figure 5.20: Profiles in the simulated SOL for the 1D independent blob case (solid lines) for shot # 36344, $t \in [2.5, 2.7]$s for: the relative fluctuation levels (a); skewness (b); and kurtosis (c). The values of kurtosis against skewness are shown (d) with the theoretical $K = 3S^2/2 + 3$ relation added (black dashed). The expected values derived from the model are included as symbols in (a–c).

Table 5.13: A table showing the shape (k) and scale (θ) input parameters (from the L-mode discharge # 36344) for the Gamma distribution functions for different locations in the SOL for three 1D independent blob case simulations with radial variation in $\tau_{\|}$ or v_x. The PDFs are shown in figure 5.21.

ρ	1.02		1.04		1.06	
Simulation type	k	θ	k	θ	k	θ
$\Delta\tau_{\|}$	1.48	0.677	1.12	0.893	0.885	1.13
Δv_x instant	1.49	0.670	1.056	0.947	0.827	1.21
Δv_x gradual	1.46	0.683	0.992	1.01	0.821	1.22

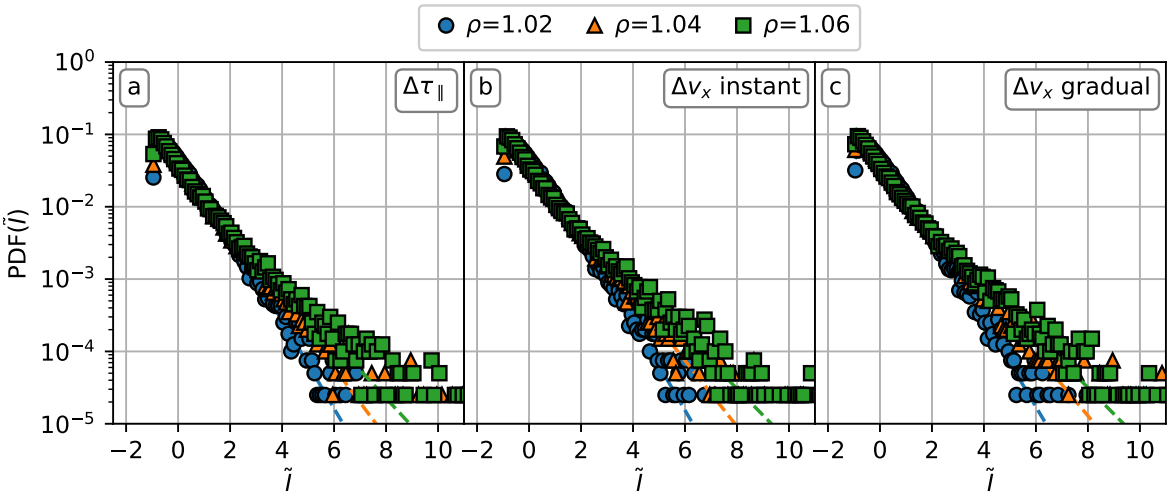

Figure 5.21: Probability distribution functions for different single locations in the SOL for the 1D independent blob case (coloured markers) for shot # 36344, $t \in [2.5, 2.7]$s. The Gamma functions calculated from the input parameters, k and θ, are included (dashed lines). The ρ positions are at $R - R_{\text{sep}} = [14, 29, 44]$mm.

for both the single blob and independent scenarios. Figure 5.22 shows a radial-poloidal cross-section of the divertor region of ASDEX Upgrade, with the R_{ch} positions plotted with coloured markers. The divertor location is found using a second order Runge-Kutta (RK2) method [87], with step-size $\mathrm{d}l = 1\,\mathrm{mm}$, tracing from R_{ch} along the magnetic field to the first contact with a material surface.

R_{ch} is towards the end of the last divertor tile in all but one of the simulations with a double parallel timescale, indicating that any change in $\tau_{||}$ could be caused by the change in surface material from the divertor to the first wall, through changes in the sheath/pre-sheath, for example. The connection lengths are shown in figure 5.23, and this point at the end of the divertor tile is shown with a star. For larger radii than this, the reduction in connection length is not so strong as to be the sole cause of any decrease in the profile decay length for shot # 36342, $t \in [2.5, 2.7]$s as a similar connection length reduction is seen in the other two examples where the profile decay length either doesn't change or increases. *As such, the change in the connection length alone cannot cannot be the sole cause of the decrease in profile decay length.* We also note that such changes in the connectivity of the upstream SOL to the divertor could be through increased poloidal flux expansion. This causes a stretching of filament cross-sections and is strongest in the vicinity of the x-point, affecting the near-SOL the most (for example, Ref. [104]). This is why some studies only measure the connection length as far as the x-point height. The crosses on figure 5.23 show

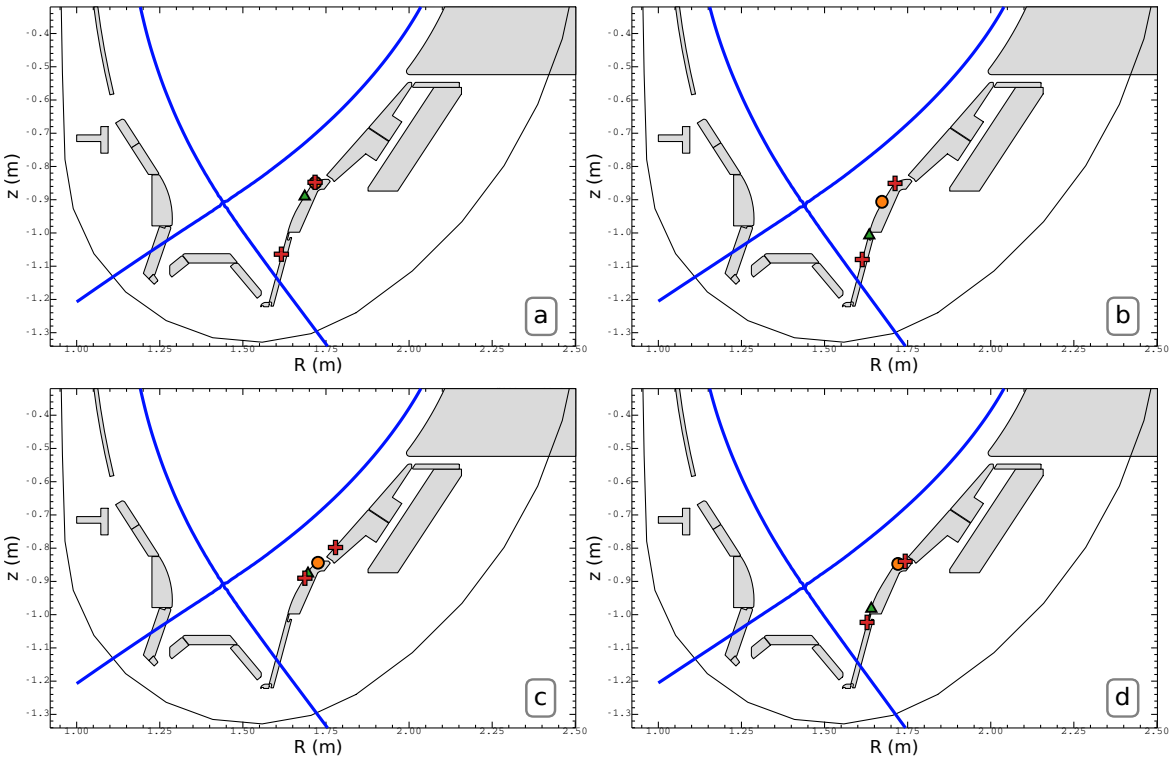

Figure 5.22: Image showing where the R_{ch} point from the outboard midplane connects along field lines to the divertor for the 1D single blob case for: shot # 36342, $t \in [2.5, 2.7]$s (a); and shot # 36344, $t \in [2.5, 2.7]$s (b); and the 1D independent case for: shot # 36342, $t \in [2.5, 2.7]$s (c); and shot # 36344, $t \in [2.5, 2.7]$s (d). The simulations included are: the $\Delta\tau_{\parallel}$ case (orange circle); the Δv_x instant case (green triangle); and the Δv_x gradual case (red plus). The blue line shows the location of the separatrix.

$R - R_{\mathrm{SOL}}$ position connects to the divertor at the approximate x-point height.

Here, the connection lengths are measured from the lithium beam location (low-field side SOL at a height of $z = 0.326\,\mathrm{m}$) to the divertor or first wall. It does not account for any non-axisymmetric structures in the tokamak, such as coils, ICRH antennas, diagnostics, etc. The last measurement on each connection length, at the largest $R - R_{\mathrm{sep}}$ is just inside the limiter shadow, and shows a steep decrease in the connection length because of this. If instead of measuring from the height of the lithium beam, the connection length is measured from the GPI viewing location, the overall trend of the connection lengths with distance into the SOL does not change, and only acts to decrease the lengths by approximately 6–7 m.

The only dual parallel timescale simulation in which R_{ch} is moved further towards the outer strike point is L-mode shot # 36344, where it has moved approximately half way down the tile, however we might consider the simulation type with distributions included as the more realistic, especially when considering how the profiles of the higher order statistics

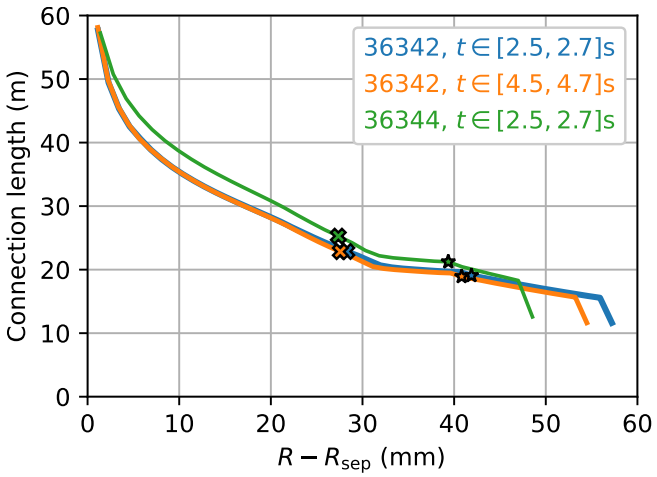

Figure 5.23: The connection lengths from the Lithium beam diagnostic to the divertor / first wall as a function of distance into the scrape-off layer. The points where the connection to the wall is the same height as the x-point (crosses) and where the connection is at the end of the second divertor tile (stars) are added. The last connection length measurement is just inside the limiter shadow.

are affected. The R_{ch} position for the instantly changing velocity case is markedly different between the two shots, being approximately halfway up the second divertor tile for shot # 36342, and at where the two divertor tiles meet for shot # 36344, always slightly behind where R_{ch} was required for changing $\tau_{\parallel}$ in both discharges. As positions correspond to the blobs' maximum positions in these simulations, rather than the centre-of-mass positions, any instance of R_{ch} being in front of x_0 could be due to this difference.

5.2 2D theoretical framework

In this section, we introduce an extra dimension into the simulation domain, where y is taken to be the bi-normal direction, analogous to the poloidal direction in the experimental measurements. We use the same input parameters for the filaments as in the 1D case, as displayed in the tables at the start of chapter 5. We start with the general equation for a blob, B, the 2D analogy of equation (5.1), given by

$$B_i(x, y, t) = A_{0,i}\Lambda(x - X(t), y - y_0 - Y(t), \delta_{x,i}, \delta_{y,i})F_i(t). \tag{5.46}$$

We can re-use the same equations (5.3) and (5.33) for $F_i(t)$, and equations (5.2), (5.36), and (5.39) for both $X(t)$ and $Y(t)$, which describe the filament positions. The y_0 term has

also been introduced, which is the y position of the filaments as it crosses the separatrix, $X_i(t-t_{0,i})=0$. We choose Λ to be a two-dimensional Gaussian function [112,116] with zero rotation, given by

$$\Lambda(x,y,w_{x,i},w_{y,i}) = \exp\left(-\frac{\big(x-X_i(t')\big)^2}{w_{x,i}^2} - \frac{\big(y-y_{0,i}-Y_i(t')\big)^2}{w_{y,i}^2}\right) \tag{5.47}$$

where $w_x^2 = \delta_x^2/4\ln(2)$ and $w_y^2 = \delta_y^2/4\ln(2)$ so that the full-width at half maximum will be equal to δ, as in the experimental filament size measurements.

All the assumptions used in the 1D framework, such that the system is ergodic, filaments are independent and invariant under transform as they propagate through the scrape-off layer, etc., still hold in the 2D frame, and the 2D version of equation (5.11) for the time average, and therefore the profile of the simulated domain, for some y-position, y_*, is written as

$$\begin{aligned}\Theta(x) &= \{B(x,y_*,t)\} \\ &= \frac{1}{\tau_w}\int_{-\infty}^{\infty}\mathrm{d}y_0\int_{-\infty}^{\infty}\mathrm{d}t\int_0^{\infty}\mathrm{d}A_0\int_0^{\infty}\mathrm{d}w_x\int_0^{\infty}\mathrm{d}w_y\left(B(x,y,t)P_{y_0}P_{A_0}P_{w_x}P_{w_y}\right)\end{aligned} \tag{5.48}$$

where we've now included the integral over the possible y_0 starting positions, with probability distribution function P_{y_0}, and the curly brackets denote the expectation value operator. Higher order statistical moments can also be found in the same way as in the 1D framework. In all the following examples, regardless of whether we are in the single blob case, or independent/dependent blob cases, P_{y_0} is the uniform distribution function over the y distance y_L, and, as in 1D, the waiting time between filaments is always exponentially distributed. In the 2D section, τ_w, the average waiting time between filaments, is taken to be 0.1 µs, 100× larger than the previous section, as we had already started to see a large flattening of the single point PDFs with the inclusion of the filament distributions, which is only exacerbated in the 2D case as filaments are distributed along y_0. Increasing τ_w helps to combat this, and as explained in the 1D case, and confirmed in the 2D simulations too, does not affect the overall trends seen, only the absolute values of profiles, PDF input parameters, etc. This will be justified in the next section.

5.2.1 Single-filament Garcia-Militello model

It is prudent to begin by exploring the simplest case in the 2D simulations. Namely, we again take the 5 MW H-mode shot # 36342, $t \in [4.5, 4.7]$s, as this has an electron density profile that can be described by a single exponential decay, with $L = 20.26 \pm 0.53$ mm. We compare this experimental profile with the simulated profile from the single-filament Garcia-Militello model, where each filament has the same amplitude, size, and velocity, in both dimensions. This is equivalent to swapping the distribution functions for these parameters with the Dirac delta function which, when integrated over, return the value they are centred around, equation (5.15), which we let be the mean values from table 5.1. Integrating over equation (5.48) then gives

$$\begin{aligned}\Theta(x) &= \{B(x, y_*, t)\} \\ &= \int_{-\infty}^{\infty}\int_{-\infty}^{\infty} \frac{A_0}{\tau_w} \exp\left(-\frac{(x - v_x t)^2}{w_x^2} - \frac{\left(y - y_0 - v_y t\right)^2}{w_{y,i}^2}\right) F_i(t)\,\mathrm{d}t\,\mathrm{d}y_0 \\ &= \int_{-\infty}^{\infty} \frac{A_0\sqrt{\pi} w_y}{L_y \tau_w} \exp\left(-\frac{(x - v_x t)^2}{w_x^2}\right) F(t)\,\mathrm{d}t\end{aligned}$$

for constant x and y velocities.

Care and consideration must be taken when integrating over time. In the 1D waveform with the Heaviside approximation, the lower integration limit $-\infty$ could be substituted with the time corresponding to the filament position, $X(x)^{-1}$, but this is no longer valid as the Gaussian waveform used in 2D stretches infinitely from its location. We choose the same starting parallel drainage function $F(t)$ from equation (5.3), and obtain

$$\begin{aligned}\Theta(x) &= \frac{A_0\sqrt{\pi} w_y}{L_y \tau_w}\left[\int_{-\infty}^{0} \exp\left(-\frac{(x - v_x t)^2}{w_x^2}\right)\mathrm{d}t + \int_{0}^{\infty} \exp\left(-\frac{(x - v_x t)^2}{w_x^2} - \frac{t}{\tau_\parallel}\right)\mathrm{d}t\right] \\ &= \frac{A_0 \pi w_x w_y}{2 L_y v_x \tau_w}\left[\operatorname{erfc}\left(\frac{x}{w_x}\right) + \exp\left(\frac{w_x^2}{4 v_x^2 \tau_\parallel^2} - \frac{x}{v_x \tau_\parallel}\right)\operatorname{erfc}\left(\frac{w_x}{2 v_x \tau_\parallel} - \frac{x}{w_x}\right)\right] \qquad (5.49)\end{aligned}$$

where erfc is the *complimentary error function*, $1 - \mathrm{erf}$. We can rewrite this generally for the n-th moment of the 2D single blob case as

$$\{B(x,t)^n\} = \frac{A_0^n \pi w_x w_y}{2 n L_y v_x \tau_w}\left[\operatorname{erfc}\left(\frac{x}{w_x}\right) + E_0\left(1 - G_0(0)\right)\right] \qquad (5.50)$$

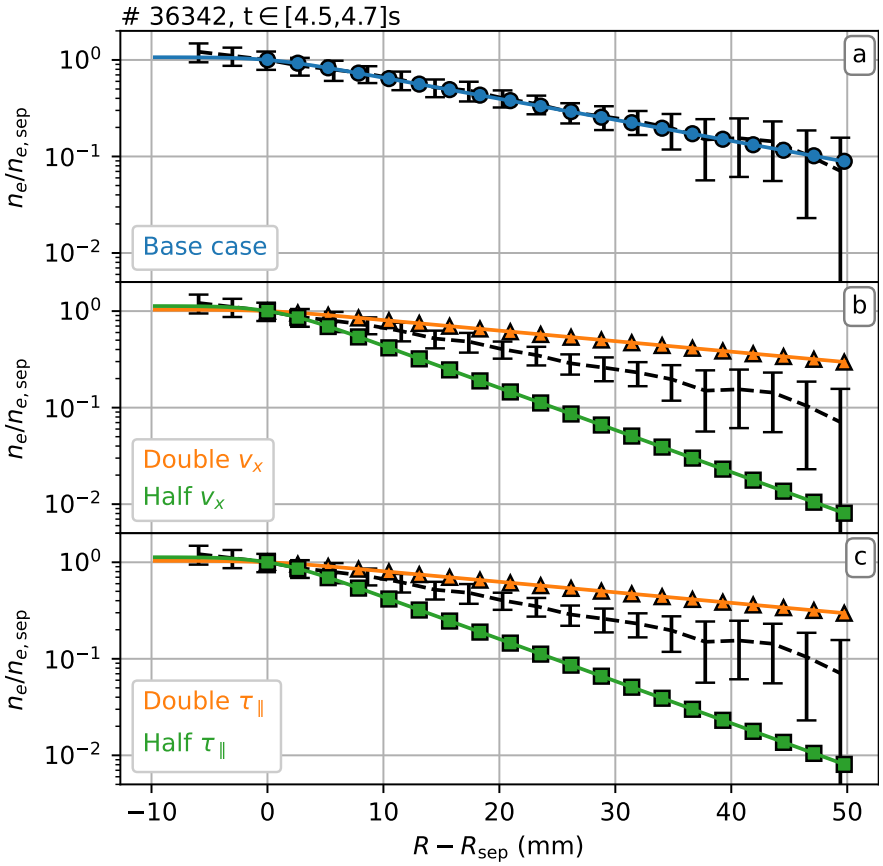

Figure 5.24: Density profile for the 5 MW H-mode experimental discharge # 36342, for $t \in [4.5, 4.7]$s (black dashed). The simulated profiles from the 2D single blob case are: the base case (a); changing v_x (b); and changing $\tau_\parallel$ (c).

where

$$E_0 = \exp\left(n\left[\frac{w_x^2}{4v_x^2\tau_\parallel^2} - \frac{x}{v_x\tau_\parallel}\right]\right) \tag{5.51}$$

and

$$G_0(z) = \mathrm{erf}\left(\sqrt{n}\left[\frac{w_x}{2v_x\tau_\parallel} - \frac{(x-z)}{w_x}\right]\right). \tag{5.52}$$

We again obtain the decay length $L = v_x\tau_\parallel$, the same as the single blob case in 1D with each of the waveforms. In fact, in the specific instance that we let $v_y = 0$, and $P_{y_0} = \delta(y_0 - y_*)$, equation (5.50) collapses to the equation for a Gaussian filament in the 1D case.

In this simulation, the only variable we can change to match the profiles is the parallel timescale, $\tau_\parallel$. This is changed to the nearest 1 µs so that the resulting exponential fit to the simulated profile is closest to the fit to the experimental profile. In this 2D base case,

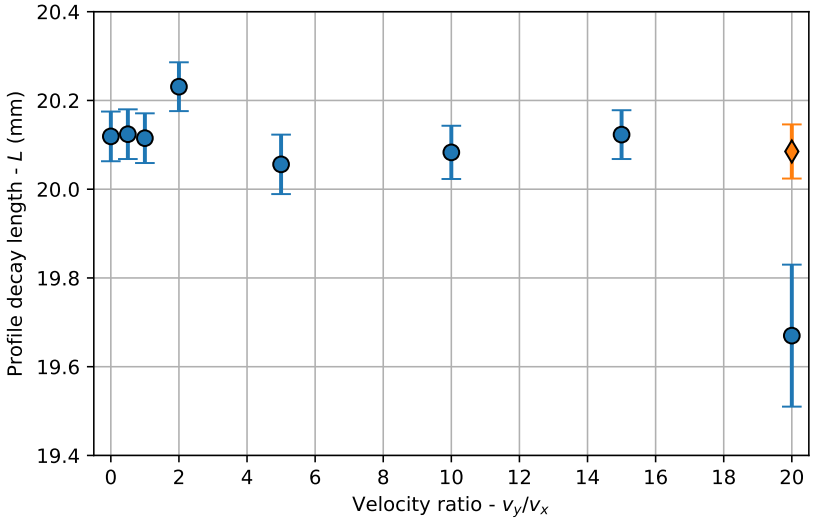

Figure 5.25: The decay length of simulated profiles in the single-filament GM model against ratio of poloidal to radial velocities by varying poloidal velocity. All other filament attributes are kept constant (blue circles), except for one instance where L_y is doubled (orange diamond).

the measured decay length is $L = 20.115 \pm 0.056\,\text{mm}$ with calculated decay length $v_x\tau_\parallel = 19.91\,\text{mm}$, using $\tau_\parallel = 75\,\mu\text{s}$, $1\,\mu\text{s}$ less than in the 1D scenario. In this scenario, $\tau_\parallel$ was changed to a precision of $1\,\mu\text{s}$. The discrepancy between the two comes from a slight deviation from an exponential just after the separatrix, caused by the condition on $F(t)$ when $x < 0$. This was not seen in the 1D simulations with the Heaviside approximation as the blob contributed nothing to the signal at any position in front if its defined position, which is not the case with the Gaussian filaments. This is captured in the weak x dependence in the error functions in equation (5.49).

Also included in figure 5.24 are the simulated profiles where the decay length was altered by changing some of the inputs to the simulations. Namely, as in the 1D case, only altering v_x and $\tau_\parallel$ changed the decay lengths, with other quantities, such as τ_w, w_x, w_y, or A_0, only affecting the absolute values of the profiles. The measured decay lengths for the profiles are shown in table 5.14. These results confirm the direct proportionality of L with v_x and $\tau_\parallel$. The outputs from the model equation (5.49) are included in 5.24 and match excellently to the simulated profiles in all cases, including the small deviation from an exponential at low values of x.

So far we have not mentioned the role of v_y. Whilst other filament attributes show up in equation (5.49) to scale the profile, the poloidal velocity appears to have no effect. This was

checked by varying the ratio of the poloidal velocity to radial velocity and measuring the corresponding fit to the simulated profiles, figure 5.25. v_x was kept constant at 256.4 m/s, varying the poloidal velocity, whilst keeping all other filament attributes the same. For values of $v_y/v_x \leq 15$, the profile decay length was found to vary less than 1 %, within the random variation expected between simulations. Only for a high velocity ratio was any difference seen. This was caused by how the simulation is run. As the poloidal velocity is increased for a given radial velocity, the angle of the paths traced by filaments with respect to the $y = \text{const}$ line increases. As such, fewer filaments pass through the sampled domain in the far SOL, causing a decrease in the profile in the far SOL. This effect can be nullified by increasing L_y, the range of y_0 values at which a filament can cross the separatrix. This only scales the profile's absolute value, and has no effect on its shape. Previous 2D work [112] avoids this effect through introducing a period boundary in the poloidal direction.

Here we note that the expression we derive in equation (5.50) different to the one obtained by Militello *et al.*, equation (9) in ref. [112]. Their expression can be reached if, instead of evaluation the time integral between $\pm\infty$, as we do, it is evaluated from $x/v_x < t < \infty$, as was done in deriving the expression for the 1D single blob case with the Heaviside approximation in section 5.1.1. Their expression, however, always underestimated the profiles when matching to our simulations. It is not thought that the difference in how our simulations treat $F(t)$ for $x < 0$ is the cause of this discrepancy, as excluding that from our derivation (by allowing $F(t)$ to be an exponential for all x) only altered the profiles' slight deviation at low positive x values. As their work doesn't show a direct comparison between their simulations and profiles derived directly from their expression, we can't speculate further on the differences between the two investigations, but given the precision to which our expression predicts our profiles in multiple cases (and the higher order statistics to come) we conclude that the reasoning behind our derivation is sound.

The higher order statistical moments from the simulations are also evaluated and are shown in figure 5.26. In the 2D simulations, these are measured at each y value in the domain and then averaged to give the profile, with the shaded regions indicating the standard deviation of these profiles over the domain. The profiles are approximately flat over the scrape-off layer, after an initial bump at $x = 0$ caused by the change of the $F(t)$ parallel drainage function as the filaments transition from the edge to the SOL. Other than some subtle differences, the results are qualitatively the same as the 1D results, where no radial

Table 5.14: A table showing the profile decay lengths for 2D single blob simulations by varying v_x and $\tau_{\|}$. For each case, $v_x = 265.4\,\mathrm{m/s}$ and $1\tau_{\|} = 75\,\mu\mathrm{s}$.

v_x (arb)	$\tau_{\|}$ (arb)	L (mm)
1	1	20.115 ± 0.056
2	1	40.19 ± 0.10
0.5	1	10.075 ± 0.032
1	2	40.19 ± 0.10
1	0.5	10.075 ± 0.032

Table 5.15: A table showing the shape (k) and scale (θ) input parameters (from the 5 MW H-mode discharge # 36342, $t \in [4.5, 4.7]$s) for the Gamma distribution function for different locations in the SOL for the 2D single blob case simulations for different values of τ_w. The PDFs are shown in figure 5.27.

ρ	1.02		1.04		1.06		1.08	
τ_w (µs)	k	θ	k	θ	k	θ	k	θ
10	0.155	6.46	0.155	6.44	0.156	6.42	0.157	6.38
1	1.62	0.619	1.62	0.619	1.61	0.621	1.60	0.623
0.1	15.7	0.0636	15.8	0.0633	15.8	0.0631	15.9	0.0631

increase in the profiles is seen, so the single blob case with constant velocity and parallel timescales cannot be a representative case of the SOL in experiments. We also note that the $K = 3S^2/2$ dependence is not present in the 2D single blob case either. The predicted profiles from the model, using equation (5.50), are also included in figure 5.26. The model tends to over-estimate compared to the values from the simulation, but the error is in the order of 1 %, however it still captures the general trend of no change in the SOL, as well as qualitatively describing the bump around $x = 0$.

Displayed in figure 5.27 are the single-point PDFs for the fluctuation signal at various radial locations in the SOL. Where the statistical moments were measured as averages over the y direction, these PDFs are measured at one bi-normal location, $y = 0$. Firstly, as there is no variation in the relative fluctuation levels with radius the PDFs are almost identical at each position, both the direct measures, and the PDFs generated by measuring k and θ from the fluctuation signal directly. The distribution inputs are shown in table 5.15.

Here we also present evidence for the justification to increase τ_w in the 2D simulations from the 1D simulations, as figure 5.27 shows the PDFs from three different 2D single blob base case scenrarios, with everything identical except for the waiting time between filaments.

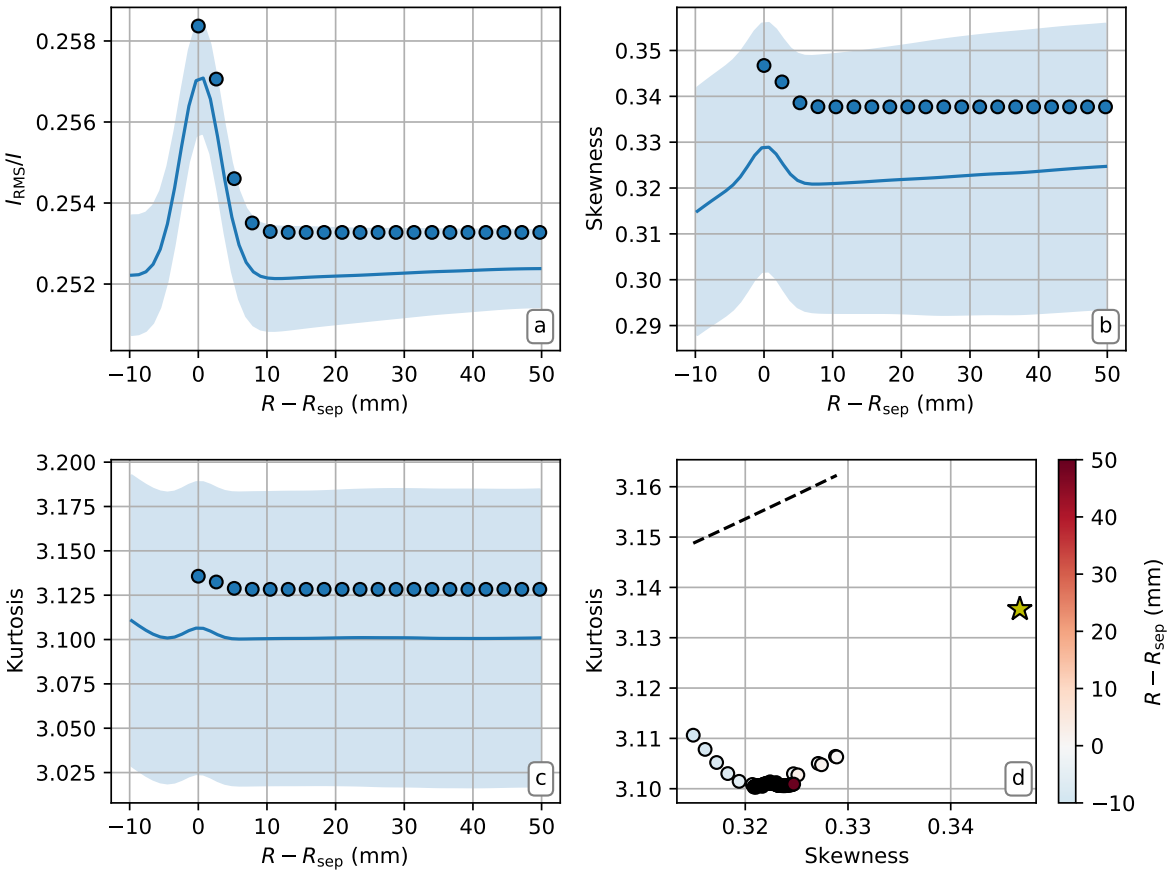

Figure 5.26: Profiles in the simulated SOL for the 2D single blob case (solid lines) for shot # 36342, $t \in [4.5, 4.7]$s for: the relative fluctuation levels (a); skewness (b); and kurtosis (c). The values of kurtosis against skewness are shown (d) with the theoretical $K = 3S^2/2 + 3$ relation added (black dashed). The theoretical values are added (blue circles, yellow stars).

When $\tau_w = 10\,\mu$s the PDFs show a similar large exponential tail to the PDFs in figures 5.18 and 5.21, where all the distributions had been included in the simulations. If we expect a similar change in the PDFs in the 2D case to the 1D case, namely a further increase in the exponential tail at larger fluctuation levels as the distributions are added, then these PDFs would become further flattened from what they already are. Decreasing τ_w to 1 µs showed a less flattened set of distirbutions, but was still comparable to the PDFs in figure 5.15 where radial variations of $\tau_{||}$ and v_x had been introduced, so τ_w was further decreased to 0.1 µs, where the PDFs are now much closer to Gaussian distributions, as experiments show the PDFs to be in the near SOL. It is here that we point out the $\frac{w_y}{y_L}$ term at the beginning of equation (5.50) is a normalisation of the waiting time from the 1D case to the 2D case, specifically the waiting time for a filament to appear at some specified y location, which for this specific case is ≈ 0.014, so a reduction of τ_w by a factor of 100 seems reasonable in this

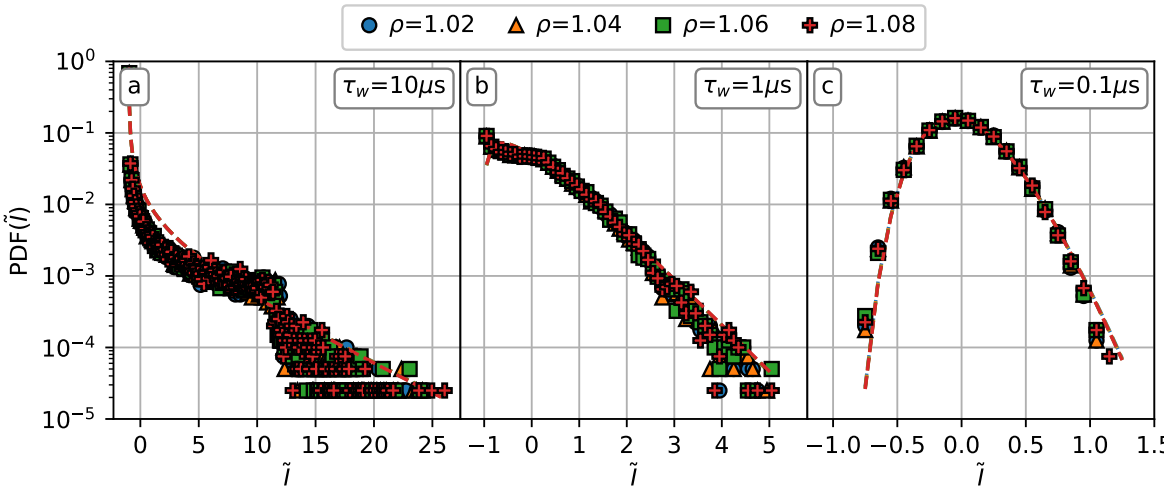

Figure 5.27: Single point probability distribution functions for different locations in the SOL for the 2D single blob case (coloured markers) for shot # 36342, $t \in [4.5, 5.7]$s, for: $\tau_w = 10\,\mu$s (a); $\tau_w = 1\,\mu$s (b); and $\tau_w = 0.1\,\mu$s (c). The Gamma functions calculated from the input parameters, k and θ, are included (dashed lines). The ρ positions are at $R - R_{\text{sep}} = [11, 23, 35, 47]$mm.

regard.

5.2.2 Distributed-filament Garcia-Militello model

We now investigate the addition of filament distributions to the previous example, where we still keep $\tau_{\parallel}$ and v_x constant throughout the SOL, so when there is a single exponential decay length that describes the profile through the whole of the scrape-off layer. Similar to section 5.1.2, we again discovered that adding in distributions for the amplitudes and radial sizes showed no change to the profile or higher order moments' profile shapes, only the absolute values, so these results are omitted in this section. As the poloidal directions were not present in the 1D simulations, we test the poloidal diameter and poloidal velocity distributions inclusion in isolation, as well as the radial velocity, and finally the effect of all the distributions in the independent case. $\tau_{\parallel}$ is again the only variable to match the simulated and experimental profiles, changed to a precision of 1 µs.

The profiles generated are shown in figure 5.28, and matched by changing $\tau_{\parallel}$ to a precision of 1 µs. The distribution inputs used are again the 5 MW H-mode experimental measurements, displayed in table 5.2, and the measured decay lengths included in table 5.16. *The addition of the poloidal diameter and poloidal velocity distributions had no effect on the profile, and these profiles look identical to the single blob case.* The effect these distributions'

Table 5.16: A table showing the profile decay lengths for 2D independent simulations for the inclusion of various distributions for the filament attributes. The experimentally measured profile's decay length is $L = 20.26 \pm 0.53$ mm, and the 2D single blob case's is $L = 20.112 \pm 0.056$ mm.

Distributed attribute	$\tau_{\parallel}$ (µs)	L (mm)
Radial velocity - v_x	106	20.36 ± 0.40
Poloidal diameter - δ_θ	75	20.116 ± 0.056
Poloidal velocity - v_θ	75	20.118 ± 0.056
All attributes, independent	106	20.25 ± 0.38
All attributes, dependent	106	19.96 ± 0.30

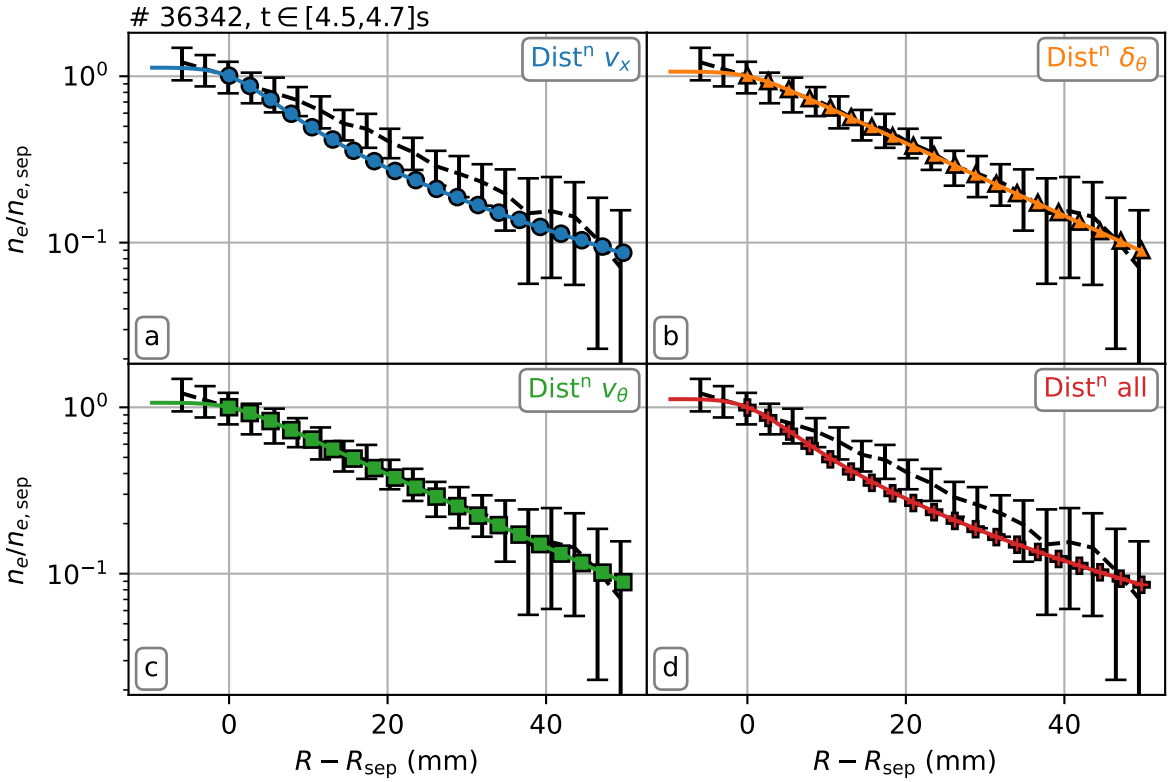

Figure 5.28: Density profile for the 5 MW H-mode experimental discharge # 36342, for $t \in [4.5, 4.7]$s (black dashed). The simulated profiles are from the single blob case with some attributes drawn from the distributions.

inclusion on equation (5.50) is to swap w_y with the mean of the poloidal distribution, of which w_y was the mean in the previous section, and the independence of equation (5.50) on v_y yields zero change from including the poloidal velocity distribution.

As in all the 1D cases, including the radial velocities from a distribution changes the shape of the profile, going from a straight exponential decay, showing a flattening of the

profile and increase in the decay length with distance into the SOL. As such, the parallel timescale needed to produce an average fit parameter near the experimentally measured one increased up to $\tau_{\parallel} = 106\,\mu s$, although we make the same comment in the 2D case that we did in the 1D cases, that the decay length is not really very well described by a single exponential decay, with the R^2 value of the fits decreasing, even if L is a close match. Equation (5.50) is modified in the same way in which we arrived at equation (5.31), by multiplying by the log-normal distribution, equation (4.14), and summing over all the radial velocities, giving

$$\{B(x,t)^n\} = \frac{A_0^n w_x w_y}{2nL_y\tau_w\sigma_{v_x}}\sqrt{\frac{\pi}{2}}\sum_i^I \frac{1}{v_{x,i}^2}\exp\left(-\frac{\ln\left(\frac{v_{x,i}}{\alpha_{v_x}}\right)^2}{2\sigma_{v_x}^2}\right)\left[\mathrm{erfc}\left(\frac{x}{w_x}\right) + E_{v_i}G_{v_i}(0)\right] \quad (5.53)$$

where E_{v_i} and $G_{v_i}(z)$ are given by equations (5.51) and (5.52), respectively, replacing v_x with $v_{x,i}$. A factor of $n!$ is needed when the filaments amplitudes are drawn from exponential distributions, as from equation (5.26). Other than weak radial dependencies on w_x in the error functions, the only radial dependence is on the radial velocity and parallel timescale, which explains why the profiles are the same for the single blob case and independent case, except when the radial velocities are randomly selected.

The dependent case was also tested. Here, the filament attributes' distribution input parameters are calculated based on the randomly chosen poloidal diameter. This determines the filament attributes at the birth of the filament at the separatrix, which are the same throughout its propagation through the simulated SOL. These attributes do not change as the poloidal size reduces due to its reduction in amplitude. As such, the dependent simulations are a test of the dependent nature of the experimentally measured 2D PDFs rather than how the radial velocity of a filament changes depending on which regime it is in. The generated profiles showed no significant deviation from the independent case, and as such are not included in figure 5.28, but the decay length is recorded in the last row of table 5.16. The profile decay length is slightly lower than in the independent case, but is within any variation we might expect to see from randomly drawn variables, and within the error of the profile fits.

The profiles for the higher order moments are shown in figure 5.29, for both the simulations and the calculated values from the model. As expected from the 1D results, the relative fluctuation level, skewness, and kurtosis, show no radial variation in the simulations

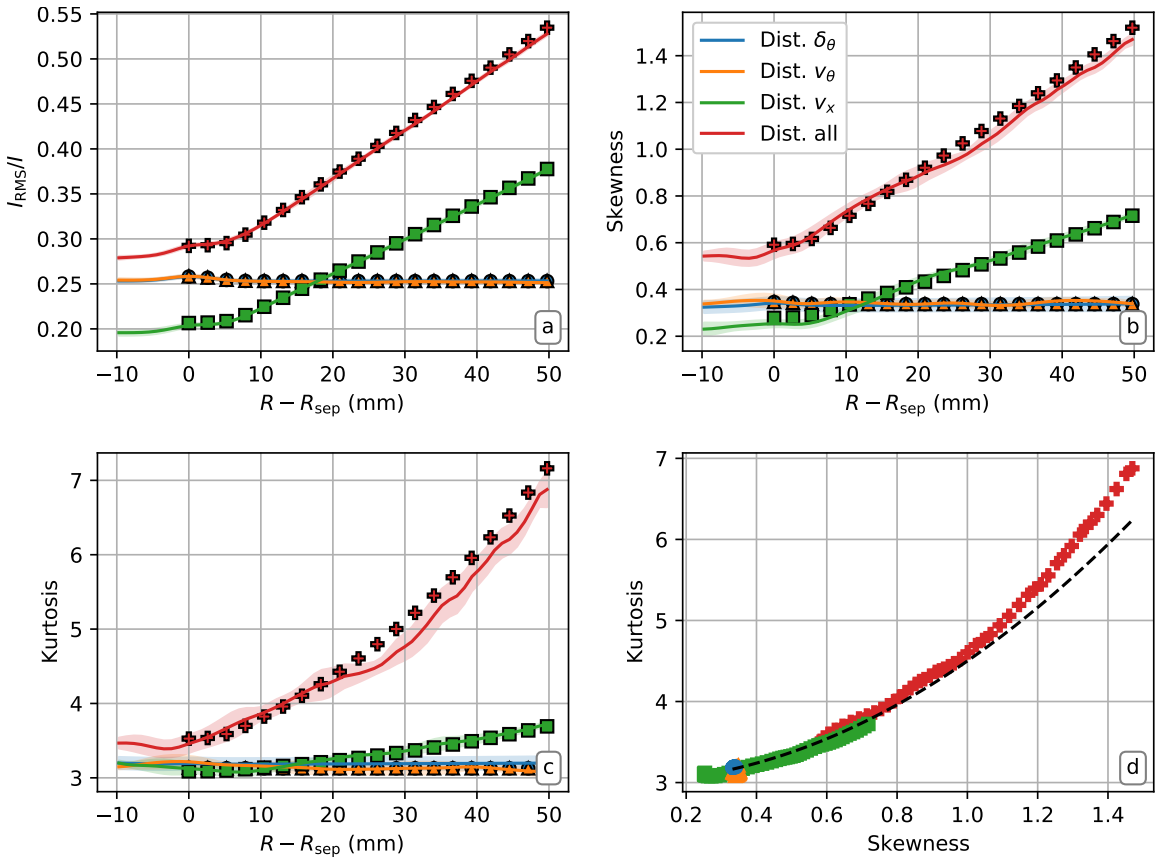

Figure 5.29: Profiles in the simulated SOL for the 2D independent case (solid lines) for shot # 36342, $t \in [4.5, 4.7]$s for: the relative fluctuation levels (a); skewness (b); and kurtosis (c). The values of kurtosis against skewness are shown (d) with the theoretical $K = 3S^2/2 + 3$ relation added (black dashed). The expected values derived from the model are included as symbols (a-c).

with just the poloidal diameter or poloidal velocity distributions included. Again turning to equation (5.50), the only radial dependence seen is the exponential terms which, outside the range of the error function, cancel in defining each of the moments. The cases with distributed poloidal sizes and velocities only are equivalent and the profiles lie on top of one another. The radial velocity distribution's inclusion is again responsible for the radial increase of each of the statistical moments, as the sum over $v_{x,i}$ means the exponential terms no longer cancel. This is the same for the case with all distributions included, which has relatively higher values for each moment due to the inclusion of the $n!$ term from the amplitude distributions.

Lastly we look at the single point PDFs for various locations in the SOL for each of the 2D independent simulations. The PDFs are shown in figure 5.30, and the Gamma input

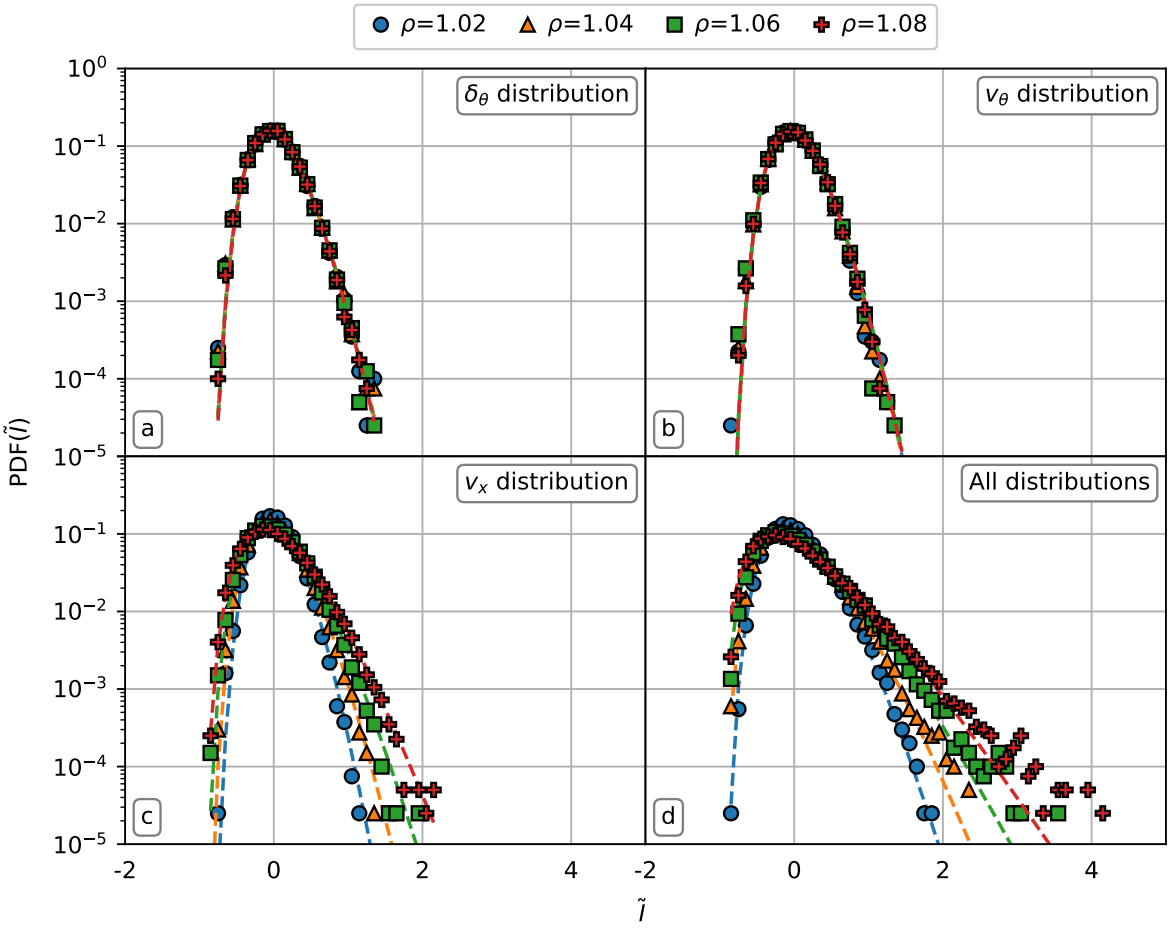

Figure 5.30: Probability distribution functions for different single locations in the SOL for the 2D independent simulations (coloured markers) for # shot 36342, $t \in [4.5, 4, 7]$s. The Gamma distributions calculated from the input parameters, k and θ are included (dashed lines). The ρ positions are at $R - R_{\text{sep}} = [11, 23, 35, 47]$mm.

parameters, k and θ, are shown in table 5.17. Any radial variation in either the case with the poloidal diameter distribution or the poloidal velocity distribution can be attributed to the finite temporal sampling used and are otherwise equal, showing no radial variation in agreement with the flat relative fluctuation profile. The case with the radial velocity distribution shows decreasing k and increasing θ with position as the PDFs deviate more from the normal distribution, and this trend is only increased in the simulation with every distribution included due to the amplitude distribution's inclusion. In these latter two cases, the PDFs recreated make good approximations of the experimental PDFs in section 4.4.1.1. By measuring the various radial statistical profiles and PDFs, we are able to conclude, for the two-dimensional framework, that the radial velocity distributions are required to recreate the experimentally measured radial change in the scrape-off layer statistics.

Table 5.17: A table showing the shape (k) and scale (θ) input parameters (from the 5 MW H-mode discharge # 36342, $t \in [4.5, 4.7]$s) for the Gamma distribution functions for different locations in the SOL for the four 2D independent blob case simulations. The PDFs are shown in figure 5.30.

ρ	1.02		1.04		1.06		1.08	
Distribution added	k	θ	k	θ	k	θ	k	θ
Poloidal diameter - δ_θ	15.4	0.0650	15.5	0.0647	15.6	0.0642	15.7	0.0637
Poloidal velocity - v_θ	15.8	0.0632	15.7	0.0635	15.4	0.0649	15.6	0.0642
Radial velocity - v_x	19.2	0.0521	13.6	0.0735	9.87	0.101	7.48	0.134
All three	9.68	0.103	6.96	0.144	4.98	0.200	3.83	0.261

Table 5.18: A table showing the fit parameters for the base case non-exponential experimental profiles, and the profiles generated in the 2D single blob case. For the 5 MW H-mode discharge, when $x = 31$ mm, $\rho \approx 1.052$, and $x = 23$ mm, $\rho \approx 1.032$ in the L-mode discharge.

Profile type		x_0 (mm)	L_1 (mm)	L_2 (mm)
H-mode	Experimental	30.76 ± 0.89	17.1 ± 1.2	5.11 ± 0.20
	$\Delta\tau_\parallel$	30.87 ± 0.17	16.95 ± 0.25	4.974 ± 0.037
	Δv_x instant	30.31 ± 0.26	17.20 ± 0.38	5.077 ± 0.056
	Δv_x gradual	30.36 ± 0.14	16.02 ± 0.14	5.655 ± 0.032
L-mode	Experimental	23.15 ± 0.32	15.888 ± 0.087	27.49 ± 0.59
	$\Delta\tau_\parallel$	23.64 ± 0.43	16.02 ± 0.43	27.72 ± 0.53
	Δv_x instant	23.17 ± 0.69	15.73 ± 0.24	27.92 ± 0.89
	Δv_x gradual	22.85 ± 0.46	16.13 ± 0.16	27.73 ± 0.51

5.2.3 Adjusted single-filament models

We now go on to use the 2D framework to recreate the density profiles that cannot be described with one exponential decay length for the whole of the scrape-off layer. The same two examples used in section 5.1.2 are used here too. The first is the 5 MW H-mode discharge # 36342, $t \in [2.5, 2.7]$s, where the far SOL decay length decreasesshown in figure 5.31, and the second is the L-mode discharge 36344, $t \in [2.5, 2.7]$s, where the far decay length increases, shown in figure 5.32. In each case, the experimental and simulation profiles are fit with the piecewise function (5.32), and are normalised to their separatrix values, as in the 1D simulations. Each filament is born with the same radial and poloidal diameters, amplitude, and radial and poloidal velocities, but with randomly generated waiting times between filaments and starting bi-normal position. The measured fit parameters are summarised in table 5.18, and filament input parameters in table 5.1.

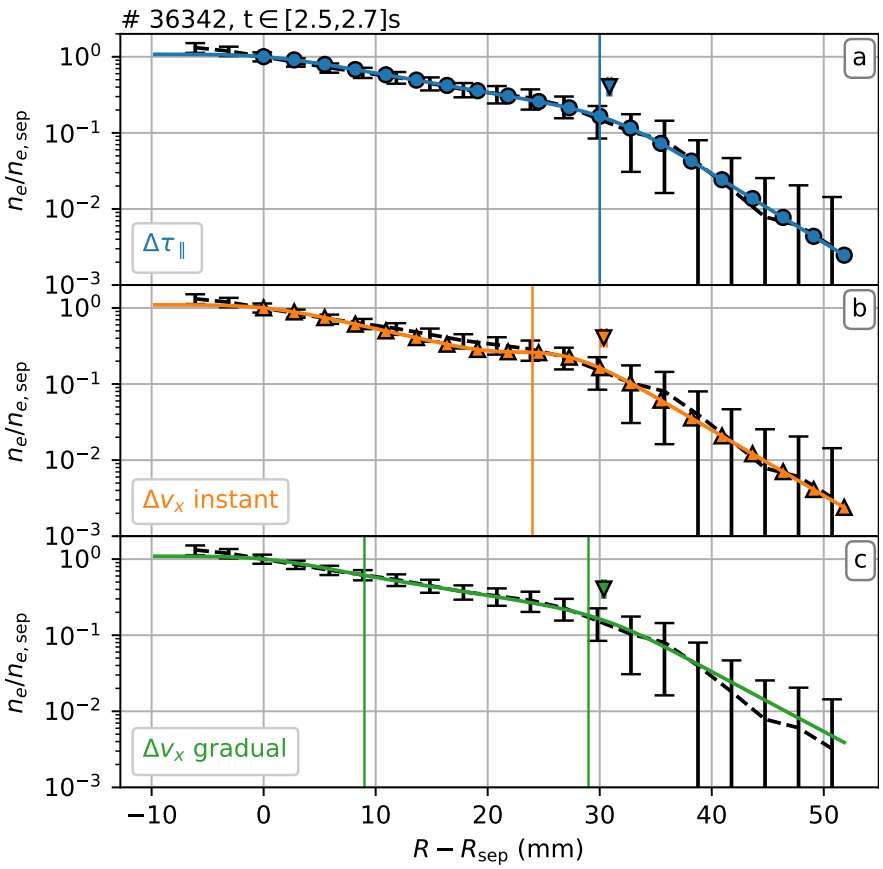

Figure 5.31: Electron density profile for the 5 MW H-mode discharge # 36342 (black dashed). Three simulation profiles from the 2D single blob case are included: changing $\tau_\parallel$ (a, blue); instantaneously changing v_x (orange); and gradually changing v_x (green). The x_0 parameters (coloured triangles) and R_{ch} values (coloured vertical lines) are included.

5.2.3.1 Single-filament dual timescale model

This is the same as in 1D, in section 5.1.3.1, with two parallel timescales used, $\tau_{\parallel,1}$ in the first part of the SOL up to R_{ch}, and then $\tau_{\parallel,2}$ from R_{ch} onwards. Equation (5.33) is used for $F(t)$, so we must to solve the equation in the statistical framework, the integration over t is broken into its constituent parts defined by the equation for $F(t)$, equation (5.33), so we must treat the region up to the separatrix independent to the near SOL, where $0 \leq x < R_{\mathrm{ch}}$ and $0 \leq t < t_{\mathrm{ch}} (= x/v_x)$, and in turn treat that differently to the far SOL where $x \geq R_{\mathrm{ch}}$

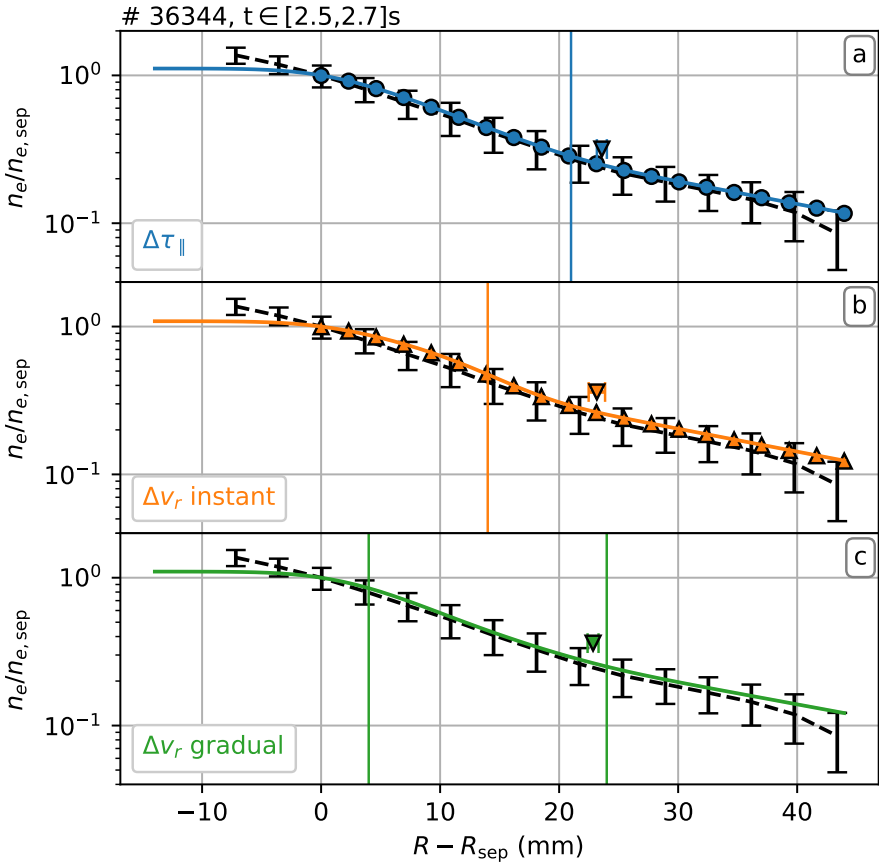

Figure 5.32: Electron density profile for the L-mode discharge # 36344 (black dashed). Three simulation profiles from the 2D single blob case are included: changing $\tau_\parallel$ (a, blue); instantaneously changing v_x (orange); and gradually changing v_x (green). The x_0 parameters (coloured triangles) and R_{ch} values (coloured vertical lines) are included.

and $t \geq t_{\mathrm{ch}}$. This gives the equation for the n-th order statistical moment as

$$\begin{aligned}\{B(x,y_*,t)^n\} = \frac{A_0^n\sqrt{\pi}w_y}{L_y\tau_w}\Bigg[&\int_{-\infty}^{0}\exp\left(-\frac{n(x-v_xt)^2}{w_x^2}\right)\mathrm{d}t \\ &+\int_{0}^{t_{\mathrm{ch}}}\exp\left(-\frac{n(x-v_xt)^2}{w_x^2}-\frac{nt}{\tau_{\parallel,1}}\right)\mathrm{d}t \\ &+\int_{t_{\mathrm{ch}}}^{\infty}\exp\left(-\frac{n(x-v_xt)^2}{w_x^2}-\frac{nt_{\mathrm{ch}}}{\tau_{\parallel,1}}-\frac{n(t-t_{\mathrm{ch}})}{\tau_{\parallel,2}}\right)\mathrm{d}t\Bigg] \\ = \frac{A_0^n\pi w_xw_y}{2nL_yv_x\tau_w}\Bigg[&\mathrm{erfc}\left(\frac{\sqrt{n}x}{w_x}\right)+E_{\tau_1}\left[G_{\tau_1}(R_{\mathrm{ch}})-G_{\tau_1}(0)\right] \\ &+\exp\left(\frac{nR_{\mathrm{ch}}}{v_x\tau_{\parallel,2}}\left[1-\frac{\tau_{\parallel,2}}{\tau_{\parallel,1}}\right]\right)E_{\tau_2}\left[1-G_{\tau_2}(R_{\mathrm{ch}})\right]\Bigg]\end{aligned} \tag{5.54}$$

where E_{τ_i} and $G_{\tau_i}(z)$ are given by equations (5.51) and (5.52), respectively, where $\tau_\parallel$ is swapped for $\tau_{\parallel,i}$. To match the simulated profile to the experimental profile, the input variables that can be changed are R_{ch}, $\tau_{\parallel,1}$, and $\tau_{\parallel,2}$. These are changed to a precision of 1 mm, 1 µs, and 1 % of $\tau_{\parallel,1}$, respectively.

5.2.3.2 Single-filament dual velocity model

Here we derive the expression for the n-th expectation value for the profiles in the single-filament dual velocity model from the statistical framework in the same way as in the previous example, treating the integration over time as three distinct regions. In 1D, section 5.1.3.2, the integration was split into only two regions, as the filament at $x < 0$ had no effect on the profile past this point when the Heaviside function was used as the filament waveform, but as the Gaussian waveform effects regions further into the SOL than the filaments current location, the blobs movement with a different parallel drainage term at $x < 0$ requires it to be treated separately. Specifically, the equation is set up and subsequently solved as

$$\begin{aligned}
\{B(x, y_*, t)^n\} = \frac{A_0^n \sqrt{\pi} w_y}{L_y \tau_w} \Bigg[& \int_{-\infty}^{0} \exp\left(-\frac{n(x - v_{x,1}t)^2}{w_x^2} \right) \mathrm{d}t \\
& + \int_{0}^{t_{\text{ch}}} \exp\left(-\frac{n(x - v_{x,1}t)^2}{w_x^2} - \frac{nt}{\tau_\parallel} \right) \mathrm{d}t \\
& + \int_{t_{\text{ch}}}^{\infty} \exp\left(-\frac{n\left(x - R_{\text{ch}} - v_{x,2}(t - t_{\text{ch}})\right)^2}{w_x^2} - \frac{nt}{\tau_\parallel} \right) \mathrm{d}t \Bigg] \\
= \frac{A_0^n \pi w_x w_y}{2 n L_y v_{x,1} \tau_w} \Bigg[& \operatorname{erfc}\left(\frac{\sqrt{n} x}{w_x} \right) + E_{v_1}\left[G_{v_1}(R_{\text{ch}}) - G_{v_1}(0) \right] \\
& + \frac{v_{x,1}}{v_{x,2}} \exp\left(\frac{n R_{\text{ch}}}{v_{x,2} \tau_\parallel} \left[1 - \frac{v_{x,2}}{v_{x,1}} \right] \right) E_{v_2}\left[1 - G_{v_2}(R_{\text{ch}}) \right] \Bigg]
\end{aligned} \tag{5.55}$$

where E_{v_i} and $G_{v_i}(z)$ are given by equations (5.51) and (5.52), respectively, with v_x swapped for $v_{x,i}$. Here, R_{ch} and $\tau_\parallel$ are again changed to 1 mm and 1 µs, respectively, and $v_{x,2}$ is changed to within 1 % of $v_{x,1}$.

5.2.3.3 Single-filament finite acceleration model

To help alleviate the effect of the instantaneous change in velocity on the profile, the 2D single-filament finite acceleration model was also implemented, using equation (5.39) for the velocity. For this model, there is no simple solution for the n-th order expectation value derived from the statistical framework, owing to the $(t-t_{\mathrm{ch},1})^2$ term in the velocity function, giving an integral of $\exp\left(-t^4\right)$, so is not included. However, the simulations were still able to be ran, and simulated profiles could be analysed. In this model, $R_{\mathrm{ch},1}$ and $R_{\mathrm{ch},2}$ are changed to within 1 mm, $\tau_{\parallel}$ is changed to within 1 µs, and a_x is changed to within 2 significant figures.

5.2.3.4 Adjusted single-filament model results

For the dual parallel timescale simulations, the required parameters were $R_{\mathrm{ch}} = 30\,\mathrm{mm}$, $\tau_{\parallel,1} = 64\,\mu\mathrm{s}$, and $\tau_{\parallel,2} = 18\,\mu\mathrm{s} \approx 0.28\tau_{\parallel,1}$ for the H-mode profile, and $R_{\mathrm{ch}} = 21\,\mathrm{mm}$, $\tau_{\parallel,1} = 34\,\mu\mathrm{s}$, and $\tau_{\parallel,2} = 67\,\mu\mathrm{s} \approx 1.97\tau_{\parallel,1}$ for the L-mode profile. The values of $\tau_{\parallel}$ are comparable to 1D values in section 5.1.3.1, particularly the ratios, and the R_{ch} positions have moved closer to separatrix due to the change in the filament waveform used. The dependence of the decay length on $\tau_{\parallel}$ is preserved in this example, namely that a decreasing decay length requires a shorter timescale, and an increased decay length requires a longer timescale. The fits to the simulated profiles are all in good agreement with the fits to the experimental profile as well, shown as solid blue lines in figures 5.31a and 5.32a. The estimations from the model, equation (5.54), are also included in these figures, shown as as blue circles, where they perfectly describe the simulated profiles.

For the dual velocity model, the input parameters used were $R_{\mathrm{ch}} = 24\,\mathrm{mm}$, $\tau_{\parallel} = 50\,\mu\mathrm{s}$, and $v_{x,2} = 0.38v_{x,1} \approx 100.9\,\mathrm{m/s}$ for the H-mode profile, and $R_{\mathrm{ch}} = 14\,\mathrm{mm}$, $\tau_{\parallel} = 45\,\mu\mathrm{s}$, and $v_{x,2} = 1.47v_{x,1} \approx 623.1\,\mathrm{m/s}$ for the L-mode profile. The input parameters are again to within a few percent of those used in the 1D simulations, except for R_{ch} which is again brought forward about $\approx 6\,\mathrm{mm}$ for both cases. The simulated profiles are made to match the experimental profiles well, particularly for the increasing decay length. These are shown as solid orange lines in figures 5.31b and 5.32b. For the H-mode example the large decrease in filament velocity required to match the far SOL manifests as a flattening of the profile around the R_{ch} location, which was also recorded in the 1D case, so although the fitted decay length of the simulated profile agrees well with the experimental fit, the match by eye isn't as good as the dual timescale case. The results of equation (5.55) have also been added

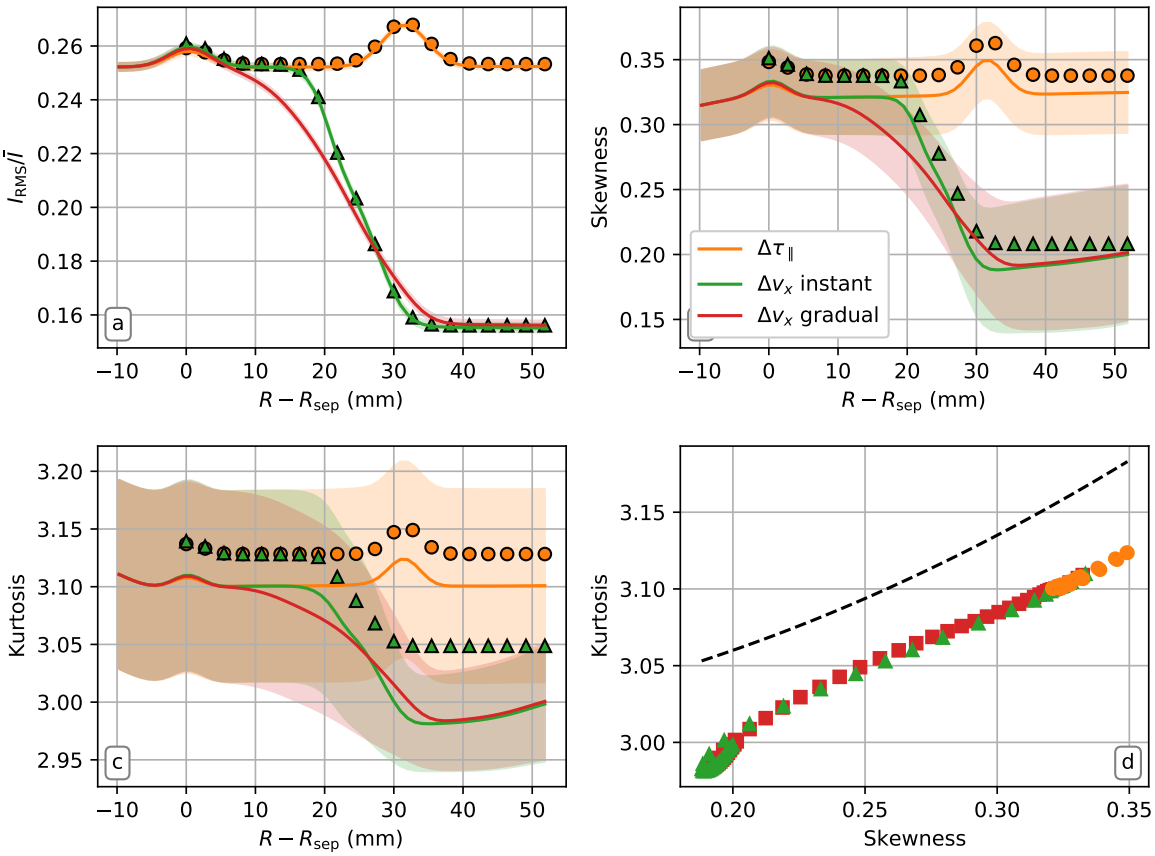

Figure 5.33: Profiles in the simulated SOL for the 2D single blob case (solid lines) for shot # 36342, $t \in [2.5, 2.7]$s for: the relative fluctuation levels (a); skewness (b); and kurtosis (c). The values of kurtosis against skewness are shown (d) with the theoretical $K = 3S^2/2 + 3$ relation added (black dashed). The expected values derived from the model are included as symbols in (a–c).

to figures 5.31b and 5.32b as orange triangles and describe the simulation profiles perfectly, including the bump around R_{ch} in the H-mode profile.

For the finite acceleration model, the required input parameters were $R_{ch,1} = 9\,\text{mm}$, $R_{ch,2} = 29\,\text{mm}$, $\tau_{\parallel} = 54\,\mu\text{s}$, and $a_x = -1.5 \times 10^6\,\text{m/s/s}$ (so $v_{x,2} = 86.2\,\text{m/s} \approx 0.32 v_{x,1}$) for the H-mode profile, and $R_{ch,1} = 4\,\text{mm}$, $R_{ch,2} = 24\,\text{mm}$, $\tau_{\parallel} = 53\,\mu\text{s}$, and $a_x = 7.0 \times 10^6\,\text{m/s/s}$ (so $v_{x,2} = 678.0\,\text{m/s} \approx 1.60 v_{x,1}$) for the L-mode profile. The simulated profiles are in figures 5.31c and 5.32c. In each of the examples, the profiles are a better match in the near SOL due to the flattening effect being spread out over a larger SOL length.

Studying the higher order radial statistical moments, we see *both similarities and differences* between the 1D results, section 5.1.4, and the 2D results. For the H-mode discharge, figure 5.33, both the changing velocity scenarios, each of the radial profile types decrease

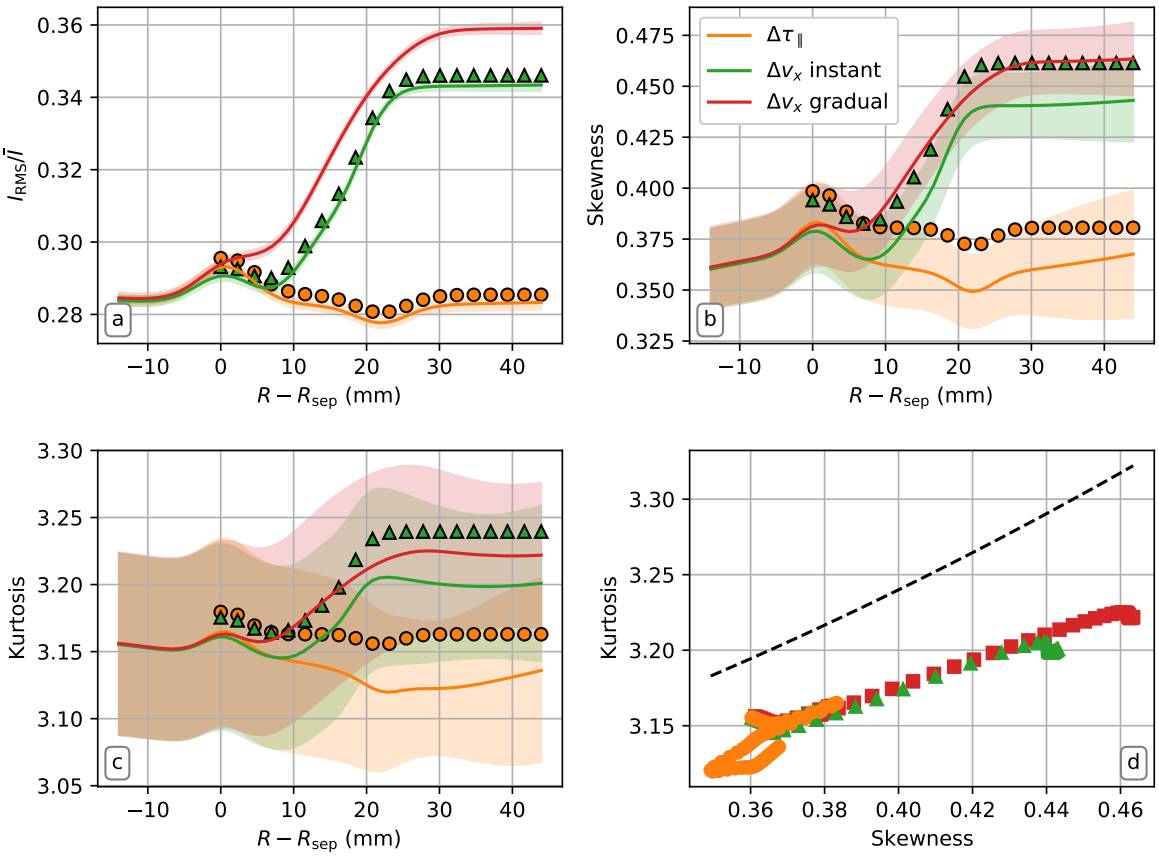

Figure 5.34: Profiles in the simulated SOL for the 2D single blob case (solid lines) for shot # 36344, $t \in [2.5, 2.7]$s for: the relative fluctuation levels (a); skewness (b); and kurtosis (c). The values of kurtosis against skewness are shown (d) with the theoretical $K = 3S^2/2 + 3$ relation added (black dashed). The expected values derived from the model are included as symbols in (a–c).

with distance into the SOL up to R_{ch}, after which they flatten out again, as in 1D. Going off the 1D results for dual parallel timescales, we would expect a rise in the statistics up to R_{ch} which flatten in the SOL. *Instead, we see approximately flat profiles through the whole SOL, but we do however see a small positive bump around* R_{ch}, even though a decrease of $\{B\}$ and $\{B^2\}$ is seen. This is due to the lack of a $\tau_{\parallel,i}$ term in the coefficient of equation (5.54) which exists in the 1D equivalent, (5.35), in the $G_{\tau,i}$ terms, whereas in equation (5.55) a $v_{x,i}$ term in the denominator causes a relative increase in the coefficient that doesn't cancel in the expressions for the relative fluctuation level, skewness, or kurtosis. The predictions from the equations are also included in figure 5.33. They accurately predict the relative fluctuation level in all cases and overestimate the skewness and kurtosis whilst qualitatively following the profiles' trends, including the bump around $x = 0$ (and R_{ch}) for the dual $\tau_\parallel$.

The higher order statistics are measured and displayed in figure 5.34 for the increasing profile decay length example. In contrast, both changing velocity simulations see an increase with x up to R_{ch}, again owing to the $v_{x,i}$ term in the coefficient denominator, which this time has increased in the far SOL, which remains flat afterwards. The dual $\tau_{\|}$ profiles again remain constant throughout the SOL, but now see a dip around R_{ch} instead of the bump seen in the H-mode example, where as 1D had previously seen a decrease in the profiles. The statistical frameworks' predictions are again plotted on the figure, agreeing quantitatively for the relative fluctuation levels in each experiment, whilst over-predicting the skewness and kurtosis whilst still capturing the general trend. In both the increasing and decreasing profile length examples, the $K = 3S^2/2 + 3$ scaling is not obeyed in either case, which was also shown for the 1D examples. By comparing the coefficient of equations (5.54) or (5.55), the $S = 8/9K^2$ scaling is returned, the same as in the 1D example. This result is important, as it shows the skewness vs kurtosis seen for Gamma distributed signals in experiments cannot be returned in the simulations, regardless of whether they are in 1D or 2D, and independent of the filament waveform used.

The single point PDFs for each of the single blob 2D cases are shown in figure 5.35, and the corresponding k and θ parameters shown in table 5.19. For each of the $\Delta\tau_{\|}$ scenarios, almost no radial change is seen due to the flatness of the relative fluctuation level profile in these scenarios, except for if the PDF is measured near the bump/dip close to the R_{ch} position. This is again different to the 1D simulations where a difference was seen where the fluctuation level changed. The instantaneous and gradual Δv_x simulations show little variation to one another in both profile types as the fluctuation levels are qualitatively similar, with the main differences being between the two discharges. As in 1D, a reduction of the filament velocity with distance into the SOL to cause a decrease in decay length leads to the PDFs to become more normally distributed at higher x opposite to experimental observations. We again may conclude that the large decrease in the profile decay length in the far scrape-off layer cannot be due to a large decrease in all filament velocities in the single blob case. With an increase in the filament velocity for the increasing decay length simulations, a slight increase in the intermittency of the PDFs is seen with radius, although this change is lesser than in the previous example, likely due to the PDFs at lowest x already flattening more than in the previous case. It should be noted that the relative change in velocity is not as strong in this case either. It is possible, based on the PDFs and statistical

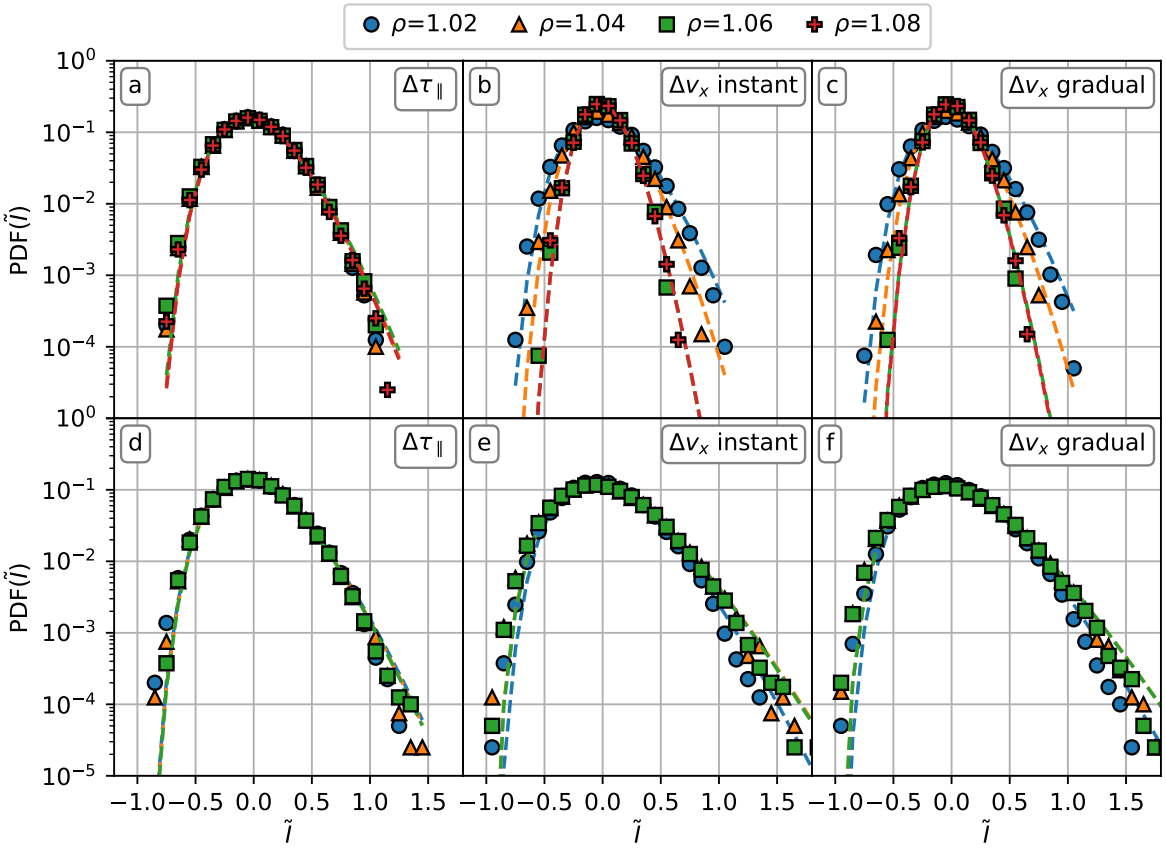

Figure 5.35: Probability distribution functions for different single locations in the SOL for the 2D single blob case (coloured markers) for shots # 36342, $t \in [2.5, 2.7]$s (a-c), and # 36344, $t \in [2.5, 2.7]$s (d-f). The ρ positions are at $R - R_{\text{sep}} = [11, 24, 36, 49]$mm, and $R - R_{\text{sep}} = [14, 29, 44]$mm, respectively. The Gamma functions calculated from the input parameters, k and θ, are included (dashed lines).

profiles, that an increasing decay length could be caused by filament velocity increase in the single blob case.

5.2.4 Adjusted distributed-filament models

Finally, we reintroduce the distribution functions for filament attributes for the two non-exponential profile examples. We again found no change to the profiles due to individually including the distributions for the filament diameters, poloidal velocity, or amplitude, only changing the absolute value at the separatrix, and that the only change was from including the radial velocity distribution, as seen in sections 5.1.2 and 5.2.3. As such, in this section, results are shown only for the case where all the attributes are independently randomly generated, as again, no qualitative difference was seen in the dependent case. We again look at

Table 5.19: A table showing the shape (k) and scale (θ) input parameters for the Gamma distribution functions for different locations in the SOL for three 2D single blob case simulations with radial variation in $\tau_{\parallel}$ or v_x shown in figure 5.35.

ρ		1.02		1.04		1.06		1.08	
H-mode	Simulation type	k	θ	k	θ	k	θ	k	θ
	$\Delta\tau_{\parallel}$	15.7	0.0636	15.7	0.0637	15.2	0.0660	15.9	0.0631
	Δv_x instant	15.7	0.0636	23.3	0.0428	41.8	0.0239	41.6	0.0240
	Δv_x gradual	16.6	0.0602	24.8	0.0403	40.5	0.0247	41.0	0.0244
L-mode	Simulation type	k	θ	k	θ	k	θ	-	-
	$\Delta\tau_{\parallel}$	12.4	0.0809	12.6	0.0792	12.7	0.0787	-	-
	Δv_x instant	10.6	0.0940	10.6	0.118	8.59	0.116	-	-
	Δv_x gradual	9.58	0.104	7.83	0.128	7.83	0.128	-	-

Table 5.20: A table showing the fit parameters for the base case non-exponential experimental profiles, and the profiles generated in the 2D independent blob case. For the 5 MW H-mode discharge, when $x = 31$ mm, $\rho \approx 1.052$, and $x = 23$ mm, $\rho \approx 1.032$ in the L-mode discharge.

Profile type		x_0 (mm)	L_1 (mm)	L_2 (mm)
H-mode	Experimental	30.76 ± 0.89	17.1 ± 1.2	5.11 ± 0.20
	$\Delta\tau_{\parallel}$	30.33 ± 0.24	17.42 ± 0.34	5.286 ± 0.053
	Δv_x instant	30.12 ± 0.94	16.9 ± 1.3	5.10 ± 0.20
	Δv_x gradual	30.53 ± 0.94	16.8 ± 1.3	5.11 ± 0.20
L-mode	Experimental	23.15 ± 0.32	15.888 ± 0.087	27.49 ± 0.59
	$\Delta\tau_{\parallel}$	23.60 ± 0.36	16.15 ± 0.12	27.43 ± 0.36
	Δv_x instant	23.60 ± 0.36	16.14 ± 0.12	27.14 ± 0.40
	Δv_x gradual	23.11 ± 0.47	15.92 ± 0.15	27.31 ± 0.55

the three cases of changing the parallel timescale, changing radial velocity instantaneously, and a gradual filament acceleration. This was again performed on the 5 MW H-mode profile with decreasing decay length and the L-mode profile with increasing decay length. The piecewise fit parameters to (5.32) for each profile type are displayed in table 5.20. As in section 5.1.4, the equations for the n-th expectation value are found by taking the corresponding equation from the single-filament model in 2D, including the contribution from the exponentially distributed amplitudes, equation (5.26), and the sum over relevant radial velocities and the equation for the lognormal distribution, equation (4.14).

5.2.4.1 Distributed-filament dual timescale model

Here, we modify the 2D single-filament $\Delta\tau_{\|}$ model, equation (5.54), and get

$$\{B(x,y_*,t)^n\} = \frac{A_0^n \pi w_x w_y (n-1)!}{2L_y v_x \tau_w} \sum_{v_{x,\min}}^{v_{x,\max}} \frac{1}{v_x\sqrt{2\pi}\sigma_{v_x}} \exp\left(-\frac{\ln\left(\frac{v_x}{\alpha_{v_x}}\right)^2}{2\sigma_{v_x}^2}\right) \left[\operatorname{erfc}\left(\frac{\sqrt{n}x}{w_x}\right) + E_{\tau_1}\left[G_{\tau_1}(R_{\mathrm{ch}}) - G_{\tau_1}(0)\right] + \exp\left(\frac{nR_{\mathrm{ch}}}{v_x\tau_{\|,2}}\left[1-\frac{\tau_{\|,2}}{\tau_{\|,1}}\right]\right) E_{\tau_2}\left[1-G_{\tau_2}(R_{\mathrm{ch}})\right]\right] \tag{5.56}$$

for the n-th order expectation value of the profiles, where E_{τ_i} and $G_{\tau_i}(z)$ are given by equations (5.51) and (5.52), respectively, where $\tau_{\|}$ is swapped for $\tau_{\|,i}$. The input variables that are changed to match the simulated and experimental profiles are R_{ch}, $\tau_{\|,1}$, and $\tau_{\|,2}$. These are changed to a precision of 1 mm, 1 µs, and 1 % of $\tau_{\|,1}$, respectively.

5.2.4.2 Distributed-filament dual velocity model

For the distributed-filament dual velocity model, the inclusion of the amplitude and radial velocity distributions into equation (5.55) yields the equation

$$\{B(x,y_*,t)^n\} = \frac{A_0^n \pi w_x w_y (n-1)!}{2L_y v_{x,1} \tau_w} \sum_{v_{x,1,\min}}^{v_{x,1,\max}} \frac{1}{v_{x,1}\sqrt{2\pi}\sigma_{v_x}} \exp\left(-\frac{\ln\left(\frac{v_{x,1}}{\alpha_{v_x}}\right)^2}{2\sigma_{v_x}^2}\right) \times \left[\operatorname{erfc}\left(\frac{\sqrt{n}x}{w_x}\right) + E_{v_1}\left[G_{v_1}(R_{\mathrm{ch}}) - G_{v_1}(0)\right] + \frac{v_{x,1}}{v_{x,2}} \exp\left(\frac{nR_{\mathrm{ch}}}{v_{x,2}\tau_{\|}}\left[1-\frac{v_{x,2}}{v_{x,1}}\right]\right) E_{v_2}\left[1-G_{v_2}(R_{\mathrm{ch}})\right]\right] \tag{5.57}$$

where E_{v_i} and $G_{v_i}(z)$ are given by equations (5.51) and (5.52), respectively, with v_x swapped for $v_{x,i}$. Here, R_{ch} and $\tau_{\|}$ are changed to within 1 mm and 1 µs, respectively, and $v_{x,2}$ is changed to within 1 % of $v_{x,1}$.

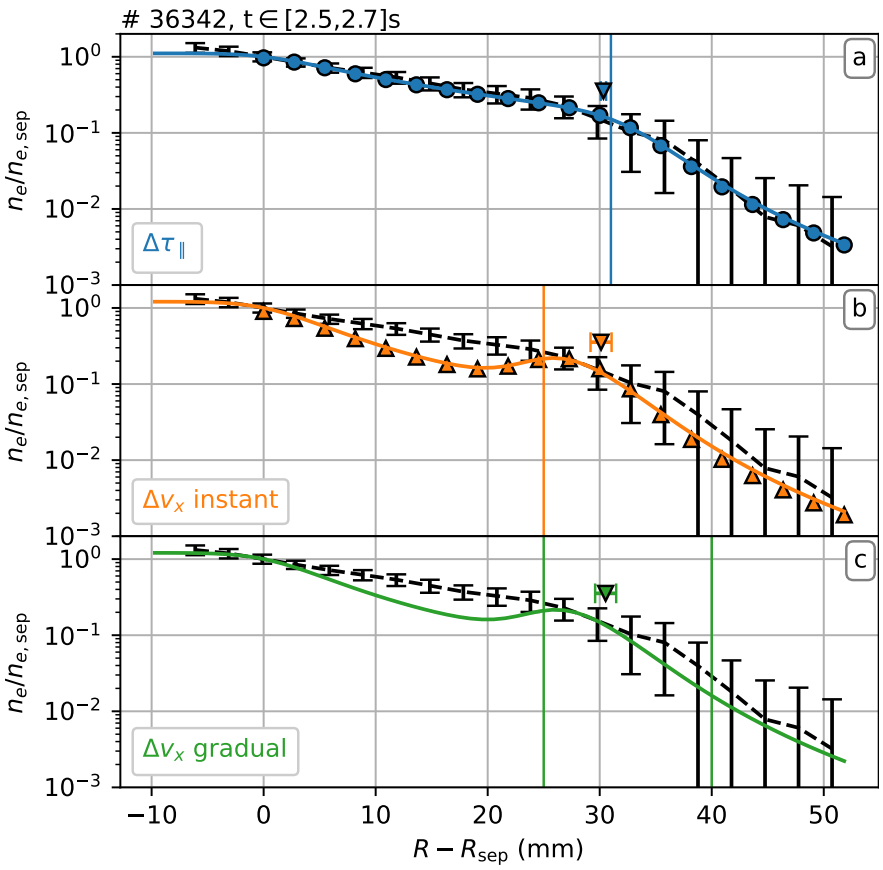

Figure 5.36: Density profile for the 5 MW H-mode experimental discharge # 36342, $t \in [2.5, 2.7]$s (black dashed). Three simulation profiles from the 2D independent blob case are included: changing $\tau_{\parallel}$ (a, blue); instantaneously changing v_x (orange); and gradually changing v_x (green). The x_0 parameters (coloured triangles) and R_{ch} values (coloured vertical lines) are included.

5.2.4.3 Distributed-filament finite acceleration model

As in section 5.2.3.3, due to the t^2 term in the position equation, equation (5.39), there is an integral of $\exp(-t^4)$ when deriving an expression for $\{B(x, y_*, t)^n\}$, and so no simple solution exists. The simulations are still run, and the simulated profiles can be analysed, but they cannot be directly compared to the analytical model. Here, the input variables that are changed are $R_{\mathrm{ch},1}$ and $R_{\mathrm{ch},2}$ are changed to within 1 mm, $\tau_{\parallel}$ is changed to within 1 µs, and a_x is changed to within 2 significant figures. As in 1D, to avoid the slower filaments reversing the direction of their propagation when they undergo a deceleration for the decreasing decay length, the minimum velocity of a blob is set to 10 % of its starting velocity, $0.1v_{x,1}$.

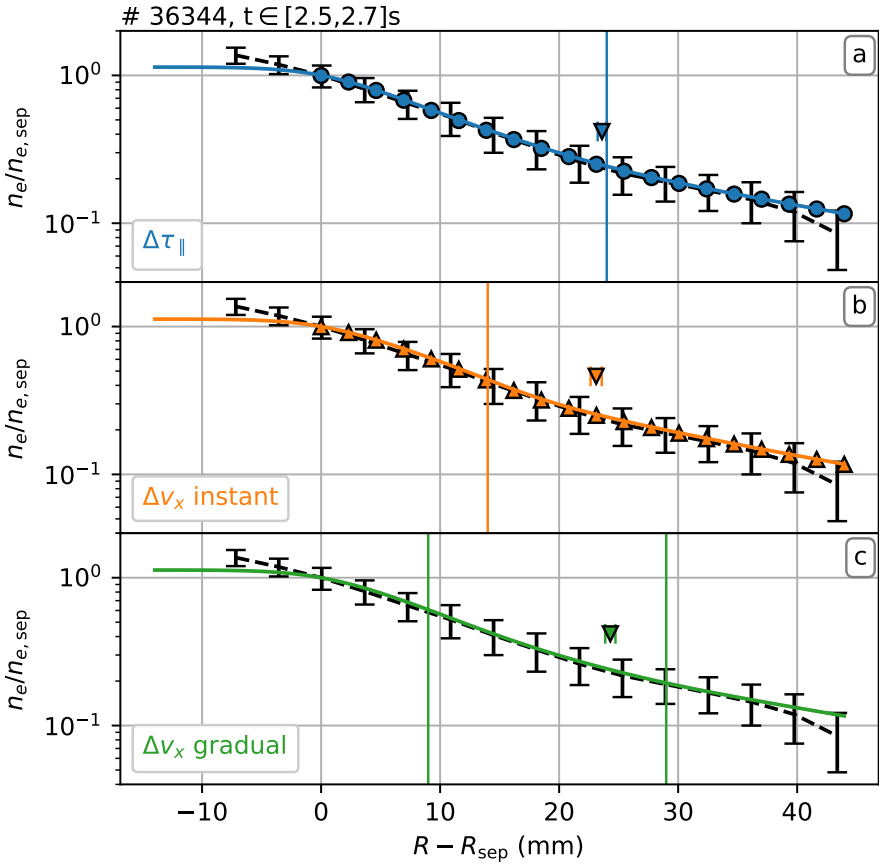

Figure 5.37: Density profile for the L-mode experimental discharge # 36344, $t \in [2.5, 2.7]$s (black dashed). Three simulation profiles from the 2D independent blob case are included: changing $\tau_\parallel$ (a, blue); instantaneously changing v_x (orange); and gradually changing v_x (green). The x_0 parameters (coloured triangles) and R_{ch} values (coloured vertical lines) are included.

5.2.4.4 Adjusted distributed-filament model results

This section describes the results for the adjusted models with distributed filament attributes. The 5-MW H-mode profiles with decreasing profile decay length are shown in figure 5.36, and the L-mode profiles with increasing profile decay length are in figure 5.37.

For the dual parallel timescale simulations, the required parameters were $R_{\mathrm{ch}} = 31\,\mathrm{mm}$, $\tau_{\parallel,1} = 118\,\mu\mathrm{s}$, and $\tau_{\parallel,2} = 11\,\mu\mathrm{s} \approx 0.093\tau_{\parallel,1}$ for the H-mode profile, and $R_{\mathrm{ch}} = 24\,\mathrm{mm}$, $\tau_{\parallel,1} = 55\,\mu\mathrm{s}$, and $\tau_{\parallel,2} = 75\,\mu\mathrm{s} \approx 1.36\tau_{\parallel,1}$ for the L-mode profile. As with 1D, introduction of the radial velocity distribution leads to a flattening of the near SOL profile so an increase in $\tau_{\parallel,1}$ is needed to match the decay length to the experimental fits. A smaller $\tau_{\parallel,2}$ is needed for the H-mode profile, resulting in a great reduction of the ratio of $\tau_{\parallel,2}/\tau_{\parallel,1}$, and whilst an increase in $\tau_{\parallel,2}$ is still needed for L-mode, the $\tau_{\parallel,2}/\tau_{\parallel,1}$ has not been reduced due to the

distribution's addition and natural flattening of the profile. A similar change in the ratios between the single blob and independent blob cases was seen in 1D. Both the simulated profiles for the dual $\tau_{\parallel}$ case, figures 5.36a and 5.37a, match to the experimental profiles well, and could be responsible for the change in the profile decay lengths. The 2D statistical framework, blue circles in the graphs, given by equation (5.56), also describes the simulated profiles excellently.

The inputs for the instantaneously changing radial velocity simulations were $R_{\mathrm{ch}} = 25\,\mathrm{mm}$, $\tau_{\parallel} = 53\,\mu\mathrm{s}$, and $v_{x,2} = 0.11 v_{x,1}$, and $R_{\mathrm{ch}} = 14\,\mathrm{mm}$, $\tau_{\parallel} = 63\,\mu\mathrm{s}$, and $v_{x,2} = 1.23 v_{x,1}$, for the decreasing and increasing profile decay lengths, respectively. As with the 1D case, the addition of the velocity distribution reduced the ratio of $v_{x,2}/v_{x,1}$ when compared with the single blob case. As such, the flattening of the near SOL profile in the 5 MW case was compounded by the reduced velocity, and the velocity distribution, and $\tau_{\parallel}$ is higher than compared to the single blob case. For the L-mode example, the simulated profile is found to match well with the experimental one and a good match could possibly be made using the natural flattening from the velocity distribution, although this has not been tested.

As with the 1D case, we see that when a large decrease of the decay length is needed by a large decrease in the filaments' velocities, the simulated profile is not a good match for the experimental one even if the fit parameters agree, because the piecewise fit function is not a suitable approximation here. In figure 5.36b a local maxima is seen centred around R_{ch} caused by the instantaneous slowing of the blobs in the simulation. Not only is this a poor match in this example, but an increasing density bump like this is never seen in the experimental SOL profiles. Despite this, the solution to the statistical framework, equation (5.57), yields profiles that agree well with those obtained from the fit for in both the profile examples shown here, and even recreates the local maxima in the H-mode example.

Finally, we also investigate the case with gradually accelerating filaments. For this, the input parameters used were $\tau_{\parallel} = 53\,\mu\mathrm{s}$ with the filament accelerating at $a_x = -4.0\times10^8\,\mathrm{m/s/s}$ between $R_{\mathrm{ch},1} = 25\,\mathrm{mm}$ and $R_{\mathrm{ch},2} = 40\,\mathrm{mm}$ for the H-mode discharge, and $\tau_{\parallel} = 61\,\mu\mathrm{s}$ with $a_x = 1.9 \times 10^6\,\mathrm{m/s/s}$ between $R_{\mathrm{ch},1} = 9\,\mathrm{mm}$ and $R_{\mathrm{ch},2} = 29\,\mathrm{mm}$ for the L-mode discharge, with the profiles displayed in 5.36c and 5.37c, respectively. In the H-mode example with $a_x < 0$, only filaments with a starting velocity greater than 3482 m/s, the fastest 0.05 % of the randomly generated velocities, end with a velocity greater than this imposed minimum of 10 % of $v_{x,1}$.

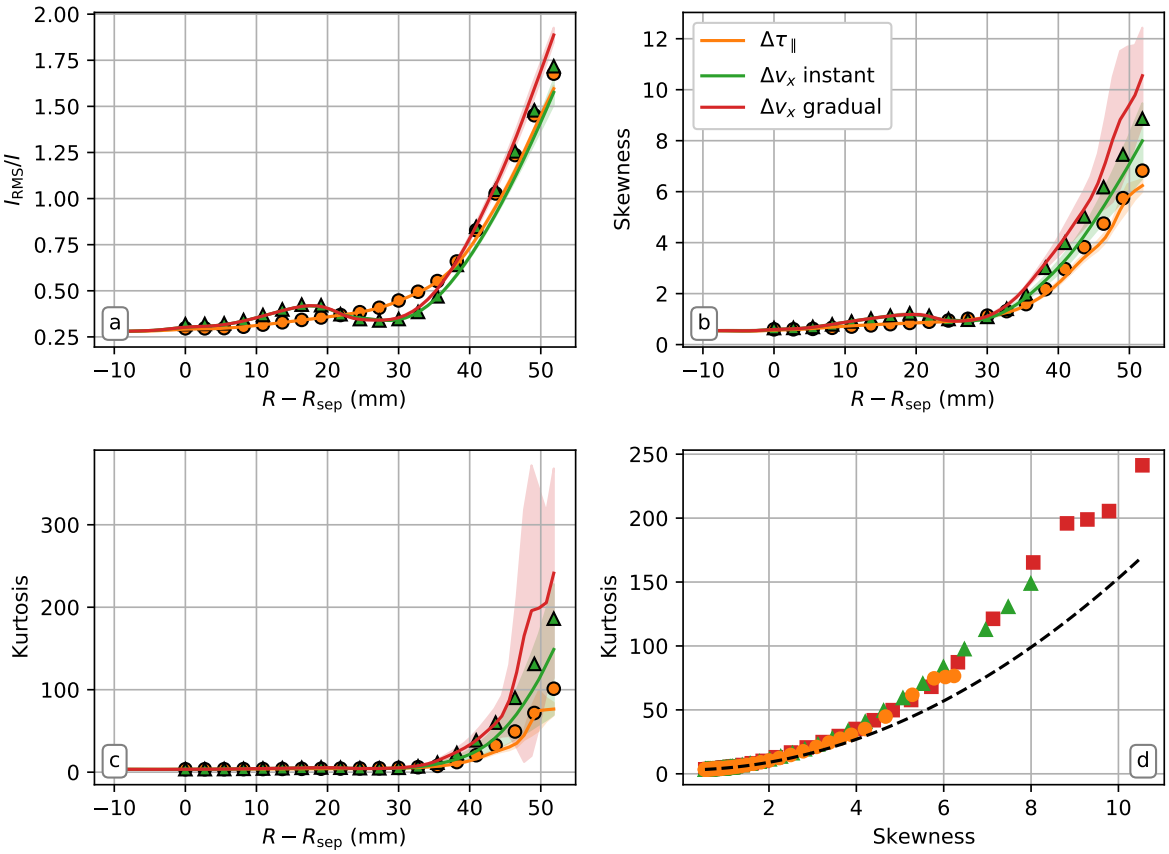

Figure 5.38: Profiles in the simulated SOL for the 2D independent blob case (solid lines) for shot # 36342, $t \in [2.5, 2.7]$s for: the relative fluctuation levels (a); skewness (b); and kurtosis (c). The values of kurtosis against skewness are shown (d) with the theoretical $K = 3S^2/2 + 3$ relation added (black dashed). The expected values derived from the model are included (a-c).

As such a large filament deceleration is required to match the decreasing decay length profiles, the local maxima is seen just after $R_{\mathrm{ch},1}$ and the piecewise fit function is not a good approximation of this simulated profile. We also saw an increase in the magnitude of the deceleration needed with the velocity distributions introduced but over a smaller distance between $R_{\mathrm{ch},2}$ and $R_{\mathrm{ch},1}$, as in 1D, but the match between simulation and experimental profiles could not be made any better. For an increasing decay length, the required filament acceleration was decreased with the addition of the velocity distributions, mirroring the 1D result.

From the profiles alone, we may conclude that a decrease in the profile decay length cannot be caused by a decreasing filament velocity, even when a gradual change of velocity is implemented, if the decrease in the decay length is too great and would more likely be caused

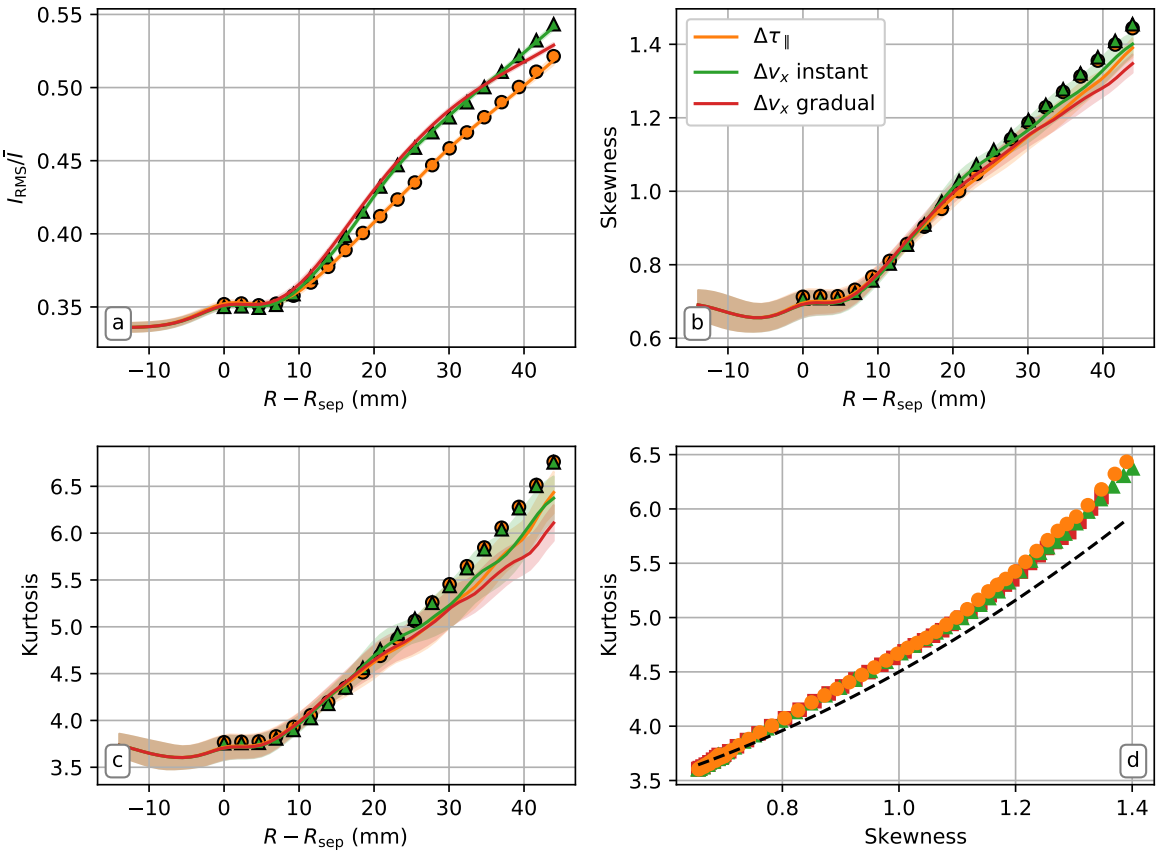

Figure 5.39: Profiles in the simulated SOL for the 2D independent blob case (solid lines) for shot # 36344, $t \in [2.5, 2.7]$s for: the relative fluctuation levels (a); skewness (b); and kurtosis (c). The values of kurtosis against skewness are shown (d) with the theoretical $K = 3S^2/2 + 3$ relation added (black dashed). The expected values derived from the model are included (a-c).

by a decrease in the parallel timescales, however accelerating filaments could be responsible for a change in profile decay length, such as shoulder formation.

The radial profiles for the higher order statistics are shown in figure 5.38 for the H-mode simulations and in figure 5.39 for the L-mode simulations. In the 2D single blob case an increase in the statistics with radius was only seen when filament velocity increased (as well as a local increase around R_{ch} for decreasing $\tau_{\parallel}$). Now that the velocity distributions are included, each of the profiles are seen to increase with distance into the scrape-off layer, although a local minima around R_{ch} is seen in the profiles for each of the H-mode dual Δv_x profiles.* The relative increase in the profiles for the H-mode discharge is larger than the L-mode, particular for the skewness and kurtosis, mirroring the larger change in decay length

*The local minima is also seen in the kurtosis if zoomed in.

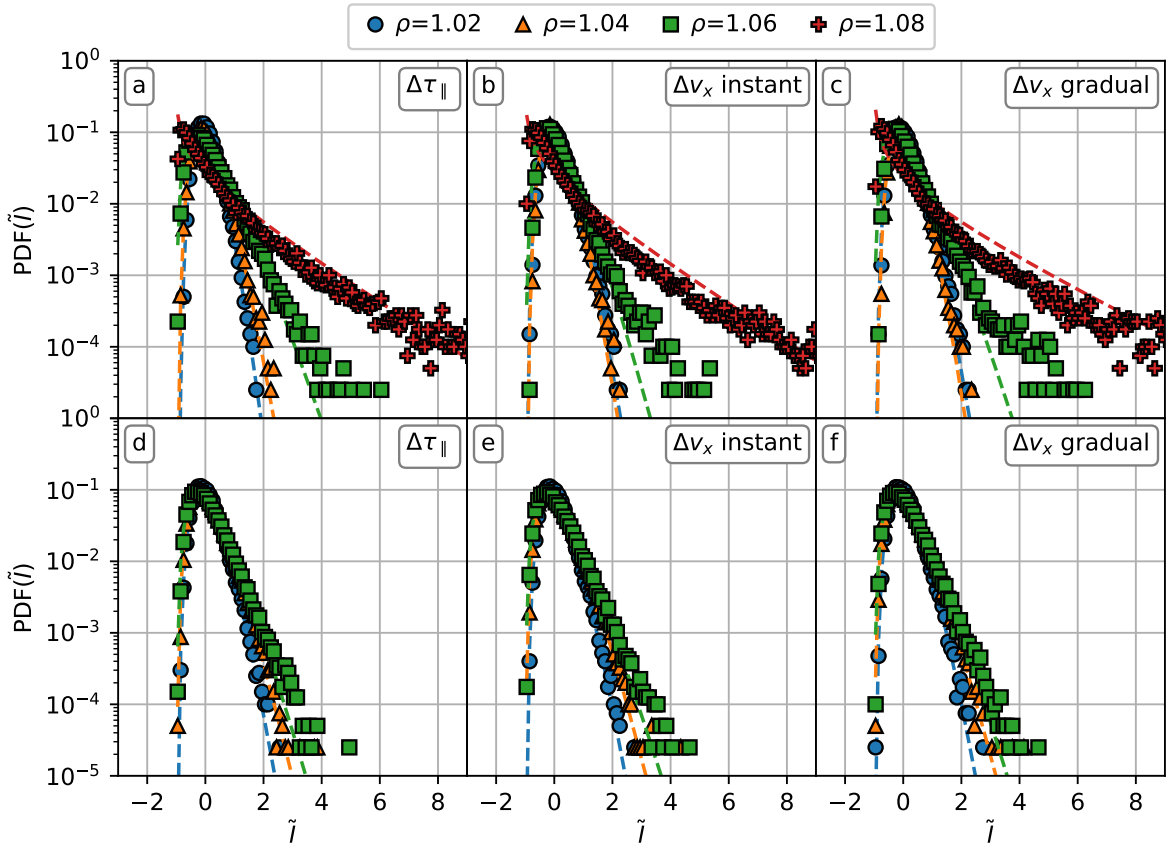

Figure 5.40: Probability distribution functions for different single locations in the SOL for the 2D independent blob case (coloured markers) for shots # 36342, $t \in [2.5, 2.7]$s (a-c), and # 36344, $t \in [2.5, 2.7]$s (d-f). The ρ positions are at $R - R_{\text{sep}} = [11, 24, 36, 49]$mm, and $R - R_{\text{sep}} = [14, 29, 44]$mm, respectively. The Gamma functions calculated from the input parameters, k and θ, are included (dashed lines).

between the two discharge types.

The expected statistical moments from the model have also been calculated for the $\Delta\tau_{\|}$ and instant Δv_x cases and included in the figures. They are seen to match well with the profiles, as well as accurately predict the relative difference in magnitude between the two examples, and capturing the local minimum in the Δv_x cases in figure 5.38. Figures 5.38d and 5.39d show the kurtosis vs skewness. The experimentally observed $K = 3/2S^2$ scaling is seen for the lower values of S and K, which correspond to the SOL locations closest to the separatrix, but diverges as distance into the SOL increases. Whilst some divergence is seen in the experimental results (section 4.4.2.1), the divergence here is larger. If the values of S and K are evaluated at $x = 0$ using equation (5.54) with the adjustment for the distributions, we do return $3/2S^2$ for K, but this is no longer true for $x > 0$ as the other terms in the

Table 5.21: A table showing the shape (k) and scale (θ) input parameters for the Gamma distribution functions for different locations in the SOL for three 2D independent blob case simulations with radial variation in $\tau_{\parallel}$ or v_x shown in figure 5.40.

ρ		1.02		1.04		1.06		1.08	
H-mode	Simulation type	k	θ	k	θ	k	θ	k	θ
	$\Delta\tau_{\parallel}$	9.92	0.0101	7.04	0.142	3.05	0.328	0.548	1.82
	Δv_x instant	7.40	0.135	7.96	0.126	4.07	0.246	0.563	1.78
	Δv_x gradual	7.40	0.135	8.26	0.121	3.33	0.300	0.421	2.38
L-mode	Simulation type	k	θ	k	θ	k	θ	-	-
	$\Delta\tau_{\parallel}$	6.86	0.146	4.81	0.208	7.80	0.263	-	-
	Δv_x instant	6.62	0.151	4.39	0.228	3.44	0.291	-	-
	Δv_x gradual	6.45	0.155	4.31	0.232	3.60	0.278	-	-

equation are included.

We also study the single point PDFs for the 2D independent blob simulations, shown in figure 5.40, with the PDF input parameters in table 5.21. These are again dictated by the relative fluctuation levels, and different simulation PDFs have decreasing shape parameters and increasing scale parameters as radius increases, giving PDFs that resemble the PDFs recorded in experiments. The PDFs all deviate more from normal distributions, whilst still following Gamma distributions, as we increase the distance into the scrape-off layer. As the decreasing decay length example has the largest relative fluctuation levels, these PDFs are the most skewed and flattened, showing PDFs more flattened than any we see in the experimental results, however this could be fine tuned by adjusting other input parameters to the simulations, τ_w or L_y for e.g., without altering the profiles. It is therefore difficult from the PDFs and radial profiles to discern whether a change in filament velocity or parallel timescale is most likely to be the cause of a change in the density profiles in experiments.

5.3 Summary

This chapter used a statistical framework that uses the statistical experimental observations of filaments measured in chapter 4 to describe their effect on the electron density profiles in the scrape-off layer. It is firstly used in the Garcia-Militello model to describe the effect on profiles that have a single decay length throughout the SOL domain. In the single-filament GM model, where all filaments used have the same properties (size, velocity, amplitude, etc.), it is shown that the SOL decay length has a direct proportionality on the filament

velocity and the parallel timescale, a measure of how quickly a filament reduces in amplitude, simulating parallel loses. In this situation, however, no radial variation is seen in any of the SOL statistics (relative fluctuation levels, skewness, kurtosis or single-point PDFs) that are recorded in experiment. This was seen by directly measuring the outputs of the simulations, as well as deriving expressions directly from the statistical framework.

The model has been further advanced here by including the experimentally measured distribution functions of filament attributes in the distributed-filament GM model. Distributions for the filament size had no effect on the profile or the other statical measures. Exponential distributions for the filament amplitudes were necessary to recover the $K = 3/2S^2$ scaling seen for Gamma distributed time-series in experiments. Only the radial velocity distribution had any effect on the profiles, introducing a natural increase of the decay length with distance into the SOL caused by filaments with larger velocities propagating further for a given reduction in amplitude. A relative increase in the parallel timescale was needed to compensate for this, although the exponential function is not a particularly accurate description of the profiles in this instance. This distribution alone was unable to recover the quadratic kurtosis scaling, but was able to cause a radial increase of higher order statistics and increased flattening of single-point PDFs. The distributions of the filament attributes were also accounted for in the theoretical framework. Expressions for the profiles, and the radial profiles of the higher order statistics, were successfully derived, and were good approximations of the simulation outputs.

The model was then used to explore how filaments can be responsible for SOL profiles that cannot be described with a single exponential decay length, such as in shoulder formation. Three different mechanisms were investigated: using a second parallel timescale in the far SOL; using a second radial velocity in the far SOL; and a finite filament acceleration through some region of the SOL. The same approximate result was seen when trying to match these profiles, that a decreasing profile decay length required either a reduced parallel timescale or reduced filament velocity (or negative acceleration), and *vice versa*. However, too much of an instantaneous change in the filament velocity was shown to cause the near SOL profile to largely deviate from an exponential curve, an effect that could be somewhat alleviated in the finite acceleration examples. These results were shown with profiles from simulations, and predictions for those profiles were also derived directly out of the statistical framework.

In these double decay length simulations, some variation was now seen in the near SOL

region of the higher order statistics and the single-point PDFs. For a decreasing decay length, decreasing $\tau_{\parallel}$ caused the relative fluctuation amplitude, skewness, and kurtosis to increase with radius (up to R_{ch}), as seen in experiment results, whereas a decreasing velocity caused these to decrease. A decrease in the filament velocity however, caused the profiles to decrease. It is therefore suggested that, in the single-filament models, the decrease in parallel timescale is likely to be the cause in the decreased profile decay length. Conversely, the case with increased decay length is more likely to be caused by the increase in filament velocity, as this caused the expected increase with radius in the profiles of the higher order statistical quantities. These behaviours were also shown to be derivable from the model too.

Expanding the adjusted models to the adjusted distributed-filament models produced a more complicated picture. Again, a natural increase of the decay length of the profile through the radial velocity distribution required an increase in the parallel timescales, as well as a relative increase in the difference between $\tau_{\parallel,2}/\tau_{\parallel,1}$ ($v_{x,2}/v_{x,1}$) for a reduced decay length. In the example used here, the decrease in the radial velocity was so large that a local density maximum around R_{ch} was produced, an effect that isn't seen in experimental profiles, and as such the large velocity decrease is thought not to be the cause of the decreasing profile decay lengths. Oppositely, a reduced difference of $\tau_{\parallel,2}/\tau_{\parallel,1}$ ($v_{x,2}/v_{x,1}$) was needed for an increasing profile decay length as now the natural change to the decay length by the velocity distribution was working in the same direction as the profile change. In fact, it is postulated that now for some profiles no change in v_x or $\tau_{\parallel}$ would be needed to reproduce some shoulder formation profiles, although this hasn't been tested here.

When the velocity distributions are introduced in the modelling, the higher order radial statistics all increase with distance into the SOL regardless of whether $\tau_{\parallel}$ or v_x increased or decreased, and their behaviour can no longer be used as a way to distinguish which mechanism may be responsible for a change in the profile decay length. These changes are again seen as output from the simulations, but have also been derived from the first principles of the statistical framework.

The results summarised so far have been conducted in both 1D and 2D simulations and model. Any significant differences between the 1D and 2D results can be largely attributed to a difference in the waveform of the filament used and do not affect the qualitative results. It was seen that inclusion of the poloidal sizes and poloidal velocities in the 2D cases had no effect on the profiles generated in the simulations, nor did it affect the profiles in the

modelling. There was also no dependence of the profiles on the ratio between the poloidal and radial velocities, so long as the range of y_0 values that filaments crossed the separatrix at was sufficiently large enough that filaments would track through the furthest part of the simulated SOL.

Chapter 6

Summary, conclusion, and further work

This thesis aimed to make experimental observations of filaments in the scrape-off layer of the ASDEX Upgrade tokamak and characterise them in a way that links their properties and behaviour back to the electron density profiles in the scrape-off layer. This study used the helium gas puff imaging diagnostic, covering a $\approx 6 \times 6\,\mathrm{cm}$ region just below the outboard midplane at a 200 kHz sampling frequency. A simple analytic model was constructed that allowed us to take the images of filaments with the GPI diagnostic and account for the smearing of objects due to the non-perfect alignment between local magnetic field and the diagnostic's line-of-sight, and the finite toroidal size of the gas puff. With this, detailed measurements of filament diameters and velocities in the radial and poloidal directions were made for filaments from four different discharge types: L-mode, L-mode with nitrogen seeding, H-mode with 2.5 MW of NBI heating, and H-mode with 5 MW of NBI heating.

A brief summary of the main results are as follows:

- Radial profiles of relative fluctuation amplitude, skewness, and kurtosis increase with increased distance into the SOL, due to the presence of filaments whose characteristics vary as the propagate radially. The PDFs of the fluctuation signal from single GPI detector pixels follow Gamma distributions, which become increasingly skewed and flattened with increasing radius.

- The L-mode discharge with nitrogen seeding has the largest increase in radial statistics, and greatest skewing and flattening of PDFs, at the furthest into the SOL when

compared to other discharges. This is thought to be due to changes in the filaments, which is corroborated with 2D measurements of the filaments themselves, showing larger mean filament amplitudes and poloidal diameter cross-sections at comparative locations.

- Independent measurements of filament poloidal sizes and radial velocity are made, showing nearly all filaments have diameters larger than the fundamental blob size, and velocities under the maximum predicted by the inertial regime velocity scaling. The exception is at $\rho = 1.02$ in L-mode and N_2 seeded discharges, where half the filaments are smaller than the fundamental blob size, and their velocities are described by the inertial scaling.

- Filament size distributions are measured, with the poloidal size of filaments increasing going from L-mode, to N_2 seeding L-mode, to H-mode discharge types. Filaments in the 5 MW H-mode discharge had the smallest radial diameters, thought to be caused by increased poloidal magnetic shear.

- Radial velocity distributions for L-mode and N_2 seeded discharges show larger velocities at $\rho = 1.02$ compared with other discharge types and positions, although few filaments could be tracked this close to the separatrix in H-mode.

- Poloidal filament velocity distributions are approximately normally distributed, with a low mean velocity in L-mode and N_2 seeded discharges, with a mean that approaches that found in H-mode discharges. The inter-filament poloidal flow was also measured, which showed similar values. This is contrary to the expected poloidal $E \times B$ velocity from the radial electric field, as measured experimentally in Alcator C-mod [67], but does qualitatively agree with the trend previously measured experimentally on ASDEX Upgrade [80].

- 2D distribution functions of filament parameters suggest amplitudes and radial diameters increase as poloidal diameters increase, as well as suggest the largest filaments have the smallest radial velocities, consistent with the inertial filament regime.

- In the single-filament Garcia-Militello model, the decay length of electron density profiles is directly proportional to the radial velocity and the parallel loss timescale of

filaments only, and the model does not produce a radial change in the profiles of higher order statistics, or a change of the single-point PDFs of fluctuations.

- In the distributed-filament GM model, only the introduction of a distribution for the radial velocity of filaments changes the density profile, compared to the single-filament GM model, by increasing the decay length of the profile as distance into the SOL increases. The velocity distribution also increases relative fluctuation levels, skewness, and kurtosis with distance into the SOL.

- If only the filament amplitudes drawn randomly from an exponential distribution, with all other attributes held fixed as in the single-filament GM model, then no change to the profile shape is seen, but the $K = 3/2S^2$ scaling, seen for Gamma distributed fluctuation signals, is returned.

- In the adjusted models, changes to either v_x or $\tau_{\|}$ in the SOL can change the decay length of the density profile, creating profiles that are best described by two exponential decay lengths. For a sufficiently large decrease in the far SOL decay length, it is most likely to be caused by a decrease in $\tau_{\|}$ rather than v_x due to how the latter unrealistically affects the near SOL profile.

- We were able to reproduce the independently measured mean SOL electron density profile shapes by applying a distributed-filament GM model that used measured filament characteristics as inputs. Furthermore, the implication of this is that far SOL profiles are primarily are primarily determined by filament transport and filament physics.

- As the model is extended into 2D, no change of the general results is seen. As such, in this model, the SOL density profiles to not depend on perpendicular filament size or velocity. This is shown directly in the derivations of the expressions from the model, as well as an investigation of the simulated profiles when increasing poloidal-to-radial velocity ratio.

Radial profiles of the relative fluctuation levels, skewness, and kurtosis of the He I line-emission signals from GPI are shown to increase with distance into the SOL due to the advection of filaments through the SOL. The probability distribution functions of the signal intensities from individual GPI pixels are also shown to be nearly normally distributed near the separatrix, showing positive skewness and flattening as distance increases into the SOL,

but are described by Gamma distributions for all positions. The nitrogen seeded discharges had the most skewed and flattened PDFs in the far SOL, as well as the largest range of fluctuations from all the discharges.

Filament amplitudes are found to be exponentially distributed in each discharge type and at every position checked in the SOL. N_2 seeded filaments have a larger mean amplitude than their purely L-mode counterparts, although H-mode discharges had approximately equal large mean amplitudes for their locations in the far SOL. The means of the distributions were found to increase with distance into the SOL as ambient SOL plasma density decreases.

Waiting times between filaments are also found to be exponentially distributed in accordance with a Poisson process, and as such the filaments are uncorrelated with one other. The average waiting times between filaments are found to be approximately equal for all discharge types in the near-to-mid SOL, but increase at larger radii. The L-mode discharges show a larger average waiting time than the H-mode discharges, where the waiting time is also seen to decrease with increased additional NBI heating, suggesting filaments could play a role in power balance of the confined plasma. We note that the waiting times here are unlikely to be the true waiting time of the filaments as it is known that the current method for detecting filaments using a threshold based on the signal's variance does not capture all filaments.

The GPI diagnostic has been used to make simultaneous measurements of the radial and poloidal diameters and velocities of filaments due to its 2D spatial and temporal resolution, and as such distributions of these filament attributes can be measured. Poloidal sizes of filaments are seen to increase in H-mode discharges compared to L-mode, and increases in size with NBI power are also seen between the two H-mode discharge types. The L-mode discharges with and without nitrogen seeding show similar distributions in the near SOL, but those with N_2 show larger sizes in the far SOL, again suggesting a change in the filaments' parallel dynamics that results in more upstream plasma transport. Radial diameters are approximately similar between most discharge types, except in the highest power H-mode. It is suggested that the additional poloidal magnetic shear in that discharge plays a role in reducing the filaments' extent. This mechanism could also be responsible for the larger poloidal sizes seen in these discharge types, causing filaments with non-ciruclar cross-sections to rotate their primary axis so that it aligns to the poloidal direction.

Radial velocity distributions for the L-mode and nitrogen seeded discharges show that

the filaments nearest to the separatrix ($\rho = 1.02$) have the highest velocity than elsewhere in the SOL. Very few filaments can be tracked this close to the separatrix in H-mode and distribution measurements for this location in these discharges couldn't be made with any statistical significance. The rest of the SOL shows approximately similar radial velocity distributions in each discharge type. In addition, the radial velocity of filaments was compared to their poloidal size with respect to the Myra filament velocity model. The overwhelming majority of filaments were measured to be larger than the fundamental blob size, with radial velocities well described by the inertial regime scaling. Velocities that were larger than this scaling could potentially be explained through the addition of warm ions, or were possibly in the resistive x-point regime instead. It was only in L-mode and N_2 seeding discharges at $\rho = 1.02$ where a significant number of filaments, approximately half, were measured to have poloidal sizes smaller than the fundamental blob size, and were instead described by the inertial regime. In these two discharge types, the fastest filaments were again found in the near SOL. Inter-filament flow velocities were also determined for each discharge. The largest radial velocities are again determined to be closest to the separatrix, gradually reducing to zero at the furthest parts of the SOL.

Filament poloidal velocities were inferred and shown to be well approximated by normal distributions. The two L-mode discharges had mean filament velocities in the order of 200 m/s, where as the H-mode discharges were centred around 0 m/s with approximately equal numbers of filaments propagating with positive and negative poloidal velocities. A similar change of the the inter-filament poloidal velocity was also recorded, where the standard deviation of the measurement covered the 0 velocity well. A slight variation of this inter-flow velocity was seen with position but was within the variance of the measurement.

2D distribution functions of filament properties were also investigated. From this, it was found that the filaments with the largest poloidal diameters had the smallest radial velocities, whilst the smallest filaments had the largest range of velocities. It was also generally seen that the larger a filament was in poloidal diameter, the larger it was in radial diameter too, although this seemed to reach a soft maximum size for the distributions in the 5 MW discharge, and again it was postulated that the increased poloidal magnetic field shear in this discharge was breaking up filaments. A positive correlation between poloidal diameter and filament amplitude was also seen.

Future research should look to conduct similarly detailed investigations of the SOL in

the manner of this thesis, as nuances of SOL and filaments from single-point measurements can be lost, for e.g., the average waveform of filaments cannot untangle the size from the velocity. But even these measurements and conclusions have areas for improvement. In order to make any meaningful measurements of filament distributions or statistics in the SOL, the measurements have had to be averaged and all time resolution of the measurements is lost, and as such direct comparison between the filament properties and the macroscopic plasma parameters at the time of the measurements, such as line averaged density for example, could not be made.

Two obvious ways in which this may be improved immediately leap to mind. Repeated plasma discharges with identical parameters could be made, and distributions made from equivalent times in multiple discharges. This may be problematic depending on how well a plasma can be repeated in a tokamak from one shot to another. It is also noted that tokamak time is limited, and alternative scenarios and proposals vying for plasmas could make it difficult to justify multiple repeated plasmas.

One other improvement over the current research would be for changes in the GPI diagnostic equipment to be made. A detector with a higher sensitivity than the Phantom v711 used here would require less gas to be puffed for equivalent signal-to-noise ratios, allowing for higher frequency puff rates, covering a larger percentage of a shot and allowing for more filaments to be included in the analysis. This has the added benefit of potential redesigns to the diagnostic's design, such as better alignment to the magnetic field. Whilst the individual filament measurements could be corrected for this smearing with our toy model, the line-of-site integration for measurements such as the single-point PDFs, or radial statistical profiles could not.

The experimentally measured filament properties were used as inputs to a statistical model of the scrape-off layer. Simulations of this model were based on the characteristics of the ASDEX Upgrade filaments inferred from analysis of the experimental data, randomly generated from filament PDFs and then propagated through the simulated domain. The filament attributes could either be fully controlled, such as enforcing all filaments to be generated with the same size, velocity and amplitude, or could be randomly generated from specified distributions.

The simulation outputs were temporally averaged to produce simulated density profiles created by the filaments, and then the parallel timescale, the characteristic time over which

filament amplitudes reduce due to parallel losses, were changed to match the simulated profiles to experimental ones. Higher order statistical measures of the simulated domain were benchmarked against experimental observations to draw conclusions about the validity of the model used. The simulations and model were conducted in 1D and 2D.

It was concluded that in the single-filament Garcia-Militello mode, where all filaments are identical, the product of the filament velocity and parallel timescale gives the profile decay length. This was found empirically through analysis of the simulations, as well through deriving statistical moments from the model directly. In the 2D single-filament GM model, where a 2D Gaussian was used for the filament waveform, the derived expression for the profile was found to differ to that in Ref. [112], but produced excellent and improved predictions of the simulated profile. These single-filament models, however, could not account for radial increases in the relative fluctuation amplitudes, skewness, or kurtosis, nor for the positive skewing of PDFs, that are universally measured in experiments. Other filament parameters, such as the diameter, velocity, or waiting time between filaments, had no effect on the profile, but did act to scale the profiles.

In the distributed-filament GM model, filament attributes were randomly generated from distributions and introduced one attribute at a time in order to determine their effect. Changing from single filament diameters to distributed diameter sizes had no effect on the profile shapes or any of the higher order measurements. The filament amplitude distribution was found to play no role in altering the profile decay length, but was responsible for the $K = 3/2S^2$ scaling measured universally in experiment SOLs. This was still insufficient to introduce any radial variation in higher order statistical moments, or single-point PDFs. The model was successfully extended and solved to incorporate these distributions and was able to accurately predict the radial statistics.

The only change on profile shapes seen when going from the single-filament to distributed-filament modelwas seen with the inclusion of the radial velocity distributions. These caused a natural increase of the profile decay length with distance into the SOL caused by the fastest filaments propagating further for a given amplitude reduction. In these situations an increased $\tau_{||}$ is required for an equivalent SOL decay length to simulations with no radial velocity distribution, although the profiles now deviate from perfect exponential decay. It was also shown that the radial velocity distributions were necessary for introducing increases in relative fluctuation levels, skewness, and kurtosis, both in terms of measurements of

the simulations and through the addition of the velocity distributions into the statistical framework.

The model and the simulations were extended to generate profiles with double exponential decay lengths. As the scrape-off layer decay lengths have been shown to depend on the parallel timescale and radial velocity, these two parameters are varied independently to generate these non-exponential profiles. Changing parallel timescale simulates a change in the parallel motion of plasma, such as through changes in downstream conditions, or changes in the parallel connection length. Changing the radial velocity simulates either an acceleration or deceleration in the filaments.

In adjusted single-filament models, a decrease in $\tau_{\parallel}$ or v_x was found to cause a decrease in the density profile decay lengths, whilst reducing $\tau_{\parallel}$ was found to cause a radial increase in higher order statistics and positive skewing and flattening of PDFs. On the other hand, decreasing v_x was found to have the opposite effect on the higher order statistics. The opposite effect on the density profile can be obtained when increasing either $\tau_{\parallel}$ or v_x, when increasing the far SOL decay length, but only the increase in velocity would cause the expected increase in higher order statistical profiles.

In each scenario, amplitude distributions were again shown to be necessary, both in simulations of the experimental measurements and in derivations of the statistical framework, in order to regain the $K = 3/2S^2$ scaling of SOL signals, and the velocity distribution necessary to cause an increase in each higher order statistical profile. With distributed radial velocities included, it was difficult to reproduce well matched profiles with decreasing decay lengths by decreasing the filament velocity, however greater matches were found through decreasing the parallel timescale. This leads us to conclude that such a large decrease in profile decay length is more likely to be due to decreases in the parallel timescales rather than decreases in radial velocity. These simulated results were also corroborated with predictions from the quantities derived from the model.

In this work, this statistical model of the scrape-off layer profiles with filaments has been extended to incorporate two methods by which the profile decay length can be changed, as well as the profiles being changed through the inclusion of distributed filament attributes. This was done in terms of implementing the changes into the simulations, as well as changes to the analytical model to derive new expressions for the profiles and higher order statistical profiles. There are ways in which this can be taken further.

For example, the discontinuity caused by a sudden change in the filament velocity was alleviated through the inclusion of a finite filament acceleration over some part of the SOL. In some cases, this could help to make the simulated profiles more accurately match experimental profiles, and in some cases the model could also be solved and the analytical expression matched to the simulated profiles. It would be pertinent to include a similar gradual change in the parallel timescale in the model, for example, a $\tau_{\parallel}$ dictated by spatially-continuous changes in the plasma sound speed and SOL connection length.

The single-filament Garcia-Militello model used prescribes each filament attribute for the time is crosses the separatrix, based off experimental measurements from one location, and these do not change as it propagates through the SOL, with the exception of the amplitude. For the dependent case, the velocity is drawn randomly based on the filament's starting poloidal diameter, which again do not change. A natural extension of this model would be to introduce a change in filament size, either increasing or decreasing in poloidal diameter, which would then have an effect on the radial velocity. This could be achieved either by changing the randomly drawn velocity based on the relative change in expectation velocity as the poloidal size changes, or through prescribing exact velocities for a filament based on filament velocity scaling laws that change as a filament goes from one regime to another.

This model has been extremely useful in elucidating how changes in filament characteristics or dynamics affected various profiles, however, these changes have not been directly linked to changes in the plasma. Further simulations could dynamically solve for a filaments' density and temperature as it propagates through the SOL, accounting for changes at the target, such as decreases in temperature or increases in neutral particle densities. This would ideally be done in a way in which the user still obtains control over the starting filament attributes like in this model, in order to also continue to evolve the statistical framework.

The addition of a synthetic diagnostic may also help to improve the confidence, not only in this statistical framework, but in the validity of any conclusions drawn from various diagnostics. For example, a synthetic gas puff imaging diagnostic that allowed the user to change the alignment between the diagnostic's line-of-sight and the filament would allow one to investigate the effect this may have on higher order statistical moments.

Appendix A

Error calculations

This section will go into detail about how the errors are estimated for various measurements in this thesis. Each time, the law of combination of errors is used [59] to estimate the error σ_f for some function $f(x_1, x_2, \ldots, x_N)$ of N independent variables. The formula used is

$$\sigma_f^2 = \sum_{i=1}^{N} \left(\frac{\partial f}{\partial x_i} \right)^2 \sigma_{x_i}^2 \tag{A.1}$$

where σ_{x_i} is the error of variable x_i.

A.1 Transform angle error

The transform angle, $\phi_{r,\theta}$, is given by equation (4.6) and depends on the quadratic coefficient A, and the reference location R_{ref}, with associated errors σ_A and $\sigma_{R_{\text{ref}}}$. As $\sigma_{R_{\text{ref}}} \ll \sigma_A$, the error on R_{ref} can be neglected, and including it does not affect the error on the transform angle until the 9th decimal place. As such, combining equations (4.6) and (A.1) gives

$$\sigma_{\phi_{r,\theta}} = \frac{2R_{\text{ref}}}{4A^2R_{\text{ref}}^2 + 1}\sigma_A \tag{A.2}$$

which, for the values given in section 4.3.3, gives $\sigma_{\phi_{r,\theta}} = 1.3^\circ$ (0.022 rad).

A.2 Diameter error

The Euclidean distance between the edges of the blob is used to measure the diameter and is given by

$$\delta_x = \sqrt{(R_1 - R_2)^2 + (z_1 - z_2)^2} \tag{A.3}$$

where δ_x is the diameter along either the radial, r, or poloidal, θ, direction vectors, and $(R_i, z_i)_{i=1,2}$ are the pair of position coordinates that define the edge of the blob. An estimate of ± 1 pixel is used as the error in the positions of (R_i, z_i), the largest separations of which are given in table A.1. Equation (A.2) remains unchanged for each direction, as does the expression for the error. δ_x must be differentiated by each variable, giving

$$\begin{aligned}
\frac{\partial \delta_x}{\partial R_1} &= \frac{-(R_2 - R_1)}{\sqrt{(R_1 - R_2)^2 + (z_1 - z_2)^2}}, \\
\frac{\partial \delta_x}{\partial R_2} &= \frac{(R_2 - R_1)}{\sqrt{(R_1 - R_2)^2 + (z_1 - z_2)^2}}, \\
\frac{\partial \delta_x}{\partial z_1} &= \frac{-(z_2 - z_1)}{\sqrt{(R_1 - R_2)^2 + (z_1 - z_2)^2}}, \\
\frac{\partial \delta_x}{\partial z_2} &= \frac{(z_2 - z_1)}{\sqrt{(R_1 - R_2)^2 + (z_1 - z_2)^2}},
\end{aligned} \tag{A.4}$$

where we note the denominator of each derivative is equal to δ_x. Substituting the partial derivatives into equation (A.1), with the errors errors for R_i and z_i as σ_R and σ_z respectively, gives

$$\begin{aligned}
\sigma_{\delta_x}^2 &= \frac{(R_2 - R_1)^2}{\delta_x^2}\sigma_R^2 + \frac{(R_2 - R_1)^2}{\delta_x^2}\sigma_R^2 + \frac{(z_2 - z_1)^2}{\delta_x^2}\sigma_z^2 + \frac{(z_2 - z_1)^2}{\delta_x^2}\sigma_z^2 \\
&= \frac{2}{\delta_x^2}\left[(R_2 - R_1)^2 \sigma_R^2 + (z_2 - z_1)^2 \sigma_z^2\right]
\end{aligned}$$

which, in the approximation of $\sigma_R \approx \sigma_z \equiv \sigma_x$, simplifies to

$$\begin{aligned}
\sigma_{\delta_x}^2 &= \frac{2\sigma_x}{\delta_x^2}\left[(R_2 - R_1)^2 + (z_2 - z_1)^2\right] \\
\sigma_{\delta_x} &= \sqrt{2}\sigma_x = 0.16\,\text{cm}
\end{aligned} \tag{A.5}$$

for the Phantom v711 setup described in this thesis.

Table A.1: A table of error values used in calculating radial and poloidal diameters and velocities.

Variable	Error
R_1 & R_2	1.1 mm
z_1 & z_2	1.0 mm
$\phi_{r,\theta}$	3.0°

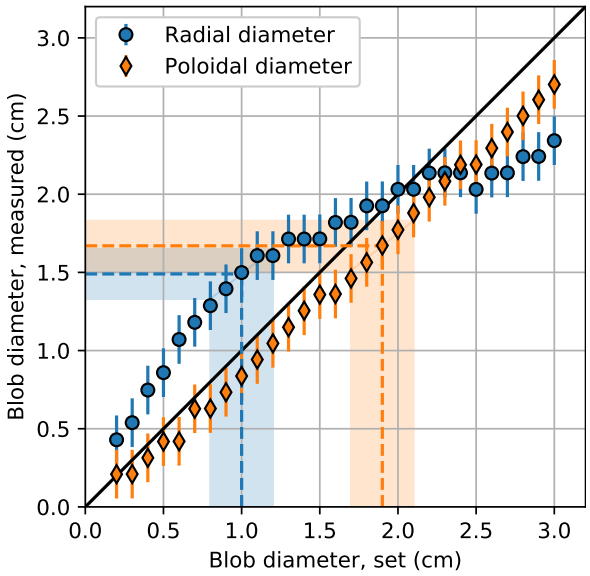

Figure A.1: The measured filament radial diameters (blue circles) and poloidal diameters (orange diamonds) against the filament's set diameter in the synthetic GPI diagnostic for position $[R, z] = [2.150, -0.153]$m. This corresponds to the example blob in figure 4.5, with the measured diameters (horizontal, dashed) and calibrated diameters (vertical dashed) indicated. The shaded areas indicate estimates for the errors. The y=x line is added in black. The y-error plotted is $\sigma_{\delta_x} = 0.16\,\text{cm}$.

As described in section 3.3, a synthetic diagnostic is used to account for the finite toroidal extent of the gas puff and the non-perfect alignment between the line-of-sight of the diagnostic and the magnetic field, which introduces an extra error in the filament diameter measurements. An example for position $[R, z] = [2.150, -0.153]$m, which corresponds to the example blob shown in figure 4.5, is shown in figure A.1. From the diameter measured directly in the GPI frame, and upper and lower bound on the measured diameters can be estimated using $\sigma_{\delta_x} = 0.16\,\text{cm}$ and an upper and lower bound on the calibrated diameters can be estimated using these curves. The typical error associated with the filament diameter is then taken to be half the difference between the upper and lower estimates. This is typically on the order of a few millimetres.

A.3 Velocity error

Equations (4.8) and (4.9) are used to calculate filament velocities. Combing these equations gives full equations for v_r and v_θ as

$$v_r = \sqrt{v_R^2 + v_z^2}\cos\left(\arctan\left(\frac{v_z}{v_R}\right) - \phi_{r,\theta}\right), \tag{A.6}$$

$$v_\theta = \sqrt{v_R^2 + v_z^2}\sin\left(\arctan\left(\frac{v_z}{v_R}\right) - \phi_{r,\theta}\right) \tag{A.7}$$

The error on $\phi_{r,\theta}$ has already been discussed in section A.1, and the error given in table A.1. The velocities v_R and v_z are given by equation (4.7), and only depend on their starting position x_1 at time $t1$, and their end position x_2 at time $t_2 = t_1 + \Delta t$, where x is the R or z coordinate, and Δt is the time between frames, equal to 5 µs in these experiments. Any error on the time is assumed to be negligible, and any error on x_i is assumed to be ± 1 pixel, where the largest pixel errors are given in table A.1.

Here we will go through a detailed breakdown of the error analysis for v_r. We start by calculating the partial derivatives of equation (A.6) to give

$$\begin{aligned}
\frac{\partial v_r}{\partial v_R} &= \frac{v_R\cos\left(\arctan\left(\frac{v_z}{v_R}\right) - \phi_{r,\theta}\right) + v_z\sin\left(\arctan\left(\frac{v_z}{v_R}\right) - \phi_{r,\theta}\right)}{\sqrt{v_R^2 + v_z^2}},\\
\frac{\partial v_r}{\partial v_z} &= \frac{-v_R\sin\left(\arctan\left(\frac{v_z}{v_R}\right) - \phi_{r,\theta}\right) + v_z\cos\left(\arctan\left(\frac{v_z}{v_R}\right) - \phi_{r,\theta}\right)}{\sqrt{v_R^2 + v_z^2}},\\
\frac{\partial v_r}{\partial \phi_{r,\theta}} &= \sqrt{v_R^2 + v_z^2}\sin\left(\arctan\left(\frac{v_z}{v_R}\right) - \phi_{r,\theta}\right).
\end{aligned} \tag{A.8}$$

To obtain expressions for the errors on v_R and v_z, we first differentiate each by the required variable, so

$$\frac{\partial v_x}{\partial x_1} = \frac{-1}{\Delta t}, \qquad \frac{\partial v_x}{\partial x_2} = \frac{1}{\Delta t}, \tag{A.9}$$

which, with the error propagation formula (A.1), gives

$$\begin{aligned}
\sigma_{v_x}^2 &= \frac{1}{\Delta_t^2}\sigma_x^2 + \frac{1}{\Delta_t^2}\sigma_x^2\\
\sigma_{v_x} &= \frac{\sqrt{2}}{\Delta t}\sigma_x.
\end{aligned} \tag{A.10}$$

Using the definition of α in equation (4.9), we start to build the expression for σ_{v_r} by substituting equations (A.8) and (A.10) into equation (A.1), using the assumption that $\sigma_{v_R} \approx \sigma_{v_z} \equiv \sigma_v$

$$\begin{aligned}
\sigma_{v_r}^2 &= \left(\frac{v_R\cos(\alpha) + v_z\sin(\alpha)}{|\mathbf{v}|}\right)^2 \sigma_v^2 + \left(\frac{-v_R\sin(\alpha) + v_z\cos(\alpha)}{|\mathbf{v}|}\right)^2 \sigma_v^2 + |\mathbf{v}|^2 \sin^2(\alpha)\sigma_{\phi_{r,\theta}}^2 \\
\sigma_{v_r}^2 &= \left(v_R^2\left(\sin^2(\alpha) + \cos^2(\alpha)\right) + v_z^2\left(\sin^2(\alpha) + \cos^2(\alpha)\right)\right)\frac{\sigma_v^2}{|\mathbf{v}|^2} + |\mathbf{v}|^2 \sin^2(\alpha)\sigma_{\phi_{r,\theta}}^2 \\
\sigma_{v_r}^2 &= \left(v_R^2 + v_z^2\right)\frac{\sigma_v^2}{|\mathbf{v}|^2} + |\mathbf{v}|^2 \sin^2(\alpha)\sigma_{\phi_{r,\theta}}^2 \\
\sigma_{v_r} &= \sqrt{2\frac{\sigma_x^2}{\Delta t^2} + |\mathbf{v}|^2 \sin^2(\alpha)\sigma_{\phi_{r,\theta}}^2}.
\end{aligned} \tag{A.11}$$

A similar treatment for v_θ on equation (A.7) gives

$$\sigma_{v_\theta} = \sqrt{2\frac{\sigma_x^2}{\Delta t^2} + |\mathbf{v}|^2 \cos^2(\alpha)\sigma_{\phi_{r,\theta}}^2}. \tag{A.12}$$

A.4 Averaging diameter error

In section 4.4.2.2 the average blob size over several frames is used, instead of an instantaneous blob measurement, and as such, the error analysis differs slightly. The mean diameter, $\bar{\delta}_x$, is given by

$$\bar{\delta}_x = \frac{1}{N}\sum_{i=1}^{N} \delta_{x,i} \tag{A.13}$$

where each individual measure of the diameter has an uncertainty, discussed in section A.2. Each partial derivative of equation (A.13) is simply

$$\frac{\partial \bar{\delta}_x}{\partial \delta_{x,i}} = \frac{1}{N}. \tag{A.14}$$

Equations (A.13), and (A.14) combine with the error propagation formula (A.1), to give

$$\begin{aligned}
\sigma^2_{\bar{\delta}_x} &= \sum_{i=1}^{N} \left(\frac{1}{N}\right)^2 \sigma^2_{\delta_{x,i}} \\
\sigma^2_{\bar{\delta}_x} &= \frac{1}{N^2} \sum_{i=1}^{N} \sigma^2_{\delta_{x,i}} \\
\sigma_{\bar{\delta}_x} &= \frac{1}{N} \sqrt{\sum_{i=1}^{N} \sigma^2_{\delta_{x,i}}}.
\end{aligned} \tag{A.15}$$

A.5 Averaging velocity error

In section 4.4.2.3, the average filament velocity over multiple frames is used. The instantaneous velocity can be expressed as $\mathbf{v}_i = (\mathbf{r}_{i+1} - \mathbf{r}_i)/\Delta t$, so the velocity average is

$$\begin{aligned}
\bar{\mathbf{v}} &= \frac{1}{N} \sum_{i=1}^{N} \mathbf{v}_i \\
\bar{\mathbf{v}} &= \frac{1}{N} \left(\frac{\mathbf{r}_2 - \mathbf{r}_1}{\Delta t} + \frac{\mathbf{r}_3 - \mathbf{r}_2}{\Delta t} + \frac{\mathbf{r}_4 - \mathbf{r}_3}{\Delta t} + \ldots \frac{\mathbf{r}_{N+1} - \mathbf{r}_N}{\Delta t} \right) \\
\bar{\mathbf{v}} &= \frac{1}{N} \frac{\mathbf{r}_N - \mathbf{r}_1}{\Delta t}.
\end{aligned} \tag{A.16}$$

This is no different to equation (4.7) bar the factor of $1/N$. Equations (A.9) and (A.1) now become

$$\frac{\partial v_x}{\partial x_1} = \frac{-1}{N\Delta t}, \qquad \frac{\partial v_x}{\partial x_2} = \frac{1}{N\Delta t}, \tag{A.17}$$

and

$$\sigma^2_{v_x} = \frac{\sqrt{2}}{N\Delta t} \sigma_x, \tag{A.18}$$

respectively. A similar process method to section A.3 is used, and equations (A.11) and (A.12) become

$$\sigma_{\bar{v}_r} = \sqrt{2\frac{\sigma_x^2}{N^2\Delta t^2} + |\mathbf{v}|^2 \sin^2(\alpha) \sigma^2_{\phi_{r,\theta}}} \tag{A.19}$$

$$\sigma_{\bar{v}_\theta} = \sqrt{2\frac{\sigma_x^2}{N^2\Delta t^2} + |\mathbf{v}|^2 \cos^2(\alpha) \sigma^2_{\phi_{r,\theta}}}, \tag{A.20}$$

where $|\mathbf{v}|$ is now the average velocity magnitude between $\mathbf{r}_N$ and $\mathbf{r}_1$.

List of References

[1] J. Ongena and G. V. Oost. Energy for Future Centuries: Will Fusion Be an Inexhaustible, Safe, and Clean Energy Source? *Fusion Science and Technology*, 45(2T):3, 2004.

[2] L. L. Lucas and M. P. Unterweger. Comprehensive Review and Critical Evaluation of the Half-Life of Tritium. *Journal of Research of the National Institute of Standards and Technology*, 105(4):541, 2000.

[3] E. Joffrin, et al. Overview of the JET preparation for deuterium-tritium operation with the ITER like-wall. *Nuclear Fusion*, 59(11):112021, 2019.

[4] J. Wesson. *Tokamaks*. Oxford University Press, Oxford, 3rd edition, 2004.

[5] S. Le Pape, et al. Fusion Energy Output Greater than the Kinetic Energy of an Imploding Shell at the National Ignition Facility. *Physical Review Letters*, 120(24):245003, 2018.

[6] I. Cziegler. *Turbulence and Transport Phenomena in Edge and Scrape-Off-Layer Plasmas*. Ph.D. thesis, Massachusetts Institute of Technology, 2011.

[7] T. Munsat and S. J. Zweben. Derivation of time-dependent two-dimensional velocity field maps for plasma turbulence studies. *Review of Scientific Instruments*, 77(10):103501, 2006.

[8] D. A. D'Ippolito, J. R. Myra, and S. J. Zweben. Convective transport by intermittent blob-filaments: Comparison of theory and experiment, 2011.

[9] F. van Wyk, E. G. Highcock, A. R. Field, C. M. Roach, A. A. Schekochihin, F. I. Parra, and W. Dorland. Ion-scale turbulence in MAST: anomalous transport, subcritical transitions, and comparison to BES measurements, 2017.

[10] T. Klinger, et al. Overview of first Wendelstein 7-X high-performance operation. *Nuclear Fusion*, 59(11):112004, 2019.

[11] H. Meyer, et al. Overview of physics studies on ASDEX Upgrade. *Nuclear Fusion*, 59(11):112014, 2019.

[12] F. Wagner, et al. Regime of Improved Confinement and High Beta in Neutral-Beam-Heated Divertor Discharges of the ASDEX Tokamak. *Physical Review Letters*, 49(19):1408, 1982.

[13] A. Kallenbach. The ASDEX Upgrade tokamak. Technical report, Max Planck Institute for Plasma Physics, Garching bei München, 2016.

[14] J. C. Fuchs, P. J. McCarthy, W. Schneider, and the ASDEX-Upgrade Team. libkk: Routines and Tools for Working with Equilibria Data. Technical report, Max Planck Institute for Plasma Physics, Garching bei München, 2019.

[15] Y. C. Ghim, A. R. Field, D. Dunai, S. Zoletnik, L. Bardóczi, A. A. Schekochihin, and the MAST Team. Measurement and physical interpretation of the mean motion of turbulent density patterns detected by the beam emission spectroscopy system on the mega amp spherical tokamak. *Plasma Physics and Controlled Fusion*, 54(9):095012, 2012.

[16] H. S. Bosch, et al. 2D modelling of the ASDEX-Upgrade scrape-off layer and divertor plasma. *Journal of Nuclear Materials*, 220-222:558, 1995.

[17] J. R. Myra, D. A. Russell, and D. A. D'Ippolito. Collisionality and magnetic geometry effects on tokamak edge turbulent transport. I. A two-region model with application to blobs. *Physics of Plasmas*, 13(11):112502, 2006.

[18] A. Bencze, M. Berta, A. Buzás, P. Hacek, J. Krbec, and M. Szutyányi. Characterization of edge and scrape-off layer fluctuations using the fast Li-BES system on COMPASS. *Plasma Physics and Controlled Fusion*, 61(8):085014, 2019.

[19] S. J. Zweben, J. L. Terry, D. P. Stotler, and R. J. Maqueda. Invited Review Article: Gas puff imaging diagnostics of edge plasma turbulence in magnetic fusion devices. *Review of Scientific Instruments*, 88(4):041101, 2017.

[20] M. Agostini, S. J. Zweben, R. Cavazzana, P. Scarin, G. Serianni, R. J. Maqueda, and D. P. Stotler. Study of statistical properties of edge turbulence in the National Spherical Torus Experiment with the gas puff imaging diagnostic. *Physics of Plasmas*, 14(10):102305, 2007.

[21] M. V. Umansky, S. I. Krasheninnikov, B. LaBombard, and J. L. Terry. Comments on particle and energy balance in the edge plasma of Alcator C-Mod. *Physics of Plasmas*, 5(9):3373, 1998.

[22] B. LaBombard, M. V. Umansky, R. L. Boivin, J. A. Goetz, J. Hughes, B. Lipschultz, D. Mossessian, C. S. Pitcher, and J. L. Terry. Cross-field plasma transport and main-chamber recycling in diverted plasmas on Alcator C-Mod. *Nuclear Fusion*, 40(12):2041, 2000.

[23] O. E. Garcia, J. Horacek, R. A. Pitts, A. H. Nielsen, W. Fundamenski, V. Naulin, and J. J. Rasmussen. Fluctuations and transport in the TCV scrape-off layer. *Nuclear Fusion*, 47(7):667, 2007.

[24] T. Farley, et al. Filament identification in wide-angle high speed imaging of the mega amp spherical tokamak. *Review of Scientific Instruments*, 90(9):093502, 2019.

[25] J. Cavalier, N. Lemoine, F. Brochard, V. Weinzettl, J. Seidl, S. Silburn, P. Tamain, R. Dejarnac, J. Adamek, and R. Panek. Tomographic reconstruction of tokamak edge turbulence from single visible camera data and automatic turbulence structure tracking. *Nuclear Fusion*, 59(5):056025, 2019.

[26] J. A. Boedo, et al. Transport by intermittency in the boundary of the DIII-D tokamak. *Physics of Plasmas*, 10(5 II):1670, 2003.

[27] G. S. Xu, et al. Blob/hole formation and zonal-flow generation in the edge plasma of the JET tokamak. *Nuclear Fusion*, 49(9):092002, 2009.

[28] S. J. Zweben, et al. Edge turbulence imaging in the Alcator C-Mod tokamak. *Physics of Plasmas*, 9(5):1981, 2002.

[29] G. Y. Antar, S. I. Krasheninnikov, P. Devynck, R. P. Doerner, E. M. Hollmann, J. A. Boedo, S. C. Luckhardt, and R. W. Conn. Experimental Evidence of Intermittent

Convection in the Edge of Magnetic Confinement Devices. *Physical Review Letters*, 87(6):65001, 2001.

[30] C. Killer, B. Shanahan, O. Grulke, M. Endler, K. Hammond, L. Rudischhauser, and W7-X Team. Plasma filaments in the scrape-off layer of Wendelstein 7-X. *Plasma Physics and Controlled Fusion*, 62(8):085003, 2020.

[31] M. Spolaore, N. Vianello, M. Agostini, R. Cavazzana, E. Martines, P. Scarin, G. Serianni, E. Spada, M. Zuin, and V. Antoni. Direct measurement of current filament structures in a magnetic-confinement fusion device. *Physical Review Letters*, 102(16):165001, 2009.

[32] N. Katz, J. Egedal, W. Fox, A. Le, and M. Porkolab. Experiments on the propagation of plasma filaments. *Physical Review Letters*, 101(1):015003, 2008.

[33] M. Willensdorfer, G. Birkenmeier, R. Fischer, F. M. Laggner, E. Wolfrum, G. Veres, F. Aumayr, D. Carralero, L. Guimarãis, and B. Kurzan. Characterization of the Li-BES at ASDEX Upgrade. *Plasma Physics and Controlled Fusion*, 56(2):025008, 2014.

[34] J. L. Terry, S. J. Zweben, M. V. Umansky, I. Cziegler, O. Grulke, B. LaBombard, and D. P. Stotler. Spatial structure of scrape-off-layer filaments near the midplane and X-point regions of Alcator-C-Mod. *Journal of Nuclear Materials*, 390-391(1):339, 2009.

[35] S. I. Krasheninnikov. On scrape off layer plasma transport. *Physics Letters, Section A: General, Atomic and Solid State Physics*, 283(5-6):368, 2001.

[36] J. R. Myra, D. A. D'Ippolito, D. P. Stotler, S. J. Zweben, B. P. LeBlanc, J. E. Menard, R. J. Maqueda, and J. Boedo. Blob birth and transport in the tokamak edge plasma: Analysis of imaging data. *Physics of Plasmas*, 13(9):92509, 2006.

[37] S. I. Krasheninnikov and A. I. Smolyakov. Dynamics and generation mechanisms of mesoscale structures in tokamak edge plasmas. *Physics of Plasmas*, 15(5):055909, 2008.

[38] D. A. D'Ippolito, J. R. Myra, and S. I. Krasheninnikov. Cross-field blob transport in tokamak scrape-off-layer plasmas. *Physics of Plasmas*, 9(1):222, 2002.

[39] D. Carralero, P. Manz, L. Aho-Mantila, G. Birkenmeier, M. Brix, M. Groth, H. W. Müller, U. Stroth, N. Vianello, and E. Wolfrum. Experimental Validation of a Filament Transport Model in Turbulent Magnetized Plasmas. *Physical Review Letters*, 115(21):215002, 2015.

[40] O. E. Garcia, N. H. Bian, and W. Fundamenski. Radial interchange motions of plasma filaments. *Physics of Plasmas*, 13(8):082309, 2006.

[41] G. Q. Yu and S. I. Krasheninnikov. Dynamics of blobs in scrape-off-layer/shadow regions of tokamaks and linear devices. *Physics of Plasmas*, 10(11):4413, 2003.

[42] P. Manz, D. Carralero, G. Birkenmeier, H. W. Müller, S. H. Müller, G. Fuchert, B. D. Scott, and U. Stroth. Filament velocity scaling laws for warm ions. *Physics of Plasmas*, 20(10):102307, 2013.

[43] D. Carralero, G. Birkenmeier, H. W. Müller, P. Manz, P. Demarne, S. H. Müller, F. Reimold, U. Stroth, M. Wischmeier, and E. Wolfrum. An experimental investigation of the high density transition of the scrape-off layer transport in ASDEX Upgrade. *Nuclear Fusion*, 54(12):123005, 2014.

[44] D. Carralero, et al. Recent progress towards a quantitative description of filamentary SOL transport. *Nuclear Fusion*, 57(5):056044, 2017.

[45] D. Carralero, et al. Implications of high density operation on SOL transport: A multimachine investigation. *Journal of Nuclear Materials*, 463:123, 2015.

[46] B. Nold, G. D. Conway, T. Happel, H. W. Müller, M. Ramisch, V. Rohde, and U. Stroth. Generation of blobs and holes in the edge of the ASDEX Upgrade tokamak. *Plasma Physics and Controlled Fusion*, 52(6):065005, 2010.

[47] G. Y. Antar, G. Counsell, Y. Yu, B. Labombard, and P. Devynck. Universality of intermittent convective transport in the scrape-off layer of magnetically confined devices. *Physics of Plasmas*, 10(2):419, 2003.

[48] F. Militello, P. Tamain, W. Fundamenski, A. Kirk, V. Naulin, and A. H. Nielsen. Experimental and numerical characterization of the turbulence in the scrape-off layer of MAST. *Plasma Physics and Controlled Fusion*, 55(2):12, 2013.

[49] N. R. Walkden, A. Wynn, F. Militello, B. Lipschultz, G. Matthews, C. Guillemaut, J. Harrison, and D. Moulton. Statistical analysis of the ion flux to the JET outer wall. *Nuclear Fusion*, 57(3):036016, 2017.

[50] A. Theodorsen, O. E. Garcia, R. Kube, B. Labombard, and J. L. Terry. Universality of Poisson-driven plasma fluctuations in the Alcator C-Mod scrape-off layer. *Physics of Plasmas*, 25(12):122309, 2018.

[51] D. Carralero, et al. On the role of filaments in perpendicular heat transport at the scrape-off layer. *Nuclear Fusion*, 58(9):096015, 2018.

[52] O. E. Garcia, I. Cziegler, R. Kube, B. LaBombard, and J. L. Terry. Burst statistics in Alcator C-Mod SOL turbulence. *Journal of Nuclear Materials*, 438(SUPPL):S180, 2013.

[53] J. Horacek, R. A. Pitts, and J. P. Graves. Overview of edge electrostatic turbulence experiments on TCV. In *Czechoslovak Journal of Physics*, volume 55, pages 271–283. 2005.

[54] J. P. Graves, J. Horacek, R. A. Pitts, and K. I. Hopcraft. Self-similar density turbulence in the TCV tokamak scrape-off layer. *Plasma Physics and Controlled Fusion*, 47(3):L1, 2005.

[55] P. J. Davis. Leonhard Euler's Integral: A Historical Profile of the Gamma Function: In Memoriam: Milton Abramowitz. *The American Mathematical Monthly*, 66(10):849, 1959.

[56] O. E. Garcia. Stochastic modeling of intermittent scrape-off layer plasma fluctuations. *Physical Review Letters*, 108(26):265001, 2012.

[57] O. E. Garcia, S. M. Fritzner, R. Kube, I. Cziegler, B. Labombard, and J. L. Terry. Intermittent fluctuations in the Alcator C-Mod scrape-off layer. *Physics of Plasmas*, 20(5):055901, 2013.

[58] O. E. Garcia, R. Kube, A. Theodorsen, B. LaBombard, and J. L. Terry. Intermittent fluctuations in the Alcator C-Mod scrape-off layer for ohmic and high confinement mode plasmas. *Physics of Plasmas*, 25(5):056103, 2018.

[59] R. J. Barlow. *Statistics: A Guide to the Use of Statistical Methods in the Physical Sciences*. John Wiley & Sons Ltd, Chichester, 1st edition, 1989.

[60] O. E. Garcia, R. A. Pitts, J. Horacek, A. H. Nielsen, W. Fundamenski, J. P. Graves, V. Naulin, and J. J. Rasmussen. Turbulent transport in the TCV SOL. *Journal of Nuclear Materials*, 363-365(1-3):575, 2007.

[61] B. Labit, I. Furno, A. Fasoli, A. Diallo, S. H. Müller, G. Plyushchev, M. Podestà, and F. M. Poli. Universal statistical properties of drift-interchange turbulence in TORPEX plasmas. *Physical Review Letters*, 98(25):1, 2007.

[62] A. Theodorsen, O. E. Garcia, J. Horacek, R. Kube, and R. A. Pitts. Scrape-off layer turbulence in TCV: Evidence in support of stochastic modelling. *Plasma Physics and Controlled Fusion*, 58(4):044006, 2016.

[63] R. Kube, A. Theodorsen, O. E. Garcia, B. Labombard, and J. L. Terry. Fluctuation statistics in the scrape-off layer of Alcator C-Mod. *Plasma Physics and Controlled Fusion*, 58(5):054001, 2016.

[64] R. Kube, O. E. Garcia, A. Theodorsen, D. Brunner, A. Q. Kuang, B. LaBombard, and J. L. Terry. Intermittent electron density and temperature fluctuations and associated fluxes in the Alcator C-Mod scrape-off layer. *Plasma Physics and Controlled Fusion*, 60(6):065002, 2018.

[65] A. Theodorsen, O. E. Garcia, and M. Rypdal. Statistical properties of a filtered Poisson process with additive random noise: Distributions, correlations and moment estimation. *Physica Scripta*, 92(5):054002, 2017.

[66] A. Theodorsen and O. E. Garcia. Level crossings and excess times due to a superposition of uncorrelated exponential pulses. *Physical Review E*, 97(1):012110, 2018.

[67] I. Cziegler, J. L. Terry, J. W. Hughes, and B. Labombard. Experimental studies of edge turbulence and confinement in Alcator C-Mod. *Physics of Plasmas*, 17(5):056120, 2010.

[68] R. Kube, A. Theodorsen, O. E. Garcia, D. Brunner, B. Labombard, and J. L. Terry. Comparison between mirror Langmuir probe and gas-puff imaging measurements of

intermittent fluctuations in the Alcator C-Mod scrape-off layer. *Journal of Plasma Physics*, 86(5):905860519, 2020.

[69] A. Theodorsen and O. E. Garcia. Probability distribution functions for intermittent scrape-off layer plasma fluctuations. *arXiv*, 60(3):034006, 2018.

[70] B. LaBombard, R. L. Boivin, M. Greenwald, J. Hughes, B. Lipschultz, D. Mossessian, C. S. Pitcher, J. L. Terry, and S. J. Zweben. Particle transport in the scrape-off layer and its relationship to discharge density limit in Alcator C-Mod. *Physics of Plasmas*, 8(5 II):2107, 2001.

[71] K. McCormick, G. Kyriakakis, J. Neuhauser, E. Kakoulidis, J. Schweinzer, and N. Tsois. Particle and energy transport scalings in the ASDEX scrape-off layer. *Journal of Nuclear Materials*, 196-198(C):264, 1992.

[72] N. Asakura, Y. Koide, K. Itami, N. Hosogane, K. Shimizu, S. Tsuji-Iio, S. Sakurai, and A. Sakasai. SOL plasma profiles under radiative and detached divertor conditions in JT-60U. *Journal of Nuclear Materials*, 241-243:559, 1997.

[73] B. Lipschultz, B. LaBombard, C. S. Pitcher, and R. Boivin. Investigation of the origin of neutrals in the main chamber of Alcator C-Mod. *Plasma Physics and Controlled Fusion*, 44(6):733, 2002.

[74] F. Militello, L. Garzotti, J. Harrison, J. T. Omotani, R. Scannell, S. Allan, A. Kirk, I. Lupelli, and A. J. Thornton. Characterisation of the L-mode scrape off layer in MAST: Decay lengths. *Nuclear Fusion*, 56(1):016006, 2015.

[75] J. L. Terry, et al. Transport phenomena in the edge of Alcator C-Mod plasmas. *Nuclear Fusion*, 45(11):1321, 2005.

[76] M. Greenwald, J. L. Terry, S. M. Wolfe, G. H. Neilson, M. G. Zwebellben, S. M. Kaye, and G. H. Neilson. A new look at density limits in tokamaks. *Nuclear Fusion*, 28(12):2207, 1988.

[77] A. Wynn, et al. Investigation into the formation of the scrape-off layer density shoulder in JET ITER-like wall L-mode and H-mode plasmas. *Nuclear Fusion*, 58(5):056001, 2018.

[78] A. D. Light, S. C. Thakur, C. Brandt, Y. Sechrest, G. R. Tynan, and T. Munsat. Direct extraction of coherent mode properties from imaging measurements in a linear plasma column. *Physics of Plasmas*, 20(8):082120, 2013.

[79] S. C. Thakur, C. Brandt, A. Light, L. Cui, J. J. Gosselin, and G. R. Tynan. Simultaneous use of camera and probe diagnostics to unambiguously identify and study the dynamics of multiple underlying instabilities during the route to plasma turbulence. *Review of Scientific Instruments*, 85(11):11E813, 2014.

[80] G. Fuchert, G. Birkenmeier, D. Carralero, T. Lunt, P. Manz, H. W. Müller, B. Nold, M. Ramisch, V. Rohde, and U. Stroth. Blob properties in L- And H-mode from gas-puff imaging in ASDEX upgrade. *Plasma Physics and Controlled Fusion*, 56(12):125001, 2014.

[81] M. Griener, et al. Fast piezoelectric valve offering controlled gas injection in magnetically confined fusion plasmas for diagnostic and fuelling purposes. *Review of Scientific Instruments*, 88(3):033509, 2017.

[82] M. Griener, E. Wolfrum, M. Cavedon, R. Dux, V. Rohde, M. Sochor, J. M. Muñoz Burgos, O. Schmitz, and U. Stroth. Helium line ratio spectroscopy for high spatiotemporal resolution plasma edge profile measurements at ASDEX Upgrade (invited). *Review of Scientific Instruments*, 89(10):10D102, 2018.

[83] I. H. Hutchinson. *Principles of Plasma Diagnostics*. Cambridge University Press, Cambridge, 2nd edition, 2002.

[84] R. M. McDermott, C. Angioni, R. Dux, A. Gude, T. Pütterich, F. Ryter, G. Tardini, and t. A. U. Team. Effect of electron cyclotron resonance heating (ECRH) on toroidal rotation in ASDEX Upgrade H-mode discharges. *Plasma Physics and Controlled Fusion*, 53(3):035007, 2011.

[85] M. Goto. Collisional-radiative model for neutral helium in plasma revisited. *Journal of Quantitative Spectroscopy and Radiative Transfer*, 76(3-4):331, 2003.

[86] D. Stotler. Collisional Radiative Model for Helium, 2013. <`https://w3.pppl.gov/degas2/he_crII.txt`> (Accessed: 2021-06-17).

[87] D. R. Durran. *Numerical Methods for Fluid Dynamics*. Springer, New York, 2nd edition, 2010.

[88] A. Scarabosio, C. Fuchs, A. Herrmann, and E. Wolfrum. ELM characteristics and divertor heat loads in ASDEX Upgrade helium discharges. *Journal of Nuclear Materials*, 415(Supplement 1):S877, 2011.

[89] M. Farge. Wavelet transforms and their applications to turbulence. *Annual Review of Fluid Mechanics*, 24:395, 1992.

[90] W. Zhang, et al. Blob distortion by radio-frequency induced sheared flow. *Nuclear Fusion*, 59(7):074001, 2019.

[91] G. Birkenmeier, et al. Magnetic field dependence of the blob dynamics in the edge of ASDEX upgrade L-mode plasmas. *Plasma Physics and Controlled Fusion*, 56(7):075019, 2014.

[92] A. Theodorsen, O. E. Garcia, R. Kube, B. LaBombard, and J. L. Terry. Relationship between frequency power spectra and intermittent, large-amplitude bursts in the Alcator C-Mod scrape-off layer. *Nuclear Fusion*, 57(11):114004, 2017.

[93] V. Antoni, V. Carbone, E. Martines, G. Regnoli, G. Serianni, N. Vianello, and P. Veltri. Electrostatic turbulence intermittency and MHD relaxation phenomena in a RFP plasma. *Europhysics Letters*, 54(1):51, 2001.

[94] M. Bonamente. *Statistics and Analysis of Scientific Data*. Springer, New York, 2nd edition, 2017.

[95] A. Q. Kuang, B. LaBombard, D. Brunner, O. E. Garcia, R. Kube, and A. Theodorsen. Plasma fluctuations in the scrape-off layer and at the divertor target in Alcator C-Mod and their relationship to divertor collisionality and density shoulder formation. *Nuclear Materials and Energy*, 19(C):295, 2019.

[96] G. Y. Antar, M. Tsalas, E. Wolfrum, and V. Rohde. Turbulence during H- and L-mode plasmas in the scrape-off layer of the ASDEX Upgrade tokamak. *Plasma Physics and Controlled Fusion*, 50(9):095012, 2008.

[97] G. Antar, S. Assas, V. Bobkov, J. M. Noterdaeme, E. Wolfrum, A. Herrmann, and V. Rohde. Convective transport suppression in the scrape-off layer using ion cyclotron resonance heating on the asdex upgrade tokamak. *Physical Review Letters*, 105(16):165001, 2010.

[98] P. J. McCarthy, P. Martin, and W. Schneider. The CLISTE Interpretive Equilibrium Code, IPP Report 5/85. Technical report, Max Planck Institute for Plasma Physics, Garching bei München, 1999.

[99] J. Horacek, J. Adamek, H. W. Muller, J. Seidl, A. H. Nielsen, V. Rohde, F. Mehlmann, C. Ionita, and E. Havlíčková. Interpretation of fast measurements of plasma potential, temperature and density in SOL of ASDEX Upgrade. *Nuclear Fusion*, 50(10):105001, 2010.

[100] S. I. Krasheninnikov, D. A. D'Ippolito, and J. R. Myra. Recent theoretical progress in understanding coherent structures in edge and SOL turbulence. *Journal of Plasma Physics*, 74(5):679, 2008.

[101] R. Kube, O. E. Garcia, A. Theodorsen, A. Q. Kuang, B. LaBombard, J. L. Terry, and D. Brunner. Statistical properties of the plasma fluctuations and turbulent cross-field fluxes in the outboard mid-plane scrape-off layer of Alcator C-Mod. *Nuclear Materials and Energy*, 18:193, 2019.

[102] L. Wang, G. R. Tynan, R. Hong, L. Nie, Y. Chen, R. Ke, T. Wu, T. Long, P. Zheng, and M. Xu. Edge turbulence evolution and intermittency development near the density limit on the HL-2A tokamak. *Physics of Plasmas*, 26(9):092303, 2019.

[103] T. P. M. Farley. *Analysis of Plasma Filaments with Fast Visible Imaging in the Mega Ampère Spherical Tokamak*. Phd thesis, University of Licerpool, 2019.

[104] N. Offeddu, et al. Cross-field and parallel dynamics of SOL filaments in TCV. *Nuclear Fusion*, 62(9):096014, 2022.

[105] H. Sakoe and S. Chiba. Dynamic Programming Algorithm Optimization for Spoken Word Recognition. *IEEE Transactions on Acoustics, Speech, and Signal Processing*, 26(1):43, 1978.

[106] G. M. Quénot, J. Pakleza, and T. A. Kowalewski. Particle image velocimetry with optical flow. *Experiments in Fluids*, 25(3):177, 1998.

[107] Y. W. Enters, S. Thomas, M. Hill, and I. Cziegler. Quantifying the uncertainties associated with imaging velocimetry techniques. *In Progress*, 2022.

[108] P. C. Stangeby. *The Plasma Boundary of Magnetic Fusion Devices*. IOP Publishing, Bristol, 2000.

[109] W. A. Gracias, P. Tamain, E. Serre, R. A. Pitts, and L. García. The impact of magnetic shear on the dynamics of a seeded 3D filament in slab geometry. *Nuclear Materials and Energy*, 12:798, 2017.

[110] F. Militello and J. T. Omotani. Scrape off layer profiles interpreted with filament dynamics. *Nuclear Fusion*, 56(10):104004, 2016.

[111] O. E. Garcia, R. Kube, A. Theodorsen, and H. L. Pécseli. Stochastic modelling of intermittent fluctuations in the scrape-off layer: Correlations, distributions, level crossings, and moment estimation. *Physics of Plasmas*, 23(5):052308, 2016.

[112] F. Militello, T. Farley, K. Mukhi, N. Walkden, and J. T. Omotani. A two-dimensional statistical framework connecting thermodynamic profiles with filaments in the scrape off layer and application to experiments. *Physics of Plasmas*, 25(5):056112, 2018.

[113] F. Militello and J. T. Omotani. On the relation between non-exponential scrape off layer profiles and the dynamics of filaments. *Plasma Physics and Controlled Fusion*, 58(12):125004, 2016.

[114] D. W. Jordan and P. Smith. *Mathematical techniques: An introduction for the engineering, physical, and mathematical sciences*. Oxford University Press, Oxford, 3rd edition, 2002.

[115] H. L. Pécseli. *Fluctuations in Physical Systems*. Cambridge University Press, Cambridge, 2000.

[116] J. T. Omotani, F. Militello, L. Easy, and N. R. Walkden. The effects of shape and amplitude on the velocity of scrape-off layer filaments. *Plasma Physics and Controlled Fusion*, 58(1):014030, 2015.